Mapping the phase diagram of Quantum Chromodynamics via fluctuations

by

Maneesha Sushama Pradeep
Master of Science, 2015 (5 year Integrated Programme)

Thesis submitted in partial fulfillment of the requirements
for the degree of Doctor of Philosophy in Physics
in the Graduate College of the
University of Illinois at Chicago, 2023

Chicago, Illinois

Defense Committee:
Mikhail Stephanov, Chair and Advisor
Ho-Ung Yee
Olga Evdokimov
Dirk Morr
Gokce Basar, University of North Carolina, Chapel Hill

This thesis is dedicated to my beloved physics teacher, Shankaranarayan Sir .

ACKNOWLEDGMENTS

First and foremost, I want to express my sincere gratitude to my thesis advisor Prof. Mikhail Stephanov for his constant encouragement and support throughout my Ph.D studies. His keen intuition and timely guidance has changed the trajectory of this thesis into directions that were unforeseen by me. I am amazed by the clarity he seeks in his understanding, leading to creative and non-trivial insights. He also introduced me to collaborations and gave me ample opportunities to attend summer schools, conferences and meetings which helped me to meet and discuss with experts in wide range of topics. Beyond all this, I am deeply indebted to him for his kindness, patience and the time that he invested in me and consider it as one of my biggest privileges to have had the opportunity to learn from him.

I want to thank my thesis committee members for devoting their time for this thesis and for the valuable comments and questions. I am thankful to my collaborators Prof. Krishna Rajagopal and Prof. Yi Yin for their time and expertise that they devoted for our projects which form an integral part of this thesis. I have immensely benefitted from their foresights and broad knowledge in the subject. I also want to gratefully acknowledge the contributions of Ryan Weller, who collaborated with us in the initial stages of this project on dynamics of fluctuations.

I have also greatly benefitted from my interactions with Prof. Ho-Ung Yee during our lunch meetings. Some parts of this thesis have been substantially refined due to my interactions with him. I am also thankful to the past and current members of our group and other collabora-

ACKNOWLEDGMENTS (Continued)

tors, namely Dr. Noriyuki Sogabe, Dr. Masaru Hongo, Dr. Gokce Basar, Dr. Shiyong Lee, Dr. Xin An and Dr.Jamie Karthein for influential discussions. I also want to thank James Nell and Melissa Mattingly for always being kind and ready to help whenever I had an administrative need. I also would like to express my gratitude to my guides and mentors from NISER,Bhubaneswar and TIFR,Mumbai in India.

Chicago will always be my second home, due to my friends here who became my family. I specifically want to mention James, Mahesh, Prolay, and Radwa, for being there for me at difficult times. I am thankful to Agnieszka, Lipei, Shuzhe and Xin for our zoom discussions during the pandemic , providing a space to connect with fellow students and learn during the covid times. Thank you James and Tuffy for inviting me to be a part of your Thanksgiving traditions, I have never felt more at home in the US. Thanks to Prof. Anne George and family for making me a part of their Christmas celebrations and feeding me my most favorite dosas and appams whenever I missed them. Thanks to Irin, Abdul, Shruti and Linta for celebrating Onam, Vishu and Eid with me.

I fall short of words to express my gratitude to my parents, Pradeep and Sushama and my aunt, Swapna for their relentless support and love throughout my life . Thanks to my grandmother, Leela for sending me thoughtful letters once in awhile. Thanks to my sister, Nimisha and cousin Prarthana for listening and bearing with my silly and meaningless rantings during these years. Inexpressible love and thanks to my fiancee' Srijit for being there as my best friend and partner throughout this journey.

ACKNOWLEDGMENTS (Continued)

Last but not the least, I want to thank my physics teacher since my teenage days, whom I fondly call Shankaranarayanan Sir, for motivating me to pursue physics for higher studies. Had I not crossed paths with you, I don't think I would have remained a student of physics, let alone come close to finishing a Ph.D. This thesis is dedicated to you. I hope you continue to inspire and motivate many more generations to come.

CONTRIBUTION OF AUTHORS

Various chapters in this dissertation are based on my previous publications. The Chapter. (3) is based on the paper with M. Stephanov in Ref. [1]. The work presented in Chapter. (4) and Chapter. (5) are based on my work with K.Rajagopal, M.Stephanov and Y.Yin in Ref. [2,3], that was also discussed briefly in Subsection. (8.3) of this review paper [4] which I co-authored. Chapter.(6) is based on my work with M.Stephanov in Ref. [5]. All reproduction of part of my previous publications in this dissertation is in accordance with the copyright policies of the corresponding publishers.

TABLE OF CONTENTS

TABLE OF CONTENTS (Continued)

CHAPTER **PAGE**

TABLE OF CONTENTS (Continued)

CHAPTER **PAGE**

LIST OF FIGURES

LIST OF FIGURES (Continued)

LIST OF FIGURES (Continued)

FIGURE **PAGE**

FIGURE **PAGE**

LIST OF FIGURES (Continued)

LIST OF FIGURES (Continued)

LIST OF FIGURES (Continued)

FIGURE **PAGE**

LIST OF ABBREVIATIONS

HIC	Heavy-Ion Collisions
LHC	Large Hadron Collider
QCD	Quantum Chromdynamics
QGP	Quark-Gluon plasma
RHIC	Relativistic Heavy-ion Collider
BES	Beam Energy Scan
nPI	n-particle irreducible
LG	Landau-Ginsburg
LGW	Landau Ginsburg Wilson

SUMMARY

An intriguing question about the phase diagram of QCD is the existence and the location of the critical point on the boundary between the two phases – the hadron gas and the quark-gluon plasma. Heavy-ion collisions provide a unique opportunity to look for signatures of this critical point via the event-by-event fluctuations of particle multiplicities. In order to make conclusive inferences from the experimental data, we need a theoretical framework to connect QCD thermodynamics to the particle spectra and correlations observed by the detectors. In this thesis, I use quantum-field-theoretic techniques to develop necessary ingredients to describe the thermodynamics, dynamics, and freeze-out of fluctuations in such a framework. In the first part of the thesis, we use universality of critical phenomenon and the lightness of physical quark masses to deduce certain non-trivial scaling features of the QCD equation of state (EoS). In the second part of the thesis, we demonstrate how slowing down near the critical point affects the growth of hydrodynamic fluctuations relative to the equilibrium expectations obtained using the EoS. In the final part, we propose a generalization to the half-a-century old Cooper-Frye freeze-out procedure to convert the fluctuations of hydrodynamic densities into particle correlations based on the universal maximum entropy principle. Applying the procedure, we derive relations to obtain important phenomenological constants that determine the magnitude of observed particle multiplicity fluctuations directly in terms of the QCD EoS.

CHAPTER 1

INTRODUCTION

Phase transitions, in particular critical points are ubiquitous in nature. The theory of critical points unites systems as varied as a spins in a magnetic-field to liquid-gas systems to the electroweak and QCD phase transitions that also have relevance in the early history of the universe. The unification stems from the observation that the thermodynamic quantities show universal scaling power law relations at the critical point. We know today that the mathematical similarity of the equations that demonstrate the scaling behavior is not a coincidence and can be explained using statistical field theory.

Phase transitions are macroscopic phenomena that happen in many body systems. The mathematical similarity that underlies these phenomenon in these systems downplays the diversity of the fundamental interactions between its microscopic constituents. The forces that govern the interactions in a liquid-gas phase transition are electromagnetic in nature, QCD is the theory of strong interaction which acts between the constituents of nuclei, and electro-weak theory underlies the electroweak phase transition. All the elementary fermions in the universe and the gauge bosons which mediate the interactions described above, along with the Higgs boson which gives mass to the elementary fermions together form the Standard Model. The Standard Model has been tremendously successful in describing most of visible phenomena and in discovering new particles like W, Z and Higgs bosons. In this thesis, we'll be concerned with the QCD sector of the Standard model. The elementary fermions that interact via strong interactions are called quarks and the interactions between them are mediated by gauge bosons called gluons which interact amongst themselves due to the non-abelian nature of QCD. The atoms and molecules around us have protons and neutrons in their nucleus. But at high energies or extreme environments like high temperature and/or pressure (for example, in the cores of neutron stars) the nuclear matter can "vaporize" forming a plasma of quarks and gluons. In the early moments of the universe, it is believed that the universe was indeed made up of a de-confined plasma comprised of colored quarks and gluons which then transitioned into colorless hadronic matter that we see around us today. This phase transition which happened approximately three minutes after the Big Bang comprised of a continuous change (cross-over) in the thermodynamic properties. The nature of this phase transition at large baryon densities is still an unresolved question.

In this thesis, we'll discuss the phase transition in Quantum Chromodynamics (QCD). This phase transition from confined to de-confined nuclear matter is innately related to the chiral symmetry breaking restoring phase transition in the limit of massless-quarks. Spontaneous breaking of chiral symmetry is believed to account for about 99% of the mass of the nucleons (less than 1% is accounted for by Higgs Mechanism). Apart from its relevance in the early history of the universe, quark-gluon plasma can also occur inside the core of neutron stars, whose mergers can now be studied using gravitational waves emitted by them. Moreover, the heavy-ion collisions provide a unique opportunity [15] to recreate the quark-gluon plasma that existed in the early moments after the Big Bang, in terrestrial laboratories and thereby study the phase diagram of QCD [7, 16, 17]. It is conjectured that the cross-over transition at zero baryon chemical potential (similar to the conditions at Big Bang) turns into a first-order phase transition at some non-zero baryon chemical potential. If this is the case, then there must be a critical point demarcating the two scenarios on the phase diagram. The signature of a critical point lies in the enhanced and characteristic fluctuations of thermodynamic quantities. These fluctuations should leave an imprint in the cumulants of hadron multiplicities observed in heavy-ion collisions when the trajectory of the fireball on the phase diagram passes close to the critical point. In this thesis, we use quantum field theory to develop some essential ingredients for a theoretical fluctuation framework to study the fluctuations of observable particle multiplicities in heavy-ion collisions. Such a framework is crucial for comparing theory with the experimental data from Beam Energy Scan program at Relativistic Heavy-Ion Collider [14, 17].

The thesis work presented here is mainly a compilation of the papers that I co-authored during my study [1, 2, 5] and my notes. The dissertation is organized as follows:

In **Chapter. (2)**, we review the important features of QCD, our current understanding about the phase diagram of QCD and the experimental and theoretical efforts in mapping the same.

In **Chapter. (3)**, we discuss the Equation of State and the thermodynamic properties in general by mapping QCD near its conjectured critical point to the 3D Ising model near its critical point. The main result from this chapter is the statement that in the small quark mass limit, the mapping parameters show unique scaling behavior which can be explained using universal arguments. This Chapter is derived from my published work in [1].

In **Chapter. (4)**, we discuss the dynamics of fluctuations of hydrodynamic densities near the critical point and demonstrate the hydrodynamic simulation with fluctuations in two simplified scenarios. This Chapter is derived from my published work in [2].

In **Chapter. (5)**, we introduce a novel freeze-out scheme inspired by an effective field theory near the critical point to convert the hydrodynamic fluctuations into cumulants of particle multiplicities. For a simplified hydrodynamical simulation with fluctuations, I demonstrate the freeze-out procedure in practice by estimating the Gaussian cumulants of proton and pion cumulants. This Chapter is derived from my published work in [2].

In **Chapter. (6)**, we introduce a more general freeze-out procedure based on the principle of maximum entropy. This Chapter is derived from my published work in [5].

In **Chapter. (7)**, the conclusions of this thesis are summarized.

CHAPTER 2

QCD PHASE TRANSITION

This thesis is about building theoretical tools to aid the heavy-ion program for critical point search in the phase diagram of Quantum Chromodynamics (QCD). The present chapter which serves as an introduction to the problem at hand and the thesis as a whole, is organized as follows. In Section. (2.1), we discuss important features of QCD. In Section. (2.2), we review our theoretical understanding about the spontaneous breaking of the chiral symmetry at higher temperatures leading to a possibly rich phase diagram. In Section. (2.3), we describe how fluctuations of thermodynamic quantities can be used as probes of the critical point. In Section. (2.4), we review our current knowledge about the QCD Equation of State at non-vanishing temperatures and/or baryon densities. In Section. (2.5), we describe the study of quark-gluon plasma (QGP) and the search for critical point via heavy-ion collisions. In Section. (2.6), we summarize the essential components of a systematic theoretical fluctuation framework, required to connect predictions from QCD thermodynamics to experimental data from Beam Energy Scan program at RHIC. The rest of the thesis will be about developing some of these components and studying them in simplified scenarios.

2.1 Quantum Chromodynamics

The theory of strong interactions, namely Quantum Chromodynamics (QCD) describes the interactions between the elementary particles called quarks and gluons, that form the fundamental constituents of all nuclear matter in the universe. Quarks and gluons are the degrees of freedom in the Lagrangian of this non-abelian quantum field theory. The QCD spectra is composed of hadrons, which are composite objects of these quarks and gluons.

Quarks and antiquarks are fermions which carry spin, color and flavor degrees of freedom. Gluons are spin-1 massless bosons with color degrees of freedom. QCD is described by a $SU(N_c)$ non-abelian gauge theory (where N_c is the number of colors) coupled to N_f fermions(denoted by ψ) in the fundamental representation of $SU(N_c)$. The invariance of the Lagrangian under local color gauge transformations of $SU(N_c)$ necessitates the existence of $N_c^2 - 1$ vector fields A_μ^a corresponding to the gluons which mediate the strong interaction between quarks. The Lagrangian of QCD is :

$$\mathcal{L}_{\text{QCD}} = \sum_q \bar{\psi}_\alpha^{c,q} \left(i\not{D} - m_q \right) \psi_\alpha^{c,q} - \frac{1}{4}(F_{\mu\nu}^a)^2 \tag{2.1}$$

where c, q and α label the color, flavor and dirac indices of the fermion and

$$F_{\mu\nu}^a = \partial_\mu A_\nu^a - \partial_\nu A_\mu^a + g f^{abc} A_\mu^b A_\nu^c \tag{2.2}$$

is the stress-energy tensor. f^{abc} are the structure constants appearing in the Lie algebra of the generators of the $SU(N_c)$, denoted by the Hermitian matrices t^a, where $a \in \{1, \ldots, N_c^2 - 1\}$. From now on, we will take $N_c = 3$, therefore there are eight generators.

$$[t^a, t^b] = if^{abc}t^c \tag{2.3}$$

The covariant derivative is represented in terms of the generators of QCD as:

$$D_\mu = \partial_\mu - igA_\mu^a t^a \tag{2.4}$$

The notation $\not{D} \equiv \gamma^\mu \partial_\mu$ where γ^μ are the 4×4 Dirac matrices which behave as singlet in the color and flavor space.

This deceptively simple looking Lagrangian hides within it some important properties. While the degrees of freedom in Lagrangian of the non-abelian gauge theory described above are quarks and gluons, free quarks are never observed in the experiments or in our day to day experiences. The list of all observed hadrons and their properties like mass, spin, lifetimes etc.. are documented in the particle data group (PDG) [6]. The non-observability of quarks is a consequence of confinement. At low energies or large distances, the coupling strength between the quarks becomes very strong such that they inevitably form bound objects which we call hadrons (eg., protons, neutrons etc..). Implicitly stated in the previous sentence is a profound feature of QCD that the coupling strength in QCD depends on the momentum scales of the interaction.(Figure 1) shows the coupling constant $\alpha_s = g^2/(4\pi)$ as a function of the momentum

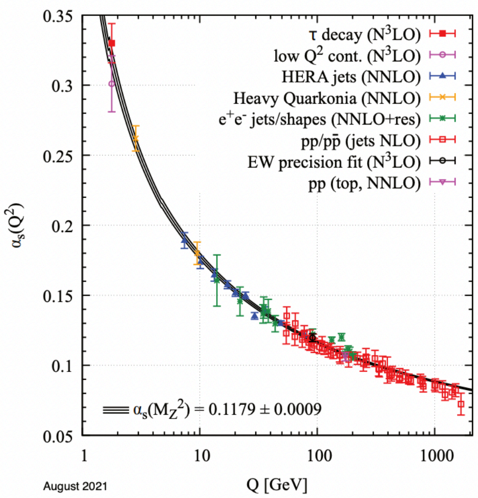

Figure 1: Figure taken from the reference [6]. The figure shows the latest summary of measurements of α_s, the strong coupling constant as a function of the energy scale Q. The order of QCD perturbation theory used in the extraction of α_s is indicated in the legends. For more details refer to [6]. The the large Q behavior, $g^2(Q) \sim (\log Q)^{-1}$ is termed as "asymptotic freedom". The divergence of α at low Q is a consequence of color confinement.

scale. The divergence of the coupling strength in the infrared limit is called infrared slavery and is a consequence of "confinement" in QCD. In the UV limit the coupling goes to zero, this property is called asymptotic freedom. The momentum scale at which the coupling becomes of the order of unity is denoted as Λ_{QCD} and is taken to be equal to 200 MeV. At energy scales much larger than Λ_{QCD}, the theory becomes perturbative due to asymptotic freedom, and the physical phenomena can be well described by doing Taylor expansion in α_s.

We will now discuss the flavor symmetries of the Lagrangian that exists in the limit of small quark masses. When $m_q = 0$ (referred to as the chiral limit), the Lagrangian of QCD is invariant under $U_L(N_f) \times U_R(N_f) \equiv U_V(1) \times U_A(1) \times SU_V(N_f) \times SU_A(N_f)$ transformations where L, R, V, and A correspond to left, right, vector and axial parts of the symmetry respectively. The currents associated with these symmetries are:

$$j^{\mu} = \bar{\psi}\gamma^{\mu}\psi\,, \quad j^{\mu 5} = \bar{\psi}\gamma^{\mu}\gamma^{5}\psi \tag{2.5}$$

$$j^{\mu a} = \bar{\psi}\gamma^{\mu}\tau^{a}\psi\,, \quad j^{\mu 5 a} = \bar{\psi}\gamma^{\mu}\gamma^{5}\tau^{a}\psi \tag{2.6}$$

where τ^as, $a \in \{1, \ldots N_f^2 - 1\}$ are the generators of $SU(N_f)$. j^{μ} is the total baryon current , conservation of which implies conservation of baryon number which we know to be true in strong interaction mediated processes. $j^{\mu 5}$, the axial current is not conserved due to quantum effects. The breaking of the isospin singlet axial current $j^{\mu 5}$ conservation by quantum effects is termed the chiral anomaly and is given by the Adler-Bell-Jackiw equation:

$$\partial_{\mu} j^{\mu 5} = -\frac{g^2 N_f}{32\pi^2} \epsilon^{\alpha\beta\mu\nu} F^{c}_{\alpha\beta} F^{c}_{\mu\nu} \tag{2.7}$$

An experimental consequence of this breaking is that there are no chiral partners of equal mass seen in the hadronic spectrum. This reduces the symmetry group of QCD to $U_V(1) \times SU_V(N_f) \times SU_A(N_f)$ in the chiral limit. This symmetry will be termed as chiral symmetry. The physical world has two light quarks, u and d which are known to have masses,$m_u \approx 2\,\mathrm{MeV}$ and $m_d \approx 5\,\mathrm{MeV}$, which are small compared to other scales in QCD like Λ_{QCD}. Since the difference between the light quark masses are small compared to Λ_{QCD}, we can consider them to be approximately equal i.e $m_u \approx m_d = m_q$. Furthermore, smallness of $m_q/\Lambda_{\mathrm{QCD}}$ implies that there could be some features of the approximate $N_f = 2$ chiral symmetry in the real world, although strictly speaking chiral symmetry is explicitly broken at the Lagrangian level itself. It turns out that $SU_A(2)$ is spontaneously broken by the ground state of QCD leading to the generation of a light pseudoscalar isospin triplet of pions (pseudo-Goldstone bosons) which have a mass of about $140\,\mathrm{MeV} \gg m_q$. Hence, the chiral symmetry is spontaneously broken to $U_V(1) \times SU_V(2)$.

Chiral symmetry breaking is a non-perturbative phenomenon. At sufficiently high temperatures, the theory becomes perturbative and quarks and gluons become the effective degrees of freedom. In this limit, we expect chiral symmetry (approximate due to smallness of m_q) to be effectively restored. The nature and order of this phase transition depends upon various factors that we discuss below.

2.2 Phase diagram of QCD

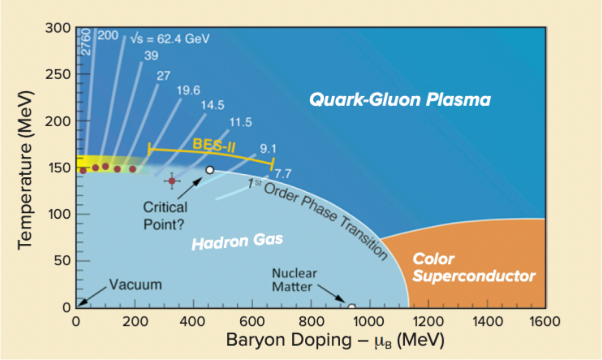

Figure 2: Figure taken from the Long Range Plan for Nuclear Science 2015 [7]. The figure shows the conjectured phase diagram for QCD with the freeze-out points for the mid-rapidity regions of the fireball at different center of mass energies.

The spontaneous breaking of the (approximate $N_f = 2$) chiral symmetry could result in non-analytic transitions on the phase diagram of QCD. The conjectured phase diagram of QCD in the physical world (where the mass of the lightest quarks, m_q is non-zero) is shown in Figure 2. Much of this phase diagram is schematic except for the zero and low baryon-chemical potential region where it is known from experiments as well as first-principle calculations using Lattice QCD that the transition is a cross-over. The pseudo critical temperature at $\mu = 0$ has been obtained as $T_{pc} = 156.6 \pm 1.5\,\text{MeV}$ from lattice computations [18]. The study of the regime of non-zero chemical potential from first principles is hindered by the sign problem [19] and therefore, one has to resort to model studies. Although these models elucidate qualitative features of the phase diagram with the possibility of a critical point, the quantitative features of these models, like the position of the critical point don't agree with each other and could be very different from QCD [20].

In the chiral limit, the physical state doesn't show chiral symmetry at zero temperatures, but exhibits exact chiral symmetry at large temperatures. This means the domain between these phases on the phase diagram have to be separated by non-analytic phase transition lines. [1] In subsection, we'll discuss the possibility of a second-order phase transition in $N_f = 2$ QCD by reviewing the renormalization group studies searching for infrared stable fixed points, that characterize second-order phase transitions. We discuss how a probable phase diagram scenario in the chiral limit leads to a Z_2 critical point in the real world, where $m_q \neq 0$. In subsection. (2.2.2), we'll review the developments from lattice QCD at $\mu = 0$, which gives us insights into the QCD phase diagram at physical quark masses at non-zero μ.

2.2.1 Phase transition in the chiral limit

As discussed above, when the quarks are massless, there is an exact chiral symmetry at the Lagrangian level, but the ground state breaks this symmetry. Below we will discuss the nature and order of the phase transition that restores this symmetry for the equilibrium state at large temperatures based on deductions from symmetry arguments and RG analysis by Pisarski and Wilczek and later by various other authors. The knowledge about the spatial dimensionality

---

[1] This is not a requirement at non-zero quark masses as the chiral symmetry is explicitly broken.

and the relevant symmetries of the theory allows us to write the most general Landau-Ginsburg-Wilsonian Lagrangian for the low-energy description of the order parameter. One can then look for stable infrared (IR) fixed points in this general theory. Existence of stable infrared fixed points allows for the possibility of second order phase transitions.

In the chiral limit, one can consider the chiral order parameter denoted by Φ_{ij}, the bilinear condensate, $\Phi_{ij} = \frac{1}{2}\langle\bar{\psi}_i(1+\gamma_5)\psi_j\rangle$ [21]. Under $SU_L(N_f) \times SU_R(N_f)$ transformations, Φ transforms as $\Phi \to U_L \Phi U_R^\dagger$. In the chiral symmetry restored phase, i.e when $SU_A(N_f)$ is a symmetry of the physical state, $\Phi_{ij} = 0$ and in the broken phase it is non-zero. $U_L(N_f) = U_R(N_f)$ (i.e $U_V(1) \times SU_V(N_f)$) is an unbroken symmetry as explained earlier. The most general effective Lagrangian for Φ_{ij}, which is parity invariant and respects $U(1) \times SU(N_f)$ symmetry was constructed by Pisarski and Wilczek:

$$L_0 = \frac{1}{2}\mathrm{Tr}|\partial_\mu \Phi|^2 - \frac{1}{2}m^2 \mathrm{Tr}|\Phi|^2 + \frac{\pi^2}{3}g_1 \mathrm{Tr}(|\Phi|^2)^2 + \frac{\pi^2}{3}g_2(\mathrm{Tr}|\Phi|^2)^2 \tag{2.8}$$

Due to anomaly, we must also add terms that reduce the symmetry to $U_V(1) \times Z(N_f) \times SU_L(N_f) \times SU_R(N_f)$ which are parity invariant. $N_f = 2$, i.e QCD with two massless flavors resembles the closest to our universe. Keeping all such terms that have naive scaling dimension less than or equal to four in four dimension for $N_f = 2$, we get [22]:

$$L_A = c(\det\Phi + \det\Phi^\dagger) + y(\det\Phi + \det\Phi^\dagger)\mathrm{Tr}\Phi^\dagger\Phi + z((\det\Phi)^2 + (\det\Phi^\dagger)^2) \tag{2.9}$$

The Lagrangian $L = L_0 + L_A$ is the most general renormalizable Lagrangian invariant under parity transformation that respects $SU_A(2) \times SU_V(2) \times U_V(1)$ symmetry. [1]

Φ_{ij} can be represented as $\Phi_{ij} = (\phi + i\eta)\, I + (\Delta + i\Pi)_i\, \sigma^i$, where ϕ, η, Δ and Π are real fields, I is 2×2 identity matrix and σ_i are the Hermitian matrices which are generators of $SU(2)$. In the absence of anomaly, the effective Lagrangian description given by (2.8) leads to three infrared fixed points, i.e the Gaussian fixed point and two $O(8)$ fixed points. [23]. Out of these, one of the $O(8)$ fixed points has been shown to be stable with regard to RG flows [23]. The presence of stable IR fixed point allows the possibility of having a second-order phase transition if the physical theory falls in the basin of attraction of the IR fixed point. [2] In the presence of anomaly, all the terms of scaling dimension four are same for $N_f = 2$. The theory can have an infrared stable $O(4)$ fixed point [21, 22]. For $N_f = 3$ case, with three massless quarks, the phase transition cannot be second order in the presence of anomaly [21]. [3]

---

[1] We know that axial symmetry($U_A(1)$) is always absent due to the non-conservation of the axial current. However, the strength of the anomaly coefficients c, y, z can become very small due to some mechanism, resulting in an effective restoration of the axial symmetry at the chiral symmetry restoration temperature.

[2] This first RG study for the $N_f = 2$ case in the absence of anomaly performed by Pisarski and Wilczek in ϵ expansion upto one loop reported that there are no stable IR fixed points when anomaly is absent. However a stable IR fixed point has been discovered by various other authors using higher-order perturbative expansions [23, 24].

[3] For $N_f = 3$ case, in the absence of the anomaly Pisarski and Wilczek demonstrated that effective theory described by Eq. (2.8) has no stable infrared fixed point by calculating the β functions to leading order in ϵ. However, in a recent work [25], the authors report the possibility of a stable IR fixed-point in three dimensions for $N_f = 3$ in the absence of anomaly.

The presence of a stable IR fixed point allows for the possibility of a second order phase transition in the physical theory, if it falls in the attractive basin of the IR fixed point. The inference that we make from the above results is that $N_f = 2$ QCD, i.e QCD with two massless quarks allows for the possibility of a second order phase transition [26, 27], but the nature and the universality class of the transition crucially depend on the strength of the anomaly. It also depends on the mass of the strange quark in the theory, since $N_f = 3$ theory in the presence of anomaly has a first-order phase transition, and therefore, for sufficiently small strange quark masses it is likely that this remains first-order. In the next subsection, we will give a very brief review of our understanding of the nature of the phase transition from lattice QCD, one of the powerful non-perturbative tools at our disposal to study QCD.

2.2.2 Insights into phase diagram at $\mu = 0$ from Lattice QCD

Simulating QCD on discrete space-time via Markov chain Monte Carlo methods, commonly called Lattice QCD is one of the reliable non-perturbative approaches to study QCD. It has two inherent limitations. Monte Carlo simulations at non-zero real values of baryon chemical potential become increasingly difficult due to the fermion determinant becoming complex. The second limitation is its reduced reliability in performing simulations with near vanishing quark masses due to the non-invertability of the fermion determinant in the chiral limit. Despite these limitations, lattice QCD has greatly succeeded in advancing our knowledge about QCD at regimes were it is indeed capable of performing precise and reliable calculations. Some of the insights into the phase diagram from Lattice QCD are summarized below [28, 29].

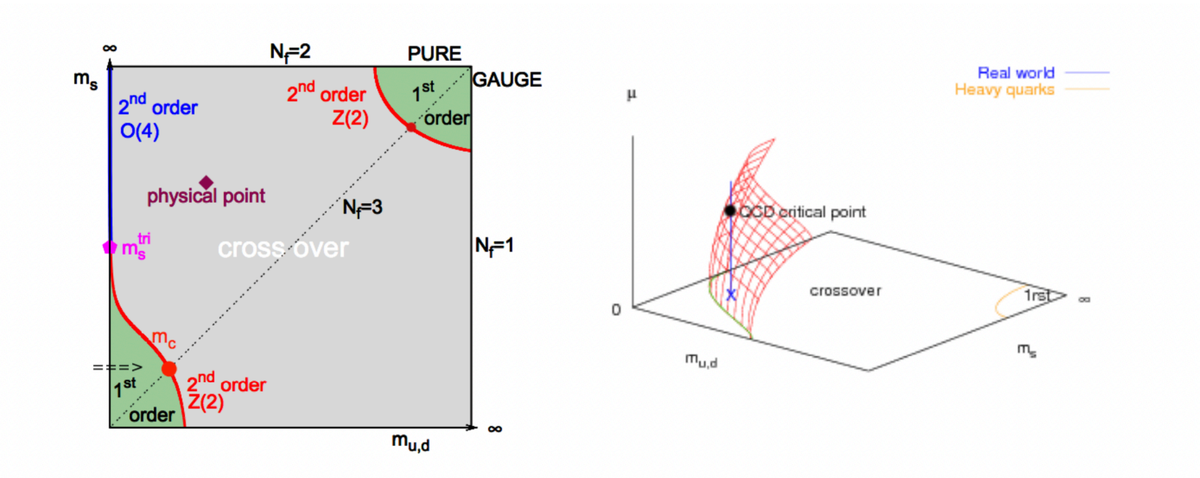

Figure 3: Both the images shown above are taken from the reference [8] is the famous Columbia plot, showing the nature of phase transitions expected in the $\mu = 0$ limit for QCD with two degenerate flavors of mass $m_{u/d}$ and another flavor of mass m_s (left) ; The conjectured Z_2 critical point at non-zero μ for non-zero light quark masses m_q is expected to lie at the intersection of $m_{u/d}$ = physical quark mass and the surface swept by the extension of the Z_2 critical line at $\mu = 0$(right).

The results on our understanding about the nature of phase transition along $\mu = 0$ as a function of the mass of the degenerate quarks $m_{u,d}$ and the mass of the strange quark m_s is often summarized in the form of the famous Columbia plot [8] (Figure 3). The original Columbia plot has undergone various modifications as a result of the advancements in lattice QCD. Below, we review the status of Columbia plot at $\mu = 0$ that may be relevant for the critical point in the QCD with physical quark masses.

- **Second-order phase transition in QCD with two massless quarks and a strange quark with physical mass :** The results for chiral susceptibility with light quark masses, m_q is consistent with scaling arguments for a second order phase transition in the chiral limit that falls in the 3D O(4) universality class. The chiral critical temperature at $\mu = 0$ has been extrapolated to be $T_{c,0} = 132^{+3}_{-6}\,\text{MeV}$. [30]

- **Cross-over for theory with two light quarks and one massive quark :**The phase transition in QCD with two light $(0 < m_q \ll \Lambda_{QCD})$ flavors of quarks and one massive quark (physical strange quark mass) is a cross-over at zero chemical potential [31–33].

- **Pseudo-critical temperature at physical quark masses along $\mu = 0$:** Lattice calculations at physical quark masses extracted from the maximum of several fluctuation observables gives a pseudo critical temperature $T_{pc} = 156.6 \pm 1.5\,\text{MeV}$ [18].

- **Order of phase transition with three massless quarks is unresolved :** Symmetry considerations by Pisarski-Wilczek in the presence of anomaly suggest a first-order phase transition for a three massless flavor QCD. Given the transition is second-order for two massless quarks and one quark at physical strange quark mass, the argument due to Pisarski and Wilczek imply the presence of a tri-critical point at some non-zero strange quark mass, m_{s3}, lower than the physical strange quark mass. The exact location of this tri-critical point would depend on the strength of the anomaly [9] . As one can see, the first-order region in the lower left corner of Columbia plot which follows from this reasoning must then be demarcated from the intermediate mass-region where the phase transition is a cross-over via a curve of Z_2 critical points. Lattice calculations along

$m_u = m_d = m_s$ have not so far seen a non-analytic transition at $\mu = 0$ for pion masses as low as $m_\pi \approx 50\,$, MeV constraining the Z_2 line to appear only at smaller pion masses [34]. The conjectured Z_2 critical point at non-zero μ for non-zero light quark masses m_q is considered to be extension of this conjectured Z_2 line on the $\mu = 0$ plane which is not yet found.

- **First order phase transition in pure SU(3) gauge theory (no dynamical quarks) :** In pure $SU(3)$ gauge theory with infinitely large quark masses, it has been well established that the phase transition is first-order [35]. The broken symmetry here is the center symmetry Z_3 which is related to confinement/deconfinement and Polyakov loop serves as an appropriate order parameter [36, 37]. A curve of Z_2 critical points separates the region with first-order phase transition in the infinite mass limit with the cross-over region at finite masses.

For some non-zero μ, the crossover may become a first-order phase transition (resulting in a critical point) as various models suggest. If this is true for QCD at physical quark masses, we expect the curve of first order phase transitions emanating from $T = 0$ and non-zero chemical potential which we denote by μ_1, should end in a Z_2 critical point at some non-zero chemical potential and temperature. Assuming that this critical point is the closest singularity to the $\mu = 0$ at $T = T_c$, the critical point must leave its signature in the radius of convergence estimators obtained along the $\mu = 0$ from Lattice QCD.EoS and thermodynamic properties are known for zero and low values of μ_B/T [10, 38, 39]. The current lattice QCD calculations of the Taylor expanded EoS as a function of $(\mu/T)^2$ disfavors the existence of a critical point for $\mu/T \leq 2$ and $T/T_{pc} \geq 0.9$ [39].

2.2.3 Phase diagram at non-zero μ with physical quark masses

The Landau Ginsburg effective potential for $N_f = 2$ in the presence of anomaly can be written in terms of the real ϕ and $\vec{\pi}$ fields as follows. [9]

$$\Omega(\phi) = \frac{d}{2}\left(\phi^2 + \vec{\pi}^2\right) + \frac{e}{4}\left(\phi^2 + \vec{\pi}^2\right)^2 + \frac{f}{6}\left(\phi^2 + \vec{\pi}^2\right)^3 - m_q\phi + \ldots \tag{2.10}$$

where we have kept only the lowest order terms upto $O(\phi^6)$. The linear term in ϕ explicitly breaks the chiral symmetry. For $m_q = 0$, a mean-field analysis of the above Lagrangian, elucidates the following features of the phase diagram in the chiral limit [9]:

- $d(\mu, T) = 0, e > 0$ gives a line of critical points.
- $d(\mu, T) = e(\mu, T) = 0$ corresponds to a tri-critical point where the leading interaction goes as $\left(\phi^2 + \vec{\pi}^2\right)^3$ [1]
- A triple line, meaning a line of points on the phase diagram with three co-existing phases occurs along $d = 3e^2/(16f), e < 0$.

In the presence of non-zero quark mass, the tricritical point turns into a Z_2 critical point and the triple line becomes a first-order phase transition line. The massless mode in this case

---

[1] Near the tricritical point, the contributions due to fluctuations are logarithmically suppressed in three dimensions and the mean-field theory can be used.

corresponds to the fluctuations of ϕ about its value at the critical point (ϕ_c) , i.e $\phi - \phi_c$. The pions become massive at this point with a mass given by [40]:

$$m_\pi^2 = d + e\phi_c^2 + f\phi_c^4 \tag{2.11}$$

The schematic phase diagram based on these arguments is shown in (Figure 4). The coefficients d, e, f depend upon the value of the strange quark mass. Hence the position of the tri-critical point and the Z_2 line varies with the strange quark mass. For strange quark mass smaller than some critical value, it is expected that the phase transition at $\mu = 0$ in $N_f = 2$ turns into first order. This results in a tri-critical point in the $N_f = 2$ at some critical strange quark mass value, m_{s3}. (Figure 4) assumes that physical strange quark mass is greater than m_{s3}. In this scenario, when the light quark mass, m_q [1] is turned on, the triple line and the line of second order points shown by a dashed and dotted line respectively in the chiral limit become a first-order curve and a cross-over line respectively. The tri-critical point hence turns into a critical point, which marks the end of line of first order phase transition.

The phase structure of various toy models of QCD at non-zero quark masses have been studied. Many of these models possess a first-order phase transition at a chemical potential , (sometimes denoted by μ_1) along the $T = 0$ axis for physical quark masses. [2] Some of

---

[1] In this thesis, we'll use m_q to denote the mass of two degenerate light quark masses and m_s to indicate the mass of the strange quark.

[2] Note that this is different from the nuclear liquid-gas phase transition which also has a first order phase transition along $T = 0$, $\mu = \mu_0$ such that $\mu_0 < \mu_1$.

these models are the MIT Bag Model [41,42], Nambu-Jona Lasinio(NJL) [43–45] , PNJL based models [46], Random Matrix Model [47,48], 2-flavor QCD with interactions between quarks induced via instantons [49–51], Bottom-up Einstein-Maxwell-Dilaton holographic model [52,53] etc..

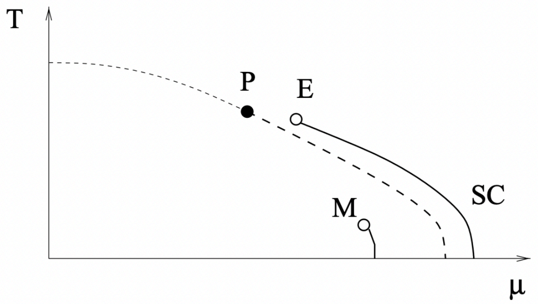

Figure 4: Figure taken from the reference [9] is a schematic phase diagram of QCD. The dashed lines represent the boundary of the phase with spontaneously broken chiral symmetry in QCD in the chiral limit with $N_f = 2$. The line of second order and first-order transitions meet at a tri-critical point denoted by P. The point E which represents the Z_2 critical point of the real world is connected to the tri-critical point via a line of Z_2 critical points. Point M (the familiar liquid-gas phase transition which is probed in low energy multi-fragmentation experiments) and point S (the superconducting phase of QCD) are irrelavant for the discussion presented in this thesis.

2.3 Fluctuations as probes of the critical point

A mean-field analysis near a second order phase transition can be performed using a Landau Ginsburg potential for a scalar field ϕ with upto ϕ^4 terms. Landau-Ginsburg (LG) theory cannot describe fluctuations. However, the LG free-energy potential helps us to understand the importance of fluctuations near the critical point qualitatively. At a first-order phase transition, the free-energy has two degenerate minima. The critical point appears as the end point of the first-order phase transition curve where the two minima merge into each other. At this point the curvature of the free-energy function becomes zero. Transition from one minima (phase) to the other comes at zero energy cost. This is the reason for enhanced fluctuations near the critical point. Critical opalescence [54] which is the phenomenon of a liquid turning milky at its critical point is due to the multiple scatterings which occur because of the enhanced fluctuations in the densities [55].

The enhancement in fluctuations also results in the breakdown of mean-field theory near the critical point in low dimensions ($d < 4$). We can describe the equilibrium fluctuations near QCD critical point using a local scalar σ^4 field theory in three dimensions. The fluctuations of the order parameter, σ is determined by a probability functional $P[\sigma] = \exp\left[-\Omega(\sigma)/T\right]$ where [40]

$$\Omega(\sigma) = \int d^3x \left[\frac{(\nabla\sigma)^2}{2} + \frac{m_\sigma^2}{2}\sigma^2 + \frac{\lambda_3}{3}\sigma^3 + \frac{\lambda_4}{4}\sigma^4 + \dots\right] . \tag{2.12}$$

The fluctuations of the order parameter field when averaged over volumes larger than ξ show the following characteristic leading singular behavior in three dimensions [56, 57]:

$$\langle\sigma^2\rangle = VT\xi^2\,, \quad \langle\sigma^3\rangle = 2VT^{3/2}\tilde{\lambda}_3\xi^{4.5}\,, \quad \langle\sigma^4\rangle = 6VT^2\left(2\tilde{\lambda}_3^2 - \tilde{\lambda}_4\right)\xi^7 \tag{2.13}$$

The order parameter for QCD with physical quark masses is an unknown linear combination of entropy density and baryon number density. The enhancements in fluctuations of the order parameter can be directly related to the divergence of susceptibilities (higher derivatives of pressure with respect to temperature and chemical potential). The leading behavior of the baryon number susceptibilities diverge with the specific powers of correlation length, ξ,

$$\frac{\partial^k P}{\partial\mu_B^k} \sim \xi^{\frac{k(5-\eta)}{2}-3}\,, \tag{2.14}$$

where $\eta \approx 0.04$ is the well-known Ising critical exponent [58, 59]. These derivatives of pressure, are related to the cumulants of baryon number-multiplicities as follows:

$$\left\langle\delta n_B^k\right\rangle_{\text{eq}} = \left(\frac{T}{V}\right)^{k-1}\frac{\partial^k P(T,\mu_B)}{\partial\mu_B^k} \tag{2.15}$$

The scaling form and the leading singular behavior of the pressure near the critical point can be deduced from universality of critical phenomenon which is described in more detail in Chapter. (3). The current understanding of the EoS at zero chemical potential and near the conjectured critical point is reviewed in the next section.

2.4 Equation of State of QCD

Equation of State (EoS) is a relation connecting the pressure with number densities (baryon number, electric charge, strangeness, etc..) and energy densities or equivalently, pressure with temperature and chemical potentials. The QCD EoS at zero chemical potential $P(T)$ has been calculated from first principles [10, 38, 60]. $P(T)$ from [10] is shown in Figure 5. One can see that the EoS at low-temperatures agrees well with the hadron resonance gas model and the high-temperature limit approaches the Stefan Boltzmann limit. The transition between these asymptotic descriptions happen around 150-200 MeV. The Taylor expansion of QCD EoS upto sixth order in baryon , strangeness and electric charge chemical potentials are obtained in [39]. The Taylor expanded QCD EoS upto eighth order in chemical potentials in strangeness-neutral matter is also available [61]. The EoS becomes non-analytic near a phase transition and therefore, the Taylor expansions of EoS cannot be extrapolated to larger values of chemical potential if there is a critical point on the phase diagram. The QCD critical point if it exists belongs to the 3D Z_2 universality class for which 3D Ising model is a prototype example. The EoS of QCD near the critical point can be then mapped to the EoS of 3D Ising model using universality [1, 62–64]. This mapping depends on some non-universal coefficients which depend upon the microscopic details and hence are unknown. A class of EoSs with different choices of these parameters that match with the lattice data at $\mu = 0$ has been constructed in [63]. In chapter (3), we will discuss different aspects of this non-universal mapping between 3D Ising model and QCD. In addition to providing essential information about the phase diagram of QCD, EoS is also a crucial input for these hydrodynamical simulations.

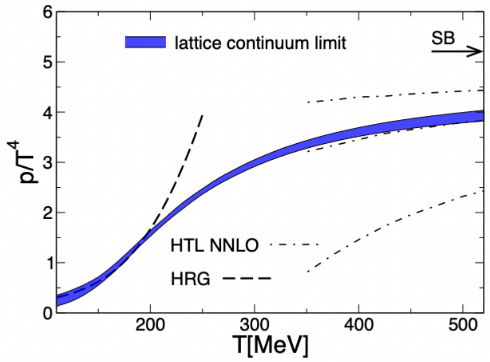

Figure 5: Figure taken from the reference [10] shows EoS at zero baryochemical potential obtained in (2+1) flavor lattice QCD with physical quark masses compared to HRG model prediction at low temperatures and hard thermal loop calculations from [11] (with different renormalization scales) at large temperatures.

The pseudo-critical temperature at $\mu = 0$ from lattice QCD and model calculations of QCD phase transition indicate that the transition from quark-gluon to hadron degrees of freedom happens at temperatures of $100 - 200\,\mathrm{MeV} \sim 10^{12}K$. Such high temperatures can be reached in heavy-ion collisions. In the next section, we will discuss how heavy-ion collisions serve as laboratories to study the phase diagram of QCD [17,65] and determine the EoS of QCD [66–69].

2.5 Heavy-ion collisions to study the phase diagram

There are various heavy-ion collider facilities that are either already functioning or in their developmental stage around the globe, for example Relativistic Heavy Ion Collider (RHIC) at BNL in USA; the Super Proton Synchrotron (SPS) and Large Hadron Collider (LHC) at CERN in Switzerland; the High Acceptance Di-Electron Spectrometer (HADES) and Facility for Antiproton and Ion Research (FAIR) in Germany to name a few [15, 70]. These facilities differ from each other in their center of mass energies, luminosities, acceptances of the detectors, colliding nuclei etc based on the main goals behind their installation. Together, they scan different regions of the phase diagram. One of these facilities namely, the RHIC at BNL is highly versatile and different from its counterparts as it allows to scan a varying range of center of mass energies from 3 GeV to 200 GeV, allows collisions of different nuclei and also can work both in collider and fixed target capacities. These unique specialties of this facility opened the scope for a Beam Energy Scan (BES) program specifically designed to study the critical point and importantly discover the critical point of QCD if it exists in the regime of the phase diagram probed at these center of mass energies [17, 71].

By studying the particle spectra and their correlations in momenta, we are essentially probing the state of the system at the hypersurface of their last elastic and inelastic scatterings called thermal and chemical freeze-out respectively. The yields of the stable hadrons and some light nuclei across wide range of energies are consistent with a thermal model which predict an equilibrated Fermi-Dirac/Bose-Einstein hadron resonance gas at freeze-out [12, 72].The parameterization for the freeze-out curves discussed in [12, 73] and shown in Figure 6 have been obtained by fitting to experimental data. These empirical fits indicate that the freeze-out temperature changes little, while the chemical potential at freeze-out is more sensitive to change of center of mass energy across BES energies. Lattice QCD calculations of pseudo-critical temperatures for low values of chemical potential obtained with degenerate light quarks and one massive strange quark at physical pion and kaon masses suggest that for $\mu \leq 300\,\mathrm{MeV}$ chemical freeze-out lies close to the QCD phase boundary [18]. This suggests that the enhancement of fluctuations expected on the pseudo critical curve close to the critical point, may survive until it freezes out and therefore, can be observed in the correlations of observed particle multiplicities.

2.5.1 Quark-gluon plasma, heavy-ion collisions and hydrodynamics

Heavy-ion collisions at sufficiently large energies can reach temperatures as high as 300 GeV or more where we expect from theoretical calculations of QCD that the state of matter can be described in terms of a plasma of quarks and gluons. Quarks and gluons which are no longer confined to distance less than the size of a hadron at such high temperatures and roam freely within the volume of the fireball exhibiting asymptotic freedom [74]. The plasma expands, the temperature drops down and the final state that we observe at the detectors is that of a thermalized gas of stable hadrons at a much lower temperature. However, we can infer about the properties of the quark gluon plasma (QGP) formed during the course of the collision from the final state distribution [75].

One might expect due to asymptotic freedom at large energies at RHIC and LHC, the coupling between the quarks and gluons are weak so that interactions are not strong enough to reach equilibrium. This is indeed true at extremely high temperatures. However, as the temperature

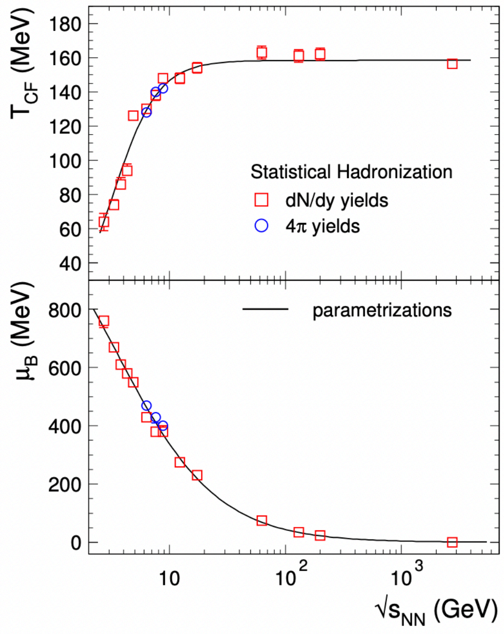

Figure 6: Figure taken from the reference [12] shows the values of temperature and chemical potential at freeze-out as a function of center of mass energies.

drops down, the system becomes strongly coupled. Due to this strong coupling, the dense quark-gluon plasma achieves local equilibrium in rather short times ($\leq 1\,\text{fm}$ or so) at temperatures as high as 300 MeV such that one can use hydrodynamics to describe the subsequent evolution of QGP [76]. The observables that demonstrate the agreement between hydrodynamic description are properties like flow coefficients which can be obtained from the azimuthal distribution of single particle observables in heavy-ion collisions [77–79]. The anisotropy characterized by the Fourier coefficients of the azimuthal particle distribution function, denoted by v_ns are in agreement with hydrodynamical descriptions [77–82]. Flow coefficients can also be calculated from multiple particle correlations [83].

The inference that QGP evolves hydrodynamically for a significant fraction of its lifetime can be made from the elliptic and higher order flow data obtained from single particle distributions as well as multi-particle correlations from experiments [84–86]. If the QGP was close to a weakly interacting gas, then any anisotropy in the initial state of the colliding nuclei would disappear from the final state due to the random scatterings in the gas and subsequent isotropization. However, in a fluid, the initial state anisotropies in the coordinate space would get translated into final state anisotropies in the momentum distribution of the particles. The latter case is supported by the experimental data. The experimental findings are consistent with a nearly perfect fluid with $\eta/s \leq 0.2$ [82]. This value has to be compared with the η/s ratio of a large class of theories with many degrees of freedom and infinite coupling which provides the conjectured lower bound for η/s ratio as equal to $1/4\pi$ [87].

A (viscous) hydrodynamic description is clearly not applicable for the entirety of the life time of the fireball. For instance, the system just after the collision is highly out of equilibrium and is clearly beyond the regime of applicability of hydrodynamics. Similarly an expanding system that is finite in size eventually becomes dilute enough such that hydrodynamics is no longer a valid tool to describe the dynamics. Ab-initio quantum simulation of the dynamics of the two nuclei colliding and evolving in real-time from first principles, analogous to what happens in heavy-ion collisions is a formidable task that is beyond the capabilities of our current theoretical and computational infrastructure. Therefore, one needs to resort to modeling techniques

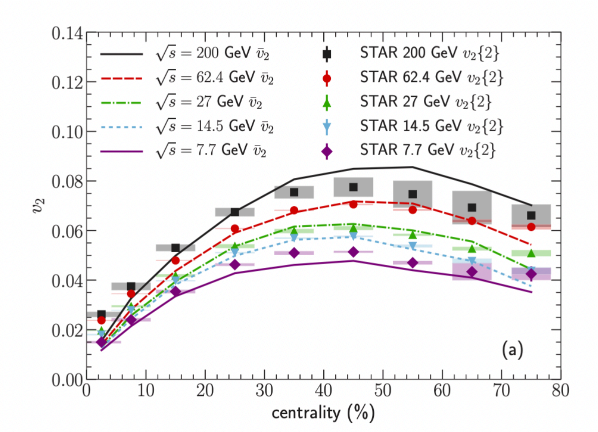

Figure 7: Figure taken from the reference [13]. The figure shows the dependence of elliptic flow coefficients v_2 on centrality and the agreement between experimental data with 3+1 D hybrid dynamical simulation discussed in [13].

to describe various stages in the heavy-ion collision. This involves a hybrid framework, which comprises of a description for the initial stages which are far away from equilibrium [78], the intermediate hydrodynamic evolution and later a kinetic description for hadrons [69, 88], when the fluid becomes sufficiently dilute for the hydrodynamic description to be invalid. The final results from this hybrid framework have to be compared to the experimental data. Modeling each of these stages often involve many parameters which apriori cannot be determined from theory. One can however find the best set of parameters that describe the wealth of experimental data using a sophisticated Bayesian analysis [89–94]. For a comprehensive review of this multistage description refer to [17, 78, 95, 96].

2.5.2 Experimental scan of the QCD phase diagram

The main experimental variable parameters that one can tune to study the phase diagram to look for critical signatures in heavy-ion collision are beam energy, centrality, ion size and rapidity/ acceptance windows. By decreasing the center of mass energy, the trajectory of the fireball moves to larger and larger baryon chemical potentials as it becomes more and more difficult to produce ant-baryons. Therefore, by varying the center of mass - energies we can study properties of nuclear matter at different regions on the phase diagram. Since the correlation functions of fluctuations of thermodynamic variables in equilibrium grow as a function of the distance of the freeze-out point to the critical point, we expect to see a non-monotonic dependence of these quantities as a function of the center of mass energy of the collision [56] . Beam-size or ion-size can be used to reduce the number of participant nucleons in the nuclear collision or the effective size of the fireball, thereby manipulating the evolution duration and freeze-out times in the process. Varying acceptance windows will allow us to study the interplay of thermal fluctuations with effects such as global conservation.

2.5.3 Event by event fluctuations for probing the phase diagram

Event by event fluctuations of various observables in heavy-ion collisions have been proposed as important tools to study the static and dynamic correlations and collective behavior in the system, that may not obtainable from the single particle spectra [97]. Examples include the event by event analysis of transverse momentum distribution [98, 99], temperature fluctuations for studying the heat capacity [46], fluctuations of particle ratios and abundances as signals of QGP [100, 101], average fluctuations of net baryon number and electric charge as probes of confinement [102]. In the context of critical point search, fluctuations of baryon number show characteristic divergence as the freeze-out point in the collision moves closer to the critical point. It may be impossible to reconstruct the baryon multiplicity distribution for all baryons produced from the aftermath of the collision, especially since the neutral particles like neutrons are undetected. Non-monotonic behavior of baryon number fluctuations should also reflect in the behavior of individual particle multiplicities fluctuations like that of protons or pions to which the order parameter field σ couples. A combination of event-by-event observables, including enhanced fluctuations in the multiplicity of soft pions were proposed as experimentally observable signatures of the critical point in [9, 40]. [103] demonstrated that the long range correlations of the order parameter field induces a characteristic correlation between protons thereby making fluctuations of proton multiplicities a good proxy for cumulants of baryon number. The significance of non-Gaussian fluctuations of experimental observables as more sensitive probes of the critical point signatures was realized in [56].The observables in a HIC are particle multiplicity distributions in the momentum space.

In order to quantify the fluctuations, it will be useful to introduce two kinds of fluctuation observables, cumulants and factorial cumulants. Let X and Y be the multiplicity of two particle species in one event. Let $\langle X\rangle$ and $\langle Y\rangle$ be their corresponding mean values obtained by averaging over many events. Let $\delta X = X - \langle X\rangle$ and $\delta Y = Y - \langle Y\rangle$ be the deviations of these multiplicities from their event-by-event average. The cumulant of X and Y, denoted by C_n are given by following expressions, $C_{2X} = \langle(\delta X)^2\rangle\,, \quad C_{3X} = \langle(\delta X)^3\rangle\,, \quad C_{4X} = \langle(\delta X)^4\rangle - 3\langle\delta X^2\rangle^2\,.$ Cumulants of independent variables X and Y are additive, i.e $C_{i(X+Y)} = C_{iX} + C_{iY}$. In equilibrium the cumulants of baryon multiplicity are directly related to the derivatives of the EoS as we have seen in Eq. (2.14). Therefore, they are suitable for situations when the direct comparison between experimental observables and lattice QCD results are possible. As we shall see, such a direct comparison is not straightforward near the critical point due to the dynamical effects that play a role in HICs. It has been argued in [104], that a more convenient measure for fluctuation observables of particle multiplicities are the factorial cumulants. Factorial cumulants subtract the non-interesting trivial correlations that occur as a result of self interactions in a gas of particles. It is indeed the leading singular behavior of the factorial cumulants that can be related to critical fluctuations. The factorial cumulants, κ_ns are given by, $\kappa_2 = C_3 - C_1\,, \quad \kappa_3 = 2C_1 - 3C_2 + C_3, \kappa_4 = -6C_1 + 11C_2 - 6C_3 + C_4$ etc.. The critical contribution to third and fourth cumulants of proton, pion and their mixed multiplicities were obtained by studying their leading singular behavior in [105]. Qualitative and quantitative knowledge about the fluctuations of these variables in an equilibrated system is important for estimating these cumulants in heavy-ion collisions and there have been enormous advancements in this regard in the last decade [57,62,63,106–108].

One of the main goals of the Beam Energy Scan (BES) experiment at the Relativistic Heavy Ion Collider (RHIC) is to study the phase diagram of QCD and locate the landmark high-temperature critical point if it exists. The initial phase of the BES showed intriguing hints, such as indications of non-monotonic variation of certain measures of fluctuations from their non-critical baseline as a function of the center of mass energy denoted by $\sqrt{s}$ [7,14] (See Figure 8), which prompted further experimental efforts in the second phase of BES with higher statistics. The STAR collaboration collected BES II data during 2019-2021 by conducting heavy-ion collisions at various collision energies, corresponding to a scan in the baryonic chemical potential. Currently, the data is being analyzed, and there is a significant anticipation to learn more from these measurements.

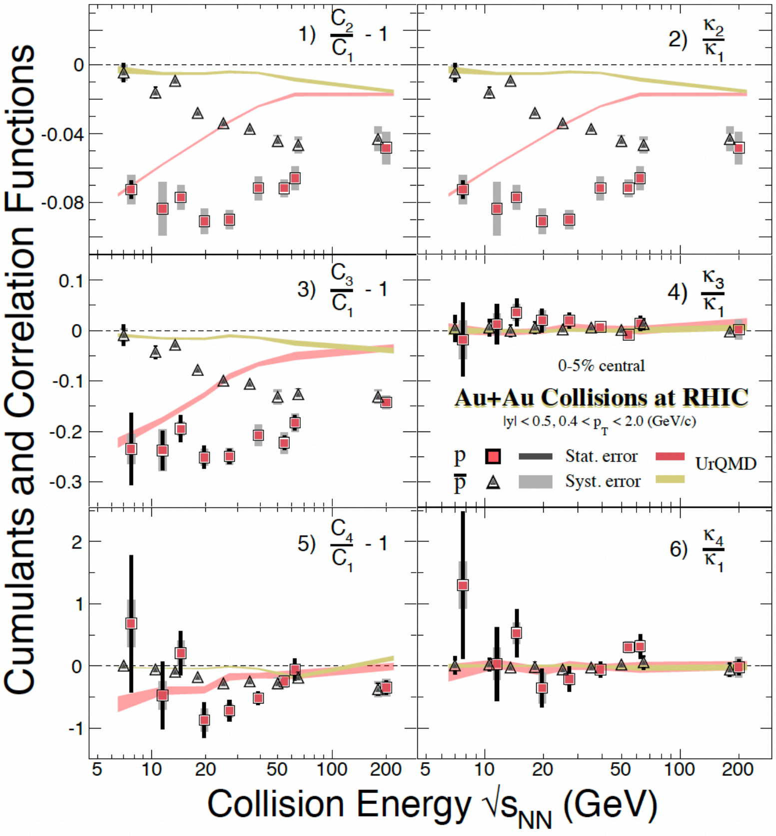

Figure 8: Figure taken from the reference [14]. The figure shows the cumulants, C_n (left panel) and the factorial cumulants(κ_n) (right panel) of proton and anti-proton multiplicities at varying center of mass energies. Comparisons to URQMD baseline are also shown. The non-monotonic deviation from the URQMD baseline is suggestive of the presence of a critical point. However, better statistics and experimental precision along with comprehensive theoretical estimate for these quantities in a dynamical fluctuation framework is necessary to make conclusions.

2.6 Cumulants of particle multiplicities in a beam-energy scan

2.6.1 Sources of fluctuations in heavy-ion collisions

As argued in Sections. (2.5.3), non-monotonic dependence of the cumulants of particle multiplicities with center of mass energy is one of the signatures of the critical point predicted from QCD thermodynamics. These cumulants describe the correlations between the event by event fluctuations of the particle multiplicities. It is ofcourse, the thermal fluctuations which carry the information about the EoS of QCD and hence the phase diagram of QCD. In a heavy-ion collision, there are various other sources of fluctuations which donot come disentangled from these genuine correlations due to the critical point. In order to perform a quantitative analysis of the particle multiplicity correlations in a Beam Energy Scan program, we would need a comprehensive framework which takes into account all these sources of fluctuations. Some of the important contributions to fluctuations come from:

- **Initial state fluctuations :** Fluctuations in the initial stage description are caused due to fluctuations in momenta and position distribution of the nucleon (or quark) degrees of freedom inside the colliding nuclei, and uncertainties in the parameters that are used to model their interactions. The fluctuations at this stage serve as initial conditions for the hydrodynamic evolution thereafter. For more details, refer to [13, 109]. As we will see in Chapter. (4), the initial conditions are important for making quantitative estimates for cumulants since conservation effects play a crucial role.

- **Thermal fluctuations :** Thermal fluctuations are directly related the derivatives of EoS, and hence give crucial information about the phase properties. Their dynamic evolution also becomes relevant near the critical point (More details in Chapter. (4) and Chapter. (5)).
- **Fluctuations at freeze-out :** The transition from a hydrodynamic description into hadron gas description is a stochastic process. This will be explained in detail in Chapter. (6).
- **Detector efficiencies :** Detectors have finite acceptances and limited efficiencies. The detector inefficiencies should also be accounted in estimating the fluctuations observables.

2.6.2 Dynamics of fluctuations

In the earlier sections, we reviewed the theoretical advancements in our understanding of the thermodynamics of QGP at non-vanishing chemical potentials. One can make predictions for observable consequences for the critical fluctuations in heavy-ion collisions assuming that the fluctuations of thermodynamic properties of QGP formed in the heavy-ion collisions while cooling down and traversing close to the critical point stays in equilibrium [9,17,40,56,57,103, 105,110–112]. This is a highly simplifying assumption, but not realistic near the critical point.

Critical fluctuations are characterized by their correlation length denoted by ξ, which increases near the critical point. As a result, the typical timescale for the evolution of critical fluctuations also increases. This is known as critical slowing down. Due to this phenomenon, critical fluctuations in the rapidly cooling droplets of QGP generated in heavy ion collisions cannot be described by their equilibrium values that are controlled by hydrodynamic fields.

However, a lot of progress has been made in describing the non-equilibrium evolution of hydrodynamic fluctuations, which exhibit distinctive behavior at long wavelengths governed by the universality of critical phenomenon [4, 113–141]. Some of these developments will be reviewed in more detail in Chapter. (4) where we discuss how dynamical factors such as conservation and critical slowing down modify the equilibrium predictions using a simplified simulation with hydrodynamic fluctuations. In Chapter. (4), we'll study how out of equilibrium fluctuations can be modeled to look for semi-quantitative and qualitative signatures of the critical point. For recent reviews on relativistic dynamics in heavy-ion collisions and dynamics of fluctuations in particular refer to [96] and [4, 126] respectively.

2.6.3 Freeze-out of fluctuations

One also needs a procedure to establish a connection between the hydrodynamic fluid – including its critical fluctuations – and the observed particle yields – and their fluctuations. The Cooper-Frye freeze-out procedure [142] is a well-known method that maps the local fluid velocity $u(x)$ and hydrodynamic fields like $T(x)$ and $\mu_B(x)$ on the freeze-out surface (a space-time hypersurface) to a simplified hadronic description using kinetic distribution of an expanding ideal resonance gas of hadrons. The resonance interactions are encoded, and their later decay modifies the distributions ultimately measured by experiments. The average densities of conserved quantities like energy or baryon number are guaranteed to match as long as the hadron resonance gas provides a good description of the equation of state, including the relations between T and μ_B and ε and n in that regime. For more than four decades, the Cooper-Frye freeze-out procedure [142] has been successfully used to describe average particle yields and spectra from high-energy heavy-ion collision data. The procedure ensures that the event-averaged baryon number and energy-momentum densities are matched between the hydrodynamic and kinetic theory descriptions. However, the Cooper-Frye framework does not account for fluctuations in either the hydrodynamic fluid or the kinetic description of particles. Therefore, this procedure has to be extended to a freeze-out scenario that includes the fluctuations as well. We devote two chapters, namely Chapter (5) and Chapter. (6) in this thesis to the discussion on freeze-out. In Chapter. (5), we develop a novel freeze-out procedure for critical fluctuations. In this Chapter we also describe the limitations of this procedure which motivates us to introduce a more general freeze-out procedure based on the principle of maximum entropy in Chapter. (6).

2.6.4 A hybrid paradigm

The hybrid paradigm comprising of initial stage+ viscous hydrodynamics+ hadronic afterburner+Bayesian optimization has been enormously successful in describing the flow patterns and single particle observables at high energies. Below, we summarize the main ingredients necessary for constructing a similar framework for the study of fluctuations in order to determine the cumulants of particle multiplicities in heavy-ion collisions [17, 96]. Note that a fluctuation analysis also depends on the background, the description of the averages, which is given by hybrid dynamical framework for studying single particle observables.

- Description of the initial stage in a collision : The far from equilibrium dynamics of the fireball immediately after the collision determines the initial conditions for the hydrodynamic stage that follows it [13, 109, 127, 143, 144]. Similarly the fluctuations at this stage will play an important role in determining the magnitude of the cumulants of particle multiplicities at freeze-out due to charge conservation.

- Equation of state which also includes critical point : The critical features of the EoS are essential in implementing the singular features of the speed of sound and the transport coefficients in the hydrodynamical equations. The equilibrium form of the thermodynamic fluctuations to which the the fluctuations of the hydrodynamic densities eventually relax into is determined by the susceptibilities obtained from the EoS. As mentioned in the previous section and will be described in much more detail in Chapter. (3), the critical features can be implemented by matching the QCD variables to 3D Ising model [62,63].

- Evolution of the hydrodynamic densities and fluctuations : A dynamical treatment of fluctuations coupled to the hydrodynamic evolution becomes essential near the critical point due to critical slowing down. For a comprehensive review in this frontier, refer to [126]. Some of the qualitative and semi-quantitative consequences are described in Chapter. (4).

- A freeze-out procedure to convert the hydrodynamic densities and fluctuations into particle distribution functions and their fluctuations : Freeze-out of fluctuations is discussed in detail in Chapters. (5) and (6).

- Hadronic transport after freeze-out : The mean and cumulants of particle multiplicities generated at freeze-out could then be evolved through a hadronic after-burner [69,88,145, 146]. This stage is important to determine how the decays of the resonances and the other inelastic and elastic processes modify the cumulants determined at freeze-out [147].

- Bayesian analysis to obtain the best-fit parameters based on the experimental data : In addition to the parameters that enter the hydrodynamic description of the conserved densities, the fluctuation framework also introduces new parameters namely the matching parameters to 3D Ising Model. Bayesian techniques will play an important role in determining the best fit parameters to the experimental data [148].

In this thesis, we'll discuss some aspects of mapping QCD to 3D Ising Model in Chapter (3), about the dynamical evolution of fluctuations of hydrodynamic densities in Chapter. (4) and freeze-out of these hydrodynamic fluctuations in Chapter. (5) and Chapter. (6).

CHAPTER 3

THERMODYNAMICS NEAR THE QCD CRITICAL POINT

This Chapter is based on the published work in [1] which I co-authored with my advisor, M.Stephanov.

As discussed in Chapter. (2), the straightforward reliable determination of the phase diagram of QCD at non-vanishing densities is hindered by the notorious sign problem [19]. However, if there is a critical point on the phase diagram, one can infer some features of the Equation of State (EoS) near it from universality. In this chapter we assume that there is a Z_2 critical point in QCD in the $T - \mu_B$ plane at the physical quark masses at some temperature and chemical potential values denoted by T_c and μ_c respectively. With this assumption, we then ask what features of the EoS near the critical point can be deduced via the universality of the critical phenomenon. In this chapter we shall focus on static thermodynamic properties. Dynamic universality near QCD critical point will be discussed in Chapter. (4). QCD EoS is an essential input for hydrodynamic calculations aimed at describing the heavy-ion collisions and identifying the signatures of the critical point.

The universality of static critical phenomena allows us to predict the leading singular behavior of thermodynamic functions, such as pressure $P(\mu, T)$ on temperature and chemical potential. The leading singular contribution to the QCD equation of state is essentially the same as the singular part of the equation of state of the Ising model with μ and T in QCD mapped onto (reduced) temperature $r = T - T_c$ and ordering (magnetic) field h of the Ising model. The parameters of the mapping are not universal and are generally treated as unknown parameters.

In this chapter, we shall investigate the properties of this mapping in order to constrain or determine a reasonable domain for the values of the unknown mapping parameters. The central result of this work follows from the fact that, due to the smallness of the (light) quark mass m_q the *critical* point is close, in parameter space, to the *tricritical* point [9] – the point separating the second and first-order finite temperature chiral restoration transition.[1] Thermodynamics near the tricritical point is also universal, albeit the universality class is different from the one of the Ising model. We point out that certain properties of the $(\mu, T)/(h, r)$ *mapping* near the critical point are universal in the limit of small quark masses due to the proximity of the tricritical point. The mapping becomes singular in a specific way. Most importantly, we observe that the slopes of the $r = 0$ and $h = 0$ lines in the (μ, T) plane become increasingly aligned near the critical point, with the slope difference vanishing with a specific power of the quark mass: $m_q^{2/5}$.

The chapter is organized as follows: In Section. (3.1) to (3.3), we describe various aspects of the mapping between different systems in the universality class of 3D Ising model and derive expressions for the mapping parameters. In Sections. (3.4) and (3.5), we apply the results from the previous sections to the special case of mean-field theories and provide an example of a

---

[1] These considerations would also apply, *m*utatis mutandis, to the tricritical point separating the second and first-order transitions as a function of the strange quark mass [27, 149], instead of the baryon chemical potential.

van der Waals gas near the critical point. In Section 3.6 we apply the results of Sections 3.2 and 3.4 to determine mapping parameters in a special case where a critical point is close to a tricritical point, which is also described by Ginzburg-Landau theory. Here, we derive the main result of this chapter about the scaling of the slope difference of h and r axes on the $T-\mu$ plane with quark mass. We illustrate the same and estimate values for the mapping parameters using Random Matrix Model of QCD in Section. (3.7). In Section 3.8 we investigate the effect of fluctuations, i.e., go beyond mean-field approximation using epsilon expansion. We show that the main conclusion – convergence of the slopes with difference of order $m_q^{2/5}$ is robust at least to two-loop order. Some results about the application of universality to determining the critical value of chemical potential and the Lee-Yang singularities are detailed in Appendix. (A). The calculation of the pseudo-critical curve from the Taylor expanded EoS at $\mu = 0$ is analyzed in Random Matrix Model in Appendix. (B). We conclude in Section 3.9 and discuss possible phenomenological implications.

3.1 Universality of critical phenomenon

The universality near a critical point, follows from the observation that the macroscopic phenomenon near it becomes insensitive to the microscopic details of the theory. This happens because the range over which the fluctuations are correlated becomes larger than the microscopic length scales such as the distance between the constituent particles. It follows that a physical system near its critical point can be described by the universal properties near a stable infrared fixed point which can be reached from the system Hamiltonian via a series of transformations involving averaging over shorter length scales or equivalently integrating over larger momentum modes [150–155]. The relevant directions at a fixed point, correspond to the directions along which small perturbations takes the system away from criticality. The subspace spanned by the irrelevant directions near the fixed point, is called the basin of the fixed point. The universality of critical phenomenon follows from the fact that the long-distance behavior of all systems (Hamiltonians) that fall in the basin of the same fixed point are the same. The perturbations along relevant and marginal directions at the infrared fixed point can be described via a low energy effective LGW Hamiltonian as we have seen before. The general form of the LGW Hamiltonian depends on the spatial dimensionality and the symmetries in the system of interest. QCD with non-zero quark masses do not possess any continuous symmetry that gets broken/restored at the critical point. It therefore falls into the default Z_2 universality class in three dimensions which describes the liquid-gas phase transitions, electroweak phase transition [156] and the phase transition in the 3D Ising Model.

3.2 Mapping QCD to 3D Ising Model

Due to this universality, all the liquid-gas critical points can be mapped onto the critical point of the Ising model since all of them flow to the same infrared fixed point described by the one-component ϕ^4 theory at the Wilson-Fischer fixed point. The field theory becomes conformal near the critical points due to the diverging correlation length. The universality class associated with this conformal fixed point is the most common in nature[1] and the QCD critical point, if it exists, belongs to it.

There are two relevant parameters in the ϕ^4 theory near the Wilson-Fischer fixed point: these correspond to the coefficients of the two relevant operators, ϕ and ϕ^2. These need to be tuned to zero to reach the critical point. Ising model has a global Z_2 symmetry, $\phi \to -\phi$. In this case, the relevant parameters simply map onto the ordering (magnetic) field h and reduced temperature $r = T - T_c$. On the other hand, the Z_2 symmetry that emerges in the scaling regime near the critical point of QCD or a generic liquid-gas critical point cannot be related to any such global symmetry in the respective system. Therefore one should expect a generic mapping $h(\mu, T)$ and $r(\mu, T)$.

3.2.1 Definition of mapping parameters

The universality results in the equivalence between the partition functions of QCD and 3D Ising model near their critical points. This correspondingly means the logarithms of these

---

[1] Unlike for other universality classes, it is not required to maintain degeneracy between the different components of the order-parameter field, such as in the case of $O(3)$ Heisenberg ferromagnet.

partition functions essentially the dominant singular part of pressure in QCD and the Gibbs free energy of the Ising model can be non-trivially related to each other as follows:

$$P_{\text{sing}}(\mu, T) = -AG(r(\mu, T), h(\mu, T))\,, \tag{3.1}$$

where P_{sing} is the dominant singular term in the QCD pressure at the critical point and G is the singular term in the Gibbs free energy of the Ising model, or equivalently ϕ^4 theory. A is a regular dimensionful function of μ and T, which can be chosen to be a constant to describe the leading singular behavior. We'll discuss more about the mapping $h(\mu, T)$ and $r(\mu, T)$ shortly.

Scaling, an important feature of the Ising Gibbs free energy can be expressed as:

$$G(\lambda r, \lambda^{\beta\delta} h) = \lambda^{\beta(\delta+1)} G(r, h) \tag{3.2}$$

with well-known critical exponents β and δ. The Z_2 symmetry is apparent from the relation:

$$G(r, -h) = G(r, h)\,. \tag{3.3}$$

From Eqs. (3.2) and (3.3) it follows that the function G can be written in terms of an even function g of a single variable:

$$G(r, h) = r^{\beta(\delta+1)} g(hr^{-\beta\delta})\,. \tag{3.4}$$

where g is multivalued, but a universal scaling function. In the complex plane of its argument $x \equiv hr^{-\beta\delta}$ the primary Riemann sheet describes the equation of state at high temperatures $T > T_c$, i.e., $r > 0$. We shall denote the value of g on this sheet as $g_+(x)$. On the primary (high temperature) sheet the function is analytic at $x = 0$. The closest singularities are on the imaginary x axis and are known as Lee-Yang edge singularities [157, 158] (see also recent discussions in Refs. [159, 160]). A secondary Riemann sheet describes the low temperature phase, $r < 0$. We shall denote the value of g on this sheet as $g_-(x)$.

The equivalence property (3.1) and the resulting mapping between (μ, T) and (h, r) variables was introduced by Rehr and Mermin and termed "revised scaling"[1] in Ref. [162]. In relativistic field theories, the mapping has been discussed with regard to QCD critical point, e.g., in Refs. [62,63,118,163–165], and, earlier, in the context of the electroweak transition in Ref. [156].

We will denote the position of the QCD critical point on the baryon-chemical potential-temperature plane by (μ_c, T_c). As we shall not be describing the sub-leading singularities, non-linear terms in $\Delta T = T - T_c$ and $\Delta\mu = \mu - \mu_c$ in the mapping functions $h(\mu, T)$ and

---

[1] The original version of scaling equation of state by Widom in Ref. [161] mapped r to $T - T_c$ directly, without allowing for mixing with h, which did not account for the asymmetry on the coexistence line found in liquid-gas transitions (e.g., discontinuity of susceptibility). This original scaling corresponds, in the notations used in this chapter, to $\alpha_2 = 0$.

$r(\mu, T)$ can be ignored. We will use the convention for the coefficients of the linear mapping introduced in Ref. [63]:

$$\begin{aligned} h(\mu, T) &= h_T \Delta T + h_\mu \Delta\mu = -\frac{\cos\alpha_1 \Delta T + \sin\alpha_1 \Delta\mu}{w T_c \sin(\alpha_1 - \alpha_2)}; \\ r(\mu, T) &= r_T \Delta T + r_\mu \Delta\mu = \frac{\cos\alpha_2 \Delta T + \sin\alpha_2 \Delta\mu}{\rho w T_c \sin(\alpha_1 - \alpha_2)}, \end{aligned} \tag{3.5}$$

where we denoted by a subscript T or μ the partial derivative with respect to the corresponding variable, e.g., $h_T \equiv \partial h / \partial T$ at fixed μ. The scale factors w and ρ provide absolute and relative normalization of h and r setting the size and shape of the critical region (see Section. 3.3). The slopes of the lines $h = 0$ (r axis) and $r = 0$ (h axis) on the (μ, T) plane can be expressed using angles α_1 and α_2, as shown in Figure 9:

$$\left(\frac{dT}{d\mu}\right)_{h=0} = -\frac{h_\mu}{h_T} = -\tan\alpha_1; \tag{3.6}$$

$$\left(\frac{dT}{d\mu}\right)_{r=0} = -\frac{r_\mu}{r_T} = -\tan\alpha_2\,. \tag{3.7}$$

The mapping can also be expressed in terms of the conjugate densities of the QCD variables (μ, T) and Ising variables (h, r). The conjugate densities in QCD are the number density $n = (\partial P/\partial\mu)_T$ and the entropy density, $s = (\partial P/\partial T)_\mu$. The conjugate densities in Ising model are the magnetization $m = (\partial G/\partial h)_r$ and the Ising entropy density, $\sigma = (\partial G/\partial h)_r$. The mapping between the densities can be expressed as:

$$\begin{pmatrix} m \\ \sigma \end{pmatrix} = \frac{1}{A(r_\mu h_T - h_\mu r_T)} \begin{pmatrix} r_T & -r_\mu \\ h_T & -h_\mu \end{pmatrix} \begin{pmatrix} \Delta n \\ \Delta s \end{pmatrix} \tag{3.8a}$$

$$= A^{-1}\, w\, T_c \begin{pmatrix} \cos\alpha_2 & -\sin\alpha_2 \\ -\rho\cos\alpha_1 & \rho\sin\alpha_1 \end{pmatrix} \begin{pmatrix} \Delta n \\ \Delta s \end{pmatrix} \tag{3.8b}$$

where $\Delta n = n - n_c$ and $\Delta s = s - s_c$ where n_c and s_c are the critical number and entropy densities in QCD respectively.

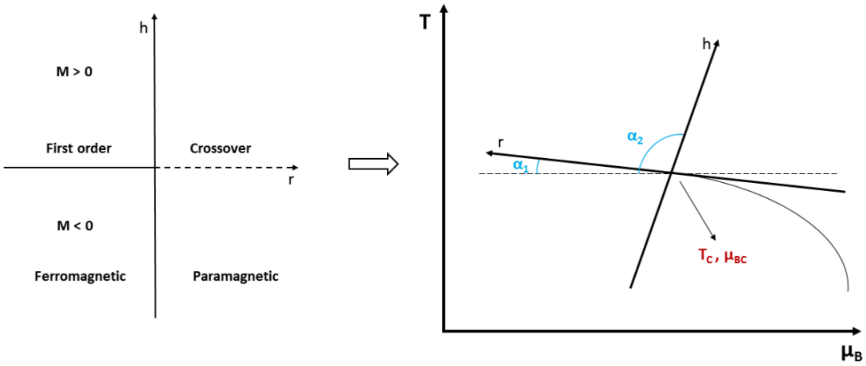

Figure 9

The mapping between QCD and Ising variables given by Eq. (3.5). Note that, since the sign of h is a matter of convention, the mappings with α_2 and $\alpha_2 \pm \pi$ are essentially equivalent. The figure is taken from Ref. [63].

3.2.2 Relating mapping parameters to pressure derivatives

If the equation of state $P(\mu, T)$ is known, one should be able to determine the mapping parameters. In this Subsection, for further applications, we shall derive expressions which can be used to do that.

We shall take all derivatives of pressure below on the crossover line, i.e., at $h = 0$ for $r > 0$ and keep only the most singular terms. In this Chapter, a subscript with respect to μ or T implies differentiation with respect to that variable when the other is kept fixed. Below, we also use indices X and Y to represent either T or μ. We find, at $h = 0$:

$$P_{XY} = -Ah_X h_Y r^{\beta-\beta\delta} g_+^{''}(0) + \ldots; \tag{3.9a}$$

$$P_{XXX} = 3A(\beta\delta - \beta) h_X^2 r_X r^{\beta-\beta\delta-1} g_+^{''}(0) + \ldots; \tag{3.9b}$$

$$\begin{aligned} P_{XXYY} = & -Ah_X^2 h_Y^2 r^{\beta-3\beta\delta} g_+^{''''}(0) \\ & +2\beta(\delta-1)(\beta(\delta-1)+1)\left(h_X^2 r_Y^2 + h_X h_Y r_X r_Y + h_Y^2 r_X^2\right) r^{\beta-\beta\delta-2} g_+^{''}(0) + \ldots . \end{aligned} \tag{3.9c}$$

The dots represent the terms which are subleading to the terms explicitly written in the limit $r \to 0$. From the above equations, it is easy to see that

$$h_X = \lim_{\substack{h=0 \\ r\to 0^+}} \left(\frac{P_{XX} r^{\beta\delta-\beta}}{-Ag_+''(0)} \right)^{1/2}; \tag{3.10}$$

$$r_X = \lim_{\substack{h=0 \\ r\to 0^+}} \frac{P_{XXX} r}{3(\beta - \beta\delta) P_{XX}} . \tag{3.11}$$

Therefore:

$$\tan\alpha_1 = \frac{h_\mu}{h_T} = \lim_{\substack{h=0\\ r\to 0^+}} \frac{P_{\mu\mu}}{P_{\mu T}}\,; \tag{3.12}$$

$$\tan\alpha_2 = \frac{r_\mu}{r_T} = \lim_{\substack{h=0\\ r\to 0^+}} \frac{P_{\mu\mu\mu}}{P_{TTT}}\frac{P_{TT}}{P_{\mu\mu}}\,. \tag{3.13}$$

Eq. (3.12) simply means, in particular, that the slope of the contour of critical number density ($n = P_\mu$) at the critical point is equal to the slope of $h = 0$. Eq. (3.13) relates the slope of $r = 0$ to the ratios of third and second derivatives of pressure evaluated along the cross-over line. These equations could be compared and contrasted with the expressions obtained by Rehr and Mermin in Ref. [162] using the discontinuities of the derivatives of pressure along the first-order line. As noted by Rehr and Mermin [162], mixing leads to two non-trivial consequences namely the average density at first order phase transition in liquid gas systems $\rho_d = (\rho_l + \rho_g)/2$ where ρ_l and ρ_g are the densities in the liquid and gas phase respectively, becomes singular and goes as,

$$\rho_d = \rho_c - (2-\alpha) r_\mu g_-(0) r^{1-\alpha} + \ldots \tag{3.14}$$

which is consistent with the experimental observations.The dependence of ρ_d on r_μ is evident from Eq. (3.14) and is also shown in (Figure 18): Similarly, the derivatives of susceptibility on

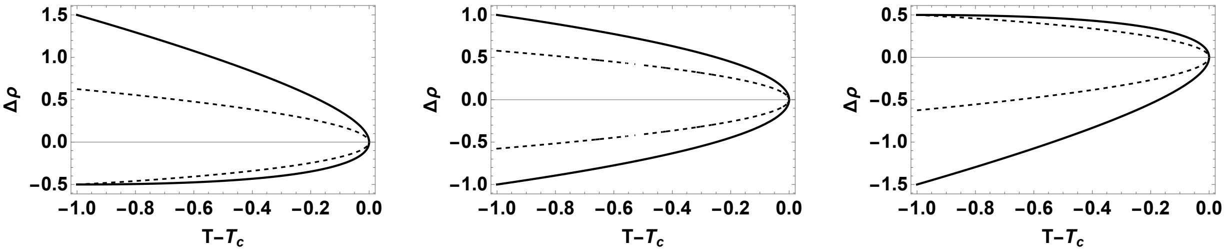

Figure 10: $\Delta\rho = \rho - \rho_c$ along the first-order line in a ϕ^4 model described by Eq. (3.43) in Section. (3.4.1) is shown by thick black curve for $r_\mu < 0$ (left), $r_\mu = 0$ (middle) and $r_\mu > 0$ (right). The axis are scaled by arbitrary units. Notice that $\rho_d - \rho_c$ is positive, zero and negative for $r_\mu < 0$ (left), $r_\mu = 0$ (middle) and $r_\mu > 0$ (right) respectively. The dashed curve is the spinodal line where the second derivative of pressure with respect to number density ρ vanishes. Therefore, the region inside the spinodal curve where $\partial^2 P/\partial\rho^2 < 0$ is unstable.

the first-order line also shows the following divergence:

$$\Delta\frac{\partial\rho}{\partial\mu} \quad = \quad -4\beta\frac{\partial h}{\partial\mu}\frac{\partial r}{\partial\mu}g_-^{'}(0_\pm)r^{\beta-1} + \ldots \tag{3.15}$$

$$\tag{3.16}$$

and the specific heat at constant volume (or equivalently at constant number density) diverges as:

$$\frac{C_v}{T} \quad = \quad -(2-\alpha)(1-\alpha)\left(\frac{\partial r}{\partial T}\right)^2_{h=0} f_-(0)r^{-\alpha} + \ldots \tag{3.17}$$

$\left(\frac{\partial r}{\partial T}\right)_{h=0}$ can be related to r_μ, h_μ, h_T and r_T as follows:

$$\left(\frac{\partial r}{\partial T}\right)_{h=0} = r_T - \frac{h_T r_\mu}{h_\mu} \tag{3.18}$$

Similarly, the parameters ρ and w in the mapping can also be related to pressure derivatives. In order to do that we also need an expression for r:

$$r \quad = \quad \left(-\frac{g''(0)^2 A\, P_{\mu\mu TT}}{g''''(0) P_{\mu\mu} P_{TT}}\right)^{-\frac{1}{\beta(\delta+1)}} \quad . \tag{3.19}$$

Using that expression in Eqs. (3.10) and (3.11) we can obtain ρ and w by substituting h_X and r_X into the following expressions:

$$\rho \quad = \quad \sqrt{\frac{h_\mu^2 + h_T^2}{r_\mu^2 + r_T^2}}; \tag{3.20}$$

$$w T_c \quad = \quad \frac{\sqrt{r_\mu^2 + r_T^2}}{|r_T h_\mu - r_\mu h_T|}. \tag{3.21}$$

The normalization convention in Ref. [63] which we follow corresponds to $A = T_c^4/2$. The angles α_1 and α_2 do not depend on this normalization whereas ρ and w do. (See next subsection for more details.) To fix the normalization of h and r we follow the standard convention, also used in Ref. [63]:

$$g'_-(0^+) = -(-1)^\beta \,, \qquad \lim_{x\to\infty^+} x^{-1/\delta} g'_\pm(x) = -1 \,. \tag{3.22}$$

Using equations in this subsection we can determine α_1, α_2, ρ and w given the EoS as a function of μ and T. There are many ways of expressing α_1, α_2, ρ and w in terms of ratios of pressure derivatives. We chose to present the expressions that treat T and μ variables the most symmetrically.

Recall that, the two point correlation function of number density is related to baryon susceptibility as follows

$$\langle \delta n^2 \rangle = \frac{T}{V} \frac{\partial^2 P}{\partial \mu^2} \tag{3.23}$$

and similarly, the two point correlation function of entropy density is similarly related to the derivatives of pressure as follows:

$$\langle \delta s^2 \rangle = \frac{T}{V} \frac{\partial^2 P}{\partial T^2} \tag{3.24}$$

$$\langle \delta s \delta n \rangle = \frac{T}{V} \frac{\partial^2 P}{\partial T \partial \mu} \tag{3.25}$$

Let δx and δy be any two linear combinations of δn and δs. Upon re-expressing the mapping in terms of the conjugate densities of the two systems, given by Eq. (3.8), we find that the leading singular behavior of the two point correlations of δx and δy along the coexistence line goes as:

$$\langle \delta x \delta y \rangle \quad \sim \quad r^{\beta - \beta\delta} \text{ if } \delta x \not\propto \sigma \not\propto \delta y \tag{3.26}$$

$$\langle \delta x \delta y \rangle \quad \sim \quad r^{\beta - 1} \text{ if either } \delta x \not\propto \delta y \propto \sigma \text{ or } \delta y \not\propto \delta x \propto \sigma \tag{3.27}$$

$$\langle \delta x \delta y \rangle \quad \sim \quad r^{\beta + \beta\delta - 2} \text{ if } \delta x \propto \delta y \propto \sigma \tag{3.28}$$

From Eq. (3.26),we note that most of the two point correlations have the same leading singular behavior which goes as $r^{-\gamma}$ $(\gamma = \beta - \beta\delta)$ along the cross-over line.

3.2.3 Corrections to scaling due to uncertainties in α_1, α_2, ρ and w

We discussed how to obtain $\alpha_!, \alpha_2, \rho$ and w when the EoS is known. But for most important applications of universality of critical phenomenon, the EoS of one of the systems is not known. However, one may be able to make some informed guesses based on the available information. In these circumstances, it is important to know the corrections to scaling part of the EoS due to uncertainties in the parameters. This will be discussed in this subsection.

In the equations given below, the following notations are used:

$$c_{12} \equiv \cos(\alpha_1 - \alpha_2)\,, \quad s_{12} \equiv \sin(\alpha_1 - \alpha_2)\,, \quad x \equiv hr^{-\beta\delta} \tag{3.29}$$

The change in pressure due to small changes in α_1, α_2, ρ and w are shown below:

- Case1: $\alpha_2 \to \alpha_2 + \delta\alpha_2$

$$dP_{\alpha_2} = -r^{2-\alpha}\delta\alpha_2 \left\{ \frac{c_{12}}{s_{12}} g^{'}(x)x + r^{\beta\delta-1}\left[-\frac{2-\alpha}{\rho s_{12}} g(x)x + \frac{\beta\delta}{\rho s_{12}} g^{'}(x)x^2 \right] \right\} \tag{3.30}$$

- Case 2: $\rho \to \rho + \delta\rho$

$$dP_\rho = -r^{2-\alpha}\frac{\delta\rho}{\rho}\left[-(2-\alpha)g(x) + \beta\delta g^{'}(x)x \right] \tag{3.31}$$

- Case 3:$w \to w + \delta w$

$$dP_w = -r^{2-\alpha}\frac{\delta w}{w}\left[-(2-\alpha)g(x) + (\beta\delta - 1)xg^{'}(x)\right] \tag{3.32}$$

- Case 4:$\alpha_1 \to \alpha_1 + \delta\alpha_1$

$$dP_{\alpha_1} = -r^{2-\alpha}\delta\alpha_1\left\{r^{1-\beta\delta}g^{'}(x)\frac{\rho}{s_{12}} + \left[-\frac{(2-\alpha)c_{12}}{s_{12}}g(x) + \frac{\beta\delta c_{12}}{s_{12}}g^{'}(x)x\right]\right\} \tag{3.33}$$

Some special linear combinations of these transformations that are discussed below correspond to an equivalent change of the mapping parameters α_1, α_2, ρ and w as shown below:

- $r \to r + vh$

  This transformation is equivalent to the following change in the mapping parameters:

$$\delta\alpha_2 = v\rho s_{12}\,, \quad \delta\rho = -vc_{12}\rho^2\,, \quad \delta w = vw\rho c_{12}\,, \quad \delta\alpha_1 = 0 \tag{3.34}$$

  This changes pressure by:

$$\Delta P = vr^{2-\alpha+\beta\delta-1}\left[(2-\alpha)g(x)x - \beta\delta g^{'}(x)x^2\right] \tag{3.35}$$

- $h \to h + vr$

  This change is equivalent to the following transformation:

$$\delta\alpha_1 = -v\frac{s_{12}}{\rho}\,, \quad \delta\rho = vc_{12}\,, \quad \delta w = 0\,, \quad \delta\alpha_2 = 0 \tag{3.36}$$

  Note that $\delta w = 0$, which was not expected. The change in pressure due to this transformation is:

$$\Delta P = vr^{3-\alpha-\beta\delta} g'(x) \tag{3.37}$$

- While matching the Gibbs free energy of the Ising model to the QCD pressure, the scale factor A was arbitrary. The choice of A determines the magnitude of w and ρ. $P \to AP$, is equivalent to the following transformation

$$\rho \;\to\; A^{\frac{\beta\delta-1}{\beta(\delta+1)}}\rho\,, \quad w \to A^{-\frac{\delta}{1+\delta}}w \tag{3.38}$$

$$\delta\log\rho \;\to\; \frac{\beta\delta-1}{\beta(\delta+1)}\log A\,, \quad \delta\log w \to -\frac{\delta}{1+\delta}\log A \tag{3.39}$$

  Therefore a change of A when accompanied by a change of $\rho \to A^{-\frac{\beta\delta-1}{\beta(\delta+1)}}\rho$ and $w \to A^{\frac{\delta}{1+\delta}}w$ leaves the pressure unchanged.

3.3 The size of the critical region

As discussed before, the mapping parameters determine the size of the critical region. This region is where the dominant singular contribution to a thermodynamic quantity at the critical point is larger than the the regular terms. We note that this an ambiguous definition and depends crucially on the quantity used as a measure for the singularity. Pressure itself doesn't diverge at the critical point. However, we could use any of its derivatives which diverge at the critical point to defined this characteristic region. Here we use the baryon susceptibility, $\chi_2 = P_{\mu\mu}$ as a reasonable measure to describe the size of this region. We shall evaluate the size of the critical region along the crossover, $h = 0$, line. The singular part of χ_2 is given by, at $h = 0$,

$$\chi_2^{sing} \sim AG_{\mu\mu}(r,0) \sim AG_{hh}(r,0)h_\mu^2 \sim Ar^{-\gamma}\left(\frac{s_1}{wT_c s_{12}}\right)^2 \sim A\left(\frac{\Delta\mu}{\rho w T_c c_1}\right)^{-\gamma}\left(\frac{s_1}{wT_c s_{12}}\right)^2 \quad (3.40)$$

where $s_1 = \sin\alpha_1$, $c_1 = \cos\alpha_1$ and $s_{12} = \sin(\alpha_1 - \alpha_2)$. Comparing this to the regular contribution of order $\chi_2^{reg} \sim T_c^2$, we find for the extent of the critical region in the μ direction:

$$\Delta\mu_{CR} \sim T_c \rho w c_1 \left(\frac{s_1\sqrt{A}}{wT_c^2 s_{12}}\right)^{2/\gamma} \quad (3.41)$$

Therefore, while increasing parameters ρ and A increases the size of the critical region, the effect of increasing the parameter w is the opposite: $\Delta\mu_{CR} \sim w^{1-2/\gamma}$. In the mean-field theory $\gamma = 1$ and $\Delta\mu_{CR}$ is inversely proportional to w. Another quantity that may be used to define the critical region is kurtosis, which is related to the fourth derivative of pressure. This has been done in [108].

3.4 Mean-field Equation of State

3.4.1 Symmetry and scaling in mean-field theory

If one neglects fluctuations, the equation of state near the critical point can be described using a mean-field Landau-Ginsburg potential. The pressure, thus is given by the minimum of this potential, which is a function of the mean-field order parameter, ϕ:

$$P(\mu, T) = -A \min_{\phi} \Omega(\phi, \mu, T)\,. \tag{3.42}$$

We make a simple and useful observation: by changing the variable $\phi \to f(\phi)$ we can obtain a family of potentials $\hat{\Omega}(\phi)$ obeying $\hat{\Omega}(\phi) = \Omega(f(\phi))$ each of which gives the same pressure. We shall refer to this property as reparametrization invariance.

Close to the critical point, Ω can be expanded around the critical value of ϕ (chosen to be $\phi = 0$):

$$\Omega(\phi, \mu, T) = \Omega_0 - h\phi + \frac{r}{2}\phi^2 + \frac{u}{4}\phi^4 + \dots\,, \tag{3.43}$$

where we eliminated cubic term ϕ^3 by a shift of variable ϕ (such an operator or term is called redundant in renormalization group terminology). Parameters Ω_0, h, r and u are analytic functions of μ and T. The critical point is located at $h = 0$ and $r = 0$ (with $u > 0$). If we truncate the expansion at order ϕ^4 as in Eq. (3.43) the ϕ-dependent part, $\Omega - \Omega_0$, possesses two important properties. The first is the Z_2 symmetry:

$$\phi \to -\phi, \quad h \to -h, \quad r \to r\,. \tag{3.44}$$

The second is scaling:

$$\phi \sim r^{1/2}, \quad h \sim r^{3/2}, \quad \Omega - \Omega_0 \sim r^2\,. \tag{3.45}$$

This corresponds to the scaling of the Gibbs free energy G in Eq. (3.2) with mean-field exponents $\beta = 1/2$ and $\beta\delta = 3/2$.

One could be tempted to expand the coefficients h and r in Eq. (3.43) to linear order in ΔT and $\Delta\mu$ and identify the mixing parameters α_1, α_2, etc., by using Eq. (3.5). This, however, is not entirely correct as it would ignore the fact that the mixing of h and r described by Eq. (3.5) necessarily violates scaling, since $h \sim r^{3/2}$ and r have different scaling exponents. Therefore, we need also to look at the omitted terms which violate scaling in Eq. (3.43), or more precisely, provide corrections to scaling of relative order $h/r \sim r^{1/2}$ (i.e., $r^{\beta\delta-1}$). Furthermore, mixing of h and r also violates Z_2 symmetry in Eq. (3.44), i.e., we need also to look at omitted Z_2 breaking terms in Eq. (3.43).

Since $\phi \sim r^{1/2}$, omitted higher order terms in Eq. (3.43) represent corrections to scaling. The leading correction is due to the ϕ^5 term. Because in mean-field theory this term is smaller by exactly a factor of $r^{1/2}$ compared to the terms in Eq. (3.43), and also because it violates the Z_2 symmetry in Eq. (3.44) (being odd), this term will affect the mixing of h and r.

3.4.2 The effect of the ϕ^5 term

Let us denote the coupling of the ϕ^5 term by vu, i.e.,

$$\Omega = \Omega_0 - \bar{h}\phi + \frac{1}{2}\bar{r}\phi^2 + \frac{u}{4}\phi^4 + vu\phi^5 + O(\phi^6), \tag{3.46}$$

where we also changed the notation for the coefficients of the ϕ and ϕ^2 terms in anticipation of them being different from h and r in Eq. (3.5).

To understand the effect of the ϕ^5 term on the mixing of h and r we can use reparametrization invariance of pressure to change the variable ϕ in such a way as to eliminate the ϕ^5 term from Ω. This can be achieved by the following transformation:

$$\phi \to \phi + v\left(\frac{\bar{r}}{u} - \phi^2\right), \tag{3.47}$$

which eliminates ϕ^5 and as well as ϕ^3 term at order up to $r^{5/2}$:

$$\Omega = \left(\Omega_0 - \frac{v\bar{h}\bar{r}}{u}\right) - \left(\bar{h} - \frac{v\bar{r}^2}{u}\right)\phi + \left(\frac{\bar{r}}{2} + v\bar{h}\right)\phi^2 + \frac{u}{4}\phi^4 + \mathcal{O}(\phi^6, r^3), \tag{3.48}$$

where we kept only terms up to order $r^{5/2}$, since we are interested in the leading correction to scaling. From Eq. (3.48) we can now read off the parameters h and r:

$$h = u^{-1/4}\left(\bar{h} - \frac{v\bar{r}^2}{u}\right) = u^{-1/4}\bar{h} + \mathcal{O}(\bar{r}^2), \tag{3.49}$$

$$r = u^{-1/2}\left(\bar{r} + 2v\bar{h}\right), \tag{3.50}$$

which match Eq. (3.48) onto a mean-field potential without leading asymmetric (Z_2-breaking, non-Ising) corrections to scaling. The additional rescaling $\phi \to u^{-1/4}\phi$ was applied to bring the potential to the canonical form:[1]

$$\Omega = -h\phi + \frac{r}{2}\phi^2 + \frac{1}{4}\phi^4. \tag{3.51}$$

The scaling function $g(x)$ corresponding to this potential via $G = \min_\phi \Omega = r^2 g(hr^{-3/2})$ (see Eq. (3.4)) satisfies

$$x + g'(x) + g'^3(x) = 0, \tag{3.52}$$

which agrees with the normalization in Eq. (3.22). Therefore, parameters h and r in Eqs. (3.49) and (3.50) are the parameters which appear in the mapping equations (3.5).

---

[1] The rescaling does not affect the slopes of $h = 0$ or $r = 0$ (angles α_1 and α_2), but needs to be taken into account when calculating ρ and w.

Note that the main effect of the asymmetric corrections to scaling is to modify $\bar{r}$ in Eq. (3.50) by a term *linear* in $\bar{h}$, which has direct effect on the angle α_2 determining the slope of the $r = 0$ axis. The slope of the $h = 0$ axis is not affected as the shift of $\bar{h}$ in Eq. (3.49) is quadratic in $\bar{r}$.

3.4.3 Direct relation to derivatives of the potential

It is also useful to relate mapping parameters h_X and r_X, where $X = T$ or μ, directly to the Ginzburg-Landau potential Ω. The relation can be obtained straightforwardly from Eqs. (3.9a-3.9c) using

$$P_{XX} = -\Omega_{XX} + \Omega_{X\phi}^2 \Omega_{\phi\phi}^{-1}\,, \tag{3.53}$$

$$P_{XXX} = -\Omega_{XXX} - 3\Omega_{\phi\phi}^{-2}\Omega_{X\phi}(\Omega_{X\phi}\Omega_{X\phi\phi} - \Omega_{\phi\phi}\Omega_{XX\phi}) + \Omega_{\phi X}^3 \Omega_{\phi\phi}^{-3}\Omega_{\phi\phi\phi}\,. \tag{3.54}$$

To simplify the expressions we shall first consider potential $\hat{\Omega}$ obtained from Ω by bringing it into the "Ising" form in Eq. (3.43) with no ϕ^3 or ϕ^5 terms (up to order $r^{5/2}$). We showed that this can be always achieved by a reparametrization as in Eq. (3.47), Eq. (3.48). In this case,

$\hat{\Omega}_{\phi\phi\phi} = 0$ on the $h = 0$ line along which we take the limits in Eqs. (3.10), (3.11) and expressions simplify:

$$\tan\alpha_1 = \frac{\hat{\Omega}_{\phi\mu}}{\hat{\Omega}_{\phi T}}\,; \tag{3.55}$$

$$\tan\alpha_2 = \frac{\hat{\Omega}_{\phi\phi\mu}}{\hat{\Omega}_{\phi\phi T}}\,; \tag{3.56}$$

$$\rho = \left(\frac{\hat{\Omega}_{\phi\phi\phi\phi}}{6}\right)^{1/4} \sqrt{\frac{\hat{\Omega}^2_{\phi\mu} + \hat{\Omega}^2_{\phi T}}{\hat{\Omega}^2_{\phi\phi\mu} + \hat{\Omega}^2_{\phi\phi T}}}\,; \tag{3.57}$$

$$wT_c = \left(\frac{\hat{\Omega}_{\phi\phi\phi\phi}}{6}\right)^{1/4} \frac{\sqrt{\hat{\Omega}^2_{\phi\phi\mu} + \hat{\Omega}^2_{\phi\phi T}}}{|\hat{\Omega}_{\phi\mu}\hat{\Omega}_{\phi\phi T} - \hat{\Omega}_{\phi T}\hat{\Omega}_{\phi\phi\mu}|}\,. \tag{3.58}$$

Note that in the mean-field theory these expressions are analytic at the critical point and can be simply evaluated at the critical point without taking a limit. This is in contrast to Eqs. (3.10) and (3.11) where the derivatives of pressure are singular and a careful limit has to be taken to cancel singularities.

One can then generalize these expressions to arbitrary potential ($\Omega_{\phi\phi\phi} \neq 0$ at $h = 0$) by observing that combinations

$$\Omega_{\phi X}, \quad \Omega_{\phi\phi X} - \frac{\Omega_{\phi\phi\phi\phi\phi}\Omega_{\phi X}}{10\Omega_{\phi\phi\phi\phi}}, \quad \text{and} \quad \Omega_{\phi\phi\phi\phi}, \tag{3.59}$$

are reparametrization “covariant” to leading order in r in the sense that under $\phi \to f(\phi)$ they transform multiplicatively by factors f', $(f')^2$ and $(f')^4$, respectively. Thus, we can drop ‘hats’ and replace

$$\hat{\Omega}_{\phi\phi X} \to \Omega_{\phi\phi X} - \frac{\Omega_{\phi\phi\phi\phi\phi}\Omega_{\phi X}}{10\Omega_{\phi\phi\phi\phi}} \tag{3.60}$$

in Eqs. (3.55-3.58) to obtain general formulas applicable to any potential. Note that the last term in Eq. (3.60) corresponds to the last term in Eq. (3.50) describing the mixing of r and h due to the ϕ^5 term.

3.5 Mapping parameters for the van der Waals equation of state

In this Section, to illustrate the use of the formalism developed in Section 3.4 we shall derive the equations for the mapping parameters in the van der Waals equation of state. The well-known equation of state expresses pressure as a function of particle density n and temperature T:

$$P = \frac{nT}{1-bn} - an^2\,, \tag{3.61}$$

where a and b are van der Waals constants corresponding to the strength of the particle attraction and the hard-core volume, respectively. The van der Waals equation of state possesses a critical point at

$$n_c = \frac{1}{3b}, \quad T_c = \frac{8a}{27b}, \quad P_c = \frac{a}{27b^2}\,. \tag{3.62}$$

The equation of state (3.61) can be expressed in the mean-field (Ginzburg-Landau) form

$$P(\mu, T) = -A \min_n \Omega(n, T, \mu)\,, \tag{3.63}$$

where

$$A\Omega(n, T, \mu) = \mu n - F(T, n) \tag{3.64}$$

is expressed in terms of the free energy $F(n,T)$, which is the Legendre transform of $P(\mu,T)$:

$$F(n,T) \quad = \quad n\mu(n,T) - P(\mu(n,T),T)\,. \tag{3.65}$$

In Eq. (3.65), but not in Eq. (3.64), the chemical potential $\mu(n,T)$ must be determined as a solution to $n = \partial P/\partial\mu$. This can be done by integrating the following set of partial differential equations:

$$\left(\frac{\partial\mu}{\partial n}\right)_T = \frac{1}{n}\left(\frac{\partial P}{\partial n}\right)_T\,; \tag{3.66}$$

$$\left(\frac{\partial\mu}{\partial T}\right)_n = \frac{1}{n}\left(\frac{\partial P}{\partial T}\right)_n - \frac{s}{n}\,; \tag{3.67}$$

$$\left(\frac{\partial s}{\partial T}\right)_n = \frac{c_v n}{T}\,, \tag{3.68}$$

where c_v is the heat capacity per particle (e.g., 3/2 for monoatomic gas). Using the values of μ and s at the critical point, μ_c and s_c, as initial conditions one finds

$$\begin{aligned}\mu(n,T) \quad = \quad & T\left(\log\frac{2bn}{1-bn} - \log\frac{2bn_c}{1-bn_c}\right) + \frac{T}{1-bn} - \frac{T_c}{1-bn_c} \\ & -2a(n-n_c) - c_vT\log\frac{T}{T_c} + \left(c_v - \frac{s_c}{n_c}\right)(T-T_c) + \mu_c\,.\end{aligned} \tag{3.69}$$

Expanding the potential Ω one obtains

$$A\Omega(n,T,\mu) \quad = \quad A\Omega(n_c,T_c,\mu_c) - \left(\Delta\mu - \left(\frac{3}{2} - 3bs_c\right)\Delta T\right)\eta + \frac{27b}{8}\Delta T\eta^2 + \frac{9ab^2}{8}\eta^4 - \frac{27ab^3}{40}\eta^5 + \tag{3.70}$$

where $\eta = n - n_c$, $\Delta T = T - T_c$ and $\Delta\mu = \mu - \mu_c$. Comparing to Eq. (3.46) we identify

$$A\bar{h} = \Delta\mu - \left(\frac{3}{2} - 3bs_c\right)\Delta T, \tag{3.71}$$

$$A\bar{r} = \frac{27b}{4}\Delta T, \tag{3.72}$$

$$Au = \frac{9ab^2}{2}, \quad v = -\frac{3b}{20}. \tag{3.73}$$

Using Eqs. (3.49), (3.50) one then finds

$$h = A^{-3/4}\left(\frac{9ab^2}{2}\right)^{-1/4}\left(\Delta\mu - \left(\frac{3}{2} - 3bs_c\right)\Delta T\right) \tag{3.74}$$

$$r = -A^{-1/2}\frac{3}{10}\left(\frac{9a}{2}\right)^{-1/2}\left(\Delta\mu + 3\left(b\, s_c - 8\right)\Delta T\right) . \tag{3.75}$$

Using Eqs. (3.12), (3.13), (3.20) and (3.21) one finally obtains

$$\tan\alpha_1 = -\left(\frac{3}{2} - \frac{s_c}{n_c}\right)^{-1} ; \tag{3.76}$$

$$\tan\alpha_2 = -\left(24 - \frac{s_c}{n_c}\right)^{-1} ; \tag{3.77}$$

$$\rho = 5\left(\frac{3P_c}{T_c^4}\right)^{1/4}\sqrt{\frac{4s_c\left(s_c - 3n_c\right) + 13n_c^2}{s_c\left(s_c - 48n_c\right) + 577n_c^2}} ; \tag{3.78}$$

$$w = \frac{1}{40}\left(\frac{T_c^4}{3P_c}\right)^{3/4}\sqrt{\frac{s_c}{n_c}\left(\frac{s_c}{n_c} - 48\right) + 577} \, . \tag{3.79}$$

One can use Eq. (3.8) to rewrite the mapping in terms of the densities. From this mapping, we learn that the "magnetization" like density in van der waals gas is a linear combination of Δn and Δs.

3.6 Critical point near a tricritical point

A tricritical point arises in many systems where the order of the finite-temperature transition from broken to restored symmetry phase depends on an additional thermodynamic parameter, such as pressure or chemical potential. The point where the order of the transition changes from second to first is a tricritical point. There are reasons to believe QCD to be one of the examples of such a theory [9, 20]. A nonzero value of a parameter which breaks spontaneously broken symmetry explicitly (quark mass in QCD) removes the second order phase transition and replaces it with analytic crossover, while the first order transition then ends at a critical point.

We shall apply mean-field theory near the tricritical point. The potential needed to describe the change from a first to second order transition needs to include a Φ^6 term which becomes marginal in $d = 3$. Therefore, mean field theory should be applicable in $d = 3$ if one is willing, as we are, to neglect small logarithmic corrections to scaling.[1]

As in Section 3.4 we want to express the pressure as a minimum of the Ginzburg-Landau potential Ω. We can do that using the Legendre transform of pressure P with respect to m_q:

$$V(\Phi, \mu, T) = -P(\mu, T, m_q(\Phi)) + m_q(\Phi)\Phi\,, \tag{3.80}$$

---

[1] For example, if these corrections have negligible consequences for applications, such as heavy-ion collisions or lattice QCD simulations. To be rigorous, we can also formally consider $d > 3$. In fact, our analysis near the *critical* point is constrained by an even stronger condition, since the upper critical dimension in this case is $d = 4$ and, in practice, we work in $d = 4 - \epsilon > 3$ when we study the effects of fluctuations in Section 3.8.

where $m_q(\Phi)$ is the solution of

$$\partial P/\partial m_q = \Phi, \tag{3.81}$$

which means Φ is the chiral condensate (times N_f – the number of light quarks).

It is easy to see that the potential Ω defined as

$$A\Omega(\Phi, \mu, T, m_q) = V(\Phi, \mu, T) - m_q\Phi \tag{3.82}$$

is related to pressure by

$$P(\mu, T, m_q) = -A \min_{\Phi} \Omega(\Phi, \mu, T, m_q) \tag{3.83}$$

where we chose the normalization constant A to match Eq. (3.42).

The potential V has to be symmetric under $\Phi \to -\Phi$ (this is a discrete subgroup of the continuous chiral symmetry) and to describe a tricritical point we need terms up to Φ^6. Expanding V we find:

$$V(\Phi, \mu, T) = V_0 + \frac{a}{2}\Phi^2 + \frac{b}{4}\Phi^4 + \frac{c}{6}\Phi^6 + \dots\,, \tag{3.84}$$

where a, b and c are functions of T and μ. The tricritical point occurs when $a = b = 0$ with $c > 0$. If we truncate V at order Φ^6 as in Eq. (3.84) the Φ-dependent part of V and Ω, has the following scaling property:

$$\Phi \sim a^{1/4}, \quad b \sim a^{1/2}, \quad m_q \sim a^{5/4} \quad V - V_0 \sim a^{3/2}\,. \tag{3.85}$$

The minimum value of Ω in Eq. (3.83) is achieved at Φ satisfying, to lowest order in $a \to 0$,

$$m_q = \frac{\partial V}{\partial \Phi} = a\Phi + b\Phi^3 + c\Phi^5\,. \tag{3.86}$$

At nonzero m_q the critical point occurs when both second and third derivatives of Ω vanish at the minimum given by Eq. (3.86). I.e.,

$$\frac{\partial^2 V}{\partial \Phi^2} = \frac{\partial m_q}{\partial \Phi} = a + 3b\Phi^2 + 5c\Phi^4 = 0. \tag{3.87}$$

and

$$\frac{\partial^3 V}{\partial \Phi^3} = 6b\Phi + 20c\Phi^3 = 0. \tag{3.88}$$

Eqs. (3.86), (3.87) and (3.88), can be solved simultaneously to find the critical values of Φ, a and b for a given m_q:

$$\Phi_c = \left(\frac{3m_q}{8c}\right)^{1/5}, \quad a_c = 5c\Phi_c^4, \quad b_c = -\frac{10c}{3}\Phi_c^2. \tag{3.89}$$

As a function of m_q, the trajectory $(m_q, a_c(m_q), b_c(m_q))$ corresponds to the line of critical points on the edges of "wings" – coexistence surfaces in the m_q, T, μ phase diagram (see, e.g., Figure 12 for illustration). Note that critical values of parameters in Eq. (3.89) scale as $\Phi_c \sim m_q^{1/5}, a_c \sim m_q^{4/5}$ and $b_c \sim m_q^{2/5}$ consistent with the scaling in Eq. (3.85). We can now expand Ω around that solution:

$$A\,\Omega(\Phi;\mu,T,m_q) = A\,\Omega(\Phi_c;T_c,\mu_c,m_q)+(\Delta a\Phi_c+\Delta b\Phi_c^3)\phi+\frac{1}{2}(\Delta a+3\Delta b\Phi_c^2)\phi^2+\frac{1}{4}\left(\frac{20c\Phi_c^2}{3}+\Delta b\right)\phi^4 + \Delta b\Phi_c\phi^3+c\Phi_c\phi^5+\frac{c}{6}\phi^6\,, \quad (3.90)$$

where $\Delta a = a - a_c$, $\Delta b = b - b_c$ and $\phi = \Phi - \Phi_c$. We can now compare this expansion to the ϕ^4 theory in the previous section. The redundant term ϕ^3 can be eliminated, as usual, by a shift of ϕ. Comparing with Eq. (3.46) we find:

$$A\,\bar{h} = -(\Delta a + \Delta b\Phi_c^2)\Phi_c\,, \quad (3.91)$$

$$A\,\bar{r} = \Delta a + 3\Delta b\Phi_c^2\,, \quad (3.92)$$

$$Au = \frac{20\Phi_c^2}{3}\,, \quad v = \frac{3}{20\Phi_c}\,. \quad (3.93)$$

The ϕ^5 term causes mixing of $\bar{h}$ and $\bar{r}$ as in Eq. (3.50). Using Eqs. (3.49) and (3.50) to linear order in Δa and Δb (i.e., linear order in ΔT and $\Delta\mu$) we find

$$\begin{aligned} A\,h &= -u^{-1/4}\left(\Delta a + \Delta b\Phi_c^2\right)\Phi_c, \\ A\,r &= u^{-1/2}\left(\frac{7}{10}\Delta a + \frac{27}{10}\Delta b\Phi_c^2\right). \end{aligned}$$

Since a and b are analytic functions of T and μ near the critical point we can expand to linear order:

$$\begin{aligned} \Delta a &= a_T\Delta T + a_\mu\Delta\mu\,; \\ \Delta b &= b_T\Delta T + b_\mu\Delta\mu\,. \end{aligned} \tag{3.94}$$

Using Eqs. (3.55), (3.56), we determine the slopes at the critical point:

$$\tan\alpha_1 = -\left(\frac{dT}{d\mu}\right)_{h=0} = \frac{h_\mu}{h_T} = \frac{a_\mu + b_\mu\Phi_c^2}{a_T + b_T\Phi_c^2}\,; \tag{3.95}$$

$$\tan\alpha_2 = -\left(\frac{dT}{d\mu}\right)_{r=0} = \frac{r_\mu}{r_T} = \frac{a_\mu + 27b_\mu\Phi_c^2/7}{a_T + 27b_T\Phi_c^2/7}\,. \tag{3.96}$$

In general, the two slopes are different and non-universal (i.e., depend on the non-universal coefficients a_μ, a_T, etc. However, the limit $m_q \to 0$ is special. In this limit the two slopes approach each other with the difference vanishing as $\Phi_c^2 \sim m_q^{2/5}$ (see Eq. (3.89)):

$$\begin{aligned} \tan\alpha_1 - \tan\alpha_2 = \left(\frac{dT}{d\mu}\right)_{r=0} - \left(\frac{dT}{d\mu}\right)_{h=0} &= \frac{20}{7a_T^2}\frac{\partial(a,b)}{\partial(\mu,T)}\Phi_c^2 + \mathcal{O}(\Phi_c^4) \\ &= \frac{20}{7a_T^2}\frac{\partial(a,b)}{\partial(\mu,T)}\left(\frac{3}{8c}\right)^{2/5} m_q^{2/5} + \mathcal{O}(m_q^{4/5}) \end{aligned} \tag{3.97}$$

where $\partial(a,b)/\partial(\mu,T) = a_\mu b_T - a_T b_\mu$ is the Jacobian of the mapping in Eq. (3.94).

The relative orientation of the slopes, i.e., the sign of the slope difference, is determined by the sign of the Jacobian of the $(a,b) \to (\mu,T)$ mapping. It is positive in the case of the mapping without reflection and negative otherwise. In that sense, it is topological. We show how to determine the sign on Figure 11 by comparing the phase diagram in the vicinity of the tricritical point in (a,b) coordinates with the standard scenario of the QCD phase diagram in (μ,T) coordinates. We see that the two graphs are topologically the same: the first order transition is to the right of the tricritical point and the broken (order) phase is below the tricritical point. This means that the Jacobian of the (a,b) to (μ,T) is positive (no reflection is involved). This means that, since $h=0$ slope is negative, the $r=0$ slope must be less steep, or if α_1 itself is small, α_2 could be slightly negative. We shall see in the next Section that in the random matrix model both slopes are negative and small (i.e., $\alpha_1 > \alpha_2 > 0$ in the model).

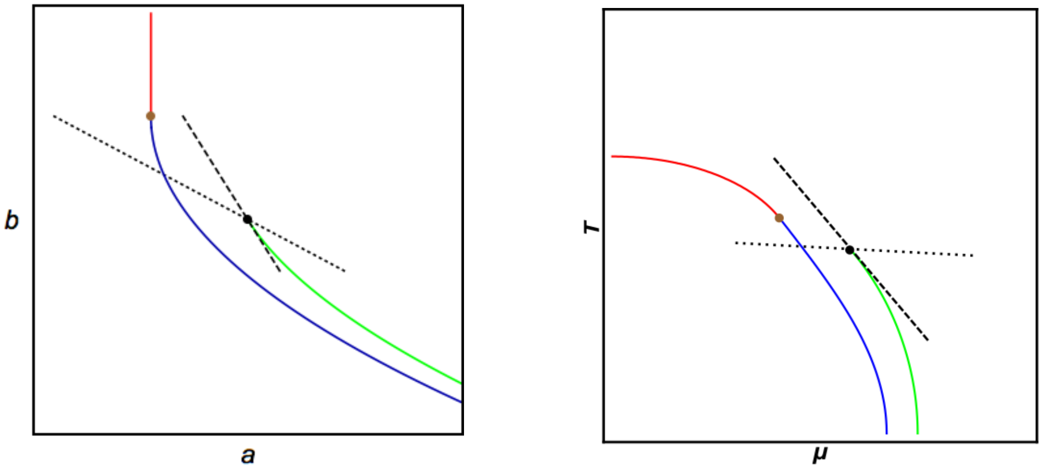

Figure 11: *Left*: The phase diagram of the Φ^6 theory described by Eq. (3.90) in the $a-b$ plane. *Right*: QCD phase diagram in the $\mu-T$ plane. The blue and red lines correspond to the first-order and second-order phase transitions at $m_q = 0$ respectively. They join at a tricritical point. The green line represents the first-order phase transition at $m_q \neq 0$ ending in a critical point. The symmetry broken (ordered) phase is in the lower left corner in both cases. The slopes of the $h = 0$ and $r = 0$ lines at the critical point are indicated by the dashed and dotted lines respectively.

The Jacobian in Eq. (3.125) can be rewritten in a more geometrically intuitive form in terms of the difference of slopes of $a = 0$ and $b = 0$ on the (μ, T) phase diagram of QCD at $m_q = 0$:

$$\frac{1}{a_T^2}\frac{\partial(a,b)}{\partial(\mu,T)} = \left(\frac{\partial b}{\partial a}\right)_\mu \left(\left(\frac{\partial T}{\partial \mu}\right)_{b=0} - \left(\frac{\partial T}{\partial \mu}\right)_{a=0}\right) . \tag{3.98}$$

The $a = 0$ slope is, of course, the slope of the chiral phase transition line at the tricritical point.

One can also determine the dependence of ρ and w on m_q using Eqs. (3.57) and (3.58). Using Eq. (3.90) we find, in the limit of $m_q \to 0$:

$$\sqrt{\Omega_{\phi\mu}^2 + \Omega_{\phi T}^2} \sim m_q^{1/5}, \quad \sqrt{\Omega_{\phi\phi\mu}^2 + \Omega_{\phi\phi T}^2} \sim m_q^0,$$
$$\Omega_{\phi\mu}\Omega_{\phi\phi T} - \Omega_{\phi\mu}\Omega_{\phi\phi T} \sim m_q^{3/5}, \quad \Omega_{\phi\phi\phi\phi} \sim m_q^{2/5}\,,$$

and thus

$$\rho \sim m_q^{3/10}, \qquad w \sim m_q^{-1/2}. \tag{3.99}$$

3.7 Random Matrix Model

To illustrate the general results derived in the previous section we consider the random matrix model (RMM) introduced by Halasz et al in Ref. [48] in order to describe the chiral symmetry restoring phase transition in QCD. This is a mean-field model which has features similar to the effective Landau-Ginsburg potential near a tricritical point discussed in the previous section. The QCD pressure in this model is given by

$$P(\mu, T, m_q) = -\mathcal{N} \min_{\phi} \Omega^{RMM}(\Phi; \mu, T, m_q)\,, \tag{3.100}$$

where

$$\Omega^{RMM}(\Phi; \mu, T, m_q) = \Phi^2 - \frac{1}{2} \ln \left\{ \left[(\Phi + m_q)^2 - (\mu + iT)^2 \right] \cdot \left[(\Phi + m_q)^2 - (\mu - iT)^2 \right] \right\} \tag{3.101}$$

and $\mathcal{N} = n_{\text{inst}} N_f$ where $n_{\text{inst}} \approx 0.5 fm^{-4}$ is the typical instanton number 4-density and $N_f = 2$ is the number of flavors of light quarks. The units for T, μ and m_q here are such that $T = 1$, $\mu = 1$ and $m_q = 1$ in these units correspond to approximately 160 MeV, 2300 MeV and 100 MeV respectively (as in Ref. [48]).

To use the results of the previous section we identify

$$A\Omega(\Phi; \mu, T, m_q) = \mathcal{N}\Omega^{RMM}(2\Phi; \mu, T, m_q)\,, \tag{3.102}$$

which takes into account that $\partial\Omega^{RMM}/\partial m_q = 2\Phi$.

The equation of state that follows from this potential, $\partial\Omega/\partial\Phi = 0$, is a fifth order polynomial equation. The phase diagram resulting from this potential is shown in Figure 12.

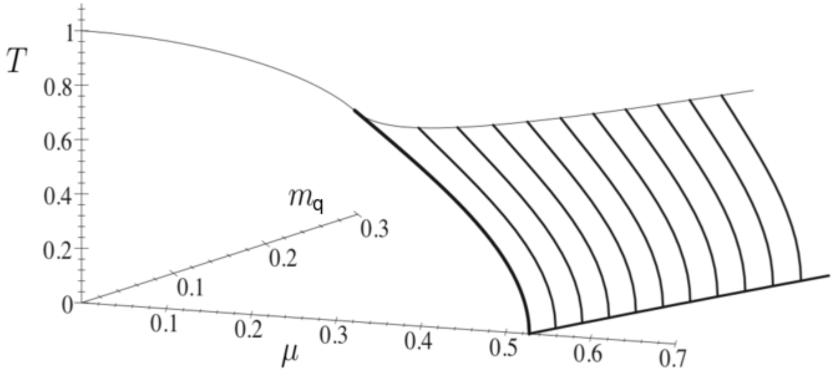

Figure 12: The phase diagram for the random matrix model in Ref. [48]. On the $m_q = 0$ plane, the thick and the thin lines represent the first-order and the second-order phase transitions respectively. Upon turning on m_q, the tricritical point where these two lines meet turns into a line of Ising-like critical points $(\mu_c(m_q), T_c(m_q))$. For the discussion that follows, we fix m_q to a particular value and obtain the map from $(\mu - \mu_c(m_q), T - T_c(m_q))$ to (h, r) variables.

The tricritical point for this model is at $(\mu_3, T_3) = \left(\sqrt{-1+\sqrt{2}}, \sqrt{1+\sqrt{2}}\right)/2$. Expanding the potential given by Eq. (3.101) we find

$$\mathcal{N}^{-1} A\,\Omega(\Phi;\mu,T) = \mathcal{N}^{-1} A\,\Omega(0;\mu,T) + \frac{a}{2}\Phi^2 + \frac{b}{4}\Phi^4 + \frac{c}{6}\Phi^6 - d\Phi + \ldots, \tag{3.103}$$

where

$$\begin{gathered} a = \frac{1}{2}\left(\frac{\mu^2 - T^2}{\left(\mu^2+T^2\right)^2} + 1\right); \quad b = \frac{\mu^4 + T^4 - 6\mu^2 T^2}{8\left(\mu^2+T^2\right)^4}; \\ c = \frac{\left(\mu^2 - T^2\right)\left(\mu^4 + T^4 - 14\mu^2 T^2\right)}{32\left(\mu^2+T^2\right)^6}; \quad d = m_q \frac{T^2 - \mu^2}{\left(T^2+\mu^2\right)^2}, \end{gathered}$$

and dots denote terms such as Φ^8, $m_q\Phi^3$, etc., which are of order a^2 and smaller, negligible compared to the terms kept (which are of order $a^{3/2}$), according to the scaling in Eq. (3.85).

For a given m_q, the critical values Φ_c, μ_c and T_c are obtained by simultaneously requiring the first, second and third derivatives of Ω with respect to Φ to vanish. As $m_q \to 0$,

$$\mu_c(m_q) = \mu_3 + O(m_q^{2/5})\,, \quad T_c(m_q) = T_3 + O(m_q^{2/5})\,, \quad \Phi_c(m_q) = (6m_q)^{1/5} + O(m_q^{3/5}) \tag{3.104}$$

Using Eq. (3.97), we can now obtain the slope difference:

$$\tan\alpha_1 - \tan\alpha_2 \;=\; \frac{20}{7}(2+\sqrt{2})(6m_q)^{2/5} + \mathcal{O}(m_q^{4/5})\,. \tag{3.105}$$

As $m_q \to 0$, the lines $h = 0$ and $r = 0$ become nearly parallel to each other with the difference in their slopes being proportional to $m_q^{2/5}$ as predicted in the previous section. Comparing Eq. (3.105) to Eq. (3.97), one can see that $\partial(a, b)/\partial(\mu, T)$ is positive, as expected.

Using more general (finite m_q) Eqs. (3.55-3.58,3.60) we computed the values for the parameters α_1, α_2, ρ and w at $m_q = 0.05$ (which corresponds to quark masses of 5 MeV in the units of Ref. [48]) in RMM:

$$\alpha_1 \sim 13^\circ, \quad \alpha_2 \sim 1^\circ, \quad \rho \sim 0.5, \quad w \sim 1.4\,. \tag{3.106}$$

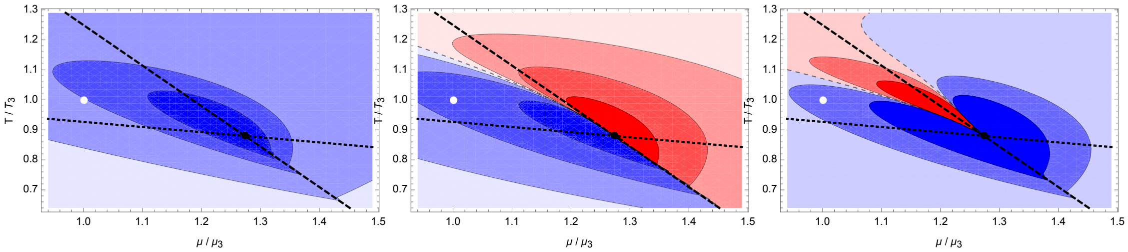

Figure 13: Contour plots of susceptibilities $\chi_2 = P_{\mu\mu}$, $\chi_3 = P_{\mu\mu\mu}$ and $\chi_4 = P_{\mu\mu\mu\mu}$ near the critical point corresponding to $m_q = 0.05$ in the RMM. The black and white dots represent the critical point and the tricritical point (at $m_q = 0$) respectively. The dotted and the dashed lines are the $r = 0$ and $h = 0$ lines respectively. The slope of $r = 0$ is negative for this value of m_q. The negative valued regions are red and positive valued regions are blue. Note that the value of χ_3 along the $h = 0$ line on the cross-over side is *negative*.

The contour plots of singular pressure derivatives $\chi_2 = P_{\mu\mu}$, $\chi_3 = P_{\mu\mu\mu}$ and $\chi_4 = P_{\mu\mu\mu\mu}$ (baryon number cumulants, or susceptibilities, of second, third and fourth order) around the critical point at small quark mass are shown in Figure 13. The following observations can be made:

- The slopes of $h = 0$ and $r = 0$ are both negative and $h = 0$ axis (coexistence line) is steeper than than $r = 0$ axis.
- $\rho < w$, which is in qualitative agreement with the small m_q scaling in Eqs. (3.99).
- The signs of the cumulants χ_2 and χ_4 on the crossover side of $h = 0$ line are in agreement with Eqs. (3.9a) and (3.9c) with $g''_+(0) = -1 < 0$ and $g''''_+(0) = 6 > 0$ according to Eq. (3.52).
- Most interestingly, the sign of χ_3 on the crossover side of $h = 0$ line, according to Eq. (3.9b), is determined by the sign of $-r_\mu$. This is clearly seen in Figure 13b where $\chi_3 < 0$ in accordance to $r_\mu > 0$ ($\alpha_2 > 0$). If the same holds true in QCD, this may have phenomenological consequences as the sign of cubic cumulant (skewness) is measured in heavy-ion collisions (see also discussion in Section 3.9).

RMM is a model of QCD, capturing some of its physics, such as chiral symmetry breaking, and missing other features, such as confinement. Its results should be treated with caution to avoid mistaking artifacts for physics. The behavior of the equation of state near the tricritical point is, however, subject to universality constraints, which we verified are satisfied by the model. The numerical values for the mapping parameters we obtained in Eq. (3.106) should be

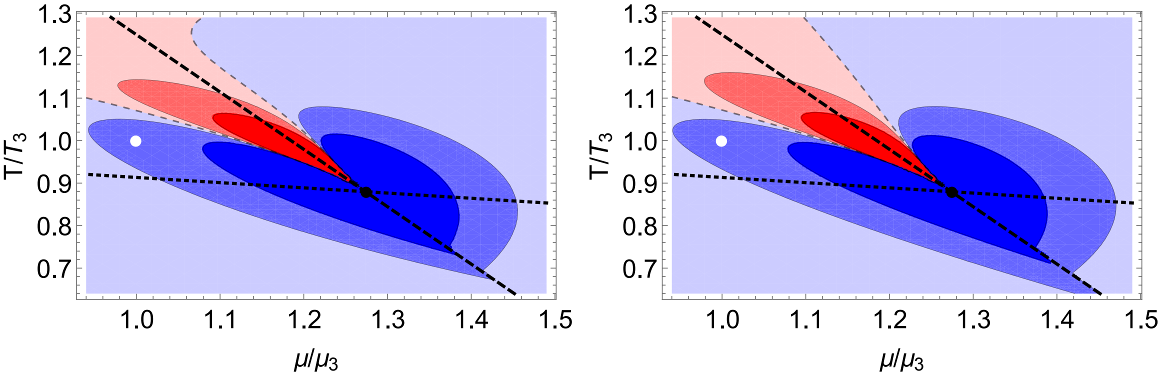

Figure 14: The contours of χ_4 obtained using RMM EoS(left) are compared with the contours of χ_4 obtained using ϕ^4 theory mapped to RMM(right) for $m_q = 5\,\mathrm{MeV}$. $T_3 \approx 120\,\mathrm{MeV}$ and $\mu_3 = 700\,\mathrm{MeV}$ are the values of the temperature and chemical potential at the tri-critical point in the chiral limit. The same contours are shown in both the plots. The striking similarity between the plots in the region of phase space shown above demonstrates that the critical region, where the singular part of χ_4 dominates over the regular part is significant. The description for the dots and the lines are same as in Figure 13.

treated as estimates, or informed guesses. These parameters are not universal. However, their dependence on m_q *is* universal, and is manifested in RMM (e.g., the slope difference is small and $\rho < w$ in accordance with Eqs. (3.99)). Since no other information about these parameters is available as of this writing, we believe our estimates in Eq. (3.106) could be helpful for narrowing down the parameter domain of the approximate equations of state constructed along the lines of Ref. [63].

3.8 Beyond the mean-field theory

In Sections 3.4-3.7, we discussed the mean-field theory near a critical point and derived scaling relations for $\tan\alpha_1 - \tan\alpha_2$, ρ and w in the $m_q \to 0$ limit in Eqs. (3.97) and (3.99). The upper critical dimension near the critical point is $d = 4$. This means that in three dimensions, the contribution of fluctuations becomes important as they become correlated at larger length scales. This leads to the breakdown of mean-field theory sufficiently close to the critical point. Ginsburg criterion provides an estimate for the range of the region where this breakdown happens. This is obtained by comparing the strength of the one-loop correction (infrared-divergent for $d < 4$) to the coupling to its tree-level value as shown in Figure 15.

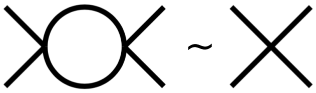

$$\begin{aligned} u^2\xi^\epsilon &\sim u \\ \xi &\sim m_q^{-2/5\epsilon} \end{aligned}$$

Figure 15: The one-loop contribution of fluctuations compared to the tree-level coupling. The fluctuation contribution diverges as ξ^ϵ, where $\epsilon = 4 - d$. The mean-field approximation breaks down at sufficiently large ξ when the contribution of fluctuations is no longer negligible. The scaling of $u \sim \Phi_c^2 \sim m_q^{2/5}$ follows from Eq. (3.90).

Since the mean-field limit is essentially weak-coupling limit, a quicker argument is to compare the coupling u expressed in *dimensionless* units, i.e., $u\xi^\epsilon$, where $\epsilon = 4 - d$ is the mass dimension of u, to unity. Since in the mean-field region $h \sim \xi^{-3}$ and $r \sim \xi^{-2}$, the boundary of the Ginsburg region where the mean-field theory breaks down is parametrically given by $h_G \sim m_q^{6/5}$, $r_G \sim m_q^{4/5}$ in $d = 3$. Note that the Ginzburg region is parametrically small for small m_q. It is also parametrically smaller than the distance between the critical and the tricritical points $b_c \sim m_q^{2/5}$, Eq. (3.89). The characteristic size and shape of the Ginzburg region is illustrated in Figure 16.

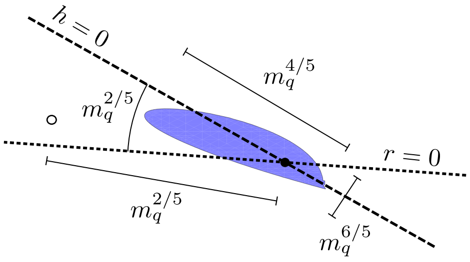

Figure 16: Schematic representation of the scaling of various parameters characterizing the location, the size and the shape of the Ginzburg region (shown in blue) around the QCD critical point in the T vs μ plane for small quark mass m_q. The empty circle denotes the location of the tricritical point at $m_q = 0$. The dotted and dashed lines are the $r = 0$ and $h = 0$ axes, respectively, with an angle between them vanishing as $m_q^{2/5}$ in the chiral limit.

In this section we will study whether the effects of the fluctuations modifies our mean-field results in the Ginzburg region. We will use ϵ expansion to order ϵ^2 to address this question. The focus will be on the key result from the previous sections on the – the convergence of the slope angles α_1 and α_2 in the chiral limit $m_q \to 0$ described by Eq. (3.97).

We notice that that an additional mixing of $r-h$ axes, that is not present in the mean-field theory is required to change the direction of $r=0$ axis relative to the $h=0$ axis. This requires contributions which break Z_2 symmetry. The contributions of the fluctuations which modify the expression for $\bar{r}$ in Eq. (3.92), for example the contibution to ϕ^2 term in the effective potential Ω from a tadpole diagram doesn't do this. These corrections simply lead to modification of the scaling exponent $\beta\delta-\beta$ (see also Ref. [166,167]). The correction to scaling exponents, obviously, doesn't change the condition $r=0$Furthermore, $r-h$ mixing violates scaling, since $h \sim r^{\beta\delta}$ and thus we need terms which violate scaling by $r^{\beta\delta-1}$. In mean-field theory this corresponds to scaling violations of order $r^{1/2}$, which are produced by terms in the potential Ω which scale as $r^{5/2}$, i.e., operators of dimension 5. We have already seen how operator ϕ^5 induces $r-h$ mixing in Section 3.4. Here we need to generalize this discussion to include effects of fluctuations.

When ϕ is a fluctuating field, in $d=4$, the scaling part of the potential Ω also includes additional dimension 4 operator, $(\nabla\phi)^2$, i.e.,

$$\Omega = \frac{1}{2}(\nabla\phi)^2 + \frac{\bar{r}}{2}\phi^2 + \frac{u}{4}\phi^4 - \bar{h}\phi + \dots\,, \tag{3.107}$$

where ellipsis denotes higher-dimension operators. Unlike in the mean-field theory, when fluctuations of ϕ are considered there are two Z_2 breaking terms: ϕ^5 (which was present in mean-field theory) and $\phi^2\nabla^2\phi$. We shall see that one special linear combination of these terms has the scaling property needed to induce $r-h$ mixing when $d<4$.

We make the following observation. The variable transformation $\phi \to \phi + \Delta\phi$, where $\Delta\phi = -v(\phi^2 - \bar{r}/u)$ similar to Eq. (3.47) cancels a certain linear combination of ϕ^5 and $\phi^2\nabla^2\phi$, while introducing an additional ϕ^2 term:

$$\Delta\Omega = \Delta\phi\frac{\partial\Omega}{\partial\phi} = -v\left(u\phi^5 - \phi^2\nabla^2\phi\right) + v\bar{h}\phi^2 + \dots\,, \tag{3.108}$$

In the above equation, ellipsis denotes terms which do not affect the mapping (being nonlinear in $\bar{r}$ or simply total derivatives). Therefore, the effect of the perturbation vV_3, where

$$V_3 = u\phi^5 - \phi^2\nabla^2\phi\,, \tag{3.109}$$

is equivalent to the shift $\bar{r} \to \bar{r} + 2v\bar{h}$. The correction to scaling induced in G due to a perturbation v_3V_3 can be absorbed by "revised scaling"

$$G(\bar{r},\bar{h}) = \bar{r}^{\beta(\delta+1)}\left(g(\bar{h}\bar{r}^{-\beta\delta}) + v_3\bar{r}^{\Delta_3}g_3(\bar{h}\bar{r}^{-\beta\delta})\right) + \dots = r^{\beta(\delta+1)}g(hr^{-\beta\delta}) + \dots\,, \tag{3.110}$$

where

$$r = \bar{r} + 2v_3\bar{h} \quad \text{and} \quad h = \bar{h}. \tag{3.111}$$

This property also guarantees [168, 169] that operator V_3 is an eigenvector of the RG matrix of anomalous dimensions which mixes $u\phi^5$ and $\phi^2\nabla^2\phi$.

The corresponding correction-to-scaling exponent is given by [168, 170]

$$\Delta_3 = \beta\delta - 1 = 1/2 + \mathcal{O}(\epsilon^2)\,, \tag{3.112}$$

which is simply the difference between h and r scaling exponents, as expected, since V_3 induces $r - h$ mixing.

The other eigenvalue of the anomalous dimension matrix is

$$\Delta_5 = 1/2 + \epsilon + \mathcal{O}(\epsilon^2)\,, \tag{3.113}$$

and the corresponding eigenvector is

$$V_5 \equiv u\phi^5 - (10S_5/3)\phi^2\nabla^2\phi. \tag{3.114}$$

The mixing parameter S_5 has been calculated in Ref. [168]:

$$S_5 = -\epsilon/108 + \mathcal{O}(u), \tag{3.115}$$

where, consistent with our interest in the $m_q \to 0$ limit, we assumed that $u \ll \epsilon$, since $u \sim m_q^{2/5}$. The eigenvalue degeneracy is lifted at one-loop order, however, the mixing only appears at two-loop order due to the sunset diagram shown in Figure 17. Despite the diagram being of order ϵ^2, the mixing, i.e., S_5, is of order $\epsilon^2/(\Delta_5 - \Delta_3) = \mathcal{O}(\epsilon)$.

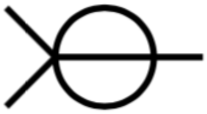

Figure 17: The two-loop diagram responsible for the mixing of ϕ^5 and $\phi^2\nabla^2\phi$ operators.

The values of the critical exponents, β, δ in the 3D Ising model and also the leading asymmetric correction to scaling are known to high precision from conformal bootstrap calculations [171]. Using the values given for the scaling dimensions presented in Table-II of [171] we compute, $\Delta_3 = \beta\delta - 1 \approx 0.56$ and $\Delta_5 \approx 1.443$. Prior to calculation of exponents using conformal bootstrap, the exponents β and δ have been determined using different methods, including experimental [172–175]. However, before the bootstrap calculations, the exponent Δ_5 was less known, with ϵ expansion estimates showing notoriusly poor convergence. Typically one found $\Delta_5 \approx 1.3 - 1.6$ from these earlier calculations [168, 176–178].

The operator V_5 does not (and cannot, in $d < 4$) change the mixing of r and h because its scaling dimension, Δ_5 is different from $\beta\delta - 1$. The corrections to scaling due to operator V_5 show up, as corrections to scaling generally do, in the form:

$$G(r,h) = r^{\beta(\delta+1)}\left(g(hr^{-\beta\delta}) + v_5 r^{\Delta_5} g_5(hr^{-\beta\delta})\right) . \tag{3.116}$$

Since $\Delta_5 > \Delta_3$ the corrections to scaling from V_5 are significantly suppressed compared to the correction accounted for by revised scaling in Eq. (3.110).

In the purely mean-field theory the operator $\phi^2\nabla^2\phi$ is essentially zero (there is no spatial dependence) and, therefore, the coefficient v_3 is undefined. In this case, however, we can completely absorb the ϕ^5 term by revised scaling as we have described in Section 3.2. On the other hand, when ϕ is a spatially-varying field and its fluctuations are important, we can only absorb the linear combination V_3, and not V_5 (in contrast to the mean-field theory where the two operators are essentially identical and equal $u\phi^5$). The coefficient v_3 of the operator V_3 which determines the revised scaling mixing depends on the coefficients of the terms ϕ^5 and $\phi^2\nabla^2\phi$.

Let us denote the contribution of the operators ϕ^5 and $\phi^2\nabla^2\phi$ to Ω in Eq. (3.107) as $\Delta\Omega^A$, and denote the coefficients of $u\phi^5$, $\phi^2\nabla^2\phi$ and their linear combinations V_3 and V_5 so that

$$\Delta\Omega^A = w_5 u\phi^5 - w_3\phi^2\nabla^2\phi = v_3V_3 + v_5V_5. \tag{3.117}$$

The coefficient v_3 responsible for the revised scaling is given by:

$$v_3 = (1 - 10S_5/3)^{-1}\ (w_3 - 10S_5 w_5/3)\ , \tag{3.118}$$

while $v_5 = (1 - 10S_5/3)^{-1}\,(w_5 - w_3)$.

For small m_q, we have already determined the coefficient of the ϕ^5 term (in $d = 4$ mean-field theory) by expanding the Φ^6 potential in powers of $\phi = \Phi - \Phi_c$ in Eq. (3.90), see Eq. (3.93):

$$w_5 = \frac{3}{20\Phi_c} \sim m_q^{-1/5}\,. \tag{3.119}$$

To find the coefficient of the $\phi^2\nabla^2\phi$ we need to consider fluctuating, i.e., spatially varying field Φ and the corresponding potential in Eq. (3.107). For small m_q, the largest contribution to $\phi^2\nabla^2\phi$ term comes from the expansion of higher-dimension term $\Phi^2(\nabla\Phi)^2$, and therefore w_3 is vanishing as $\Phi_c \sim m_q^{1/5}$ in the $m_q \to 0$ limit. Hence $w_5 \sim m_q^{-1/5} \gg w_3 \sim m_q^{1/5}$. Thus, for $m_q^{2/5} \ll \epsilon \ll 1$, the dominant contribution to v_3 in Eq. (3.118) comes from w_5 and, therefore,

$$v_3 = -\frac{S_5(\epsilon)}{2\Phi_c} + O(\epsilon^2) \sim \epsilon m_q^{-1/5}. \tag{3.120}$$

Using Eq. (3.111) we can now determine the $\mathcal{O}(\epsilon)$ correction to the slope difference:

$$\frac{h_\mu}{h_T} - \frac{r_\mu}{r_T} = \frac{\bar{h}_\mu}{\bar{h}_T} - \frac{\bar{r}_\mu + 2v_3\bar{h}_\mu}{\bar{r}_T + 2v_3\bar{h}_T} = \left(\frac{\bar{h}_\mu}{\bar{h}_T} - \frac{\bar{r}_\mu}{\bar{r}_T}\right)\left(1 + 2v_3\frac{\bar{h}_T}{\bar{r}_T}\right)^{-1}\ . \tag{3.121}$$

From Eqs. (3.91) and (3.92) we conclude that

$$\frac{\bar{h}_\mu}{\bar{h}_T} - \frac{\bar{r}_\mu}{\bar{r}_T} = \frac{2}{a_T^2}\frac{\partial(a,b)}{\partial(\mu,T)}\Phi_c^2 + \mathcal{O}(\Phi_c^4)\,, \tag{3.122}$$

and that, to leading order in $\Phi_c \sim m_q^{1/5}$, $\bar{h}_T/\bar{r}_T = -\Phi_c$. Substituting into Eq. (3.121) we find

$$\frac{h_\mu}{h_T} - \frac{r_\mu}{r_T} = \frac{2}{a_T^2}\frac{\partial(a,b)}{\partial(\mu,T)}(1 + S_5(\epsilon) + O(\epsilon^2))\Phi_c^2 + \mathcal{O}(\Phi_c^4)\,. \tag{3.123}$$

We conclude that, at two-loop order, fluctuations do not modify the *exponent* $m_q^{2/5}$ of the slope difference of $r = 0$ and $h = 0$ given by Eq.(3.122), but change the coefficient by an amount $\mathcal{O}(\epsilon)$. To summarize, the leading (and next-to-leading) singular part of QCD pressure can be expressed as

$$P_{\text{sing}}(\mu, T) = -Ar^{2-\alpha}\left(g(hr^{-\beta\delta}) + v_5 r^{\Delta_5} g_5(hr^{-\beta\delta})\right)\,, \tag{3.124}$$

where h and r are given by the map in Eq. (3.5). The leading behavior of the slope difference of $r = 0$ and $h = 0$ in the limit of small quark masses is given by

$$\tan\alpha_1 - \tan\alpha_2 = \left(\frac{dT}{d\mu}\right)_{r=0} - \left(\frac{dT}{d\mu}\right)_{h=0} = \frac{2}{a_T^2}\frac{\partial(a,b)}{\partial(\mu,T)}\left(\frac{3}{8c}\right)^{2/5}(1 + S_5(\epsilon) + O(\epsilon^2))m_q^{2/5} + \mathcal{O}(m_q^{4/5}) \tag{3.125}$$

Note that in the limit $\epsilon = 0$ this result does not agree with Eq. (3.97) in the mean-field theory. This is because in this limit $\Delta_5 = \Delta_3$ and the second term in Eq. (3.124) for pressure can, and should, be absorbed via revised scaling, modifying the slope of the $r = 0$ line (i.e., although v_3 is not well-defined in the mean-field limit, $v_3 + v_5 = w_5$ is).

Thus, we have verified the robustness of our main result, $\alpha_1 - \alpha_2 \sim m_q^{2/5}$, to fluctuation corrections up to two-loop order. This should not be unexpected since the scaling $m_q^{2/5}$ is related to the tricritical scaling exponents ($\delta_t = 5$) which are unaffected by fluctuations in spatial dimension $d = 3$ and above.

3.9 Summary, outlook and phenomenological consequences

The dominant singularity of the QCD equation of state near its critical point can be predicted using the universality of critical phenomena. This prediction is expressed in terms of the mapping of the (μ, T) variables of QCD onto (h, r) variables of the Ising model, Eqs. (3.1), (3.5). The mapping parameters are not dictated by the Ising (ϕ^4 theory) universality class and thus most of them have been treated as unknown parameters in the literature. In this work we find that, due to the smallness of quark masses, some of the properties of the other parameters are also universal. This universality follows from the closeness of the critical point to the tricritical point in the chiral limit.

Our main focus is on the slope of the $r = 0$ line in the (μ, T) plane. The slope is determined by the value of α_2 which depends on the strength of the Z_2 breaking at the Ising critical point due to leading corrections to scaling driven by irrelevant and non-scalling operators, such as ϕ^5. The central result of this study is that in the chiral limit $m_q \to 0$, when the critical point of the ϕ^4 theory approaches the tricritical point of the ϕ^6 theory, the $(\mu, T)/(h, r)$ mapping becomes singular in a specific way: the difference between the $r = 0$ and $h = 0$ slopes vanishes as $m_q^{2/5}$, Eq. (3.125).

The $h = 0$ line is essentially the phase coexistence (first-order transition) line and its slope is negative. Therefore, for sufficiently small m_q, the slope of the $r = 0$ line should also become negative, with the $r = 0$ line being less steep than $h = 0$ line.

We use the random matrix model of QCD to estimate the mapping parameters for physical value of the quark mass. The $r = 0$ slope is indeed negative, and quite small, $\alpha_2 = 1^\circ$ in this model at the physical quark mass value. We also estimate the values of scale factors in the mapping ρ and w, Eq. (3.106), and find them in agreement with small m_q scaling expectations from Eq. (3.99).

The small value of α_2 may have important implications for thermodynamic properties near the QCD critical point. In particular, an enhancement in the magnitude of the baryon cumulants, determined by the derivatives with respect to the chemical potential at fixed T is expected. This is because for $\alpha_2 = 0$ these derivatives are essentially derivatives with respect to h, which are much more singular than r derivatives: e.g., $\partial^2 G/\partial h^2 \sim r^{-\gamma}$ vs $\partial^2 G/\partial r^2 \sim r^{-\alpha}$, where $\gamma \approx 1$ and $\alpha \ll 1$. When $r_\mu = 0$ (which corresponds to $\alpha_2 = 0$), the quartic cumulant of baryon number$\langle \delta N_B^4 \rangle \sim r^{\beta - 3\beta\delta}$ close to the critical point. When $h_\mu = 0$ (which corresponds to $\alpha_1 = 0$), close to the critical point $\langle \delta N_B^4 \rangle \sim r^0$ along the cross-over line. When $0 < \alpha_2 < \alpha_1$, [108] demonstrated that there could potentially be a dip and peak in the kurtosis as a function of μ_B along the freeze-out curve, unlike the $\alpha_2 - \alpha_1 = 90^\circ$ case, where the dip wasn't observed. Assuming the freeze-out curve lies close to the cross-over line $h = 0$, the dip and the peak can be attributed to the relative dominance of the leading and subleading terms in Eq. (3.9c).

A phenomenologically relevant consequence is the relation between the sign of the $r = 0$ slope

$$\left(\frac{\partial T}{\partial \mu}\right)_{r=0} = -\frac{r_\mu}{r_T} = -\tan \alpha_2 \tag{3.126}$$

and the sign of the cubic cumulant $\chi_3 = P_{\mu\mu\mu}$ of the baryon number (or skewness) on the crossover line. This relationship can be seen directly in Eq. (3.9b) with $X = \mu$, given $g_+''(0) = -1$, and is illustrated in Figure 18 using a ϕ^4 mean-field model defined in Eqs. (3.1), (3.43). Since the skewness is measurable in heavy-ion collisions [179, 180], such a measurement could potentially provide a clue to the values of the nonuniversal parameters mapping the QCD phase diagram to that of the Ising model. This is after all a prediction based entirely on equilibrium considerations, and it remains to be checked whether the qualitative result discussed above survives after a dynamical treatment of fluctuations.

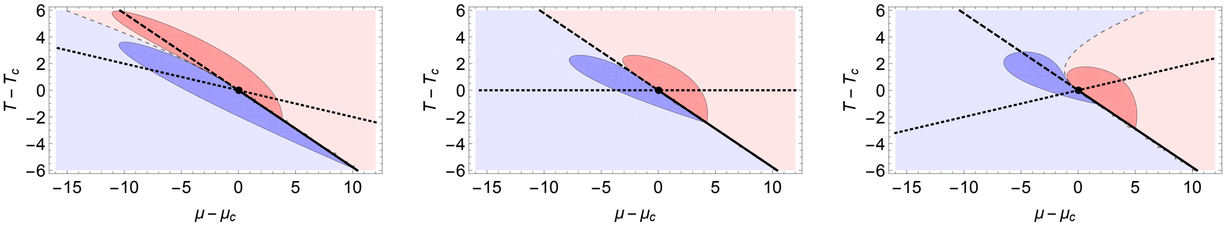

Figure 18: Contours of χ_3 when the slope (3.126) of the $r = 0$ line (dotted) is negative, zero and positive (from left to right). The contour $\chi_3 = 0$ is shown by the thin dashed line. The thick dashed line is the $h = 0$ axis (crossover). The regions of negative χ_3 are shown in red, and the regions of positive value of χ_3 are in blue. Note that χ_3 on the crossover line has the same sign as the slope of the $r = 0$ line.

The tangent of angle α_1 is equal to the slope of the first-order curve or equivalently the pseudo critical curve at the critical point. The pseudo critical curve in QCD is often estimated using the Taylor expanded EoS obtained from lattice calculations. We found that in Random Matrix Model with $m_q = 5\,\mathrm{MeV}$, α_1 estimated from the pseudo-critical obtained using a Taylor expanded form for chiral susceptibility, agrees with the actual value within $\sim 20\%$. This is studied in Appendix. (B). The only two remaining non-universal mapping parameters whose estimation we haven't detailed in this chapter correspond to the location of the critical point itself. The location of the critical point is often estimated using the ratios of successive derivatives of pressure at $\mu = 0$ (radius of convergence estimators) obtained from lattice calculations. In Appendix. (A), we have studied how universality can be employed to improve these estimates. We have also presented sample calculations using Random Matrix Model and van der Waals gas.

In this chapter, we have detailed a general framework to map QCD near its critical point to 3D Ising model. We hope the insights on the scaling features of the non-universal mapping parameters in the chiral limit and model calculations presented here will lead to future works which reliably constrain the range of parameter values quantitatively. These results combined with constraints from stability and causality requirements [63] from studies using machine learning [181] can be useful in placing bounds in the parameter space. The objective of these studies is to model the EoS of QCD in the regime of non-zero baryon chemical potential and temperature that is relevant for BES program. The general form of the EoS in this regime may be expressed as:

$$P(\mu, T) = P_{\text{reg}}(\mu, T) + A(\mu, T)P_{\text{Ising}}(\mu, T) + P_{\text{sub}}(\mu, T) \tag{3.127}$$

where $P_{\text{reg}}(\mu, T)$ accounts for all terms that are regular at $T = T_c, \mu = \mu_c$. $A(\mu, T)$ is another function that is also analytic at the critical point. $P_{\text{Ising}}(\mu, T)$ correspond to the scaling EoS obtained by matching to the Gibbs free energy of 3D Ising model as in Eq. (3.1). $P_{\text{sub}}(\mu, T)$ refers to the subleading singular corrections to scaling at the critical point. EoS obtained by mapping QCD to 3D Ising model has been discussed by various authors [62–64]. These approaches differ from each other by the choice of P_{reg}, A and P_{sub} functions. One feature that all these studies have in common is that $\alpha_2 - \alpha_1 = 90^\circ$ in each of these EoSs. The result obtained in this chapter, i.e $\alpha_1 - \alpha_2 \sim m_q^{2/5}$ for $m_q \ll \Lambda_{\text{QCD}}$ motivates further studies of these EoSs with smaller values of $\alpha_1 - \alpha_2$.

As listed above there have been various studies incorporating the universal scaling behavior described by 3D Ising model. The subleading corrections to scaling given by P_{sub} are also universal (in an RG sense, with non-universal mapping parameters) [59] and can in principle can be obtained by mapping QCD EoS to ϕ^4 theory with sub-leading corrections. We defer this to future work.

In this chapter, we described the leading singular behavior of derivatives of the EoS, which are directly related to the equilibrium correlations of particle multiplicity via Eq. (2.15). As we shall see in the next chapter, dynamics of fluctuations become important near the critical point due to critical slowing down. EoS will serve as an input for the hydrodynamical simulation with fluctuations that we discuss in the next chapter.

CHAPTER 4

DYNAMICS OF FLUCTUATIONS NEAR THE CRITICAL POINT

This Chapter is based on the reference [2] which I co-authored with K. Rajagopal, M.Stephanov and Y.Yin.

In the previous Chapter, we discussed the Equation of State (EoS) and properties of thermodynamic quantities near the QCD critical point. The non-analyticities of the QCD EoS determines the phase structure of the theory. As discussed in the introduction, hydrodynamization is achieved within 1 fm after the collision. In the hydrodynamic regime, the fluctuations of thermodynamic quantities are local. As the system approaches the critical point, the correlation length ξ begins to increase and fluctuations become long ranged. The overall magnitude of fluctuations diverges in the thermodynamic limit, $V \gg \xi^3$, where V is the system volume, as $\xi \to \infty$. We discussed that the static universality class of QCD is that of the 3D Ising model [48, 51, 58, 59], with a single scalar field becoming soft and slow at the critical point.The critical field in QCD is a linear combination of scalar operators such as the chiral condensate $\langle \bar{q}q \rangle$ and the hydrodynamic densities, baryon number density and entropy density. We discussed in Chapter. (2) that the leading singular divergence of the thermodynamic densities is given by Eq. (2.14), i.e $\left\langle \delta n_B^k \right\rangle_{\mathrm{eq}} \sim \xi^{\frac{k(5-\eta)}{2}-3}$ when the correlation length $\xi \to \infty$.

Hydrodynamics is a deterministic theory of fluid evolution with the EoS and constitutive relations for the currents and stress energy tensor taken as inputs. The hydrodynamic variables are the local fluid velocity $u(x)$ as well as *average* densities of conserved quantities like the energy density ε and the baryon number density n, or, equivalently, the corresponding conjugate variables such as the temperature T and chemical potentials (like the chemical potential for baryon number, μ_B) characterizing the local equilibrium conditions. As discussed in Section. (2.5.1), models of heavy-ion collisions involving a viscous hydrodynamic description over timescales of $1 - 10\,\mathrm{fm}$ have been found to be extremely successful in describing the experimental data from heavy-ion collisions at high energies.

The prediction based on equilibrium considerations is that the magnitude and higher cumulants of fluctuations should show characteristic non-monotonic dependence, as the location of the freeze-out point on the phase diagram moves in response to experimentally varying a parameter such as center of mass collision energy $\sqrt{s}$, approaches and then passes the location of the QCD critical point. As emphasized in the introduction, dynamically evolving the thermodynamic fluctuations and developing a new freeze-out procedure to translate the hydrodynamic fluctuations into particle correlations are necessary steps to connect the elegant scaling equation (2.14) to experimental observables. This chapter will be about dynamics of fluctuations. Connecting the hydrodynamic fluctuations to the event by event correlations in particle multiplicities will be the topic of chapters (5) and (6).

The matter produced in a heavy-ion collision expands and cools down rapidly and hence it is far from being a static thermodynamic system. There arises a question of whether fluctuations in the fluid have the time to develop in the way that they would in equilibrium. As we shall see in Section (4.1), this is determined by a competition between different times scales involved in the problem. Near a critical point, the system experiences critical slowing down, i.e the time needed for fluctuations to grow becomes longer the closer one gets to a critical point [113,114]. The description of such non-equilibrium effects is provided by an extension of hydrodynamics known as Hydro+ [116] that we shall review briefly in Section (4.1).

This chapter is organized as follows. In Section 4.1 we review some basic aspects of hydrodynamics, fluctuations of conserved densities, critical slowing down and introduce the Hydro+ equations that describe the dynamics of out-of-equilibrium fluctuations near a critical point. In Section. (4.2), we introduce a simplified set-up to study how the magnitude of hydrodynamic fluctuations are affected in a beam-energy scan "like" scenario. In Section 4.3 we solve the Hydro+ equation for the Gaussian fluctuations of $\hat{s}$ in a fluid that is undergoing boost-invariant longitudinal expansion (Bjorken scenario). In Section 4.4 we describe the dynamics in a more realistic Hydro+ simulation of Ref. [128] in which the fluid is boost invariant and azimuthally symmetric but is finite in transverse extent and thus exhibits radial flow. In Section 4.5 we compare the results from Section 4.4 with Model A evolution where the fluctuating density is not hydrodynamical. We conclude in Section 4.6 with a summary of the main qualitative lessons that we draw from our results of Sections 4.3 and 4.4.

4.1 Hydrodynamics with fluctuations

4.1.1 Hydrodynamic variables and relevant length scales

When the length scales of interest, are spatial cells of linear size b, which are much larger than microscopic lengths such as inverse temperature,$1/T$ or the typical mean-free path between the constituents, it may suffice to restrict the dynamical degrees of freedom to conserved densities which are the slowest degrees of freedom in the system. One can employ a hydrodynamic description to study the dynamics over much larger scales like the size of the fireball, say $L \gg b$. The hydrodynamics equations for the stress-energy tensor and conserved currents therefore become sufficient to describe this system of size L partitioned into fluid cells of size b when the following scale separation exists $1/T \ll b \ll L$.

Away from the critical point, the correlation length $\xi \sim T^{-1}$ and hence over length scales of order b, the correlation functions are simply delta functions in spatial separation between the points. Hydrodynamics describes small deviations from equilibrium and is an expansion in gradients of the local thermodynamic variables defined over the fluid cells. The evolution of this conserved densities to catch up with the local equilibrium values is governed by diffusive processes. If γ is the relevant diffusion constant, then local equilibrium is achieved over a length scale, denoted by $l_{\text{eq}} \sim \sqrt{\gamma \tau_{\text{ev}}} \sim \sqrt{\gamma L/c_s}$ where c_s is the speed of sound in the fluid [121]. $l_{\text{eq}} \gg b$ for typical values of $\gamma \sim T^{-1}$ and therefore for wave vectors $l_{\text{eq}}^{-1} \ll \mathbf{q} \ll b^{-1}$, equilibration is not complete. The evolution of these out-of-equilibrium fluctuations can be described either via stochastic hydrodynamic equations with a noise term [130, 134] or via deterministic equations for the n-point functions of these fluctuating quantities [117,121,182]. The stochastic evolution becomes harder to implement in a numerical simulation due to the infinite noise problem as $b \to 0$ [134]. This limitation of stochastic hydrodynamic favors the deterministic approach to studying fluctuations. The deterministic equations for the evolution of the n-point fluctuations in a systematic derivative expansion (or equivalently in powers of $\mathbf{q}$ for $l_{\text{eq}}^{-1} \ll \mathbf{q} \ll b^{-1}$) has been derived in the context of heavy-ion collisions for boost invariant scenario in [117] and for a general scenario for a neutral and charged fluid in [121] and [124,182] respectively.

The domain of applicability of hydrodynamics is restricted to $\xi \ll L$ and hence near the critical point where ξ grows rapidly , hydrodynamic description breaks down. Infact, hydrodynamics breaks down much earlier than that. It happens when the rate of evolution of the slowest non-hydrodynamic mode becomes comparable to the hydrodynamic evolution rates. The slowest non-hydrodynamic mode near a critical point corresponds to the fluctuations of the slowest hydrodynamic mode, entropy per baryon s/n, which we denote by $\hat{s}$. These modes relax on the (parametrically) longest times scale [116]. The characteristic rate for this mode goes as ξ^{-z} where z is described by the dynamic universality class relevant to the phenomenon.The dynamic universality class appropriate for the QCD critical point is Model H [183] in which $z \approx 3$ [184]. The UV cut-off b^{-1} near the critical point is set by ξ^{-1}. For $\mathbf{q} < \xi^{-1}$, the relaxation rate of the slow mode described above $\gamma_\lambda \mathbf{q}^2 \sim \gamma_\lambda \xi^{-2} \sim \xi^{-3}$ as γ_λ vanishes near the critical point as ξ^{-1}. Therefore, the hydrodynamic description has to be supplemented with a dynamical description for the slowest non-hydro mode when $\xi^3 \sim L$ [116,118,124].

The phenomenon of relaxation rates of correlation functions becoming vanishingly small as $\xi \to \infty$ is called critical slowing down [113]. "Hydro+" introduced in [116] is an effective field theory which has both the averages of the conserved densities and their fluctuations (characterized via their correlation functions) as dynamical degrees of freedom. It provides an extension to the ordinary hydrodynamics by enhancing its range of validity to wave-vectors $k = L^{-1}$ as large as $k \sim \xi^{-2}$. This limitation is imposed by the break down of Hydro+ when the relaxation rate of the next to slowest non-hydrodynamic mode becomes comparable to the k. These modes corresponds to fluctuations of the velocity vector along the components transverse to k and the dominant fluctuations of this mode have relaxation rate that vanishes as ξ^{-2}. Extension to Hydro+ with these next to slowest non-hydro modes as dynamical variables was proposed by the authors of [124] and termed "Hydro++". Summarizing, near the critical point, the hierarchy of scales $\xi^{-3} < \xi^{-2} < \xi^{-1}$ sets the cut-off for hydrodynamics, Hydro+ and Hydro++ respectively.

In this work, we'll restrict to the study of fluctuations of only the slowest hydrodynamic mode, i.e $\hat{s} \equiv s/n$. For practical applications like incorporating in models to compare with experimental data from heavy-ion collisions, this might be sufficient. [1] In this Chapter, both for simplicity and as a necessary first step, we shall focus on the *magnitude* of fluctuations of $\hat{s}$ and defer the discussion of non-Gaussianity measures to future work. The magnitude of the

---

[1] The fluctuations of $\hat{s}$ show the leading singular behavior in most cases expect in the very special scenario when the mapping parameter corresponding to the slope angle α_1 (defined in Eq.(3.5) is fine-tuned such that $\cot\alpha_1 = s_c/n_c$, where s_c and n_c are the corresponding critical values of entropy and number densities. This special case corresponds to Eq. (3.26) with $\delta x = \delta y = \delta\hat{s} \propto$, i.e when fluctuations of $\hat{s}$ are proportional to those of Ising entropy density σ. We assume this to be not the fine-tuned case here.

fluctuations is characterized by a two-point correlation function. The Wigner transform of the equal-time correlation function of $\hat{s}$ in the local rest frame of the fluid is given by:

$$\phi_{\mathbf{Q}}(x) \equiv \int_{\Delta \boldsymbol{x}} \langle \delta\hat{s}\,(x_+)\,\delta\hat{s}\,(x_-)\rangle\; e^{i\mathbf{Q}\cdot\Delta\boldsymbol{x}}\,. \tag{4.1}$$

Here $x = (x_+ + x_-)/2$ and $\Delta x = x_+ - x_- = (0, \Delta\boldsymbol{x})$ in the local rest frame of the fluid at the point x. The relaxation of this quantity to its local equilibrium value $\bar{\phi}_{\mathbf{Q}}$ is governed by the equation [116]:

$$u(x)\cdot\partial\phi_{\mathbf{Q}}(x) = -\Gamma(\boldsymbol{Q})\,\left(\phi_{\mathbf{Q}}(x) - \bar{\phi}_{\mathbf{Q}}(x)\right)\,. \tag{4.2}$$

For the purposes of this chapter, the equilibrium $\bar{\phi}_{\mathbf{Q}}$ can be adequately approximated by the Ornstein-Zernike ansatz [1]

$$\bar{\phi}_{\mathbf{Q}} \approx \frac{c_p/n^2}{1+(Q\xi)^2}\,, \tag{4.3}$$

where $Q \equiv |\boldsymbol{Q}|$ and c_p and n are the heat capacity at constant pressure and the baryon number density.

The Q-dependent relaxation rate, Γ, controls how slowly $\phi_{\mathbf{Q}}(x)$ evolves toward its equilibrium value $\bar{\phi}_{\mathbf{Q}}$ via Eq. (4.2). The leading critical behavior of Γ depends on the dynamic

---

[1] While the value of $\bar{\phi}_{\boldsymbol{Q}}$ at $\boldsymbol{Q} = 0$ in Eq. (4.2) is determined by thermodynamics, the dependence on $\boldsymbol{Q}$ in this expression is an often used approximation which takes into account the nonzero correlation length. A more sophisticated form can be found in Ref. [116].

universality class. For the QCD critical point [183], it is the one of Model H (liquid-gas critical point) in Halperin and Hohenberg's classification [184], where the linear combination of $\delta\varepsilon$ and δn given by $\delta\hat{s} = (\delta\varepsilon - (w/n)\delta n)/(Tn)$ is the slow, diffusive, scalar mode nonlinearly coupled to diffusive (transverse) momentum modes. At the same level of approximation as in Eq. (4.3), the leading critical behavior of the relaxation rate in model H is given by [185]:

$$\Gamma(\boldsymbol{Q}) = \frac{2D_0\xi_0}{\xi^3}K(Q\xi), \tag{4.4}$$

where ξ_0 is a typical value of the correlation length well away from the critical point, D_0 is a constant with the dimensions of length that we shall take as a free parameter, and

$$K(x) \equiv \frac{3}{4}\left[1 + x^2 + (x^3 - x^{-1})\arctan x\right] \, . \tag{4.5}$$

As we shall demonstrate, the most important property of the critical mode relaxation rate given by Eqs. (4.4-4.5) is that it vanishes as $Q \to 0$:

$$\Gamma(\boldsymbol{Q}) = \frac{2D_0\xi_0}{\xi}Q^2 + \mathcal{O}(Q^4)\, .$$

This reflects the fact that $\phi_{\boldsymbol{Q}}$ measures the fluctuation of hydrodynamic variables, which are conserved. The relaxation rate of the 2-point correlator of fluctuations is twice the rate of the relaxation of the corresponding mode, whose relaxation is also diffusive with a diffusion coefficient given by

$$D = D_0 \frac{\xi_0}{\xi} \tag{4.6}$$

which vanishes at the critical point, where $\xi \to \infty$. We can think of the parameter D_0 which we introduced as the diffusion constant at some reference point well away from the critical point. A crude estimate for D_0 could be obtained by using [184, 185]

$$D_0 \approx \frac{T}{6\pi\eta\xi_0} \approx \frac{2T}{3s(T)\xi_0}\,, \tag{4.7}$$

where η and s are the shear viscosity and entropy density, respectively, and where we have taken $\eta \approx s/(4\pi)$. Taking $s(T) = \tilde{s}T^3$ with $\tilde{s} \approx 6$ as is reasonable around $T = T_c$ [10, 38] and choosing $T_c = 160$ MeV and $\xi_0 = 0.5$ fm as we shall throughout, we estimate a critical contribution of $D_0 \approx 0.3$ fm. Assuming that the non-critical contribution to D_0 is not too large, we expect $D_0 > 0.3$ fm but not $D_0 \gg 0.3$ fm. To bracket the uncertainty in this estimate, we shall illustrate our results by plotting the results obtained from calculations employing $D_0 = 0.25$ fm and $D_0 = 1$ fm.

To emphasize the importance of the conservation laws in the dynamics of fluctuations and, consequently, in the experimental signatures (Chapter (5)) of the critical point we shall compare and contrast results obtained using the model H universality class with those which one would have obtained using model A universality class, in which the order parameter is *not* a conserved quantity and the relaxation rate of the fluctuations does not vanish as $\boldsymbol{Q} \to 0$. To the same

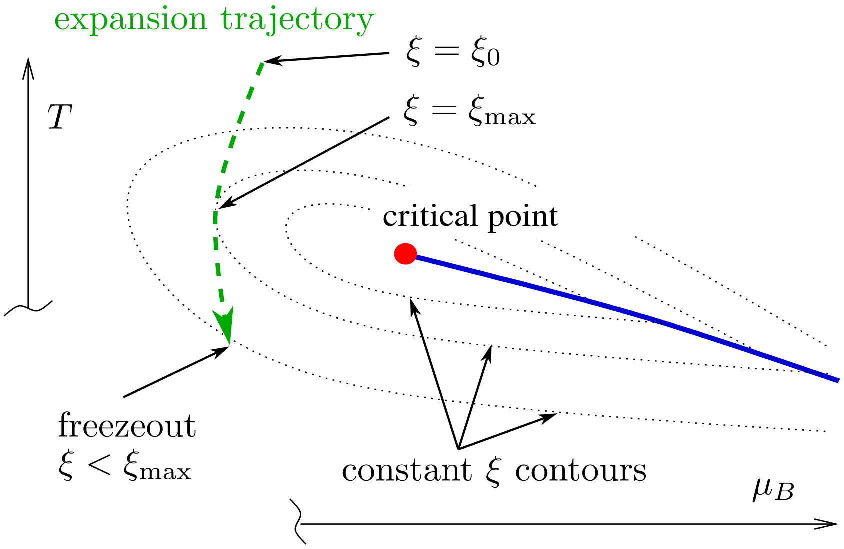

Figure 19: Schematic view of a trajectory followed by an expanding cooling droplet of matter produced in a heavy ion collision on the QCD phase diagram in the vicinity of the critical point.

level of approximation as we have been using so far we can utilize the following ansatz for the relaxation rate in model A:

$$\Gamma(\boldsymbol{Q}) = \frac{\Gamma_0 \xi_0^2}{\xi^2} \left(1 + (Q\xi)^2\right) , \qquad \text{(model A)}, \tag{4.8}$$

where Γ_0 is a constant with the dimensions of rate (1/time) which we can think of as the relaxation rate at a point well away from the critical point where the correlation length is ξ_0.

In this work, we assume that the dynamical back-reaction of the fluctuations on the equation of state and on the hydrodynamic solution is negligible. This assumption has been tested quantitatively in different model calculations [128,129] and is a good approximation: the effects of such back-reaction are typically at the sub-percent level.

The relevance of simulating dynamical fluctuations near the critical point was realized since the work of Berdnikov and Rajagopal [113], where the authors studied fluctuations of a order parameter in the dynamic universality class of Model C [186] appropriate for a system where a non-conserved order parameter couples to a one-component conserved field. Dynamics of fluctuations of a non-conserved quantity like chiral condensate was studied in [114,128,187–190]. Fluctuations of conserved density , like those in a diffusion process can be modeled by dynamic universality class of Model B and various simulations in this category have been performed in [129, 136, 137, 139, 191, 192]. In the chiral limit, the second order-phase transition at low values of baryon chemical potential is expected to be in the $O(4)$ universality class, and the dynamic universality class appropriate for an N component non-conserved order parameter that is coupled to a $N(N-1)$ component conserved field is Model G and was studied in [140]. The work presented in this chapter demonstrates the Model H dynamics, which applies to the QCD critical point at finite quark masses [183] where the fluctuations of a conserved field couples to a transverses components of a conserved field. Although performed in rather simplified scenarios via a deterministic approach, it provides crucial insights into the role of conservation and the relevance of low Q modes in determining the magnitude of fluctuations at freeze-out. Stochastic hydrodynamic simulations for Model H are harder to implement due to infinite noise-problem in the UV limit [134].

4.2 Simplified set-up to demonstrate dynamics in a beam-energy scan

We study trajectories of the fireball which lie on the cross-over side of the QCD phase diagram. With the expansion and the cooling of the fireball, the trajectory of the point characterizing the thermodynamic state of the fireball moves closer and then farther from the critical point as it evolves. The correlation length ξ as a function of chemical potential μ and temperature T varies along the trajectory of this point. The maximum value of the correlation length ξ denoted by ξ_{max} (see Figure 19) is attained at the point on the trajectory which is closest to the critical point. The parameter ξ_{max} is controlled experimentally by varying the collision energy $\sqrt{s}$ [9, 40] since collisions with lower $\sqrt{s}$ produce droplets of matter containing a greater excess in the number of quarks over the number of antiquarks, meaning a higher baryon chemical potential μ_B. Lowering the collision energy in steps, as in the Beam Energy Scan program at RHIC, moves the entire expansion trajectory in Figure 19, including the freeze-out point, rightward in steps. Therefore, similar to how $\sqrt{s}$ can be taken as a proxy to the closeness of the trajectory to the critical point, ξ_{max} becomes the proxy in our simplified set-up.

The fluctuation evolution equation (4.2) depends on the correlation length ξ via the dependence of $\bar{\phi}_{\boldsymbol{Q}}$ and $\Gamma(\boldsymbol{Q})$ on ξ. In a realistic hydrodynamic simulation, ξ will be determined upon solving the hydrodynamic equations with a given equation of state. Since our purpose in this chapter is to describe how to freeze out critical fluctuations in hydrodynamics and translate them into observables based on particle multiplicity fluctuations, we shall instead, for simplicity, choose a plausible parametrization of ξ along the expansion trajectory in terms of T.

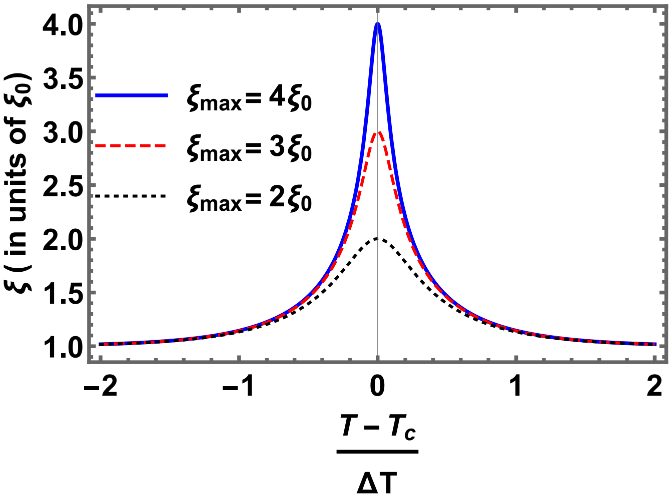

Figure 20: The dependence of the correlation length ξ on temperature for different trajectories of the fireball expansion (i.e., different ξ_{max}).

Specifically, we shall adopt the parametrization of the correlation length along the trajectory of the expanding fireball on the QCD phase diagram in terms of temperature used previously in Ref. [128]:

$$\left(\frac{\xi}{\xi_0}\right)^{-4} = \tanh^2\left(\frac{T-T_c}{\Delta T}\right)\left[1-\left(\frac{\xi_{\rm max}}{\xi_0}\right)^{-4}\right]+\left(\frac{\xi_{\rm max}}{\xi_0}\right)^{-4}, \tag{4.9}$$

with $\Delta T = T_c/5$. We shall not attempt to refine this parametrization in this work. Alternate parametrizations for the correlation length are discussed, e.g., in Refs. [105, 129]. The ansatz in Eq. (4.9) reflects the main features of $\xi(T)$ relevant for this work — the correlation length reaches a maximum value ξ_{max} at a certain temperature T_c (close to the crossover temperature) and then decreases as the system continues to cool on its way to freeze-out — as shown in Figure 20 which is how we imagine ξ varying along a trajectory like that illustrated by the green dashed line in Figure 19. In our explicit calculations, we shall choose $T_c = 160$ MeV and $\xi_0 = 0.5$ fm.

4.3 A Hydro+ simulation with Bjorken symmetric background

In this Section, we apply our approach to the well-known Bjorken scenario: a hot fluid that is undergoing idealized boost-invariant longitudinal expansion, so that it cools as a function of proper time, but that is translation-invariant and at rest in the transverse directions [193]. We shall obtain some results in this simplified scenario in analytic form (which we'll describe more in Section (5.4), thus allowing us to elucidate general features that we shall observe again in a more realistic scenario with transverse expansion in the next Section.

4.3.1 Evolution of ϕ_Q

The Bjorken scenario implies that all thermodynamics quantities such as the temperature, T, or the energy density, ε, or net baryon number density, n, as well as quantities describing the fluctuations of these conserved densities depend only on the Bjorken proper time $\tau \equiv \sqrt{t^2 - z^2}$, and are independent of the longitudinal spacetime-rapidity, η, as well as of the transverse coordinates. Thus, the hydrodynamic equations reduce to *ordinary* differential equations for functions of τ which can be solved easily for a given equation of state. We shall employ the simplified equation of state from Ref. [128] that we summarize briefly in Appendix C.The hydrodynamic evolution sets in at $\tau = \tau_i$ where the temperature $T(\tau_i) = T_i$ and it continues until freeze-out at $\tau = \tau_f$ where the temperature $T(\tau_f) = T_f$. In the Bjorken scenario where there is no radial flow, the flow velocity unit-four-vector is $u = \hat{\tau}$ in Bjorken coordinates. The evolution equation (4.2) for the fluctuation measure $\phi_{\boldsymbol{Q}}$ becomes:

$$\partial_\tau \phi_{\boldsymbol{Q}} = -\Gamma(\boldsymbol{Q}) \left(\phi_{\boldsymbol{Q}} - \bar{\phi}_{\boldsymbol{Q}}\right) , \tag{4.10}$$

where $\Gamma(\boldsymbol{Q})$ depends on τ through $\xi(\tau)$ and is specified via Eqs. (4.4,4.5,4.9). Since our focus throughout is on the effects caused by fluctuations near a critical point, for simplicity we shall assume that the initial fluctuations are in equilibrium, i.e., [1]

$$\phi_{\boldsymbol{Q}}(\tau_i) = \bar{\phi}_{\boldsymbol{Q}}\Big|_{T=T_i} . \tag{4.11}$$

Since, in the Bjorken scenario, the temperature depends only on τ, the unit four-vector normal to the isothermal freeze-out hypersurface $T(\tau_f) = T_f$ at a spacetime point x is given by $\hat{n}(x) = \hat{\tau}(x) = u(x)$.

In Figure 21 we plot $\phi_{\boldsymbol{Q}}$ obtained by solving Eq. (4.10) numerically at three values of τ. In order to highlight the significance of the conservation laws, we compare and contrast the results obtained with two choices of the relaxation rate: model A where $\Gamma(\boldsymbol{Q})$ is as given in Eq. (4.8) and model H (the universality class of the QCD critical point) where $\Gamma(\boldsymbol{Q})$ is as given by Eq. (4.4). The most important feature of the model H evolution of $\phi_{\boldsymbol{Q}}$ is that $\boldsymbol{Q} = 0$ mode doesn't evolve. On the other hand, $\phi_{\boldsymbol{0}}$ in model A "tries" to follow the dynamics that would have been obtained in equilibrium. This feature of $\phi_{\boldsymbol{0}}$ in model H is, obviously, a consequence of the conservation laws in hydrodynamics, since the $Q = 0$ mode corresponds to the volume

---

[1] As we shall see, one of the important conclusions of our study is the importance of conservation in the overall suppression of the critical signatures relative to equilibrium expectations. This motivates the need to use more realistic initial conditions as they will be crucial for estimating overall magnitude of the correlations among particles.

integrated fluctuations of conserved quantities which do not change with time , while in model A it involves volume integrations of the fluctuations a non-conserved order-parameter.

In Figure 22 we show the effect of varying the parameter D_0 in the Model H relaxation rate Eq. (4.4) on the fluctuation measure $\phi_{\boldsymbol{Q}}$ and its inverse Fourier transform $\tilde{\phi}(\Delta\boldsymbol{x}_\perp)$ defined in Eq. (5.20) at freeze-out, after Hydro+ evolution from $\tau = \tau_i$ to $\tau = \tau_f$. The large Q, or equivalently, small Δx (defining $\Delta x \equiv |\Delta\boldsymbol{x}_\perp|$) behavior of the fluctuations is not affected much as the fluctuations at short length scales equilibrate fast. The characteristic Q where the peak of $\phi_{\boldsymbol{Q}}$ is situated shifts to smaller values of Q with increasing D_0 because stronger diffusion tends to homogenize the system, including fluctuations. This can also be seen in spatial correlator $\tilde{\phi}$ becoming longer ranged. In addition, stronger diffusion (larger D_0) enhances the effect of the critical point on the fluctuations since the system is able to equilibrate more quickly towards the large equilibrium fluctuation values as it passes the critical point on its way to freeze-out. This effect results in a more pronounced (higher) peak in ϕ_Q and, correspondingly, in an enhancement of $\tilde{\phi}$ at corresponding intermediate values of Δx (of order 3 fm or so).

$\phi_{\boldsymbol{Q}}$ at $\boldsymbol{Q} = 0$ being a constant is mathematically same as keeping the integral of $\Delta x^2\,\tilde{\phi}$ constant. This means that their effect in panel (b) of Figure 22 is that if there is a (large, critical) correlation at small Δx they produce a corresponding compensating anticorrelation at longer Δx. One can also show generally that a peak in $\phi_{\boldsymbol{Q}}$ away from $Q = 0$ corresponds to the anticorrelation (i.e., negative tail) in its Fourier transform $\tilde{\phi}(\Delta x_{\perp})$. Indeed, if there exist a value of $\boldsymbol{Q}$ at which $\phi_{\boldsymbol{Q}} > \phi_{\boldsymbol{0}}$, then

$$\int d^3\Delta\boldsymbol{x}\,\tilde{\phi}(\Delta\boldsymbol{x}) < \int d^3\Delta\boldsymbol{x}\,\cos(\boldsymbol{Q}\cdot\Delta\boldsymbol{x})\,\tilde{\phi}(\Delta\boldsymbol{x}), \tag{4.12}$$

where we used the fact that $\tilde{\phi}(\Delta\boldsymbol{x})$ is an even function. Since $|\cos(\boldsymbol{Q}\cdot\Delta\boldsymbol{x})| \leq 1$, the inequality (4.12) cannot be satisfied if $\tilde{\phi}(\Delta\boldsymbol{x})$ is always positive.

In Section. (5.4), we'll analytically perform the freeze-out of the Hydro+ simulation described above and discuss how the dynamical features of critical slowing down and conservation present in ϕ_Q translate into variance of particle multiplicities.

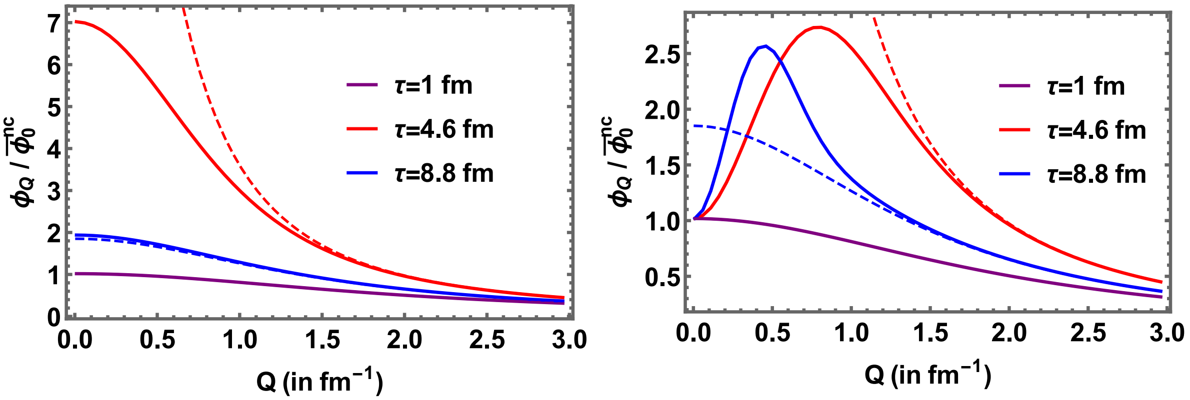

(a) Model A

(b) Model H

Figure 21: Evolution of $\phi_{\boldsymbol{Q}}$ as a function of Bjorken time τ, using model A and model H dynamics, corresponding to the relaxation rates given by Eqs. (4.8) and (4.4), respectively. We have taken $\Gamma_0 = 1\,\text{fm}^{-1}$, $D_0 = 1\,\text{fm}$ and $\xi_{\text{max}} = 3$ fm in both panels. The three solid curves in each figure correspond to different times τ as the boost-invariant, spatially homogeneous, Bjorken fluid is expanding and cooling in the vicinity of a critical point. The temperatures are given by $T = 235$, 160 and 140 MeV, for times $\tau = 1$, 4.6 and 8.8 fm, respectively. The dashed curves represent the equilibrium values $\bar{\phi}_{\boldsymbol{Q}}$ for the corresponding temperatures (times). We have initialized the hydrodynamic solution and the fluctuations at $\tau_i = 1$ fm: at that time $\phi_{\boldsymbol{Q}} = \bar{\phi}_{\boldsymbol{Q}}$ at $T_i = 235$ MeV. The dashed curves are highest at $\tau = 4.6$ fm because that is when the evolution trajectory was closest to the critical point; the fluctuations would be largest at that time if they were in equilibrium. We see that in Model H the fluctuations (in our full, out-of-equilibrium, calculation) remain considerably enhanced at $\tau = 8.8$ fm over a range of nonzero values of $\boldsymbol{Q}$. It is evident from the right plot that $\phi_{\boldsymbol{Q}}$ does not evolve at $\boldsymbol{Q} = 0$ in Model H. This is a consequence of conservation laws. In both plots, at all times shown, $\phi_{\boldsymbol{Q}}$ and $\bar{\phi}_{\boldsymbol{Q}}$ are both normalized by their non-critical value (their value at a location far enough away from the critical point that $\xi = \xi_0$) at $\boldsymbol{Q} = 0$ in equilibrium, i.e., $\bar{\phi}_{\boldsymbol{0}}^{\text{nc}} = Z\,T\,\xi_0^2$.

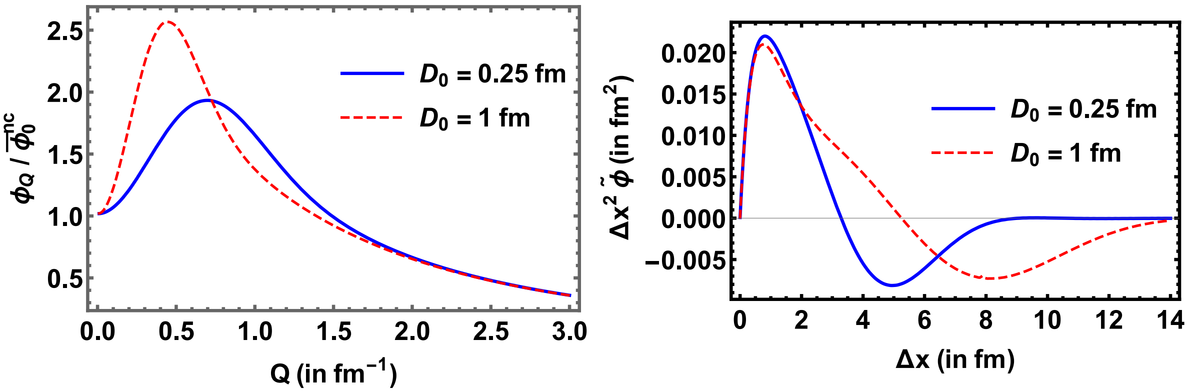

(a) ϕ at freeze-out

(b) $\tilde{\phi}$ at freeze-out

Figure 22: Normalized $\phi_{\boldsymbol{Q}}$ (a) and its inverse Fourier transform $\tilde{\phi}$ (b) at freeze-out $T_f = 140\,\text{MeV}$ after evolution according to Model H dynamics with two values of D_0. In the text, we explain the dependence of the shapes of the curves in both panels on D_0, and the consequences of the conservation laws on the shapes of these curves.

4.4 A numerical hydro+ simulation with radial expansion

The system considered here is boost-invariant along the longitudinal direction, has azimuthal symmetry, is finite in radial extent and exhibits radial flow A brief description of the details of simulation is given below. For more details the reader may refer to Ref. [128].

The evolution of the energy density, $\varepsilon(r,\tau)$ and the fluid four-velocities $u(r,\tau)$ in our simulation is determined using the standard MIS second order hydrodynamic equations as implemented in the publicly available VH1 + 1 hydrodynamic code [194–196]. The equation of state $p(\varepsilon)$ used in the simulation was introduced in Ref. [128] and was already employed in Section 4.3 and, for convenience, is reviewed in Appendix C. We set the shear viscosity to entropy density ratio to $\eta/s = 0.08$ throughout, and solve the equations numerically using a spatial (radial) lattice with 1024 points spaced by 0.0123 fm and a time step of 0.005 fm. In this Section, we initialize the hydrodynamic simulation at $\tau_i = 1\,\text{fm}$, with an initial central temperature of 330 MeV, following Ref. [194]. We set the radial flow v_r and the viscous part of the stress-energy tensor $\Pi_{\mu\nu}$ to zero initially at $\tau = \tau_i$. We employ the standard Glauber model radial profile corresponding to a central Au-Au collision at $\sqrt{s} = 200$ GeV for $\varepsilon(r)$ at $\tau = \tau_i$, again following Ref. [194].

As in Ref. [128], in our Hydro+ simulation the hydrodynamic densities $\varepsilon(r,\tau)$ and $\Pi_{\mu\nu}(r,\tau)$ and the four-velocities $u(r,\tau)$ provide the background for the evolution of the fluctuations described by $\phi_{\boldsymbol{Q}}$ according to Eq. (4.2). Again following Ref. [128], we choose to initialize the fluctuations $\phi_{\boldsymbol{Q}}$ at $\tau = \tau_i$ by setting them to the corresponding equilibrium values determined by the local temperature at this initial time, i.e. [1]

$$\phi_{\boldsymbol{Q}}(r, \tau_i) = \bar{\phi}_{\boldsymbol{Q}}\Big|_{T(r,\tau_i)} . \tag{4.13}$$

We calculate the evolution of $\phi_{\boldsymbol{Q}}$ using the same code as in Ref. [128], with two important changes. First, we employ Model H dynamics [2] which takes into account conservation laws. This gives us an opportunity to highlight the effects of conservation laws on the dynamics of $\phi_{\boldsymbol{Q}}$ and on the resulting particle multiplicity fluctuations by comparing the results of this Section to those obtained by repeating the calculations of this Section using Model A evolution. We perform this comparison in Section. 4.5. Secondly, we shall neglect the back-reaction of the fluctuations on the hydrodynamic densities. The modifications to the bulk dynamics of the hydrodynamic fluid, in particular its entropy density $s(r, \tau)$, introduced by the presence of the fluctuations was computed in Ref. [128, 129] and in fact the fluctuations and the hydrodynamic densities were computed self-consistently. However, these authors showed that including back reaction self-consistently introduces fractional changes to $\varepsilon(r, \tau)$ and $v_r(r, \tau)$ that are small, rarely comparable to 1% and typically much smaller.

---

[1] The limitations of the various assumptions made in setting up this Hydro+ simulation, as well as possible future improvements to it, are detailed in Ref. [128].

[2] Ref. [128] considered Model A dynamics for a non-conserved order parameter. We'll make a comparison of Model H to Model A results later.

In the remainder of this Section, we demonstrate the the Hydro+ simulation with the background described above for some reasonable values of D_0. After describing and illustrating the evolution of ϕ_{Q} in Subsection 4.4.1 and the fluctuations on an isothermal surface (which will become our choice for the freeze-out surface in Chapter. (5)) in Subsection 4.4.2, in Section 5.5 we describe the resulting fluctuations in particle multiplicities.

4.4.1 Evolution of $\phi_{\mathbf{Q}}$

In this Subsection, we discuss the space-time dependence of the fluctuation measure $\phi_{\boldsymbol{Q}}$ as it evolves according to the relaxation equation given by Eq. (4.2) with the Model H relaxation rate given by Eq. (4.4). The radial dependence of the flow and temperature profiles makes $\phi_{\boldsymbol{Q}}$ dependent on the radial variable r in addition to the Bjorken time τ. Several representative characteristic curves, or flow lines, determined by the flow velocity u, are shown in Figure 23.

In Figure 24, we plot our results for the fluctuation measure $\phi_{\boldsymbol{Q}}$ in the hydrodynamic background illustrated in Figure 23 at three different times τ along two hydrodynamic flow lines, one close to the center of the fireball ($r(\tau_i) = 0.7$ fm) and one further out ($r(\tau_i) = 5$ fm). We display results from simulations performed with $D_0 = 0.25\,\mathrm{fm}$ (slower diffusion) and $D_0 = 1\,\mathrm{fm}$ (faster diffusion) and $\xi_{\max} = 1\,\mathrm{fm}$ (trajectory further away from the critical point) and $\xi_{\max} = 3\,\mathrm{fm}$ (trajectory closer to the critical point). In all the panels, at $\tau = 1$ fm (black curve) ϕ_{Q} is given by its equilibrium value. In the upper (lower) four panels, the red curves at $\tau = 9.19$ fm ($\tau = 5.14$ fm) are drawn at the time when when the fluid cell moving along the flow line that started at $r_i = 0.7$ fm ($r_i = 5$ fm) has cooled to the temperature $T = T_c = 160$ MeV and the blue curves at $\tau = 11.36$ fm ($\tau = 6.72$ fm) are drawn at the time when these fluid cells have

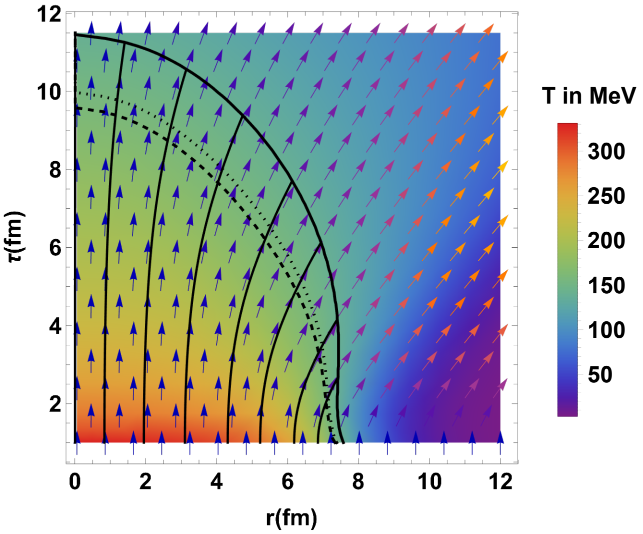

Figure 23: The space-time dependence of the temperature (represented by color) and flow velocity in the hydrodynamic simulation of the expanding cooling droplet of quark-gluon plasma. The magnitude of the radial flow at each space-time point is indicated by the tilt of the arrows. The dashed, dotted and solid black curves are the isothermal curves at $T = 160\,\mathrm{MeV}$, $156\,\mathrm{MeV}$ and $140\,\mathrm{MeV}$, respectively. Examples of fluid cell trajectories, or hydrodynamic flow lines, are illustrated by solid black lines tangential to local flow vectors.

cooled further to $T = 140$ MeV. Increasing $\xi_{\max}$, i.e., bringing the evolution trajectory closer to the critical point, causes the magnitude of equilibrium fluctuations to increase. However the relaxation to the equilibrium value becomes slower since its rate $\Gamma(Q) \propto DQ^2$ and $D = D_0\xi_0/\xi$ is proportional to $1/\xi$. We find that the former effect "wins" in the sense that $\phi_{\boldsymbol{Q}}$ at the time the fluid cell trajectory cools to $T = 140$ MeV (i.e. the blue curves in Figure 24), which is well after the fluid cell trajectory passes the point where $\xi = \xi_{max}$, see Figure 19, increases with $\xi_{\max}$, at least in the range of the parameters we have considered.

We see by comparing the left and right columns of Figure 24 that increasing the diffusion parameter D_0, which increases the relaxation rate, has the consequence that $\phi_{\boldsymbol{Q}}$ is closer to its instantaneous equilibrium form $\bar{\phi}_{\boldsymbol{Q}}$ during the course of the evolution. The value of $\phi_{\boldsymbol{Q}}$ at $\boldsymbol{Q} = 0$, however, remains invariant during the evolution due to the conservation laws inherent in model H: $\Gamma(\boldsymbol{Q} = 0) = 0$.

The Q-dependence of $\phi_{\boldsymbol{Q}}$ is shaped by two competing effects. As a given hydrodynamic cell, represented by a point on the phase diagram (see Figure 19) moving along the expansion trajectory, approaches the critical point, the “desired” equilibrium values of $\bar{\phi}_{\boldsymbol{Q}}$, to which $\phi_{\boldsymbol{Q}}$ is forced to relax by Eq. (4.2), increases across all values of $\boldsymbol{Q}$. However, while at larger Q, the relaxation is fast enough to effectively equilibrate $\phi_{\boldsymbol{Q}}$ to these larger equilibrium values, at lower Q conservation laws slow down the evolution, making the $\phi_{\boldsymbol{Q}}$ values lag behind $\bar{\phi}_{\boldsymbol{Q}}$ more significantly. This produces a peak in $\phi_{\boldsymbol{Q}}$ at a characteristic value of Q denoted by Q^{peak} in Ref. [129] which moves to lower values of Q as D_0 is increased. These features are evident in Fig. Figure 24 across the range of parameters we have considered. It is also instructive to compare and contrast Figure 24 with the results that would be obtained if the fluctuations followed model A dynamics where the relaxation rate of low-Q modes is not suppressed and, consequently, $Q^{peak} = 0$. We perform this comparison in Section 4.5; see Fig. Figure 29 from that Section which is to be compared with Figure 24.

In the simpler Bjorken scenario of Section 4.3, we described “memory effects” and looked at their dependence on Q and the diffusion parameter D_0. We can do the same here, for the ϕ_{Q} obtained in this more realistic r-dependent calculation, by displaying our results as in Fig. Figure 25, where suitably normalized $\phi_{\boldsymbol{Q}}$ and $\bar{\phi}_{\boldsymbol{Q}}$ are plotted as a function of the local temperature along a fluid cell trajectory for three different values of Q. In accordance with Eq. (4.10), the value of $\phi_{\boldsymbol{Q}}$ increases when $\phi_{\boldsymbol{Q}} < \bar{\phi}_{\boldsymbol{Q}}$ and decreases when $\phi_{\boldsymbol{Q}} > \bar{\phi}_{\boldsymbol{Q}}$, as $\phi_{\boldsymbol{Q}}$ “tries” to relax toward the rising, and later falling, equilibrium value $\bar{\phi}_{\boldsymbol{Q}}$, as the critical point is approached and later passed. For larger values of D_0 (as in the bottom half of Figure 25) the rate of relaxation is greater, meaning that $\phi_{\boldsymbol{Q}}$ rises more rapidly, and therefore higher, in the critical region. Although it also drops more rapidly as the temperature drops further, overall a larger D_0 yields larger fluctuations, at least within the reasonable range of values of D_0 that we explore. For small Q (see the left column in Figure 25), the value of $\phi_{\boldsymbol{Q}}$ grows very slowly, and reaches values much lower that the equilibrium $\bar{\phi}_{\boldsymbol{Q}}$ before it starts decreasing. However, for low Q, the rate at which ϕ_{Q} decreases after the critical point has been passed is also slow, and as a result significant memory of the fluctuation magnitude near the critical point (albeit itself smaller than equilibrium magnitude) is retained at freeze-out. This dynamics is qualitatively similar to the dynamics first described in Ref. [113] in a very simplified model of the out-of-equilibrium evolution of critical fluctuations with no spatial- or Q-dependence.

4.4.2 Hydrodynamic fluctuations on the freeze-out surface

As in the Bjorken scenario discussed in Section 4.3, we consider two isothermal hypersurfaces with $T_f = 140\,\mathrm{MeV}$ and $T_f = 156\,\mathrm{MeV}$. Unlike in Section 4.3, here the temperature is a function of τ as well as the radial coordinate r. An isothermal surface, therefore, is not simply $\tau = const$ for all r, as in the previous section. The surface $T(\tau, r) = T_f$ can be parametrized according to the discussion in Section 5.3.3 and we use the notations and approximations discussed in that section. We choose the parameter $\alpha = r$ in Eq. (5.33).

The magnitude of fluctuations at $T = 156\,\mathrm{MeV}$ in equilibrium is several times higher than that at $T_f = 140\,\mathrm{MeV}$, since $T = 156\,\mathrm{MeV}$ is closer to the critical temperature $T_c = 160$ MeV. However, the time that the system spends in the critical region before freezing out is shorter for $T_f = 156\,\mathrm{MeV}$ than for $T_f = 140\,\mathrm{MeV}$. By comparing these two freeze-out scenarios, we can understand the sensitivity of out-of-equilibrium fluctuations to the proximity of the freeze-out temperature to the critical point.

In Figure 26, suitably normalized plots of $\phi_{\boldsymbol{Q}}$ are shown for three points on the freeze-out hypersurface, characterized by radial coordinate $r = 0, 3$ and 6 fm, for two choices of freeze-out temperature T_f and two values of the diffusion parameter D_0. These plots of $\phi_{\boldsymbol{Q}}$ should be compared to the equilibrium $\bar{\phi}_{\boldsymbol{Q}}$ at three characteristic points: at $T = T_c$, at $T = T_f$ and at a point far away from critical, where $\xi = \xi_0$, shown by the dashed and dotted curves. The left and right plots differ by the choice of the freeze-out temperature, $T_f = 156$ MeV and 140 MeV, respectively. As expected, $Q = 0$ modes are "stuck" at their initial values and are not affected by the critical point. (To see how different this would be in the absence of conservation, Fig. Figure 26 can be compared with the results obtained in the case of Model A dynamics in Figure 30 in Section 4.5.) At moderate Q the "memory" effect weakens and at large Q the modes closely track their equilibrium values, which rises and then falls as the critical point is approached and then passed. By comparing the plots in Figure 26 for different T_f, we can also see that at smaller, but not too small, Q, the "memory" causes the fluctuation measure $\phi_{\boldsymbol{Q}}$ to be larger than its equilibrium value $\bar{\phi}_{\boldsymbol{Q}}$. This effect is more pronounced for lower T_f, due to the fact that the equilibrium fluctuations are smaller there.

Having understood the effects of varying the parameter D_0 and the proximity to the critical point on the fluctuation measure $\phi_{\boldsymbol{Q}}$, as in Section 4.3 the next step toward the calculation of observable particle multiplicity fluctuations is to compute $\tilde{\phi}(\Delta \boldsymbol{x}_\perp)$, the inverse Fourier transform of $\phi_{\boldsymbol{Q}}$ defined in Eq. (5.20). In Figure 27, we plot $\Delta x^2 \tilde{\phi}(\Delta \boldsymbol{x}_\perp)$ as a function of the spatial separation $\Delta x \equiv |\Delta \boldsymbol{x}_\perp|$ between the two points in the correlator $\langle \delta\hat{s}(x_+)\delta\hat{s}(x_-)\rangle$, see Eq. (5.19). By comparing to Figure 22(b), we see that the D_0-dependence is qualitatively similar to that in the Bjorken scenario, discussed at length in Section 4.3. The small Δx (large Q) behavior of the fluctuations is not affected by changing D_0, while at the same time the spatial correlator becomes longer ranged as D_0 is increased. The correlator goes negative at larger values of Δx; this is a consequence of conservation as can be seen by comparing Figure 27 to Figure 31 in Section. 4.5 and as explained in the context of the Bjorken scenario in Eq. (4.12). Finally, consistent with what we have already seen in Figure 26, with either value of D_0 memory effects are strong enough that the magnitudes of the fluctuations are not much smaller if the freeze-out temperature is $T_f = 140$ MeV (well below the critical point) as compared to their magnitudes if $T_f = 156$ MeV (very close to $T_c = 160$ MeV) despite the fact that the equilibrium fluctuations at these two temperatures differ substantially.

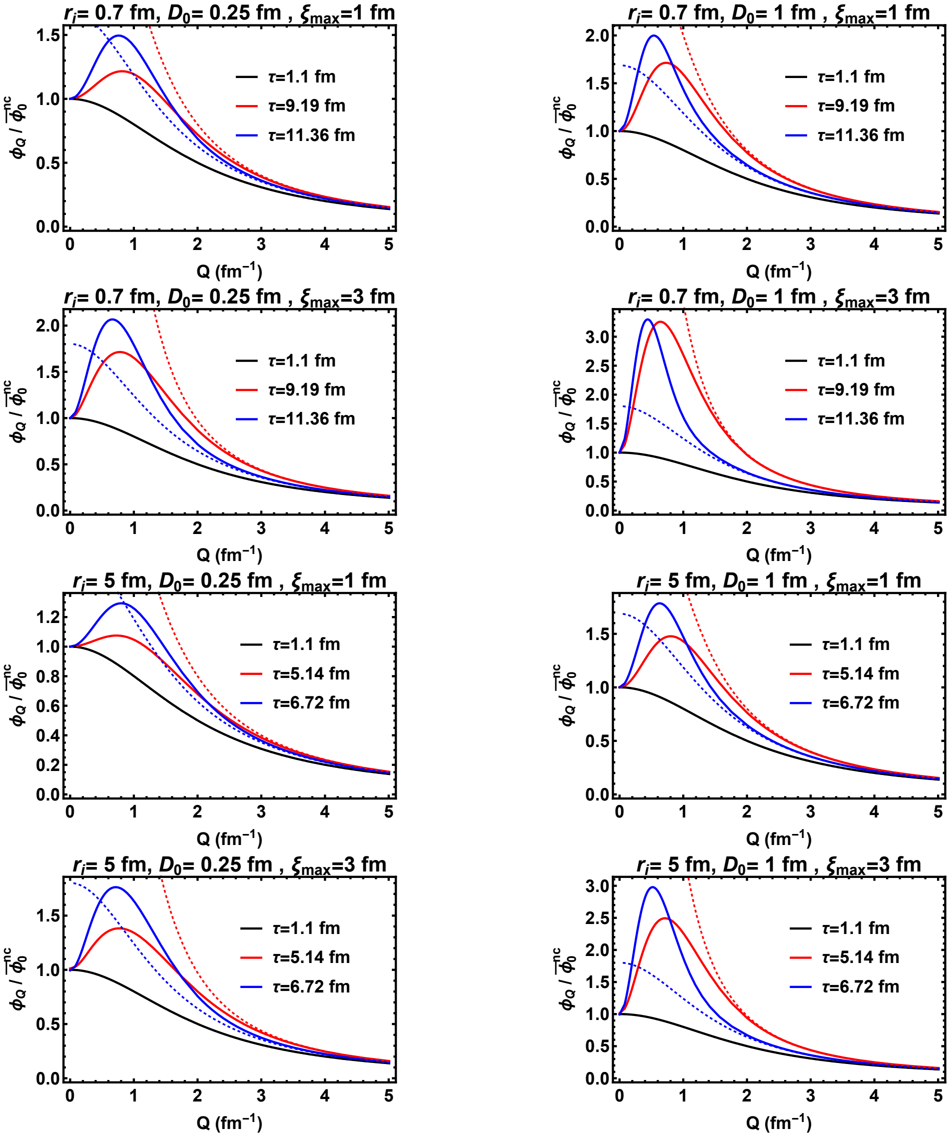

Figure 24: Hydro+ fluctuation measure $\phi_{\boldsymbol{Q}}$ along two hydrodynamic flow lines passing through $r = r_i$ at initial time $\tau = \tau_i$, with $r_i = 0.7\,\text{fm}$ (top four panels) and $5\,\text{fm}$ (bottom four panels). The four plots in the left (right) column are for $D_0 = 0.25\,\text{fm}$ ($D_0 = 1\,\text{fm}$), with $\xi_{\max} = 1\,\text{fm}$ and $\xi_{\max} = 3\,\text{fm}$ in alternating rows. The solid and dashed curves are, respectively, the $\phi_{\boldsymbol{Q}}$ and $\bar{\phi}_{\boldsymbol{Q}}$ (normalized to their values at $Q = 0$ away from the critical point, where $\xi = \xi_0$) at three times τ indicated in the plot legends; the choice of τ's is explained in the text.

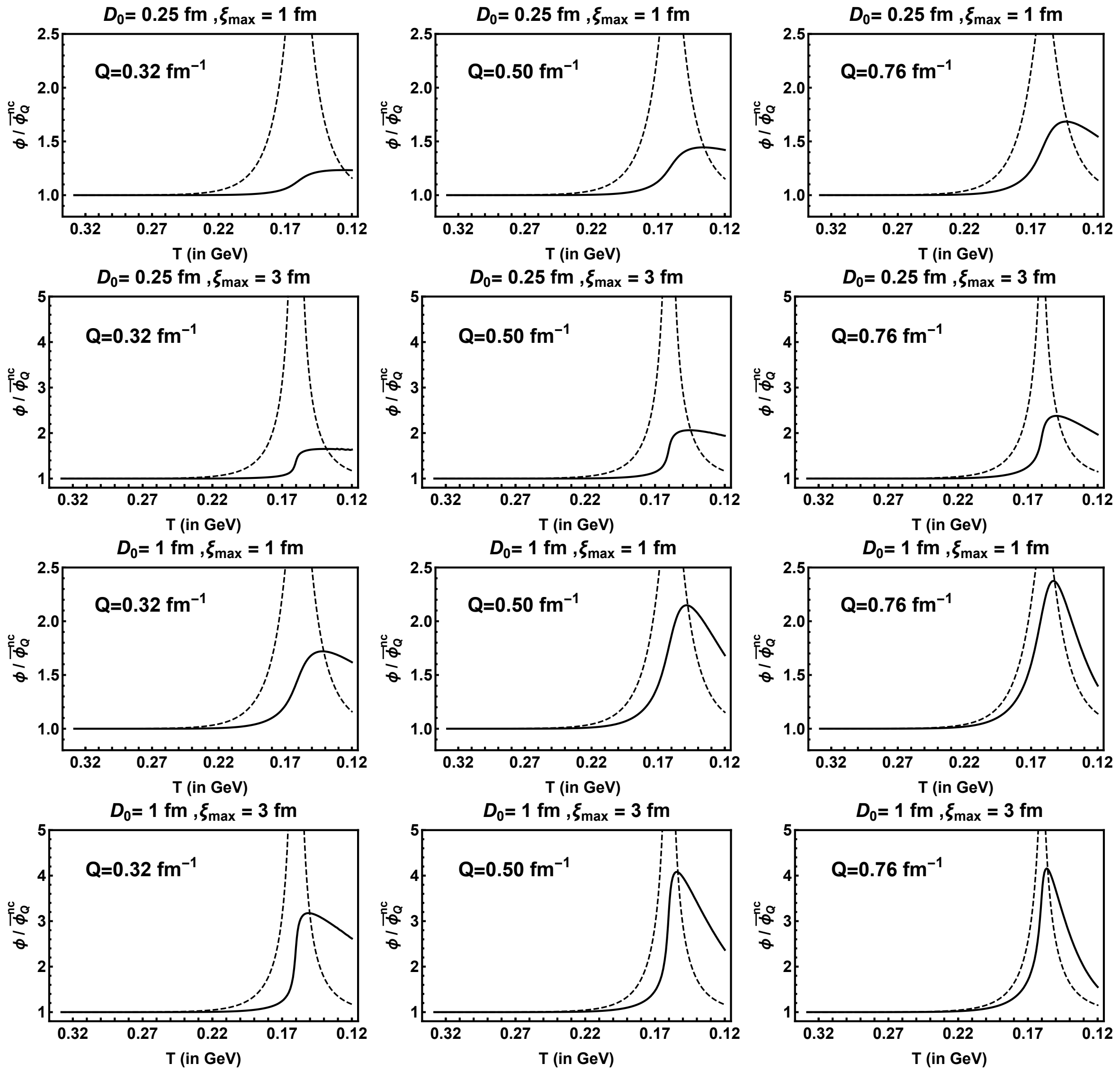
D_0= 0.25 fm ,ξ_{max} = 1 fm

D_0= 0.25 fm ,ξ_{max} = 3 fm

D_0= 1 fm ,ξ_{max} = 1 fm

D_0= 1 fm ,ξ_{max} = 3 fm

Figure 25: The values of $\phi_{\boldsymbol{Q}}$ (suitably normalized) for three representative values of Q (same for each column), and for values D_0 (same in top and bottom six panels) and ξ_{max} (same in alternating rows) as in Figure 24. The values of $\phi_{\boldsymbol{Q}}$ are taken along a fluid cell trajectory and plotted as a function of temperature, which is a monotonous function of time τ along the trajectory. The trajectory chosen for these plots begins at $r_i = r(\tau_i) = 1.8\,\text{fm}$. The dashed and solid curves represent the equilibrium $\bar{\phi}_{\boldsymbol{Q}}$ and non-equilibrium $\phi_{\boldsymbol{Q}}$, respectively.

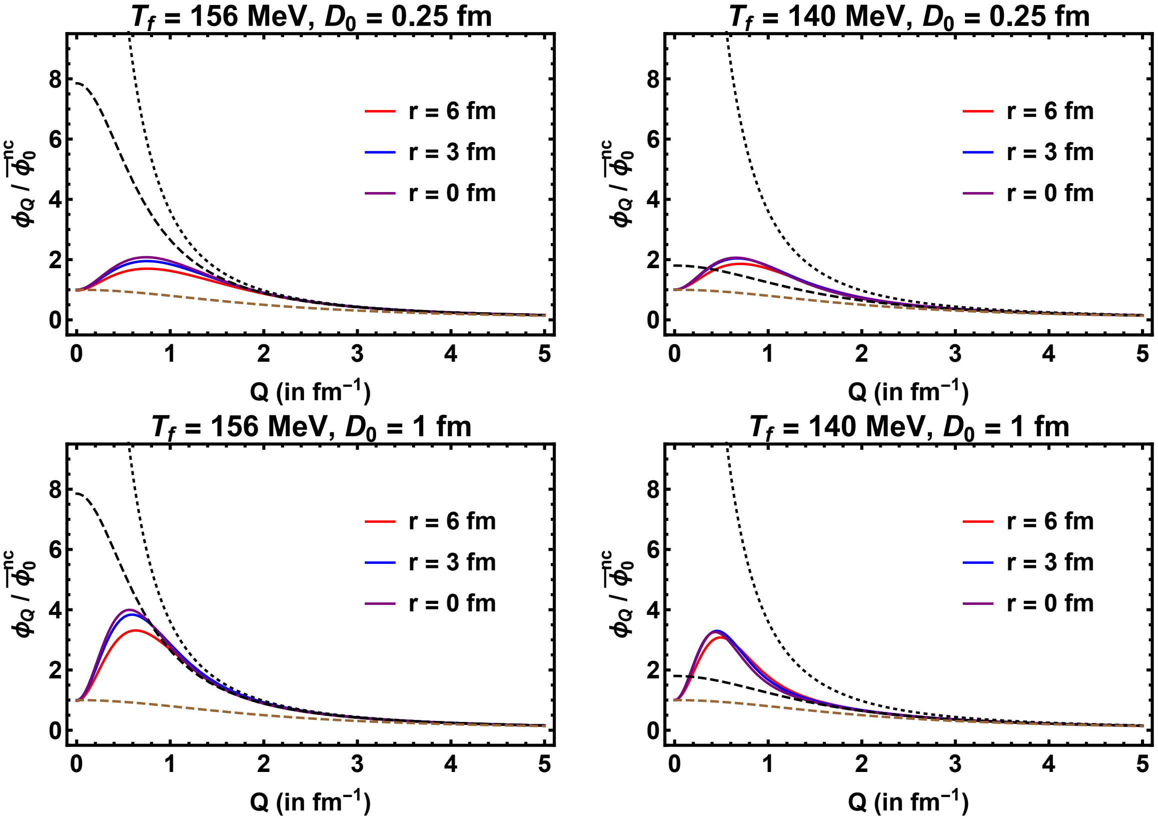

Figure 26: The Hydro+ variable $\phi_{\boldsymbol{Q}}$ (normalized to its value at $Q = 0$ away from the critical point, where $\xi = \xi_0$) at freeze-out evolved with two different diffusion parameters $D_0 = 0.25$ fm (upper panels) and 1 fm (lower panels) and $\xi_{\text{max}} = 3\,\text{fm}$. The left (right) panels show results for evolution until the decreasing temperature has reached a higher (lower) freeze-out temperature. The blue, red and purple curves show the values of $\phi_{\boldsymbol{Q}}$ at different points on the freeze-out hypersurface, characterized by the radial coordinate r. The black dashed and dotted curves are the equilibrium curves at $T = T_f$ and $T = T_c$ respectively. The dashed brown curve is the (non-critical) equilibrium curves corresponding to $\xi = \xi_0$.

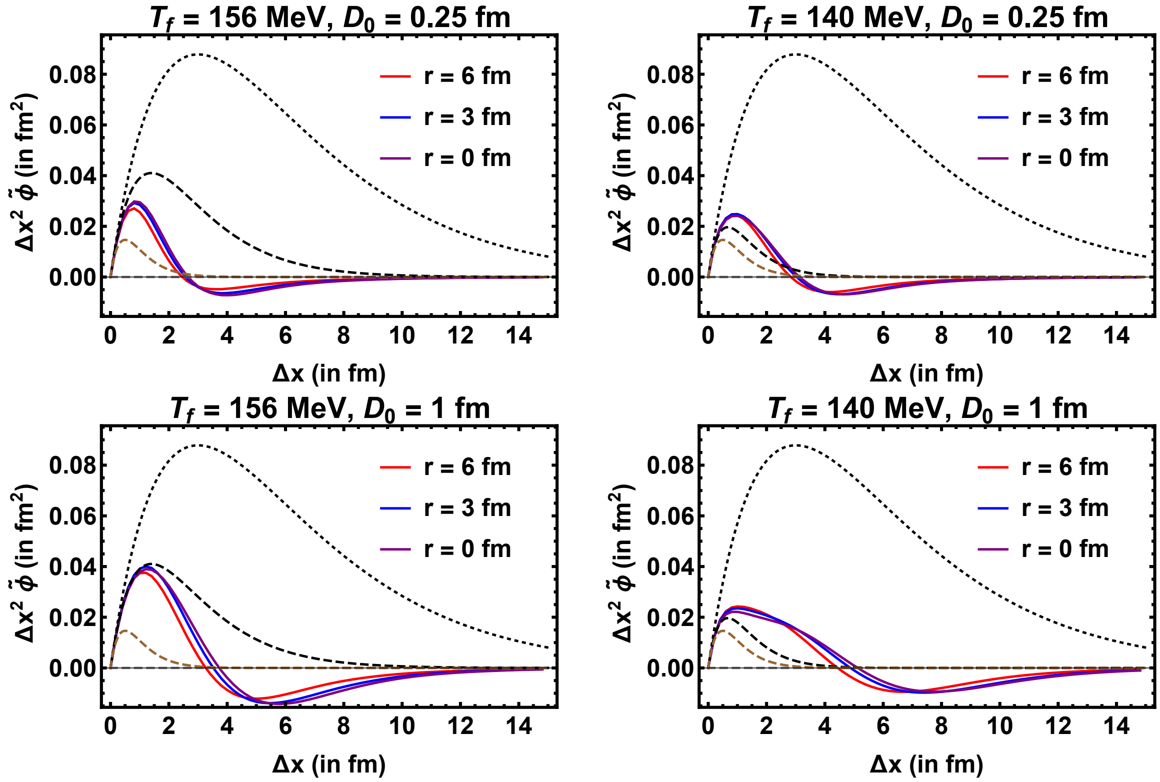

Figure 27: $\tilde{\phi} \times \Delta x^2$, the measure of fluctuations of $\hat{s}$ described by the correlator $\langle \delta\hat{s}(x_+)\delta\hat{s}(x_-)\rangle$, at freeze-out as a function of the spatial separation between the points $\Delta x \equiv |\Delta \boldsymbol{x}_\perp|$. In the calculations depicted in different panels, the $\phi_{\boldsymbol{Q}}$'s were evolved with two different D_0's until freeze-out at two different T_f's, with the inverse Fourier transform to obtain $\tilde{\phi}(\boldsymbol{x}_\perp)$ performed at T_f. In all panels, we have chosen a trajectory with $\xi_{\max} = 3\,\text{fm}$. The three r values depicted via the colored curves correspond to three r values on the freeze-out surface in the lab frame. The black dashed and dotted curves are the equilibrium curves at $T = T_f$ and $T = T_c$ respectively.

The dashed brown curve is the (non-critical) equilibrium curve corresponding to $\xi = \xi_0$.

4.5 Contrasting with Model A evolution

In this Section, we repeat the calculations of Section 4.4 with the same hydrodynamic background (as in Ref. [128]) but with the dynamical evolution of the fluctuations given by Model A universality class of Hohenberg and Halperin [184]with the relaxation rate given by Eq. (4.8), which we repeat here:

$$\Gamma(\boldsymbol{Q}) = \Gamma_0 \frac{\xi_0^2}{\xi^2} \left(1 + (Q\xi)^2\right) , \qquad \text{(model A).} \tag{4.14}$$

In contrast to Section 4.4 where the fluctuating slow mode is hydrodynamic density, here the fluctuating slow mode is not a conserved quantity. We have performed simulations with $\Gamma_0 = 1\,\mathrm{fm}^{-1}$ and $8\,\mathrm{fm}^{-1}$, which correspond to $\Gamma_0\xi_0^2 = 0.25\,\mathrm{fm}$ and $2\,\mathrm{fm}$, respectively. Comparing the results plotted in this Section to those in the analogous Figures in Section 4.4 provides us with another way to analyze the impact of conservation laws on the results from Section 4.4. The main difference between Model A and Model H evolution arises from the qualitatively different relaxation rate for the low Q modes, $Q\xi \ll 1$, which goes as $\Gamma_0\xi_0^2/\xi^2$ in Model A and as $(D_0\xi_0/\xi)Q^2$ in Model H, with the Q^2-suppression being a manifestation of conservation. We proceed now to discuss the Model A dynamics of the two point fluctuations. [1] We will be

---

[1] The plots shown below are from the original work in which the author was directly involved in, although this system with Model A dynamics was elaborately studied in Ref. [128] which the author wasn't a part of.

freezing out these Hydro+ simulations into particle multiplicity fluctuations in the Chapter. (5) in Section. (5.5.2).

4.5.1 Evolution of $\phi_{\mathbf{Q}}$

Figure 28, can be compared to the analogous Model H results shown in Figure 24. Here, we present the Model A dynamics of $\phi_{\mathbf{Q}}$ for fluid cells following two different hydrodynamic characteristic trajectories, with two choices of Γ_0 and two choices of ξ_{max}. As in Section 4.4, varying ξ_{max} corresponds to the closeness of the cooling trajectory of the fluid cell to the critical point on the phase diagram. Due to conservation $\phi_{\mathbf{0}}$ fixed to its initial value, in Figure 24 and hence $\phi_{\mathbf{Q}}$ first rises as a function of increasing Q and then falls. In the Model A dynamics of this Section the maximum value of $\phi_{\mathbf{Q}}$ is found at $Q = 0$, and this value is time dependent. In Model A, here, as in Model H in Figure 24, the fluctuations $\phi_{\mathbf{Q}}$ fall out of equilibrium, lagging behind the equilibrium fluctuations $\bar{\phi}_{\mathbf{Q}}$ as the latter change with time.

In Figure 29, which can be compared to the analogous Model H results shown in Figure 25, for all three representative Q modes that are plotted we notice the $\phi_{\mathbf{Q}}$'s lagging behind their respective $\bar{\phi}_{\mathbf{Q}}$s, with the degree to which they fall out of equilibrium greater for smaller Γ_0, meaning slower relaxation toward equilibrium. For the values of Γ_0 that we have considered in Figure 29, we can see that fluctuations do depend on whether we choose a freeze-out temperature of 156 MeV or 140 MeV. As we also observed in Figure 25, $\phi_{\mathbf{Q}}$ has an inflection point at $T = T_c$ where the relaxation rate takes its minimum value and the growth of $\phi_{\mathbf{Q}}$ stops when $\phi_{\mathbf{Q}}$ equals the instantaneous $\bar{\phi}_{\mathbf{Q}}$.

4.5.2 Fluctuations on the freeze-out surface

In Figure 30, which can be compared to Figure 26, suitably normalized plots of $\phi_{\boldsymbol{Q}}$ are shown for three points on the freeze-out hypersurface, characterized by radial coordinate $r = 0, 3$ and 6 fm, for two choices of freeze-out temperature T_f and two values of the parameter Γ_0. Most of the discussion of Figure 26 in Section 4.4 applies here also, with the one significant difference being the $\mathbf{Q} = 0$ mode which now changes with time.

As in Figure 27, in Figure 31 we have computed $\tilde{\phi}(\Delta \boldsymbol{x}_\perp)$, the inverse Fourier transform of $\phi_{\boldsymbol{Q}}$ defined in Eq. (5.20), and plotted $\Delta x^2 \tilde{\phi}(\Delta \boldsymbol{x}_\perp)$ as a function of the spatial separation Δx between the two points in the correlator $\langle \delta \hat{s}(x_+) \delta \hat{s}(x_-) \rangle$. As in the Model H evolution of Figure 27, the small Δx (large Q) behavior of the fluctuations in Figure 31 is not affected by changing Γ_0, while at the same time the spatial correlator becomes longer ranged as Γ_0 is increased. The central difference between the Model A dynamics here in Figure 31 and the Model H dynamics in Fig. Figure 27 is that here $\tilde{\phi}(\Delta \boldsymbol{x}_\perp)$ is positive at large Δx: the fact that it becomes negative in the large Δx region in Figure 27 is a direct consequence of conservation in Model H.

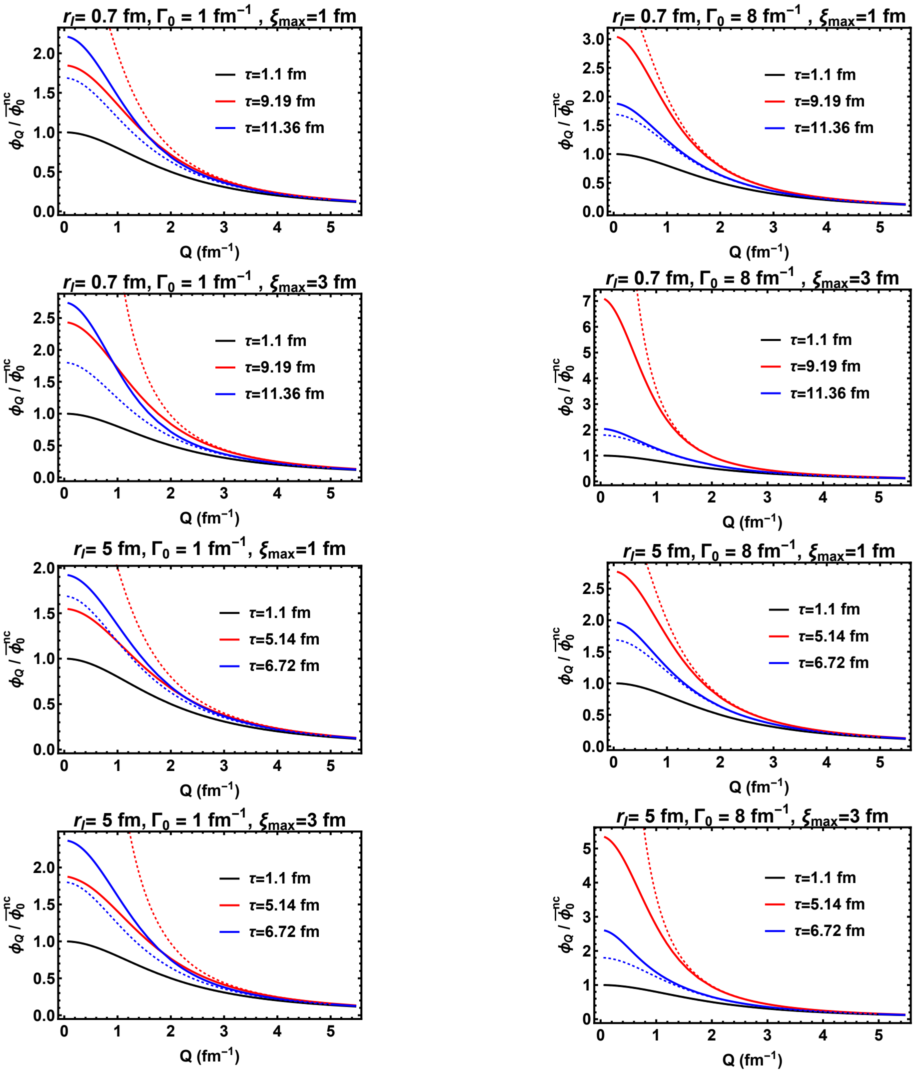

Figure 28: Hydro+ fluctuation measure $\phi_{\mathbf{Q}}$ evolved according to Model A dynamics along two hydrodynamic flow lines passing through $r = r_i$ at initial time $\tau = \tau_i$, with $r_i = 0.7\,\mathrm{fm}$ (top four panels) and $5\,\mathrm{fm}$ (bottom four panels). Plots in the left (right) column are for $\Gamma_0 = 1\,\mathrm{fm}^{-1}$ ($\Gamma_0 = 8\,\mathrm{fm}^{-1}$), with $\xi_{\max} = 1\,\mathrm{fm}$ and $\xi_{\max} = 3\,\mathrm{fm}$ in alternating rows. The solid (and dashed) curves are the $\phi_{\boldsymbol{Q}}$ (and $\bar{\phi}_{\boldsymbol{Q}}$), normalized to the zero mode of the non-critical fluctuations. The black, red and blue curves correspond to $\phi_{\mathbf{Q}}$'s at the initial time τ_i and at the times when the equilibrium temperature reaches $160\,\mathrm{MeV}$ and $140\,\mathrm{MeV}$ respectively.

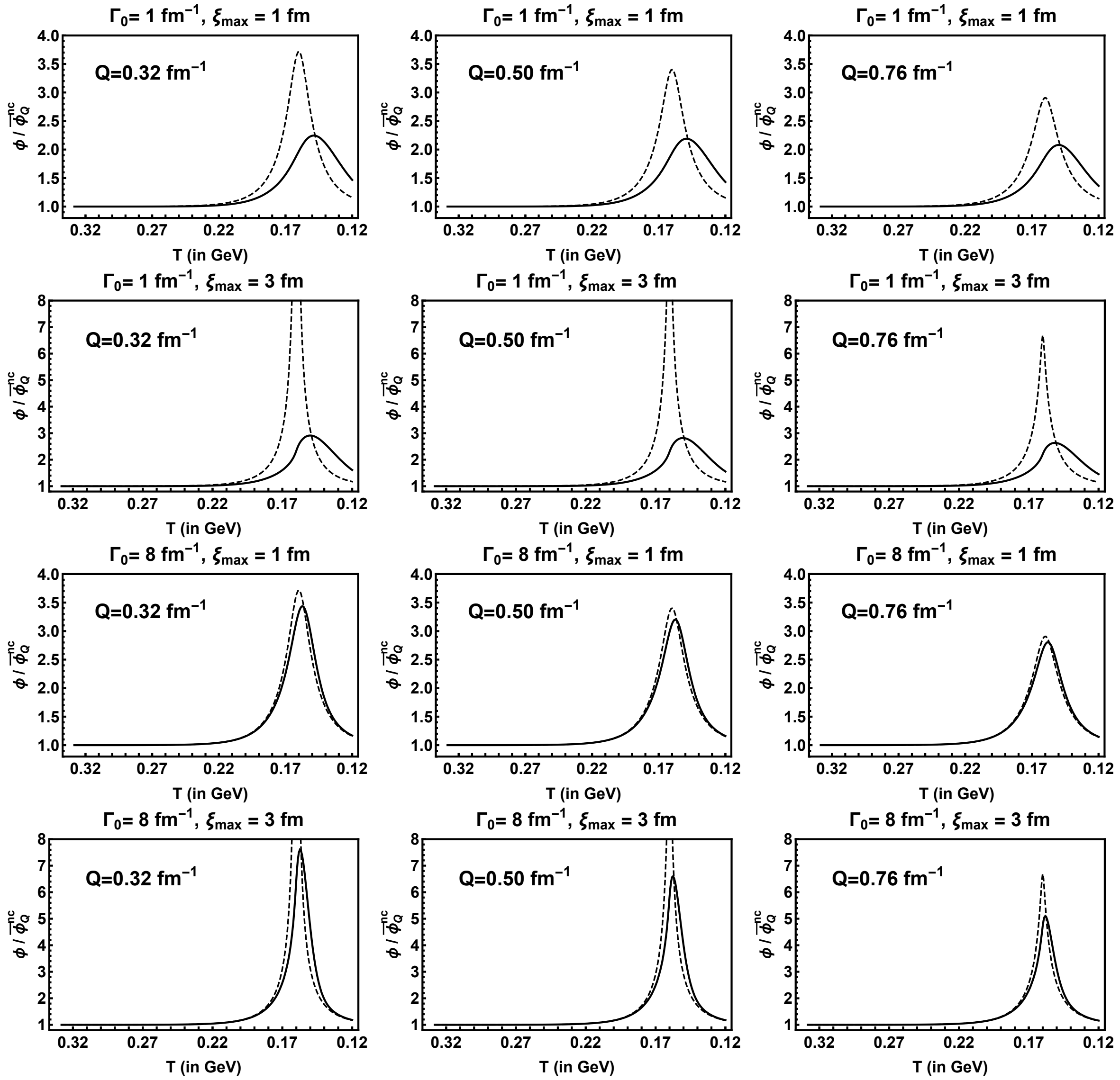

Figure 29: The values of $\phi_{\boldsymbol{Q}}$ (suitably normalized) for three representative values of Q (same for each column), and for two values Γ_0 (same in top and bottom six panels) and ξ_{max} (same in alternating rows) as in Figure 28. The values of $\phi_{\boldsymbol{Q}}$ are taken along a fluid cell trajectory and plotted as a function of temperature, which is a monotonous function of time τ along the trajectory. The trajectory chosen for these plots begins at $r_i = r(\tau_i) = 1.8\,\text{fm}$. The dashed and solid curves represent the equilibrium $\bar{\phi}_{\boldsymbol{Q}}$ and non-equilibrium $\phi_{\boldsymbol{Q}}$, respectively.

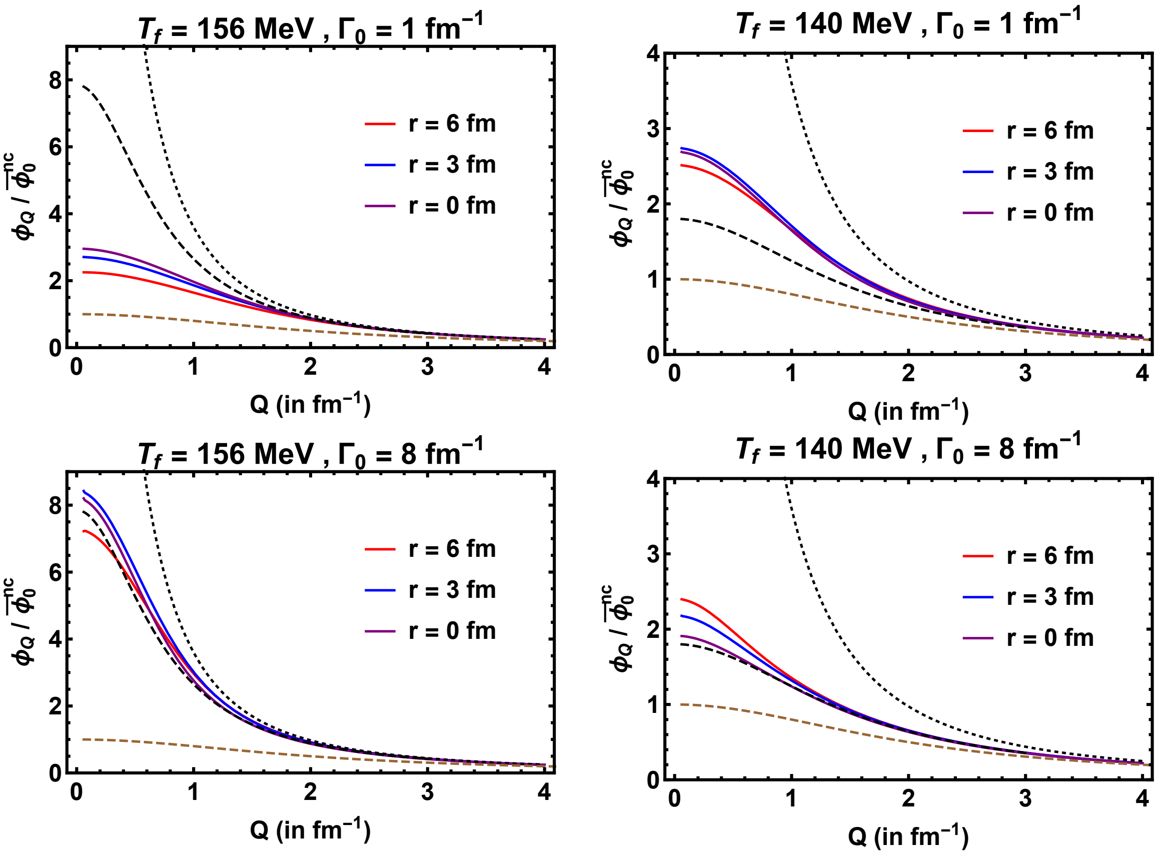

Figure 30: The Hydro+ variable $\phi_{\boldsymbol{Q}}$ (normalized to its value at $Q = 0$ away from the critical point, where $\xi = \xi_0$) at freeze-out evolved with $\Gamma_0 = 1\ \text{fm}^{-1}$ (upper panels) and $8\ \text{fm}^{-1}$ (lower panels) and with $\xi_{\max} = 3\,\text{fm}$. The left (right) panels show results for evolution until the decreasing temperature has reached a higher (lower) freeze-out temperature. The blue, red and purple curves show the values of $\phi_{\boldsymbol{Q}}$ at different points on the freeze-out hypersurface, characterized by the radial coordinate r. The black dashed and dotted curves are the equilibrium curves at $T = T_f$ and $T = T_c$ respectively. The dashed brown curve is the (non-critical) equilibrium curve corresponding to $\xi = \xi_0$.

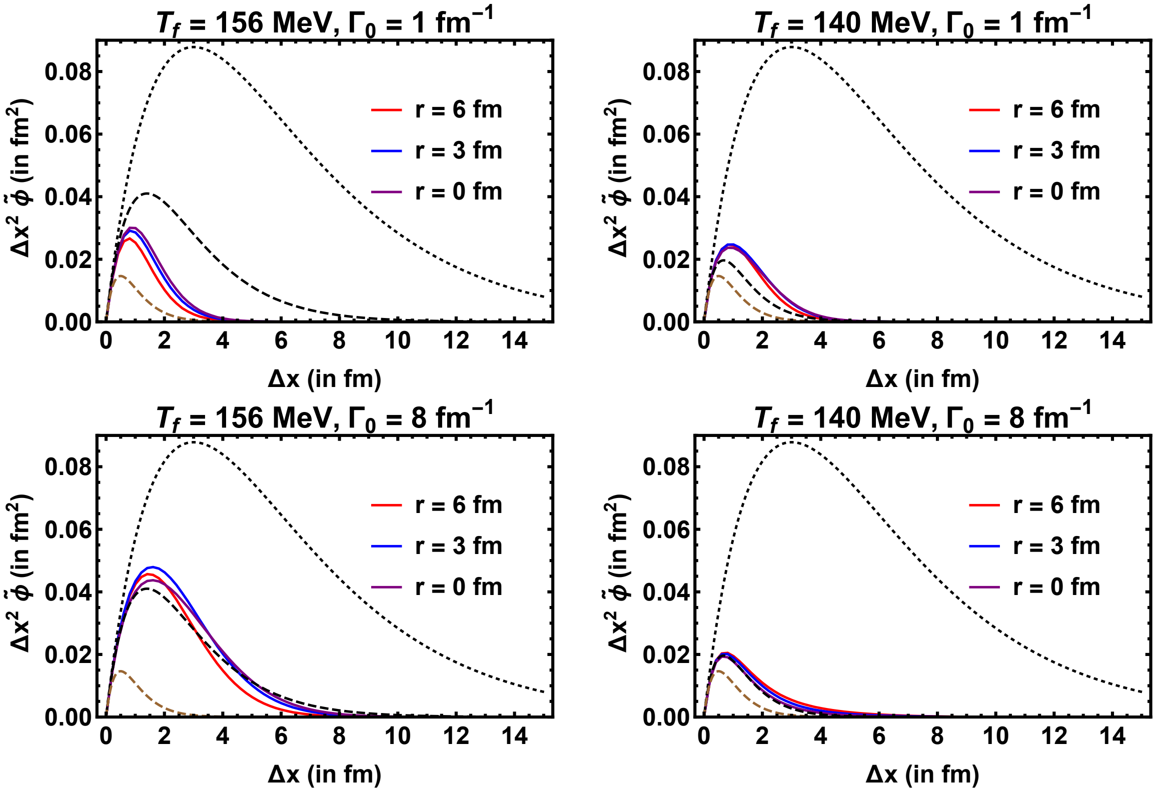

Figure 31: $\tilde{\phi} \times \Delta x^2$, the measure of fluctuations of $\hat{s}$ described by the correlator $\langle \delta\hat{s}(x_+)\delta\hat{s}(x_-)\rangle$, at freeze-out as a function of the spatial separation between the points $\Delta x \equiv |\Delta \boldsymbol{x}_\perp|$. In the calculations depicted in different panels, the $\phi_{\boldsymbol{Q}}$'s were evolved with two different Γ_0's until freeze-out at two different T_f's, with the inverse Fourier transform to obtain $\tilde{\phi}(\boldsymbol{x}_\perp)$ performed at T_f. In all panels, we have chosen a trajectory with $\xi_{\text{max}} = 3\,\text{fm}$. The three r values depicted via the colored curves correspond to three r values on the freeze-out surface in the lab frame. The black dashed and dotted curves are the equilibrium curves at $T = T_f$ and $T = T_c$ respectively. The dashed brown curve is the (non-critical) equilibrium curve corresponding to $\xi = \xi_0$.

4.6 Summary and Outlook

In this Chapter, we presented the numerical results for the dynamics of fluctuations of the slowest non-hydrodynamic mode corresponding to the fluctuations of entropy per baryon, denoted by $\hat{s}$ in the critical region in simplified scenarios. We demonstrated the effects of critical slowing down and conservation of charges and energy-momentum by varying the relaxation rate and "picking" trajectories at different proximities to the critical point, by varying a parameter denoted by $\xi_{\max}$ (Eq. (4.9)) in our model.

The main *lessons* from this study can be read off from the plots of (Figure 25) and (Figure 26) (or (Figure 22)). We find that due to conservation, the fluctuations corresponding to the wavevectors with low magnitudes are suppressed substantially in the critical region. This observation will turn out to be very important for the cumulants of particle multiplicities as the freeze-out picks out lower Q modes due to thermal smearing. This will be discussed in more detail in Chapter. (5). In the coordinate space, fluctuations at sufficiently large distances become anti-correlated as a consequence of conservation of charges and energy.

The main *limitations* of this study stem from the simplified setup that is used here which prevents us from making quantitative estimates relevant for Beam-Energy Scan program. The simplifications that could be improved in future involve using more realistic conditions for fluctuations in the initial stage, including background effects of charge diffusion, deriving the equilibrium fluctuations from a realistic EoS rather than the simplified scaling EoS determined using a parameterized ξ in this work and using a 3+1 D hydrodynamic background in place of the 1+1 scenario discussed here. Despite these limitations, we think this work is a significant advancement as it is the first Model H simulation of hydrodynamic fluctuations in a deterministic approach and adds to our qualitative understanding. We defer these quantitative calculations for future work.

In Chapter. (5) we'll demonstrate the freeze-out of the setups discussed in this chapter and estimate the effects of dynamics on Gaussian multiplicities of proton and pion multiplicities.

CHAPTER 5

FREEZE-OUT OF CRITICAL FLUCTUATIONS

This Chapter is based on the reference [2] which I co-authored with K. Rajagopal, M.Stephanov and Y.Yin.

In the last Chapter, we discussed how the dynamics of fluctuations of the slowest mode is affected by critical slowing down. In particular, we demonstrated the Model H dynamics in two semi-realistic scenarios, one corresponding to a Bjorken symmetric background and a numerical azimuthally symmetric , longitudinally boost-invariant Hydro+ simulation with radial expansion and compared it with Model A dynamics (where the order parameter was not a hydrodynamic mode). We discussed the suppression of the lower Q modes of the fluctuations due to charge and energy conservation. In this chapter, we'll develop a novel procedure to freeze-out these hydrodynamic fluctuations near the critical point, and thereby estimate the variance of proton and pion multiplicities.

Traditionally, freeze-out of hydrodynamic simulations are performed using Cooper-Frye procedure or some modifications of the same to account for viscous effects. However, prior to the work presented in this chapter, a freeze-out procedure to convert fluctuations of hydrodynamic densities into correlations of particle multiplicities wasn't available. Such a framework for freeze-out critical fluctuations is the main result of this chapter. The chapter is organized as follows. In Section 5.1 we review the standard Cooper-Frye freeze-out procedure that neglects fluctuations. With this groundwork in place, in Section 5.3, we derive and explain our freeze-out procedure that extends the Cooper-Frye approach so as to match the critical fluctuations just before freeze-out, as described by Hydro+, to observable fluctuations in particle multiplicities just after. In Section 5.4 we apply our freeze-out procedure to the Bjorken scenario: a fluid that is undergoing boost-invariant longitudinal expansion, meaning that it is cooling, but that is translation-invariant and at rest in the transverse directions. In this simplified setting, we are able to push much of the calculation through analytically and in so doing gain intuition and elucidate general features that arise again in the next Section. In Section 5.5 we illustrate the use of the freeze-out procedure that we have introduced and fully exercise its salient features by obtaining the two-point correlations of particle multiplicities from the more realistic Hydro+ simulations discussed in Chapter. (4) and Ref. [128] in which the fluid is boost invariant and azimuthally symmetric but is finite in transverse extent and thus exhibits radial flow. We conclude in Section 5.6 with a summary of the main qualitative lessons that we draw from our results of Sections 5.4 and 5.5 as well as a look ahead at important next steps.

5.1 Cooper-Frye freeze-out

Hydrodynamics describes hot and dense QCD matter created in heavy-ion collisions in terms of densities of conserved quantities such as energy or baryon charge, or the corresponding thermodynamic variables such as temperature T or baryochemical potential μ_B, as well as the local fluid velocity. Heavy ion collision experiments, on the other hand, measure multiplicities and momentum distributions of particles which emerge from the expanding and cooling droplet of fluid as it breaks up into hadrons. These multiplicities and distributions are well described by a procedure which we shall summarize below known as Cooper-Frye freeze-out [142] which starts from the output of a hydrodynamic simulation.

In the traditional Cooper-Frye procedure, the macroscopic evolution of the conserved charges and fluid velocity field obtained from a hydrodynamic calculation are converted into a microscopic description in terms of particles in a Hadron Resonance Gas model. The freeze-out hypersurface where this switching is done is determined based on some thermodynamic condition for eg., fixed temperature or energy density. The averages of the conserved densities are equated to those of a hadron resonance gas of particles via the Cooper-Frye formula. Let dS_μ be the differential element pointing along the normal vector to the freeze-out surface. The mean multiplicity of particle species A ($\langle N_A \rangle$) according to the Cooper-Frye formula is given by,

$$\langle N_A \rangle = d_A \int dS_\mu \int Dp_A \, p^\mu \, \langle f_A(x,p) \rangle \tag{5.1}$$

Here, d_A is the degeneracy of particle species A and Dp_A is the Lorentz invariant measure:

$$Dp_A = 2\frac{d^4p}{(2\pi)^3}\delta\left(p^2 - m_A^2\right)\theta(p_0)\,.$$

$\langle f_A \rangle$ is the momentum-dependent particle distribution function which is either taken to be Fermi-Dirac or Bose-Einstein based on the spin and statistics of hadron species A. For simplicity, throughout this chapter we shall ignore the spin and statistics and consider $\langle f_A \rangle$ to be the Boltzmann distribution

$$\langle f_A(x,p)\rangle = \exp\left(\frac{-p\cdot u(x) + \mu_A(x)}{T(x)}\right)\,, \tag{5.2}$$

where $T(x)$, $\mu_A(x)$ and $u(x)$ are the temperature, the chemical potential of species A, and the local fluid velocity at a point x on the freeze-out hypersurface. For mesons, $\mu_A = 0$, while for baryons/antibaryons $\mu_A = \pm\mu_B$, respectively. In addition to ignoring the modification of the distribution function due to spin and statistics, we also ignore further modifications to $\langle f_A \rangle$ due to viscous effects [197–202] in this preliminary study.

In Section 5.3 we shall turn to describing our extension of the Cooper-Frye procedure that will enable us to translate the output of a Hydro+ simulation, with traditional hydrodynamic variables as well as fluctuations described by $\phi_{\boldsymbol{Q}}(x)$, into particles in a way that faithfully turns the critical fluctuations in the fluid into fluctuations and correlations of the hadrons. We are pursuing this goal within what is often referred to as a deterministic framework for describing the fluctuations: Hydro+ adds new deterministic equations of motion to the equations of hydrodynamics, equations that describe the evolution of quantities that characterize the fluctuations starting with $\phi_{\boldsymbol{Q}}(x)$ that describes their two-point correlation function. Fluctuations can also be described stochastically, where one evolves an ensemble of configurations each with its own realization of the fluctuations [130–140]. It would be natural in a stochastic description to analyze freeze-out via extending the Cooper-Frye procedure in a manner that follows an analogous logic to that we shall employ here, but we leave this to future work.

5.2 Estimates for cumulants assuming local equilibrium

Cooper-Frye freeze-out assumes that hadrons at freeze-out are not correlated and the event-by-event fluctuations are simply of Poisson nature. Owing to the smallness of these fluctuations, this may be a justified approximation far from the critical point. One important feature Cooper-Frye freeze-out misses are the effects of local and global conservation. There have been various studies to incorporate such effects into hadron resonance gas descriptions which act as baseline for non-critical fluctuations [203–207]. Assuming that within the coarse-grained volume, local equilibrium has been achieved, one could calculate the cumulants of baryon number from the derivatives of hydrodynamic EoS , i.e using Eq. (2.14). Using an effective field theory for the fluctuations of the leading singular mode, one could estimate the cumulants for particle multiplicity. This will be described in more detail in Section. (5.3). It was found in ([105]), that estimates for the cumulants of proton multiplicities evaluated in equilibrium are huge. The acceptance dependence of the cumulants in equilibrium have been studied in [106, 111, 112].

As discussed in Chapter. (4), the approximation that fluctuations are given by their local equilibrium temperature and baryon chemical potential is not justified in the critical region due to critical slowing down of these fluctuations. In Section. (5.3), we'll describe an extension of the procedure employed in [105] to freeze-out out of equilibrium fluctuations near the critical point. In Chapter. (6), we'll discuss a more general freeze-out procedure that can be applied for freezing out hydrodynamic fluctuations anywhere in the phase diagram.

5.3 Cooper-Frye freeze-out for critical fluctuations

We shall now describe a freeze-out procedure to connect the fluctuations of hydrodynamic variables to the fluctuations of the particle multiplicities. Such a description is crucial in the special case of heavy ion collisions that freeze out in the vicinity of a critical point. In this case, fluctuations are both enhanced and of considerable interest, since it is via detecting critical fluctuations that we hope to discern the presence of a critical point [9, 40]. These fluctuations are due to thermal noise and their magnitude, or more importantly, their correlations are a sensitive signature of the proximity of a thermodynamic singularity, such as the critical point. Obviously, we cannot match these critical fluctuations using a *free* gas of hadrons which doesn't have a critical point. We discussed in Chapter. (3) that the fluctuations in equilibrium can be modeled by using a critical field theory for scalar field (which we denote by σ) in three dimensions. σ is a collective mode which becomes "soft", long-range correlated and slow, at the critical point, justifying its treatment as a collective field. One can then match the singular part of fluctuations of hydrodynamic variables to the fluctuation of the field σ. σ field couples to the observed particles, causing their masses to fluctuate at the time of freeze-out and consequently leads to observable fluctuations in particle multiplicities.

In the chiral limit $m_q \to 0$, the σ field represents the fluctuations of the chiral order parameter about its value at the tri-critical point. But at non-zero quark masses, the order parameter is not well-defined and is some general linear combination of number density and entropy density. In this Chapter, we'll be concerned only with the leading singular behavior of the fluctuations of σ near the critical point. Here, we shall match them to two-point fluctuations of $\hat{s}$, which show the same leading singular behavior except in a very special scenario mentioned in a footnote in Section. (4.1) of Chapter. (4).

In Hydro+ the two point function of this mode is given by (its Fourier transform) $\phi_{\mathbf{Q}}$. Our goal is to connect it to the two-point correlation function of the multiplicity fluctuation δf

$$f_A(x,p) = \langle f_A(x,p)\rangle + \delta f_A(x,p) \tag{5.3}$$

where $\langle f_A(x,p)\rangle$ is given by Eq. (5.2). We shall use the model of critical correlations which incorporates critical fluctuations in the hadronic description via the interaction of the hadrons with a critical σ field. Such a description of critical fluctuations in a hadron gas has been used in equilibrium [40,56,57,105,106,111,112,187,208,209] as well as with some out-of-equilibrium effects included [210]. [1] In this approach the interaction with the σ field modifies the masses of the hadrons, to linear order in σ, as follows:

$$\delta m_A = g_A \sigma\,. \tag{5.4}$$

We define the value of σ as the deviation of the critical field from its equilibrium value and thus, by definition, $\langle\sigma\rangle = 0$. The proportionality constant g_A plays the role of the coupling constant

---

[1] Unlike [210], we have connected the out of equilibrium fluctuations of σ to out of equilibrium fluctuations of hydrodynamic densities.

between the hadron species A and the σ field. [1]The critical contribution to the fluctuations of f_A is due to the dependence of the averaged particle distribution function $\langle f_A \rangle$ on the mass, and is given by

$$(\delta f_A(x,p))_\sigma = g_A \frac{\partial \langle f_A(x,p) \rangle}{\partial m_A} \sigma(x) \, ,$$

where $\langle f_A \rangle$ is the Boltzmann distribution in Eq. (5.2). As a result, fluctuations of the σ field translate into fluctuations and correlations between particles, as in

$$\begin{aligned} \langle \delta f_{A_1}(x_1,p_1) \delta f_{A_2}(x_2,p_2) \rangle = \langle f_{A_1}(x_1,p_1) \rangle \delta_{1,2} & \\ + g_{A_1} g_{A_2} \frac{\partial \langle f_{A_1}(x_1,p_1) \rangle}{\partial m_{A_1}} \frac{\partial \langle f_{A_2}(x_2,p_2) \rangle}{\partial m_{A_2}} \langle \sigma(x_1) \sigma(x_2) \rangle \, . & \quad (5.5) \end{aligned}$$

Since hydrodynamic variables, such as baryon density, are expressed in terms of momentum space integrals of the particle distribution functions, the correlation functions of hydrodynamic variables are proportional to the correlation functions of the σ field. This reproduces the essential property of fluctuations at the critical point – the critical (most singular at the critical point) contribution of all correlation functions are proportional to the correlator of a single critical scalar field.

---

[1] In this chapter, we consider g_A to be a constant independent of the particle momenta. As we shall see in the next chapter, when one enforces charge, momenta and energy conservation at freeze-out, g_A s are no longer constants and have a definite momentum dependence which we derive. We expect that this explicit dependence on momenta will not modify the qualitative and semi-quantitative estimates for Gaussian cumulants that we obtain in this chapter.

Our main focus is on the correlation functions of $\hat{s}$. Universality of critical behavior dictates that in equilibrium this critical contribution to this correlator should be also proportional to the correlator of σ. In this chapter, we shall also assume that this remains true out of equilibrium. This allows us to connect the correlations of $\hat{s}$ at the end of the Hydro+ evolution to the fluctuations of σ in the kinetic description at freeze-out and consequently to observable fluctuations and correlations of hadron multiplicities.

The equilibrium fluctuations of the critical field are dictated by the universality of critical behavior and are controlled by the probability functional $P = \exp\{-\Omega/T\}$, where $\Omega[\sigma]$ the effective action (or free energy) which can be written for small fluctuations at long wavelengths in an expansion in powers of the field σ and its gradients around its equilibrium value, $\langle\sigma\rangle = 0$, as follows:

$$\Omega(\sigma) = \int d^3x \left[\frac{(\nabla\sigma)^2}{2} + \frac{m_\sigma^2}{2}\sigma^2 + \frac{\lambda_3}{3}\sigma^3 + \frac{\lambda_4}{4}\sigma^4 + \dots\right]. \tag{5.6}$$

The equilibrium two-point correlator can be then found from Eq. (5.6) and is given by

$$\langle\sigma(\boldsymbol{x}_+)\sigma(\boldsymbol{x}_-)\rangle \approx \frac{T}{4\pi\,|\Delta\boldsymbol{x}|}e^{-|\Delta\boldsymbol{x}|/\xi} \tag{5.7}$$

where $\Delta\boldsymbol{x} = \boldsymbol{x}_+ - \boldsymbol{x}_-$ and $\xi \equiv 1/m_\sigma$ is the correlation length of the σ-field fluctuations. As we shall only be interested in the two-point correlator in this work and as we are neglecting the (small) nonzero value of the critical exponent η, we will be able to neglect the terms of order σ^3

and higher in the expansion (5.6). The Fourier/Wigner transform of the two-point correlator is then given by

$$\chi_{\boldsymbol{Q}} \equiv \int_{\boldsymbol{\Delta x}} e^{-i\boldsymbol{Q}\cdot\boldsymbol{\Delta x}} \langle \sigma(\boldsymbol{x}_+)\sigma(\boldsymbol{x}_-)\rangle \approx \frac{T\xi^2}{1+(Q\xi)^2}\,. \tag{5.8}$$

In the approximate equalities in Eqs. (5.7) and (5.8) we ignore loop corrections, which are known to be small in the 3D Ising universality class in which η is small.

We choose the units of length in Eq. (5.6) so that the value of ξ introduced in Eqs.(5.6) and (5.7) matches the value of the correlation length of the thermodynamic fluctuations introduced above, in Section 4.2. The universality of the critical behavior then dictates that the relationship between the two-point correlators of the fluctuating soft mode in the hydrodynamic description of the physics at the freeze-out point and the fluctuating σ-field in the kinetic theory description of the physics at the same point takes the simple form

$$\langle \delta\hat{s}(\boldsymbol{x}_+)\delta\hat{s}(\boldsymbol{x}_-)\rangle = Z\langle \sigma(\boldsymbol{x}_+)\sigma(\boldsymbol{x}_-)\rangle\,. \tag{5.9}$$

Equivalently, the Wigner transforms are related via the same proportionality constant Z:

$$\bar{\phi}_{\boldsymbol{Q}} = Z\chi_{\boldsymbol{Q}}\,. \tag{5.10}$$

Using Eqs. (4.3) and (5.8) we find

$$Z \approx \frac{c_p}{Tn^2\xi^2}\,. \tag{5.11}$$

Note that, while both c_p and ξ^2 diverge at the critical point, their ratio is finite in the approximation we are using.[1]

Z can be obtained in terms of the parameters h_μ, h_T, r_μ, r_T defined in Eqs. (3.5) as:

$$
\begin{aligned}
Z = \lim_{T,\mu\to T_c,\mu_c} \frac{c_p}{n^2 T \xi^{2-\eta}} &\approx \frac{1}{n_c^2 \xi^{2-\eta}} \left[h_T - \frac{s}{n} h_\mu\right]^2 \left(\frac{\partial^2 G}{\partial h^2}\right)_r && \text{(5.12a)}\\
&= \frac{1}{n_c^2 \xi^{2-\eta}} \left[h_T - \frac{s}{n} h_\mu\right]^2 \frac{M_0}{h_0} \left(\frac{\xi}{\xi_0}\right)^{2-\eta} && \text{(5.12b)}\\
&= \frac{M_0 A}{h_0 n_c^2 \xi_0^{2-\eta}} \left[(\tan\alpha_1)^{-1} - \frac{s_c}{n_c}\right]^2 \frac{\sin^2\alpha_1}{w^2 T_c^2 \sin^2(\alpha_1 - \alpha_2)} && \text{(5.12c)}\\
&= \frac{M_0 A}{h_0 n_c^2 \xi_0^{2-\eta}} \left[\left(\frac{dP}{ndT}\right)_n\right]^2 \frac{\sin^2\alpha_1}{w^2 T_c^2 \sin^2(\alpha_1 - \alpha_2)} && \text{(5.12d)}
\end{aligned}
$$

where α_1, α_2, A and w are the mapping parameters between QCD EoS and 3D Ising model near the QCD critical point with critical temperature at T_c. In Eq. (5.12a), we have approximated the second derivative of pressure with second derivative of Ising Gibbs free energy with respect to the magnetic-field h near the critical point.

We shall apply the relationship in Eq. (5.9), or equivalently in Eq. (5.10), to express the fluctuations of σ at freeze-out also when these fluctuations are out of equilibrium. While these relationships are true in equilibrium due to universality near the critical point, strictly speaking this is not justified in an out of equilibrium scenario. We assume that the deviations

---

[1] Our approximation sets the critical exponent to its mean-field value $\eta = 0$, which is a good approximation to make for a critical point in the 3D Ising universality class where $\eta \sim 0.04$. If one uses a more sophisticated, non-mean-field equation of state as in, e.g., Ref. [63], and/or more sophisticated form of $\bar{\phi}_{\boldsymbol{Q}}$ and $\chi_{\boldsymbol{Q}}$ as in Ref. [116], the value of the normalization constant will nevertheless be determined by the matching equation (5.10), which is more general than the approximation in which we have derived it.

from equilibrium are still not large, and in a partial equilibrium state where the treatment of Hydro+ is valid, we can apply the same relationship.

We shall thus determine the correlation functions of σ at freeze-out as follows:

$$\langle \sigma(x) \rangle \equiv 0 \tag{5.13a}$$

$$\langle \sigma(x_+)\sigma(x_-) \rangle = Z^{-1} \langle \delta\hat{s}(x_+)\delta\hat{s}(x_-) \rangle \tag{5.13b}$$

where Z is a normalization constant which can be obtained by matching the fluctuations obtained in the kinetic description to fluctuations (i.e., susceptibilities) obtained from the QCD equation of state using Eq. (5.10). Since in this chapter our focus is entirely on developing and exploring the implementation of the freeze-out prescription that we introduce to describe fluctuations, we shall take the constants Z in Eq. (5.13b) and g_A in Eqs. (5.4)-(5.5) as given and postpone their determination by matching a particular QCD EoS to the next chapter (6). We also note that we shall find ways to express our results that are independent of those unknown parameters. Note that there is a subtlety in defining Eq. (5.13b) relating to the choice of frame in which x_+ and x_- are at equal time; we shall discuss this in Section 5.3.1.

Due to Eq. (5.13a), the mean number of particles is unmodified by critical fluctuations and is given by Eq. (5.1). Integrating the spatial correlations given by Eq. (5.5) over the full freeze-out hypersurface and using Eq. (5.13b), we can express the leading critical contribution to the correlator of particle multiplicities N_A and N_B as:

$$\langle \delta N_A \delta N_B \rangle_\sigma = \int dS_{\mu,+} \int dS_{\nu,-}\; J_A^\mu(x_+)\, J_B^\nu(x_-)\, Z^{-1}\, \langle \delta\hat{s}(x_+)\delta\hat{s}(x_-)\rangle \tag{5.14}$$

$$J_A^\alpha(x_\pm) \equiv g_A d_A \int Dp_A\, p^\alpha\, \frac{\partial\langle f_A(x_\pm, p)\rangle}{\partial m_A} \tag{5.15}$$

with d_A the spin (and/or isospin) degeneracy of the particle species A. The subscript σ in $\langle \delta N_A \delta N_B \rangle_\sigma$ is there to remind us that this is the contribution due to critical fluctuations. The expressions (5.14) and (5.15) constitute the central result whose consequences we shall explore over the course of the rest of this chapter by making them explicit in simplified settings. In (5.14) and (5.15), we have a relationship between the critical fluctuations of hydrodynamic variable on the right-hand side of (5.14) and the correlator of observable particle multiplicities on the left-hand side.

One can obtain a straightforward generalization of Eq. (5.14) yields the form for freeze-out of leading singular higher point fluctuations as:

$$\left\langle \delta N_A^k \right\rangle_\sigma^c = \int dS_{\mu_1} \cdots \int dS_{\mu_k}\, J_A^{\mu_1}(x_1) \ldots J_A^{\mu_k}(x_k)\, Z^{-k/2}\, \langle \hat{s}(x_1) \ldots \hat{s}(x_k)\rangle_c \tag{5.16}$$

for the critical contribution to the k^{th} cumulant of the multiplicity of particle species A. We have extended the Cooper-Frye procedure in a way that will allow us to see how the critical, i.e. most singular, contribution the two-point correlations of $\hat{s}$ translates into the variance of observed particle multiplicities.

Finally, we note that the total variance of the particle multiplicity has an additional non-critical contribution which is usually taken as Poissonian:

$$\left\langle \delta N_A^2 \right\rangle = \langle N_A \rangle + \left\langle \delta N_A^2 \right\rangle_\sigma \, . \tag{5.17}$$

There can certainly be corrections to the non-critical contributions that we represent here by the Poisson distribution. These may arise from global charge conservation [203, 211] or initial fluctuations [109], for example, but we shall not discuss them in this work. This work is intended only as a prescription for freezing out the fluctuations near the critical point that encode information about the leading singularity. We will discuss freeze-out in a unified and more comprehensive framework, (treating the freeze-out of critical and non-critical parts in the same way) in the next chapter (6). The prescription that we describe here for criitcal fluctuations will emerge in that framework in a natural way, with some slight modifications which won't change the qualitative and semi-quantitative discussions in the chapter.

5.3.1 Toward explicit evaluation

We'll now turn these expressions for the extended Cooper-Frye procedure that we have derived into tools that can be used in explicit calculations.

The Wigner transform $\phi_{\boldsymbol{Q}}$, as defined in Eq. (4.1), involves integration over the hyperplane orthogonal to the 4-vector $u(x)$. That is, the points x_+ and x_- are equal-time points in the rest frame of the fluid at point x, or $\Delta x \cdot u(x) = 0$. However, in general, the freeze-out surface over which the integration in Eq. (5.14) is to be performed does not necessarily have the property that any two points on it are simultaneous in the rest frame of the fluid at their midpoint x. For example, this property holds for boost-invariant Bjorken flow. But, it does not hold for the numerical simulation with radial flow discussed in Ref. [128] and discussed in Section 4.4. In order to translate $\phi_{\boldsymbol{Q}}$ into the correlator $\langle \delta\hat{s}(x_+)\delta\hat{s}(x_-)\rangle$ in such a case one needs to be able to evolve this correlator not only in time $u \cdot x$ (using Eq. (4.2)) but also in time *difference* $u \cdot \Delta x$. We shall show below that because this evolution is slow (and especially slow at the critical point) one can neglect the effect of such evolution. This enables us to express the time correlator of interest which is un-equal in the local rest frame in terms of $\phi_{\boldsymbol{Q}}$.

Let us consider a small region of the freeze-out surface around a point x that lies on the surface and let us assume that the surface is not perpendicular to the 4-vector $u(x)$. This means that freeze-out does not happen simultaneously at all points in this region. Let us denote the velocity of the frame in which this patch of the freeze-out surface is an equal-time surface by β. ($\beta = 0$ for Bjorken flow). If the typical range of the correlator is of order ℓ_*, then the typical value of the time difference $u(x) \cdot \Delta x \sim \beta \ell_*$. The typical scale ℓ_* can be determined by the condition that the relaxation rate $\Gamma(Q_*) \sim D Q_*^2$ of the corresponding modes $Q_* = 1/\ell_*$ is of order the expansion rate $1/\tau$, where D was introduced in Eq. (4.6). That is, $\ell_* \sim \sqrt{D\tau}$.

The evolution of the correlator $\langle \delta\hat{s}(x_+)\delta\hat{s}(x_-)\rangle$ as a function of the time separation $u \cdot \Delta x$ occurs with the same rate, also of order $\Gamma(Q_*)$. As a result, the correction to the correlator is of order $\Gamma(Q_*)\, u \cdot \Delta x \sim \beta\sqrt{D/\tau}$. This quantity is small already because τ is a macroscopic scale,

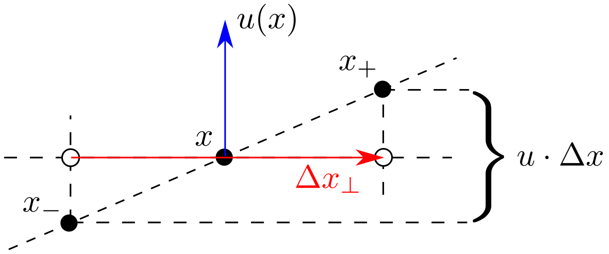

Figure 32: Geometric representation of Eq. (5.18). x_+ and x_- are on the freeze-out surface; x is the midpoint between them. The four-vector $\Delta x_\perp$ (red) is perpendicular to the fluid four-velocity at the point x, $u(x)$, meaning that in the local fluid rest frame it is a four-vector with no time-component.

while D is microscopic, i.e., $\tau \gg D$. Furthermore, near the critical point, D itself is vanishing: as seen in Eq. (4.6), it is smaller than the microscopic scale by another factor of ξ_0/ξ.

More formally, let us define a projection of the separation four-vector Δx onto the plane perpendicular to $u(x)$:

$$\Delta x_\perp \equiv \Delta x - [u(x) \cdot \Delta x]\ u(x)\,. \tag{5.18}$$

Then we can express the correlator $\langle \delta\hat{s}(x_+)\delta\hat{s}(x_-)\rangle$ in Eq. (5.14) in terms of $\phi_{\boldsymbol{Q}}$ defined in Eq. (4.1), obtaining

$$\langle \delta\hat{s}(x_+)\delta\hat{s}(x_-)\rangle = \tilde{\phi}(x;\boldsymbol{\Delta x}_\perp) + \mathcal{O}(\sqrt{D/\tau})\,, \tag{5.19}$$

where the three-component vector $\Delta\boldsymbol{x}_\perp$ is the projection of the four-vector Δx onto the equal-time hyperplane orthogonal to the vector $u(x)$ as defined in Eq. (5.18) and illustrated in Figure 32, and $\tilde{\phi}(x;\Delta\boldsymbol{x}_\perp)$ is the inverse Fourier (Wigner) transform of $\phi_{\boldsymbol{Q}}(x)$:

$$\tilde{\phi}(x;\Delta\boldsymbol{x}_\perp) \equiv \int \frac{d^3Q}{(2\pi)^3} e^{i\boldsymbol{Q}\cdot\Delta\boldsymbol{x}_\perp}\phi_{\boldsymbol{Q}}(x)\,. \tag{5.20}$$

Eq. (5.19) formalizes the qualitative argument from the preceding paragraph.

We shall be comparing our results with what one would obtain upon assuming the fluctuations are in equilibrium. Up to corrections suppressed by ratios of microscopic (e.g., correlation length ξ) to macroscopic scales (such as hydrodynamic gradient scales, e.g., τ) we can replace the correlation function in Eq. (5.7) with a delta function:

$$Z^{-1}\left\langle \delta\hat{s}(\boldsymbol{x}_+)\delta\hat{s}(\boldsymbol{x}_-)\right\rangle = \langle\sigma(\boldsymbol{x}_+)\sigma(\boldsymbol{x}_-)\rangle = T\xi^2\delta^{(3)}(\Delta\boldsymbol{x})\,. \tag{5.21}$$

Substituting into Eq. (5.14) we find

$$\langle\delta N_A\delta N_B\rangle_\sigma^{eqbm} = \int dS_\mu(x)\; J_A^\mu(x)\,\hat{n}_\nu(x)\,J_B^\nu(x)\,T(x)\xi^2(x)\,. \tag{5.22}$$

where $\hat{n}(x)$ is the unit vector along the normal on the freeze-out hypersurface at x. This expression straightforwardly generalizes existing results for equilibrium fluctuations, see for example Ref. [105], to locally equilibrated fluctuations in a (more realistic) inhomogeneous fireball. We shall make comparisons between our full results and the equilibrium fluctuation predictions (5.22) in order to highlight the importance of non-equilibrium effects, especially the effects due to conservation laws.

5.3.2 Ratios of observables

We shall calculate the contribution of critical fluctuations to the variance of the particle multiplicity of species A (we shall consider protons, $A = p$, and pions, $A = \pi$) in a specified finite rapidity and transverse momentum acceptance window. To eliminate the dependence on the volume (i.e., the transverse size) of the droplet of QGP we shall introduce the intensive ratio

$$\omega_A \equiv \frac{\langle \delta N_A^2 \rangle_\sigma}{\langle N_A \rangle} \,, \tag{5.23}$$

which was referred to as $\omega_{A,\sigma}$ in Ref. [105]. We note that ω_A depends on the choice of acceptance window. (See, e.g., Ref. [111].) Since this acceptance dependence is not the main focus of the present study, while criticality and non-equilibrium effects are, we shall often illustrate our results by plotting the ratio

$$\tilde{\omega}_A = \frac{\omega_A}{\omega_A^{\text{nc}}} \,, \tag{5.24}$$

where ω_A^{nc} is the ω_A calculated upon assuming freeze-out well away from the critical point, i.e., upon setting $\xi_{\text{max}} = \xi_0$. We have checked (for a few sets of parameters) that the acceptance dependence of the numerator and denominator in Eq. (5.24) is similar and, thus, largely cancels. In contrast, the numerator ω_A is strongly enhanced by critical fluctuations (for example, in equilibrium $\tilde{\omega}_A^{\mathrm{eqbm}} = \xi^2/\xi_0^2$) and is sensitive to the non-equilibrium effects of critical slowing down, while the denominator ω_A^{nc} is, by construction, not affected by critical fluctuations. Although ω_A defined in Eq. (5.24) depends on the unknown parameters g_A and Z via the ratio $g_A/\sqrt{Z}$, all dependence on these unknowns cancels in the ratio of ratios defined in Eq. (5.24), within the approximations that we shall make.

In this Chapter, we perform the freeze-out of the two semi-realistic Hydro+ scenarios - with a Bjorken symmetric background and a numerical simulation with radial expansion, azimuthal symmetry and longitudinal boost invariance discussed in Chapter. (4). Before we proceed to these in Sections. (4.3) and (4.4), we will establish some useful notations.

5.3.3 Notations for azimuthally symmetric boost invariant case

For a general freeze-out hypersurface, the differential element can be expressed as $d^3S_\mu = n_\mu N\, d\theta_1 d\theta_2 d\theta_3$ where $\theta_1, \theta_2, \theta_3$ are variables used to parametrize the points on the freeze-out hypersurface. The normal vector n can be expressed as:

$$n_\alpha(x) = N^{-1} \epsilon_{\alpha\beta\gamma\delta} \frac{\partial x^\beta}{\partial \theta_1} \frac{\partial x^\gamma}{\partial \theta_2} \frac{\partial x^\delta}{\partial \theta_3}(x) \tag{5.25}$$

where

$$N = \sqrt{\sum_{j=1}^{4} \left(\det \left| \frac{\partial(x^{\alpha_1^j}\,,\, x^{\alpha_2^j}\,,\, x^{\alpha_3^j}\,)}{\partial(\theta_1\,,\, \theta_2\,,\, \theta_3\,)} \right| \right)^2}\,, \qquad \alpha_i^{'} \,\epsilon\, \{0,1,2,3\} - \{j\} \tag{5.26}$$

The basis vectors can be defined for the tangent space to the normal at the freeze-out hypersurface at x along the lines of the example given in Appendix A of [121] is:

$$e_a = \mathring{e}_a + (\mathring{u} - \hat{n})\frac{\hat{n}.\mathring{e}_a}{1 - \hat{n}.\mathring{u}} \tag{5.27}$$

where $a = 1, 2, 3$ and $\mathring{e}_a$s correspond to unit vectors along the spatial coordinate in the lab frame and $\mathring{u}$ is the unit vector along the time direction in the lab-frame. $\hat{n}$ is a unit vector normal to the tangent space. Any two points $x_\pm$ on the freeze-out hypersurface can be expressed in terms of these basis vectors, their mid-point x and separation vector $\mathbf{\Delta x}$ as follows:

$$x_\pm = x \pm \frac{\Delta x^i}{2} e_i + \frac{\Delta x^i \Delta x^j}{8}(e_i \cdot \partial) e_j + \dots \tag{5.28}$$

The equations above can be used in a generalized setting. To specify the shape of an azimuthally symmetric boost-invariant freeze-out surface, it is convenient to use Bjorken coordinates defined in terms of the Cartesian coordinates $(\,t,\, x_1,\, x_2,\, x_3)$ in the lab frame via

$$t = \tau \cosh\eta, \quad x_1 = r\cos\varphi, \quad x_2 = r\sin\varphi, \quad x_3 = \tau\sinh\eta\,.$$

The mutually orthogonal set of unit vectors corresponding to each of the Bjorken coordinates can be expressed in terms of the Cartesian coordinates as

$$\hat{\tau} \;=\; (\,\cosh\eta,\, 0,\, 0,\, \sinh\eta\,) \tag{5.29}$$

$$\hat{\eta} \;=\; (\,\sinh\eta,\, 0,\, 0,\, \cosh\eta\,) \tag{5.30}$$

$$\hat{r} \;=\; (\,0, \cos\varphi, \sin\varphi, 0\,) \tag{5.31}$$

$$\hat{\varphi} \;=\; (\,0,\, -\sin\varphi,\, \cos\varphi,\, 0\,)\,. \tag{5.32}$$

The radial profile of a boost-invariant and azimuthally-symmetric freeze-out surface can then be expressed in a parametric form using an arbitrary parameter α as in Ref. [212]

$$\tau = \tau_f(\alpha), \quad r = r_f(\alpha)\,, \tag{5.33}$$

so that the point on the freeze-out hypersurface corresponding to parameters α, η, φ is given by:

$$x(\alpha,\eta,\varphi) \;=\; \tau_f(\alpha)\hat{\tau}(\eta) + r_f(\alpha)\hat{r}(\varphi)\,. \tag{5.34}$$

Then, the volume vector normal to the freeze-out hypersurface can be written as $d^3S = n\, d\alpha \tau d\eta r d\varphi$ where the vector n is given by:

$$n(\alpha,\eta,\varphi) = \frac{\partial x}{\partial\alpha} \wedge \frac{\partial x}{\tau\partial\eta} \wedge \frac{\partial x}{r\partial\varphi} = r'_f(\alpha)\hat{\tau}(\eta) + \tau'_f(\alpha)\hat{r}(\varphi)\,. \tag{5.35}$$

The flow four-velocity on the freeze-out surface is given by

$$u(\alpha, \eta, \varphi) = u^r(\alpha)\hat{r}(\phi) + u^\tau(\alpha)\hat{\tau}(\eta) \tag{5.36}$$

in the coordinates with which we are working.

In defining the two-point correlation function we shall need to specify two points on the freeze-out hypersurface. Let $x_\pm \equiv x(\alpha_\pm, \eta_\pm, \varphi_\pm)$ be any two such points on with $x \equiv (x_+ + x_-)/2$ being their midpoint and $\Delta x \equiv x_+ - x_-$ being the separation vector between them. Let us denote similarly $\tau = (\tau_+ + \tau_-)/2$, $r = (r_+ + r_-)/2$, $\eta = (\eta_+ + \eta_-)/2$, $\varphi = (\varphi_+ + \varphi_-)/2$ and $\Delta\tau = \tau_+ - \tau_-$, $\Delta r = r_+ - r_-$, $\Delta\eta = \eta_+ - \eta_-$, $\Delta\varphi = \varphi_+ - \varphi_-$. Then

$$\begin{aligned}
x &= \tau \cosh\frac{\Delta\eta}{2}\hat{\tau} + r\cos\frac{\Delta\varphi}{2}\hat{r} + \frac{\Delta\tau}{2}\sinh\frac{\Delta\eta}{2}\hat{\eta} + \frac{\Delta r}{2}\sin\frac{\Delta\varphi}{2}\hat{\varphi} && \text{(5.37a)}\\
\Delta x &= 2\tau\sinh\frac{\Delta\eta}{2}\hat{\eta} + 2r\sin\frac{\Delta\varphi}{2}\hat{\varphi} + \Delta r\cos\frac{\Delta\varphi}{2}\hat{r} + \Delta\tau\cosh\frac{\Delta\eta}{2}\hat{\tau} && \text{(5.37b)}\\
u\cdot\Delta x &= u^\tau(x)\Delta\tau\cosh\frac{\Delta\eta}{2} - u^r(x)\Delta r\cos\frac{\Delta\varphi}{2} && \text{(5.37c)}\\
\Delta x_\perp &\equiv 2\tau\sinh\frac{\Delta\eta}{2}\hat{\eta} + 2r\sin\frac{\Delta\varphi}{2}\hat{\varphi}\\
&\quad + \left[-\Delta\tau u^r(x)\cosh\frac{\Delta\eta}{2} + \Delta r u^\tau(x)\cos\frac{\Delta\varphi}{2}\right]\left(u^r(x)\hat{\tau} + u^\tau(x)\hat{r}\right), && \text{(5.37d)}
\end{aligned}$$

where $\Delta x_\perp$ was defined in Eq. (5.18). While the points x_+ and x_- are on the freeze-out surface by construction, the midpoint x, in general, is not. The displacement between the midpoint and the freeze-out surface is, however, small when the typical range of the correlator is much shorter than the typical curvature radius of the freeze-out surface. We can use an argument similar to the one preceding Eq. (5.18) to simplify the calculation by neglecting the difference between the correlator at the actual midpoint and the correlator at the point on the freeze-out surface given by

$$x \equiv \tau_f(\alpha)\hat{\tau}(\eta) + r_f(\alpha)\hat{r}(\varphi) \tag{5.38}$$

where $\alpha \equiv (\alpha_+ + \alpha_-)/2$. Henceforth, we shall use x to denote the on-hypersurface approximation (5.38) to the actual midpoint. Again, neglecting the effect of the curvature and linearizing in $\Delta\eta$, $\Delta\varphi$ and $\Delta\alpha = \alpha_+ - \alpha_-$, the projection of the separation vector $\Delta x_\perp$ from Eq. (5.37d) onto the hyperplane normal to the four-vector u can be approximated as

$$\Delta x_\perp \quad \approx \quad n \cdot u \, \Delta\alpha \, \hat{\alpha}_\perp + \tau_f \, \Delta\eta \, \hat{\eta} + r_f \Delta\varphi\hat{\varphi} \,, \tag{5.39}$$

where u is the 4-velocity of the fluid at the point x, the vector n is defined in Eq. (5.35), and we have introduced a spacelike unit vector

$$\hat{\alpha}_\perp \equiv u^r \hat{\tau} + u^\tau \hat{r} \,.$$

The vectors $\hat{\alpha}_\perp$, $\hat{\eta}$ and $\hat{\varphi}$ form a basis in the hyperplane perpendicular to the four-vector u given by Eq. (5.36) (the equal-time hyperplane in the rest frame of the fluid at the point x.)

With all of this notation established, we can now take a step toward making the expression Eq. (5.14) for the squared variance of the multiplicity of species A that we have derived above as our central result more explicit, writing it as

$$\left\langle (\delta N_A)^2 \right\rangle_\sigma = \int d\alpha_+ \, \tau_+ d\eta_+ \, r_+ d\varphi_+ \int d\alpha_- \, \tau_- d\eta_- \, r_- d\varphi_- \, (n \cdot J_A)_+ \, (n \cdot J_A)_- \, Z^{-1} \tilde{\phi}(x, \mathbf{\Delta x}_\perp) \, , \tag{5.40}$$

where $\mathbf{\Delta x}_\perp$ is a three-vector whose components in the $\hat{\alpha}_\perp$, $\hat{\eta}$, φ basis are given by Eq. (5.39) and $(n \cdot J_A)_\pm \equiv n(x_\pm) \cdot J_A(x_\pm)$, where n is given by Eq. (5.35).

The integral in Eq. (5.15) expressed in Bjorken coordinates takes the form

$$J_A(x_\pm) = \frac{d_A \, m_A}{T} \int_{y_{\min}}^{y_{\max}} \frac{dy}{2\pi} \int_0^{2\pi} d\phi \int_{p_{T,\min}}^{p_{T,\max}} \frac{p_T dp_T}{(2\pi)^2} \, \langle f_A(x_\pm, p) \rangle \, \frac{p}{p \cdot u(x_\pm)} \, , \tag{5.41}$$

where we used Eq. (5.2). The Cartesian coordinates in the lab frame of the particle four-momentum are given by

$$p = (m_T \cosh y, p_T \cos \phi, p_T \sin \phi, m_T \sinh y) \tag{5.42}$$

in terms of the particle rapidity y and transverse mass $m_T \equiv \sqrt{p_T^2 + m^2}$.

5.4 Analytical calculations in a Bjorken scenario

In Section. (4.3), we solved the relaxation equation for $\phi_{\mathbf{Q}}$ in a Bjorken symmetric background and studied how conservation and critical slowing down affects $\phi_{\mathbf{Q}}$ during its evolution. In this Section, we'll chose an isothermal surface and allows the system to freeze-out into particles via the prescription detailed above.

We begin by noting that in the Bjorken scenario we have the following expressions for x and $\Delta x_\perp$ at $\tau = \tau_f$:

$$\begin{aligned} x &= \tau_f \cosh \Delta\eta\, \hat{\tau} + x_T && \text{(5.43a)} \\ \Delta x_\perp &= \Delta x = 2\tau_f \sinh \frac{\Delta\eta}{2}\, \hat{\eta} + \Delta x_T\,. && \text{(5.43b)} \end{aligned}$$

Eqs. (5.43) are exact for two points x_+ and x_- on the freeze-out hypersurface and can be obtained by substituting $u^\tau = 1$, $u^r = 0$, $\tau = \tau_f$ and $\Delta\tau = 0$ in Eqs. (5.37). We have used x_T and Δx_T to denote the transverse parts of x and $\Delta x_\perp$, namely their projections onto the plane spanned by $\hat{r}$ and $\hat{\varphi}$. Note that because points on the freeze-out surface, including x_+ and x_-, all have the same τ in the Bjorken scenario, $\Delta x_\perp = \Delta x$ in this setting and Eq. (5.40) need not be corrected as described around Figure 32.

Next, we note that the $\tilde{\phi}$ that arises in the expression (5.40) that we wish to evaluate is the inverse Wigner transform of $\phi_{\mathbf{Q}}$, see Eq. (5.8). In the Bjorken scenario, this transform takes the form

$$\tilde{\phi}(x, \mathbf{\Delta x}) \;=\; \int \frac{d\mathbf{Q}_{\perp} dQ_{\eta}}{(2\pi)^3} e^{i2Q_{\eta}\tau_f \sinh\frac{\Delta\eta}{2} + i\mathbf{Q}_{\perp}\cdot\mathbf{\Delta x_T}} \phi_{\mathbf{Q}}(\tau_f \cosh\Delta\eta) \tag{5.44}$$

where $Q_{\eta} \equiv Q \cdot \hat{\eta}$ and $\mathbf{Q}_{\perp} \equiv \mathbf{Q} - Q_{\eta}\hat{\eta}$. Note that since points on the freeze-out hypersurface all have the same τ in the Bjorken scenario, the expression for the two-point correlator of σ between two points on the freeze-out hypersurface given by Eq. (5.19) does not receive the correction described following that equation. Note that $\phi_{\mathbf{Q}}$ that enters Eq. (5.44) is obtained by solving Eq. (4.10), as discussed in Section 4.3. Later in this Section, we shall need the formal solution to Eq. (4.10) that satisfies the initial conditions (4.11); it is given by

$$\phi_{\mathbf{Q}}(\tau) \;=\; \bar{\phi}_{\mathbf{Q}}(T_i)e^{-\int_{\tau_i}^{\tau} \Gamma(Q\xi(\tau^{'}))\, d\tau^{'}} + \int_{\tau_i}^{\tau} e^{-\int_{\tau^{''}}^{\tau} \Gamma(Q\xi(\tau^{'}))\, d\tau^{'}} \Gamma(Q\xi(\tau^{''}))\, \bar{\phi}_{\mathbf{Q}}(T(\tau^{''}))\, d\tau^{''} \tag{5.45}$$

The functional form for the evolution of temperature $T(\tau)$, which also determines $\xi(\tau)$ through Eq. (4.9), can be obtained from the condition

$$\tau s(T(\tau)) = \tau_i s(T(\tau_i)) \tag{5.46}$$

that follows from the isentropic nature and Bjorken symmetry of the flow and that must be satisfied for all $\tau_i < \tau < \tau_f$. And, we employ the equation of state $s(T)$ from Ref. [128] that we describe briefly in Appendix C.

With these preliminaries in place, we now substitute Eq. (5.44) into Eq. (5.40) and integrate over $d\mathbf{x_T}$, $d\boldsymbol{\Delta}\mathbf{x_T}$ and $d\mathbf{Q}_\perp$, obtaining

$$\langle \delta N_A^2 \rangle_\sigma \;=\; g_A^2\, A_\perp\, \tau_f^2 \int_{-\infty}^{\infty} d\eta \int_{-\infty}^{\infty} d\Delta\eta\, I_A\left(\eta_+, \eta_-\right) \int \frac{dQ_\eta}{2\pi} e^{i2Q_\eta \tau_f \sinh\frac{\Delta\eta}{2}}\, \phi_{\mathbf{Q}_\parallel}\left(\tau_f \cosh \Delta\eta\right)\,, \tag{5.47}$$

where we have defined $\mathbf{Q}_\parallel \equiv Q_\eta \hat{\eta}$, where $A_\perp$ is the transverse area in the plane spanned by $\hat{r}$ and $\hat{\varphi}$, and where we have defined

$$I_A(\eta_+, \eta_-) \equiv n(\eta_+) \cdot J_A(\eta_+)\, n(\eta_-) \cdot J_A(\eta_-)\,.$$

Upon explicit evaluation, this function is given by

$$I_A(\eta_+, \eta_-) = \int_{y_{\min}}^{y_{\max}} dy_+ \int_{y_{\min}}^{y_{\max}} dy_- F_A(y_+ - \eta_+) F_A(y_- - \eta_-) \tag{5.48}$$

where

$$F_A(y_\pm - \eta_\pm) \equiv \frac{d_A\, m_A}{T_f} \frac{dy}{2\pi} \int_{m_{T,\min}}^{m_{T,\max}} \frac{m_T dm_T}{2\pi} e^{-\frac{m_T \cosh(y_\pm - \eta_\pm)}{T_f}}\,. \tag{5.49}$$

Upon specifying $m_{T,\mathrm{min}} = m_A$ and choosing $m_{T,\mathrm{max}} = \infty$ and $y_{\mathrm{min}} = -y_{\mathrm{max}}$, F_A is given by

$$F_A(x) = d_A \frac{m_A}{T_f} \int_{m_A}^{\infty} \frac{m_T dm_T}{(2\pi)^2} e^{-\frac{m_T \cosh x}{T_f}} \tag{5.50a}$$

$$= d_A m_A (2\pi)^{-2} \mathrm{sech}^2 x \, \left(m_A \cosh x + T_f\right) \, e^{-\frac{m_A \cosh x}{T_f}} \, . \tag{5.50b}$$

Using the expressions above, Eq. (5.47) can be evaluated directly, numerically. However, to elucidate its main features we ignore the subleading corrections due to the curvature of the freeze-out hypersurface and assume that $m_A \gg T$, in both cases as discussed in Section 5.3.3. This allows us to make the following approximations:

$$\phi_{\mathbf{Q}_\parallel}\left(\tau_f \cosh \Delta\eta\right) \approx \phi_{\mathbf{Q}_\parallel}(\tau_f) \tag{5.51a}$$

$$F_A(\eta_\pm) \approx d_A m_A^2 (2\pi)^{-2} \mathrm{sech}\, \eta \, e^{-\frac{m_A}{T_f}\left[\cosh \eta \pm \frac{\sinh \eta}{2} \Delta\eta + \frac{\cosh \eta}{8} \Delta\eta^2\right]} \tag{5.51b}$$

The assumption $m_A \gg T$ has allowed us to simplify Eq. (5.51b) by expanding only the exponential term in F_A as a function of $\Delta\eta$ and not its prefactor. We have verified by explicit calculation that this assumption is well justified for protons. With the above simplifications, after defining $\Delta y \equiv y_+ - y_-$ and redefining the variables η and $\Delta\eta$ according to $\eta \to \eta - (y_+ + y_-)/2$ and $\Delta\eta \to \Delta\eta - \Delta y$, Eq. (5.47) becomes

$$\begin{aligned} &\langle \delta N_A^2 \rangle_\sigma \\ &\approx g_A^2 T_f A_\perp \tau_f^2 \int_{-\infty}^{\infty} d\eta \int_{-\infty}^{\infty} d\Delta\eta F_A(\eta+) F_A(\eta_-) \int_{-y_{\mathrm{max}}}^{y_{\mathrm{max}}} dy_+ \int_{-y_{\mathrm{max}}}^{y_{\mathrm{max}}} dy_- \int \frac{dQ_\eta}{2\pi} e^{iQ_\eta \tau_f (\Delta\eta + \Delta y)} \phi_{\mathbf{Q}_\parallel}(\tau_f) \, . \end{aligned} \tag{5.52}$$

This explicit expression for the observable measure of the fluctuations $\langle \delta N_A^2 \rangle_\sigma$ is the first main result of this Section.

5.4.1 Multiplicity fluctuations and their rapidity correlator

Upon substituting the solution to Eq. (4.10) into Eq. (5.52), or rather its inverse Fourier transform $\tilde{\phi}$, into Eq. (5.40), we can now calculate the square variance of multiplicity fluctuations $\left\langle \delta N_A^2 \right\rangle$. In the simplified setup that we are employing in this Section, we can go one step farther and exploit Bjorken boost invariance to compute explicit results for the rapidity correlator defined as

$$C_A(y_+, y_-) \;=\; \left\langle \frac{dN_A}{dy} \right\rangle^{-1} \left\langle \delta \frac{dN_A}{dy_+} \delta \frac{dN_A}{dy_-} \right\rangle_\sigma . \tag{5.53}$$

(In the next Section where we employ a more realistic hydrodynamic solution, we shall only compute $\left\langle \delta N_A^2 \right\rangle$, not C_A.) The correlator C_A measures the correlations between the multiplicity of particle species A at rapidities y_+ and y_- and can be determined similarly to Eq. (5.40) in terms of $\phi_{\boldsymbol{Q}}$ or its inverse Fourier transform $\tilde{\phi}(\boldsymbol{\Delta x}_\perp)$. For the idealized Bjorken scenario, some of the integrals in Eq. (5.40) (e.g., over transverse coordinates) can be taken analytically. In order to make even further analytical progress we shall consider the case of particles with mass much bigger than the temperature, $m_A \gg T$. This is an adequate approximation for protons and will allow us to perform an additional integral analytically in that case. We shall *not* use this approximation in the next Section, where we shall anyway be doing the analogous integrals numerically, but it will be helpful here to make the result and its general features more explicit.

Upon inspection of the result (5.52), we see that the two point rapidity space correlator occurring in $C_A(\Delta y)$ is given by

$$\left\langle \delta \frac{dN_A}{dy_+} \delta \frac{dN_A}{dy_-} \right\rangle_\sigma \approx g_A^2 T_f A_\perp \tau_f^2 \int_{-\infty}^{\infty} d\eta \int_{-\infty}^{\infty} d\Delta\eta F_A(\eta+) F_A(\eta_-) \int \frac{dQ_\eta}{2\pi} e^{iQ_\eta\, \tau_f(\Delta\eta+\Delta y)} \phi_{\mathbf{Q}_\parallel}(\tau_f) \tag{5.54}$$

$$\approx \quad \frac{1}{8\pi^{7/2}} g_A^2\, d_A^2\, Z^{-1} m_A^{7/2} T_f^{1/2}\, A_\perp\, \tau_f^2 \int d\eta\, \mathrm{sech}^{5/2}\,\eta\, e^{-\frac{2m_A \cosh\eta}{T_f}} \int \frac{dQ_\eta}{2\pi}\, e^{iQ_\eta \tau_f \Delta y}\, e^{-\frac{Q_\eta^2 \tau_f^2 T_f}{m_A \cosh\eta}}\, \phi_{\mathbf{Q}_\parallel}(\tau_f)\,. \tag{5.55}$$

The implications of Eq. (5.55) are discussed below. We see that in the simplified setup of this Section in which the fluid is translation invariant in the transverse directions, the modes that contribute in Eq. (5.55) are those whose $\mathbf{Q}$ is directed along the $\hat{\eta}$ direction. Also, the effect of the last Gaussian factor in the Q_η integral in Eq. (5.55) is to limit the range of that integral to values of order

$$Q_\eta \lesssim \left(\tau_f \sqrt{\frac{T_f}{m_A \cosh\eta}} \right)^{-1} . \tag{5.56}$$

The fact that the characteristic wavenumber Q of the fluctuations responsible for the correlations at freeze-out is not zero (despite considering a volume of fluid that is infinite in extent in rapidity η in this idealized scenario) is ultimately due to the fact that in the laboratory frame the fireball is not spatially homogeneous: the fluid velocity varies over a longitudinal distance of order τ_f due to the longitudinal expansion. One can check that taking $\tau_f \to \infty$ results in only $Q = 0$ contributing. However, the characteristic Q_η is not just $1/\tau_f$, but rather depends on the mass of the particle. This is due to the thermal smearing, or "blurring", which translates

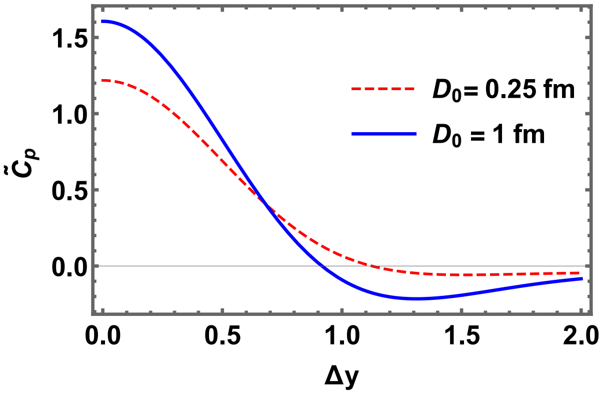

Figure 33: Normalized proton multiplicity correlator $\tilde{C}(\Delta y)$ for protons from Eq. (5.58) as a function of the rapidity gap Δy in the Bjorken scenario for two choices of the diffusion parameter D_0.

spatial Bjorken rapidity η into kinematic particle rapidity y [111, 213]. As we are assuming that $m_A \gg T$, the factor $\sqrt{T_f/(m_A \cosh\eta)}$ in Eq. (5.56) is the typical thermal rapidity of the particles at temperature $T_f/\cosh\eta$, which can be understood as the freeze-out temperature "red-shifted" by longitudinal expansion.

The final piece that we need in order to compute C_A is the denominator in Eq. (5.53). By explicit calculation starting from Eq. (5.1), in the Bjorken scenario in which we are working $\langle dN_A/dy\rangle$ is given by:

$$\left\langle \frac{dN_A}{dy} \right\rangle = d_A\, A_\perp\, \tau_f\, (2\pi)^{-2} \int_{m_A}^{\infty} m_T^2 dm_T \int d\eta\, e^{-\frac{m_T \cosh\eta}{T_f}} \cosh\eta\,. \tag{5.57}$$

Substituting Eqs. (5.55) and (5.57) into Eq. (5.53), we can evaluate C_A which, because of boost invariance, is a function of Δy only. In Figure 33, we plot our results for C_A, normalized by the its non-critical value at $\Delta y = 0$, $C_A^{\rm nc}(0)$, which we estimate by substituting $\phi_{\boldsymbol{Q}} = Z\,T\,(Q^2 + \xi_0^{-2})^{-1}$ into Eq. (5.55), where ξ_0 is, as before, the correlation length away from critical point defined in Eq. (4.9). That is, we define the ratio that we have plotted in Figure 33 as

$$\tilde{C}_A(\Delta y) \quad \equiv \quad \frac{C_A(\Delta y)}{C_A^{\rm nc}(0)}\,. \tag{5.58}$$

Since $\xi_{\rm max} > \xi_0$, critical fluctuations make the ratio $\tilde{C}_A(0)$ larger than unity.

In Figure 33 we also illustrate the dependence of the rapidity correlations on the value of the diffusion parameter D_0. Stronger diffusion (larger D_0) enhances the effects of the critical point in $\phi_{\boldsymbol{Q}}$, as we saw in Figure 22. This enhancement is reflected in the corresponding particle rapidity correlations, as seen in Figure 33 at small Δy. Due to conservation laws, anticorrelations at large Δy are also enhanced. (For any value of D_0, the consequence of conservation is that the integral under the curve $\tilde{C}_A$ over all separations Δy is independent of D_0 and is determined by the initial fluctuations. This means that when we increase D_0 and see $\tilde{C}_A(\Delta y)$ growing at small Δy, it must also become more negative at large Δy.) However, unlike the direct effect of diffusion on the *range* of the spatial correlator $\tilde{\phi}$ in 22b, the effect on the *range* of $C(\Delta y)$ in Figure 33 is minor. This is due to the fact that this range is mostly determined by the effect of thermal rapidity smearing or “blurring” [111].

Now, the variance of the particle multiplicity $\langle \delta N_A^2 \rangle_\sigma$ that in the general case takes the form (5.40) can in this Bjorken scenario be obtained from the rapidity correlator $C(\Delta y)$ by integration over the rapidity window $y_\pm \in (-y_{\max}, y_{\max})$, i.e.,

$$\frac{\left\langle \delta N_A^2 \right\rangle_\sigma}{\langle N_A \rangle} = \int_{-2y_{\max}}^{2y_{\max}} d\Delta y \left(1 - \frac{|\Delta y|}{2y_{\max}}\right) C(\Delta y)\,. \tag{5.59}$$

Upon using our expression for $C(\Delta y)$ from Eqs. (5.53), (5.55), and (5.57) and using the fact that boost invariance implies that $\langle N_A \rangle = 2y_{\max} \langle dN_A/dy \rangle$, we now obtain the result

$$\begin{aligned} \langle \delta N_A^2 \rangle_\sigma \quad \approx \quad & \frac{1}{2}\, Z^{-1}\, m_A^{7/2}\, T_f^{1/2}\, \pi^{-7/2}\, g_A^2\, d_A^2\, A_\perp\, \tau_f^2 \int d\eta \,\mathrm{sech}^{5/2}\,\eta\, e^{-\frac{2m_A \cosh\eta}{T_f}} \quad \times \\ & \int \frac{dQ_\eta}{2\pi}\, \frac{\sin^2\left(\tau_f\, Q_\eta\, y_{\max}\right)}{\tau_f^2 Q_\eta^2}\, e^{-\frac{Q_\eta^2 \tau_f^2 T}{m_A \cosh\eta}}\, \phi_{\mathbf{Q}_\parallel}(\tau_f) \end{aligned} \tag{5.60}$$

The Δy dependence of $C(\Delta y)$ translates into the rapidity acceptance window dependence of $\langle \delta N_A^2 \rangle_\sigma$, which has been discussed in the literature, e.g., in Ref. [111], and will not be discussed here.

5.4.2 Dependence of dynamical fluctuations on proximity of freeze-out to the critical point

In this chapter we focus on the magnitude of fluctuations and their dependence on the proximity of freeze-out to the critical point as well as on the diffusion parameter D_0. The proximity of the freeze-out to the critical point is controlled by two major factors. One is the proximity of the trajectory to the critical point, which in our analysis is quantified by ξ_{max} – the maximum equilibrium correlation length along the expansion trajectory on the phase diagram.

The larger the value ξ_{max}, the closer the system has passed to the critical point on its way to freeze-out. The smallest values of $\xi_{max} \approx \xi_0$ correspond to trajectories furthest away from the critical point, on the edge of the critical region. In Figure 34, we plot the normalized critical contribution to the squared variance of the proton multiplicity from Eq. (5.24) on ξ_{max}. One can see the effect of the critical point on the fluctuations at freeze-out increases as the trajectory approaches the critical point (as ξ_{max} increases).

The other factor controlling the proximity of the critical point to the freeze-out is the freeze-out temperature T_f. The higher the freeze-out temperature is (while still below critical temperature), i.e., the earlier the freeze-out occurs and the closer the freeze-out is to the critical point. Correspondingly, the fluctuations at freeze-out increase with ξ_{max} as well as with T_f in Figure 34.

The results in Figure 34 also demonstrate that the magnitude of the critical point signatures crucially depends on dynamics. As we already discussed in Figure 22 and Figure 33, stronger diffusion (larger D_0) leads to larger effects of the critical point. We can see this in Figure 34 by comparing the plots for two different values of D_0. In addition, as a result of the conservation laws the magnitude of fluctuations is significantly smaller than the equilibrium expectation at freeze-out, as can be seen by comparing to panel (c) in Figure 34. It is also apparent from this comparison that, while the equilibrium expectation in panel (c) depends very strongly on the freeze-out temperature (the higher the temperature the closer is the freeze-out to the critical point, since $T_c > T_f$), the dynamical predictions in panels (a) and (b) of Figure 34 are much less sensitive to the freeze-out temperature. This can be understood as a “memory” effect: the fluctuations at freeze-out encode some information about fluctuations at earlier times because they do not have time to equilibrate, an effect which is enhanced by critical slowing down. This has the consequence that even though freeze-out happens at a temperature below that of the critical point, effects of critical fluctuations persist until freeze-out and yield signatures in observables. The magnitude of such memory effects depends on the value of D_0. We see that the results of our out-of-equilibrium calculation at freeze-out illustrated in panels (a) and (b) of Figure 34 arise via an interplay between the suppression of fluctuations relative to their magnitude in equilibrium due to conservation and the enhancement of fluctuations arising from memory effects.

In panel (c) of Figure 34, the equilibrium magnitude of fluctuations saturates as ξ_{max} increases and the trajectory followed by the cooling plasma gets closer to the critical point. This happens because the freeze-out occurs at a temperature T_f below the critical point, where $\xi(T_f) < \xi_{max}$, and as the trajectory approaches the critical point, ξ_{max} diverges while $\xi(T_f)$ goes to some (large) constant value which is independent of ξ_{max} as $\xi_{max} \to \infty$. The saturation is less pronounced in panels (a) and (b) because of dynamical memory effects: the blue curve "remembers where it was" at earlier times.

To summarize some central results of this Section: (i) in the Bjorken scenario considered here there is a clear suppression in the normalized fluctuation measure $\tilde{\omega}_A$ at freeze-out for the values of D_0 considered, because the slow modes are fluctuations of a conserved quantity; (ii) in Model H dynamics, $\tilde{\omega}_A$ is less sensitive to the freeze-out temperature than would be the case if the fluctuations were in equilibrium throughout. In the next Section, we shall investigate how radial flow modifies these and other observations.

5.4.3 Importance of low Q modes

Eq. (5.56) and hence Eq. (5.55) signify the importance lower $\mathbf{Q}$ modes in describing the critical effects. In this Subsection, we shall demonstrate that the low Q modes of $\phi_{\mathbf{Q}}$ contribute the most to the variance of particle multiplicities, $\left\langle \delta N_A^2 \right\rangle_\sigma$ by direct comparison. We shall expand $\phi_{\mathbf{Q}}$, given by Eq. (5.45), in powers of $\mathbf{Q}$ to $O(\mathbf{Q}^2)$ and compare the result for $\left\langle \delta N_A^2 \right\rangle_\sigma$ that we obtain starting from this expansion to the result that we obtain starting from the full form of $\phi_{\mathbf{Q}}$. We denote the polynomial expansion for $\phi_{\mathbf{Q}}$ to quadratic order by

$$\phi_{\mathbf{Q}} \approx \phi^{(0)} + \phi^{(2)} Q^2 \tag{5.61}$$

where

$$\phi^{(0)} = Z\, T_f\, \xi^2(T_i) \tag{5.62a}$$

$$\phi^{(2)} = -Z\, T_f\, \xi^4(T_i) + 2D_0\xi_0\, Z\, T_f \int_{\tau_i}^{\tau_f} d\tau \left(\xi(T(\tau)) - \frac{\xi^2(T_i)}{\xi(T(\tau))} \right) . \tag{5.62b}$$

The expression (5.61) is a good approximation to $\phi_{\mathbf{Q}}$ for its low-Q modes, as we illustrate in 35a.

Upon making the low-Q approximation and working to order Q^2 as in Eq. (5.61), we can perform the Q_η integral in Eq. (5.55), obtaining

$$\begin{aligned}
&\left\langle \delta\frac{dN_A}{dy_+}\delta\frac{dN_A}{dy_-}\right\rangle_\sigma \\
&\approx \frac{g_A^2 d_A^2 A_\perp \tau_f Z^{-1} m_A^4}{(2\pi)^4}\int\frac{d\eta}{\cosh^2\eta}e^{-\frac{2m_A\cosh\eta}{T_f}\left(1+\frac{\Delta y^2}{8}\right)}\left[\phi^{(0)}+\frac{2T_f m_A\cosh\eta-\Delta y^2 m_A^2\cosh^2\eta}{4\tau_f^2T_f^2}\phi^{(2)}\right].
\end{aligned} \tag{5.63}$$

In 35b, we compare $\tilde{C}_p(\Delta y)$ (defined via Eqs. (5.53,5.57,5.58)) obtained from $\left\langle \delta\frac{dN_A}{dy_+}\delta\frac{dN_A}{dy_-}\right\rangle_\sigma$ computed without making a low-Q approximation, namely Eq. (5.55), which is plotted as the solid curves in 35b, to that computed upon working only to order Q^2, namely Eq. (5.63), which is plotted as the dashed curves in 35b. The qualitative, even semi-quantitative, agreement between them indicates that the low-Q modes contribute significantly to the variance of particle multiplicities.

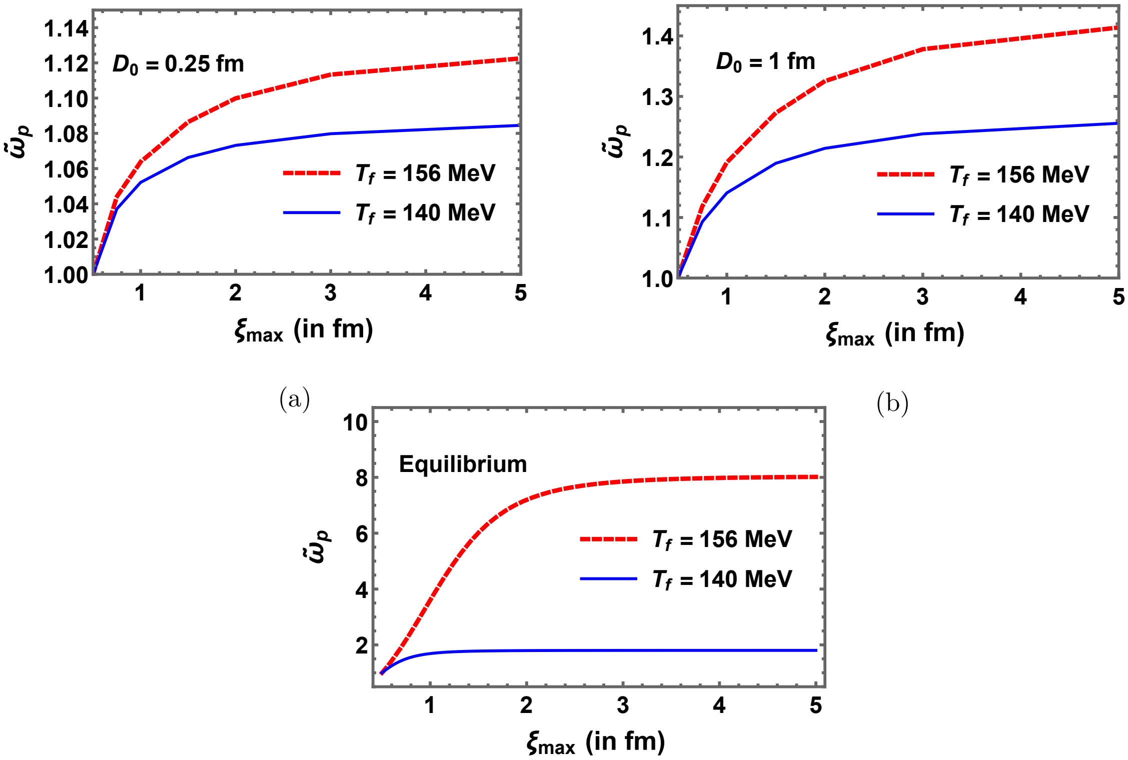

(a) (b)

(c)

Figure 34: The normalized fluctuation measure for protons, Eq. (5.24), as a function of ξ_{max}, the maximum value of the equilibrium correlation length achieved along the system trajectory. Panels (a) and (b) correspond to different diffusion strengths, quantified by D_0, while red and blue curves correspond to different freeze-out temperatures. Panel (c) shows the result that would have been obtained under the assumption that fluctuations are in equilibrium at freeze-out.

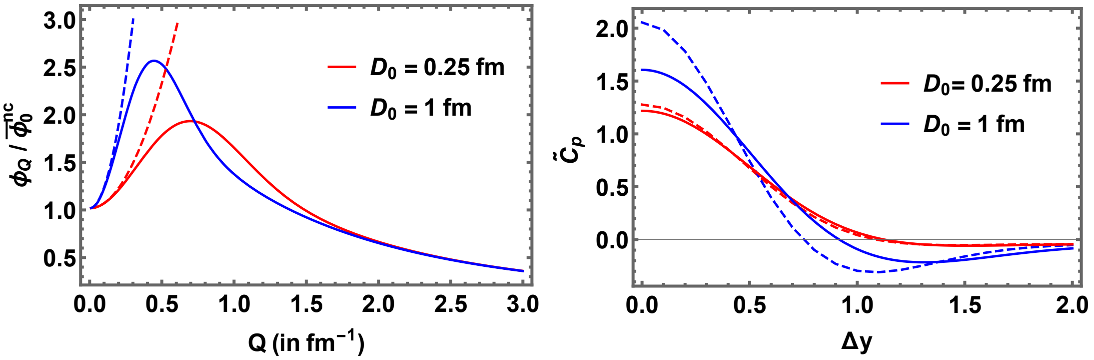

(a) ϕ at freeze-out

(b) $\tilde{C}(\Delta y)$ for protons

Figure 35: Panel (a): Normalized ϕ as a function of Q evolved according to Model H dynamics with two values of D_0, plotted at freeze-out $\tau = \tau_f$, corresponding to an equilibrium temperature of $T_f(\tau_f) = 140\,\text{MeV}$. The solid and dashed curves were obtained from the full solution (5.45) for $\phi_{\mathbf{Q}}$ and its truncated polynomial expansion (5.61) respectively. Panel (b): Normalized fluctuation measure observable (rapidity space correlator) for protons $\tilde{C}_p(\Delta y)$ obtained with the full form (solid) and truncated form (dashed) of $\phi_{\mathbf{Q}}$. The qualitative and even semi-quantitative agreement between the same colored curves in the right plot indicates that the low-Q modes contribute significantly to the variance of particle multiplicities. In obtaining these plots, $\xi_{\max}$ was set to 3 fm and the fluctuations at $\tau_i = 1\,\text{fm}$ were initialized to their equilibrium value at $\tau = \tau_i = 1$ fm with $T_i(\tau_i) = 235\,\text{MeV}$.

5.5 Freeze-out of the simulation of Hydro+ from Section. (4.4))

In this section, we will apply the freeze-out procedure discussed in Section 5.3, to extract the two-point correlations of particle multiplicities from the Hydro+ simulation presented in [128] and Section. (4.4) which have not been frozen out yet.

5.5.1 Variances of particle multiplicities with Model H dynamics

We shall obtain the variance of the multiplicity of particles of species A from $\tilde{\phi}$ by employing the general expressions in Eqs. (5.40) and (5.41). As we did in Section 5.4, we shall compute ω_A, the ratio of the variance of the multiplicity of species A to its mean, see Eq. (5.23). We can obtain the mean multiplicity of protons and pions for a rapidity acceptance window $[-y_{\max}, y_{\max}]$ and acceptance cuts in p_T using the Cooper-Frye formula,

$$\langle N_A \rangle = d_A \int dS_\mu \int_{-y_{\max}}^{y_{\max}} \frac{dy}{2\pi} \int_{p_{\mathrm{T,min}}}^{p_{T,\max}} \frac{p_T\, dp_T}{2\pi} \int_0^{2\pi} \frac{d\phi}{2\pi}\, e^{-\frac{p\cdot u}{T_f}}\, p^\mu \,, \tag{5.64}$$

employing the flow velocity $u(x)$ profile and freeze-out hypersurface for the simulation from Ref. [128] illustrated in Figure 23. The fluctuation measure ω_A is then obtained by taking the ratio of Eq. (5.40) and Eq. (5.64). In this Subsection, we present the results for the normalized fluctuation measure $\tilde{\omega}_A$ as defined in Eq. (5.24) as a function of $\xi_{\max}$ (which measures the proximity of the trajectory in the phase diagram is to the critical point) for protons and pions obtained with our two choices of D_0 and with our isothermal freeze-out scenario with two different choices of the freeze-out temperature T_f, as discussed above. In all calculations, we choose the acceptance cuts $p_T\, \epsilon\, (0.4\,\mathrm{GeV},\ 2\,\mathrm{GeV})$ and $y_{\max} = 1$. As already discussed above,

$\tilde{\omega}_A$, should not depend on the acceptance. This is explicitly the case in equilibrium and this remains approximately the case in our simulations.

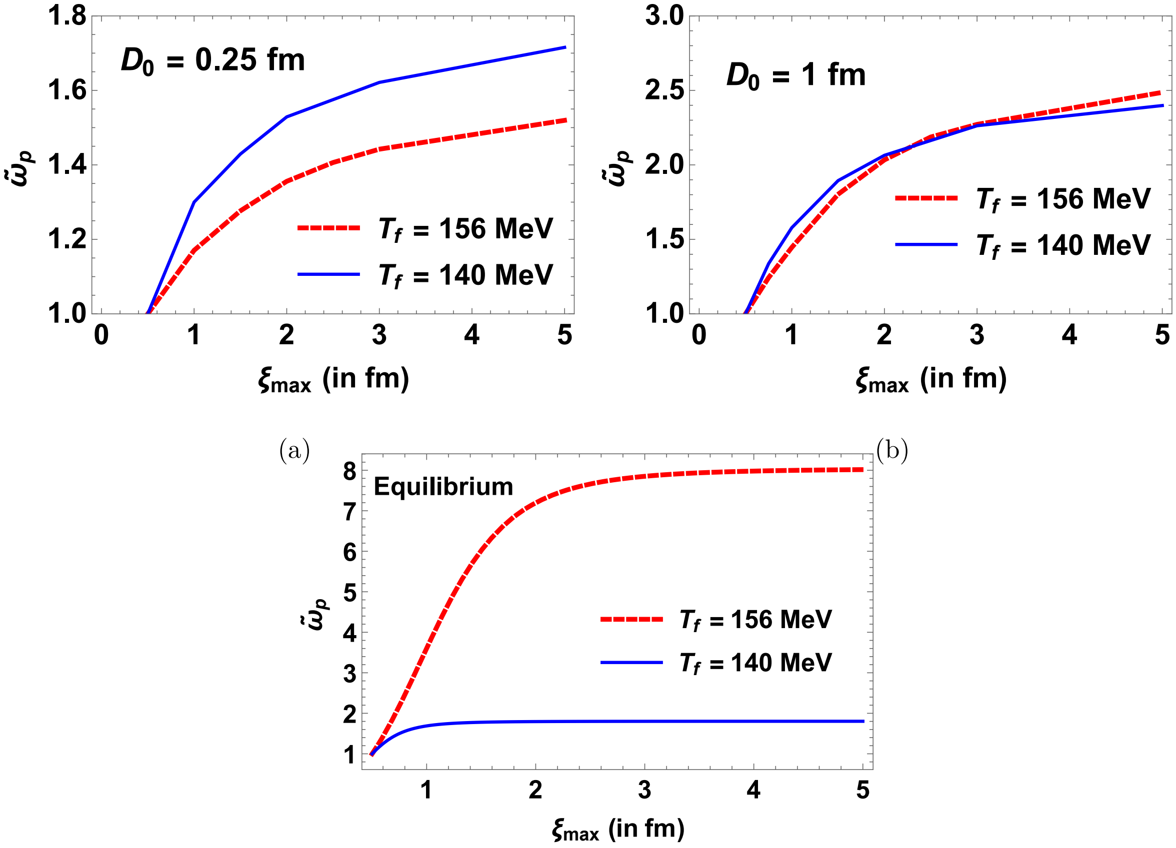

(a)

(b)

(c)

Figure 36: Normalized measure of the fluctuations in proton multiplicity, $\tilde{\omega}_p = \frac{\omega_p}{\omega_p^{\text{nc}}}$, as a function of the maximum equilibrium correlation length along the system trajectory, which is to say as a function of how closely the trajectory passes the critical point. As $D_0 \to \infty$, the $\tilde{\omega}_p$'s approach their equilibrium values shown in panel (c).

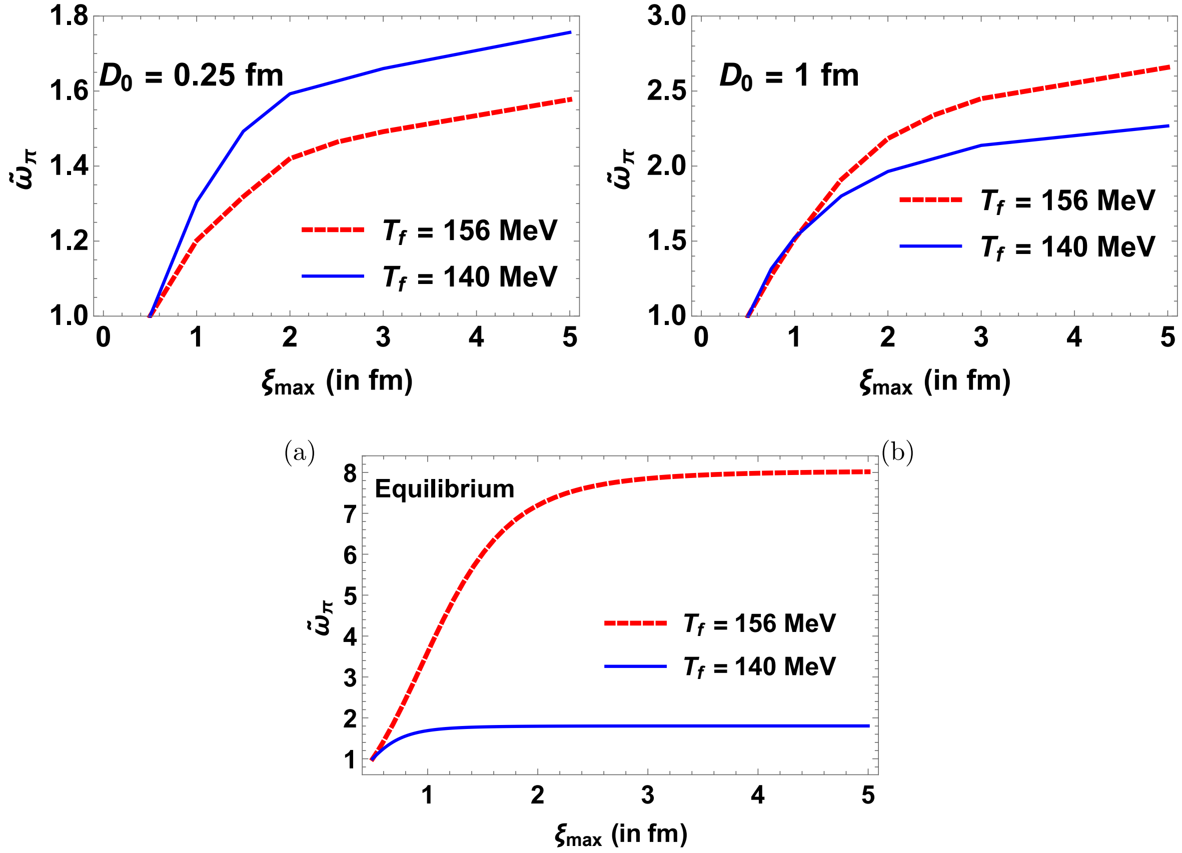

(a) (b)

(c)

Figure 37: Normalized measure of the fluctuations in pion multiplicity, $\tilde{\omega}_\pi = \frac{\omega_\pi}{\omega_\pi^{\text{nc}}}$, as a function of the maximum equilibrium correlation length along the system trajectory, which is to say as a function of how closely the trajectory passes the critical point. As $D_0 \to \infty$, the $\tilde{\omega}_\pi$'s approach their equilibrium values shown in panel (c). The definition of the normalized measure of fluctuations $\tilde{\omega}$ is such that it is species-independent in equilibrium, meaning that panel (c) here is identical to panel (c) in Figure 36.

We present our final results for the normalized fluctuation measure for protons and pions, $\tilde{\omega}_p$ and $\tilde{\omega}_\pi$, in Figure 36 and Figure 37. These results demonstrate that for trajectories passing closer to the critical point (i.e., for trajectories with larger $\xi_{\max}$) the magnitude of fluctuations is larger, as we have already seen in Figure 34 for the Bjorken expansion scenario. Again as in the Bjorken scenario, the magnitude of the effect depends on the rate of the diffusive relaxation of the fluctuations controlled by parameter D_0. The conservation laws (i.e., "memory") lead to significant suppression of the magnitude of fluctuations compared to the prediction based on the assumption that fluctuations have enough time to equilibrate. (The equilibrium predictions are shown in Figure 36(c) and Figure 37(c).) When the diffusion is slower or in other words, the value of the diffusion parameter D_0 is smaller, the stronger is the suppression.

We also compare the magnitude of fluctuations for the same value D_0 and ξ_{max}, but for two different freeze-out temperatures. Equilibrium consideration leads to a prediction of larger fluctuations at higher freeze-out temperature, since the higher temperature freeze-out occurs closer to the critical point. However, non-equilibrium effects not only suppress the magnitude of the fluctuations relative to the equilibrium prediction but also introduce memory effects that substantially reduce the decrease in the magnitude of the fluctuations that occurs between $T = 156$ MeV and the lower freeze-out temperature $T_f = 140$ MeV. This makes the fluctuations obtained upon assuming a freeze-out temperature of $T_f = 140$ MeV much more similar in magnitude to those that would be obtained if $T_f = 156$ MeV than is the case in equilibrium. So much so, in fact, that, depending on the choice of the parameters such as D_0, it is even possible to find larger fluctuations at $T_f = 140$ MeV than would have been obtained at the higher freeze-out temperature $T_f = 156$ MeV, see Figure 36(a) and Figure 37(a)! This effect arises because, as we have already discussed, the fluctuations continue to grow even after the system has passed the critical point, as long as their value is below the equilibrium, as can be seen in Figure 25. This effect is not seen in the Bjorken scenario in Section 5.4 because the drop of the temperature during the one-dimensional expansion is much slower than the temperature drop in this case where there is radial expansion also. As a result, in the Bjorken scenario the freeze-out temperatures are reached at somewhat later times, after the non-equilibrium fluctuations have begun to decrease. For the same reason, in our more realistic calculations in this Section this effect disappears for larger values of D_0 which yields faster relaxation of fluctuations toward equilibrium, see Figure 36(b) and Figure 37(b).

5.5.2 Variance of particle multiplicities with Model A dynamics

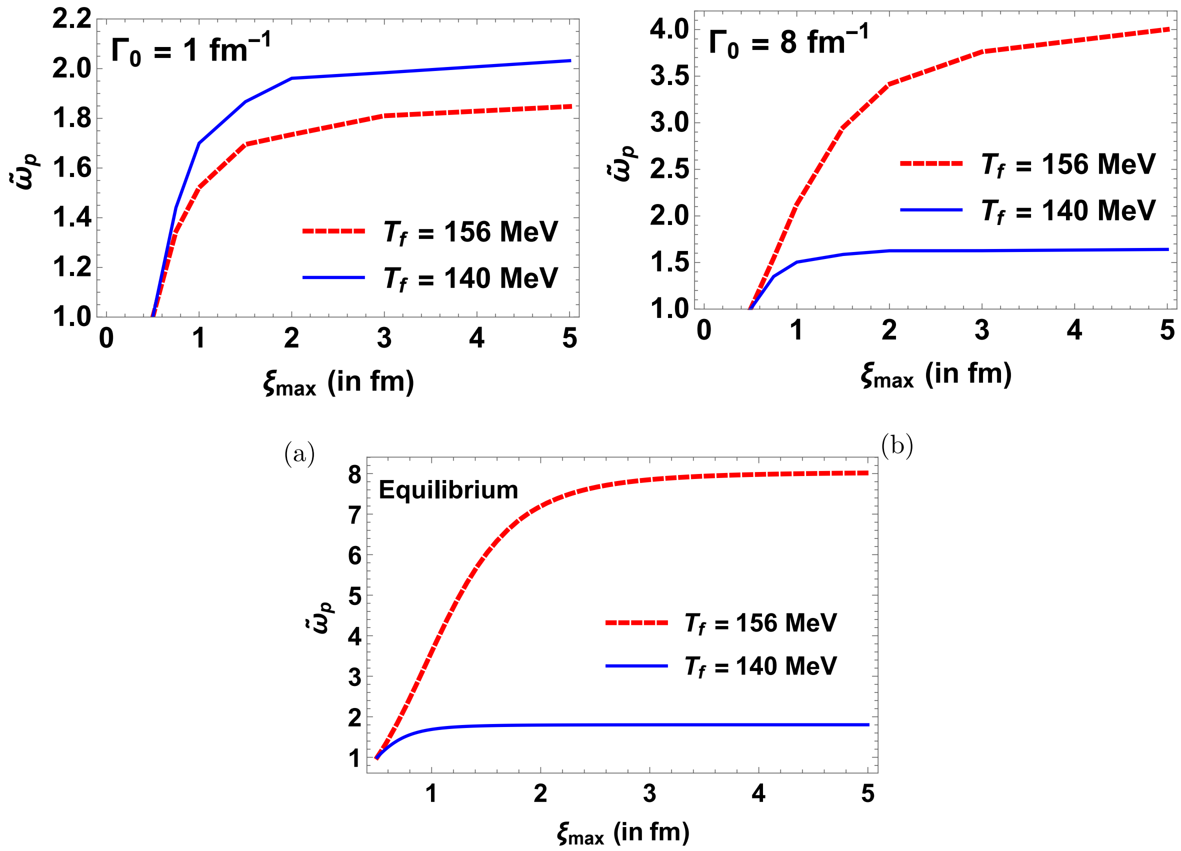

(a)

(b)

(c)

Figure 38: Normalized measure of the fluctuations in proton multiplicity, $\tilde{\omega}_p = \frac{\omega_p}{\omega_p^{\text{nc}}}$, as a function of the maximum equilibrium correlation length along the system trajectory, which is to say as a function of how closely the trajectory passes the critical point. As $\Gamma_0 \to \infty$, the $\tilde{\omega}_p$'s approach their equilibrium values shown in panel (c).

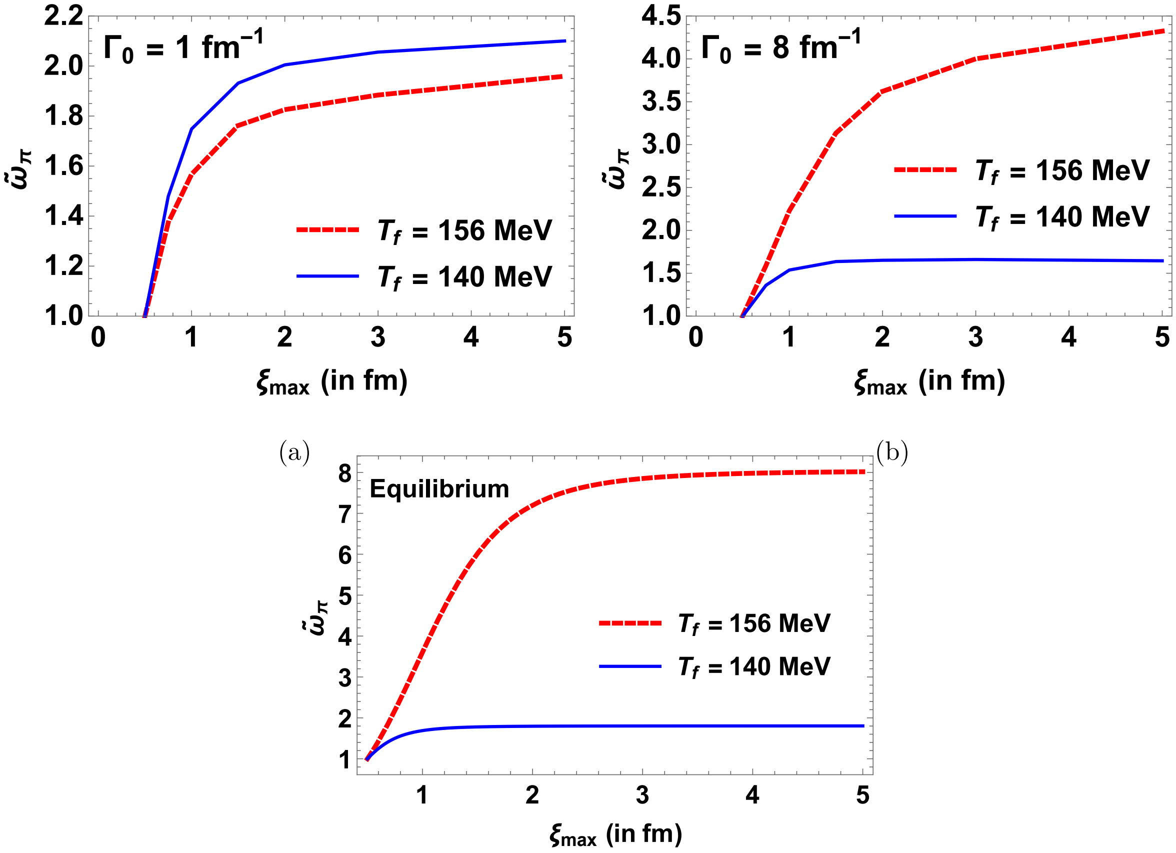

(a)

(b)

(c)

Figure 39: Normalized measure of the fluctuations in pion multiplicity, $\tilde{\omega}_\pi = \frac{\omega_\pi}{\omega_\pi^{\rm nc}}$, as a function of the maximum equilibrium correlation length along the system trajectory, which is to say as a function of how closely the trajectory passes the critical point. As $\Gamma_0 \to \infty$, the $\tilde{\omega}_\pi$'s approach their equilibrium values shown in panel (c).

As in the previous subsection, we compute and plot the normalized fluctuation measure for protons and pions, $\tilde{\omega}_p$ and $\tilde{\omega}_\pi$ with Model A dynamics, in Figure 38 and Figure 39. As in Figure 36 and Figure 37, these results demonstrate that for trajectories passing closer to the critical point (i.e., larger ξ_{max}) the magnitude of fluctuations is larger. As in Section 4.4, the magnitude of the effect depends on the rate of the relaxation of the fluctuations, controlled by parameter Γ_0. We see that for large enough values of Γ_0, eg. 8 fm^{-1}, the proton and pion fluctuations are able to come reasonably close to their equilibrium values. This means that sensitivity of the magnitude of fluctuations to the freeze-out temperature increase as D_0 is made that large. The differences that we analyzed in Section 5.5 result from the charge and energy conservation.

5.6 Summary and Outlook

In this study, a new method has been proposed to link hydrodynamic fluctuations that occur during the expansion and cooling of QGP droplets in heavy ion collisions to fluctuations in observable particle multiplicities. The approach focuses on critical fluctuations, which are the most singular, slowest, and most out-of-equilibrium modes of fluctuations near the critical point. On the particle side of the freeze-out, these fluctuations are matched by introducing a new critical scalar field called σ, which couples to observable particles. The field is considered an effective critical field, a precursor of the critical point, and has the same quantum numbers as the σ meson. The study establishes a connection between the fluctuations of this field and observable fluctuations in particle multiplicities by linking them to the Hydro+ variable $\phi_{\boldsymbol{Q}}$ [116], which describes the non-equilibrium evolution of fluctuations during the hydrodynamic stage of the collision. Prior estimates of the observable consequences of critical fluctuations assumed that the σ field and its fluctuations remain in equilibrium near the critical point due to the lack of an approach to describing their non-equilibrium evolution.

Our approach builds upon the Cooper-Frye freeze-out [142], which is a well-established method for translating hydrodynamic degrees of freedom into particle distributions. However, the Cooper-Frye procedure only deals with event-averaged single-particle quantities such as multiplicities and spectra of each hadron species, and thus cannot account for the freeze-out of fluctuations or correlations. Our more comprehensive freeze-out procedure extends this method to enable the translation or matching of hydrodynamic and fluctuation degrees of freedom described by Hydro+ to particle multiplicities and their fluctuations.

We have shown how our generalized freeze-out procedure can be applied in practice by considering two scenarios. The first scenario is a simplified case where we have analyzed the Hydro+ description of boost-invariant Bjorken expansion without any transverse expansion. This simple case allows for analytical calculations and provides useful insights. In the second scenario, we have performed a numerical Hydro+ simulation of a more realistic situation that includes both boost invariance and azimuthal symmetry and also incorporates transverse radial expansion, similar to the scenario analyzed in Ref. [128] and described in Chapter. (4).

The results from both examples showed that the non-equilibrium fluctuations were significantly suppressed compared to their equilibrium values for the parameter values considered. Additionally, we also noted that while the *equilibrium* fluctuations sensitively depend on how far below the critical temperature, the freeze-out occured, this sensitivity is almost eliminated by non-equilibrium ("memory") effects, see Figure 34, Figure 36 and Figure 37.

The Hydro+ variable $\phi_{\boldsymbol{Q}}$ is used to describe the magnitude of the fluctuations at different wavevectors $\boldsymbol{Q}$, and the characteristic value of Q that determines the magnitude of the multiplicities after freeze-out is influenced by various factors, including the inhomogeneity of the expanding fluid, radial flow, thermal velocity spread of the particles, and acceptance window in rapidity. (In the case of the Bjorken scenario, can describe analytically as in Eq. (5.56).) This characteristic Q value is typically small compared to microscopic scales and is of the order of $1/\tau_f$, where τ_f is the freeze-out time (see Eq. (5.56)). Because fluctuations at small Q are suppressed by conservation laws and the smallness of the characteristic Q relevant for freeze-out, the fluctuations are also suppressed relative to their equilibrium values, which is also a form of a "memory" effect resulting from out-of-equilibrium dynamics.

Our study focused on Gaussian measures of fluctuations. The higher, non-Gaussian, cumulants are more sensitive to the proximity of the critical point [56, 105]. It is, therefore, important to generalize our freeze-out procedure to higher-order cumulants. At this stage, the most straightforward generalization of our procedure leads to a formula for Non-Gaussian freeze-out given by Eq. (5.16). In Chapter. (6), we'll learn that this can be improved further and and more general freeze-out expression that applies equally for fluctuations not related to critical point can be derived using the maximum-entropy principle.

We could generalize to the cross-correlation of different particle species, as was done in Ref. [105] for equilibrium fluctuations in a straightforward manner. We leave an investigation of how best to combine measurements of different (cross-)correlations so as to optimize the sensitivity to critical fluctuations while reducing dilution of their effects by backgrounds to future work. We'll discuss some qualitative differences that arise for cross-correlations in Chapter. (6).

We have focused on the *dependence* of the observable fluctuations on the proximity of the critical point, either by varying ξ_{max}, which corresponds to varying freeze-out μ_B via changing collision energy $\sqrt{s}$ (see Figure 19), or by varying the freeze-out temperature (for the same trajectory). We also studied the dependence on the (thus far unknown) value of the diffusion parameter D_0. In order to illustrate these dependencies, we chose to present our results using normalized variables which did not depend on the *absolute* magnitude of the effect. In order to predict the absolute magnitude one would have to know the equation of state, i.e., the parameter

Z in Eq. (5.9) which determines the absolute strength of the singularity. Also, one would have to determine the couplings g_A of hadrons to the critical collective field σ. These couplings are, of course, also related to the equation of state and it would be interesting to make this relation more explicit. This relation will be derived in the Chapter. (6).

The freeze-out prescription that we proposed freezes-out only the leading singular and the slowest non-hydrodynamic mode. More quantitative studies on the hydrodynamic side are needed to determine the relevance of the next slowest modes , corresponding to fluctuations of pressure and hydrodynamic velocities. In Chapter. (6), we will discuss a very general freeze-out procedure based on the maximum entropy freeze-out that naturally generalizes the procedure developed here to fluctuations of all. hydrodynamic variables

We emphasize that our study focuses on fluctuations and freeze-out on the crossover side of the critical point (as shown in Figure 19). However, it is important to recognize that understanding what happens on the other side, where the first-order phase transition occurs, is also of great interest and significance. This is a challenging domain, already at the level of hydrodynamics, and is beyond the scope of our current work.

CHAPTER 6

MAXIMUM-ENTROPY FREEZE-OUT OF HYDRODYNAMICS WITH FLUCTUATIONS

This Chapter is based on the published work in [5] which I co-authored with my advisor, M.Stephanov.

In this Chapter, we'll develop a very general freeze-out procedure for hydrodynamics with fluctuations, called maximum entropy freeze-out that exemplifies the probabilistic nature of the freeze-out process. The application of this freeze-out procedure is not restricted to the critical region where critical fluctuations are dominant, as it was for the freeze-out procedure discussed in chapter. (5).

Freeze-out happens because the finite sized fireball in the strongly interacting phase becomes dilute enough after a finite time (at about $\sim 10\,\mathrm{fm}$) such that hydrodynamics is not a good description anymore. This weakly interacting gas of hadrons whose composition can be described by a set of particle distribution functions (one for each meson and baryon whose production is kinematically allowed), which interact amongst each other only through formation of resonances and/or other mean-field interactions that are modeled appropriately. In the hydrodynamic description (without fluctuations and viscous effects), the only degrees of freedom are the fields corresponding to the energy, momenta and charge densities. On the other hand, hadrons with different masses and spins also carry momenta. The process of going from hydrodynamic description to hadron gas thus involves increasing the "number" of degrees of freedom. As we shall see in Section. (6.1), there are infinitely many sets of hadron gas distribution functions that match with the hydrodynamic description. In order to convert the outcome of a hydrodynamical simulation into a prediction for the particle distribution functions, one needs a freeze-out procedure. While in principle, freeze-out is a stochastic process, the freeze-out procedure may be thought of as a well-motivated ansatz for choosing one hadron gas distribution function that satisfies the matching conditions.

The freeze-out procedure that is often used in comparison with experiments is the Cooper-Frye freeze-out (with additional modifications to involve viscous effects). Such an ansatz has been successful in describing experimental data at higher energies . As we shall see in Section (6.2), Cooper-Frye prescription follows from the principle of maximum entropy if the hydrodynamic EoS matches with the EoS of the gas model on the space-time hypersurface where the matching is done and if higher point correlations are in equilibrium. Our original contribution in this thesis work is a generalization of the maximum entropy freeze-out procedure to freeze-out of fluctuations of hydrodynamic densities. In order to do this, we need to introduce a generalization for the thermodynamic entropy to a non-equilibrium scenario. We use the connection between entropy and and information theory in Section (6.3), to introduce the concept of relative entropy, which measures the excess information in the state relative to the specified equilibrium state. This quantity is mathematically similar to the n-particle irreducible action discussed in quantum field theory literature [214]. In Section. (6.4) and Section. (6.5), we propose the maximum entropy freeze-out of Gaussian and non-Gaussian fluctuations respectively, according to which the particle distribution that is realized at freeze-out is the one which maximizes the relative entropy and agrees with all the information provided by the hydrodynamic description. In Section. (6.6), we discuss how the relevance of factorial cumulants in heavy-ion collisions naturally emerges from the maximum entropy freeze-out. Maximum entropy freeze-out as we show, also provides a solution to the long standing question of how to subtract the lower order self correlations from a higher point correlations to obtain the non-trivial correlations that appear at that order. In Section. (6.7), we show how maximum entropy freeze-out can be applied to freeze-out critical fluctuations to relate the effective coupling g_As(which were treated as unknown in the previous works and in Chapter (5)) between hadron fields and the critical field σ to the QCD EoS. In Section. (6.8), in the limit of large number of events, the probability of observing the maximally entropic distribution becomes a delta function in the space of distributions. This argument justifies its applicability in heavy-ion collisions where large number of events are recorded to obtain the probability distribution of particles. We summarize the main results from the chapter in Section. (6.9).

6.1 Matching conditions at freeze-out that follow from conservation

Hydrodynamics prescribes evolution equations for densities of conserved quantities, energy, momenta and charge expressed in terms of the stress-energy tensor, $T^{\mu\nu}$ and the charge currents J_i^μs as follows

$$\partial_\mu T^{\mu\nu} = 0\,, \quad \partial_\mu J_i^\mu = 0 \tag{6.1}$$

$T^{\mu\nu}$ is a second rank anti-symmetric tensor and J_is are four vectors. i can refer to baryon charge, electric charge, strangeness etc. For simplicity, we consider only one conserved charge, so that we can ignore the subscript i. The discussion can be generalized for a scenario with multiple charges in a straightforward manner. One also needs constitutive relations to close the system of equations. These are commonly expressed as:

$$T^{\mu\nu}_{\text{hyd}} = \epsilon u^\mu u^\nu - (p_{\text{eq}} + \Pi)\Delta^{\mu\nu} + \pi^{\mu\nu}\,, \quad J^\mu_{\text{hyd}} = n u^\mu + \Delta J^\mu \tag{6.2}$$

where

$$\Delta^{\mu\nu} = g^{\mu\nu} - u^\mu u^\nu \tag{6.3}$$

projects a vector onto the subspace normal to the velocity vector, u. ϵ and n are the energy density and charge density in the local rest frame of the fluid. $\pi^{\mu\nu}$ and ΔJ^μ represent the viscous and fluctuating corrections to stress-energy tensor and charge currents respectively.

There are $4+1$ (4 for four momenta and 1 for number of conserved charges) independent fields in the ideal hydrodynamic description, ϵu^μ, n. These need to be matched to their counterparts in the description of the gas on the three-dimensional freeze-out hypersuface, $\mathcal{S}$. In addition the EoS , $p(\epsilon, n)$ on the hydrodynamic description also has to be matched with the pressure of the hadron gas. The stress energy tensor in the kinetic description at the freeze-out is expressed in terms of the particle distribution functions f_A in the local rest frame of the fluid. A refers to the particle species labels. Following Cooper-Frye, this can be written as [142]:

$$T^{\mu\nu}_{\text{kin}}(x) = \sum_A \int Dp_A \, f_A(x) \, p^\mu_A \, p^\nu_A \tag{6.4a}$$

$$J^{\mu}_{\text{kin}}(x) = \sum_A q_A \int Dp_A \, f_A(x) \, p^\mu_A \tag{6.4b}$$

where q_A is the charge of the particle. In ideal hydrodynamics the matching conditions can be written as ([1]):

$$\epsilon = \sum_A \int d^3\mathbf{k}_A \, f_A(x, \mathbf{k}_A) \, E_A(x) \tag{6.5a}$$

$$n = \sum_A \int d^3\mathbf{k}_A \, f_A(x, \mathbf{k}_A) \tag{6.5b}$$

---

[1] Technically speaking, there is no freeze-out in ideal hydrodynamics, where the system is infinite in extent and perfectly homogeneous. In this case, we are simply matching a macroscopic description given in terms of conserved quantities to a (more) microscopic description of the gas.

$$3p(\epsilon, n) = \sum_A \int d^3\mathbf{k}_A \, f_A(x, \mathbf{k}_A) \, \frac{\mathbf{k}_A^2}{E_A(x)} \tag{6.5c}$$

$$0 = \sum_A \int d^3\mathbf{k}_A \, f_A(x, \mathbf{k}_A) \, \frac{\mathbf{k}_A}{E_A(x)} \tag{6.5d}$$

where $E_A = u \cdot p_A$ is the energy density of the particle kind A in the local rest frame at x.

The right hand side of Eq. 6.5a and Eq. 6.5b imply conservation of energy-momentum density and number density in the local rest frame of the fluid. Eq. (6.5c) enforces that the pressure $p(\epsilon, n)$ is the same in the hydrodynamic and the gas descriptions. Eq. 6.5d means that the average particle momenta points along the direction of the fluid velocity at each point on the freeze-out hypersurface (in the absence of viscous corrections to $T_{\mu\nu}$ and J_μ). Notice, that for each $x \in \mathcal{S}$, there are only six equations in (6.5), whereas the number of unknown variables is infinite since $f_A s$ are functions in momenta. Therefore, there are infinitely many solutions to these set of equations. This allows for multiple freeze-out scenarios. In Section. (6.8), we'll argue that the most probable scenario corresponds to Maximum Entropy freeze-out when the number of events are large, as in typical HICs. In what follows we'll further assume that the freeze-out happens in a thermodynamic regime where the hydrodynamic EoS, $p(\epsilon, n)$ matches with the hadron resonance gas EoS. This has been shown to be the case for typical freeze-out temperatures in references [215]. This simplification implies that matching condition given by Eq. (6.5c) is already satisfied when the other five conditions(Eq. (6.5a,6.5b,6.5d)) are met. [1]

---

[1] Note that one can use maximum entropy freeze-out even without this simplification. In that case, the matching condition Eq. (6.5c) becomes an independent condition which also needs to be satisfied.

It is customary to define f_A as the particle distribution function in the local rest frame. f_A can be defined with a different frame choice, matching conditions can be more generally expressed as:

$$\epsilon(x)u_\mu(x) = \int_A f_A(x)\, p^\mu_A \tag{6.6a}$$

$$n(x) = \int_A q_A\, f_A(x) \tag{6.6b}$$

where $\int_A$ refers to a sum over all particles and the appropriate Lorentz invariant measure in momentum space.

In nature, there are few systems that are infinite and stay in global equilibrium. The more interesting ones are described by local equilibrium and finite in extent and their dynamics can be described by low-energy effective description given by viscous hydrodynamics expressed as an expansion in gradients of the stress-energy tensor $T_{\mu\nu}$ and currents J_μs. Freezing out a system described by viscous hydrodynamics requires additional matching conditions for the gradients of these conserved densities [216]. There have been various studies to modify the Cooper-Frye freeze-out prescription to include viscous corrections in the literature [198, 216–222]. Moreover, since hydrodynamics is a coarse grained description after integrating over the high-momentum modes, a legitimate hydrodynamic description inevitably involves fluctuations whose magnitudes are related to the viscous corrections via the fluctuation-dissipation theorem. There have been attempts to develop appropriate procedure for fluctuation freezeout of two-point fluctuations, starting from [130] and freeze-out procedures catered specifically for critical fluctuations [2]. But to our knowledge, a more general approach which applies to higher point fluctuations and fluctuations of arbitrary origin has not been developed prior to this work presented in this chapter which is already published in [5].

In stochastic hydrodynamics, local energy density, number density and fluid density are fluctuating quantities. Following [121], we denote the stochastic quantities with a breve (eq. $\breve{\epsilon}$) and the mean quantities without a breve (eg. ϵ). The difference between these quantities, i.e the fluctuations is denoted with a delta preceding the quantity, (eq. $\delta\epsilon = \breve{\epsilon} - \epsilon$). We define the collective notation $\Psi^a\,, a \in \{1, \dots 5\}$:

$$\Psi^a \quad = \quad \epsilon u^a \,\text{for}\, a \in \{1, \dots 4\}\,, \quad \Psi^5 = n \tag{6.7}$$

We define the n-point connected correlations of $\delta\Psi^a$ by H:

$$H_{ab\dots}(x_a, x_b \dots) = \langle \delta\Psi^a(x_a)\delta\Psi^b(x_b)\dots\rangle_c \tag{6.8}$$

On the gas side, let $\breve{f}_A = f_A + \delta f_A$ be the fluctuating particle distribution function for particle species A. We denote their n-pont connected correlations by Gs,

$$G_{AB\dots} = \langle \delta f_A(x_A)\delta f_B(x_B)\dots\rangle_c \tag{6.9}$$

We also define P_A^a as:

$$P_A^a = p^a \delta^3(x_a - x_A)\, a \in \{1, \dots 4\}\,, \quad P_A^5 = q_A \delta^3(x_a - x_A) \tag{6.10}$$

where $p^\mu\, \mu \in \{1, \dots 4\}$ is the four-momenta of the particle and q_A is its conserved charge. Eqs. (6.6) are true on an event by event basis. We'll use these equations to write matching conditions for n-point correlations of $\delta(\epsilon u^\mu)$ and δn at freeze-out where the EoS between the hydrodynamic and gas descriptions are assumed to be equivalent. In terms of the notations defined above, the matching conditions for k-point correlation functions would read as follows:

$$H_{ab\dots k}(x_a, \dots x_k) = \int_{A,B\dots K} G_{AB\dots K} P_A^a P_B^b \dots P_K^k \tag{6.11}$$

where $\int_A$ involves integration over x_A, p_A and summation over all species A.

For example, the matching condition for the two point correlations functions of the conserved densities in the hydrodynamic and kinetic descriptions locally given by Eq. (6.11) can be expanded as:

$$\langle \delta(\epsilon(x_A) u^\mu(x_A)) \delta(\epsilon(x_B) u^\nu(x_B)) \rangle = \int_{\tilde{A}} \int_{\tilde{B}} G_{AB}\, p_A^\mu\, p_B^\nu \tag{6.12a}$$

$$\langle \delta(\epsilon(x_A) u^\mu(x_A)) \delta n(x_B)) \rangle = \int_{\tilde{A}} \int_{\tilde{B}} G_{AB}\, p_A^\mu q_B \tag{6.12b}$$

$$\langle \delta n(x_A) \delta n(x_B)) \rangle = \int_{\tilde{A}} \int_{\tilde{B}} G_{AB} q_A q_B \tag{6.12c}$$

We denote the gas correlation functions in equilibrium as $\bar{G}$ and $\bar{H}$ as follows:

$$\bar{H}^{ab}(x_A, x_B) = \int_{\tilde{A}} \int_{\tilde{B}} \bar{G}_{AB}\, P_A^a\, P_B^b \tag{6.13}$$

Since the EoSs are the same in hydrodynamic and gas descriptions, $\bar{H}$ can be either calculated using Eq. (6.13) or directly from the susceptibilities obtained using the hydrodynamic EoS.

6.2 Cooper-Frye freeze-out Vs Maximum Entropy freeze-out

In this Section, we will discuss maximum-entropy freeze-out of ordinary hydrodynamics (without considering fluctuations) and compare it with the commonly employed Cooper-Frye freeze-out procedure. The gas of particles at freeze-out is characterized by the set of particle distribution functions $f_A(x_A, p_A)$ where variable A labels the particle species with four-momentum p_A and the space-time coordinate x_A on the freeze-out hyper-surface.The entropy density for such a non-interacting gas of particles may be expressed as:

$$S_0 = \int_x \int_A S_A \tag{6.14}$$

where S_A is the entropy density of a system of non-interacting particles described by a single particle distribution function is given by:

$$S_A = -f_A \log f_A + \frac{1+\theta_A f_A}{\theta_A} \log(1+\theta_A f_A) \tag{6.15}$$

When $\theta_A = \pm 1$, it corresponds to the quantum gas which obeys Bose-Einstein/Fermi-Dirac statistics. In the limit of $\theta_A \to 0$, it corresponds to a classical Boltzmann gas. To match the hydrodynamic description (locally in equilibrium) given locally by average energy density $\epsilon(x)$, fluid velocity $u_\mu(x)$ and baryon charge density $n(x)$ with a kinetic description for a system of non-interacting particles, one needs to maximize the entropy density S given by Eq. (6.14) subject to the constraints of energy-momentum and charge conservation.

$$\epsilon u^\mu(x) = \int d^3p\, p^\mu f(x, p_A) \tag{6.16a}$$

$$n(x) = \int d^3p\, f_A(x, p_A) \tag{6.16b}$$

We introduce Lagrange parameters β_μ, α, and extremize the following functional subject to constraints of conservation.

$$S_{\{\boldsymbol{\beta},\alpha\}} = S_0 - \beta_\mu \left(\epsilon u^\mu - \int_A p^\mu f(x_A, p_A)\right) + \alpha \left(n - \int_A f_A(x_A, p_A)\right) \tag{6.17}$$

This gives,

$$\frac{\delta S_{\{\boldsymbol{\beta},\alpha\}}}{\delta f_A} = -\log \frac{f_A}{1 + \theta_A f_A} - \beta_\mu p^\mu + \alpha = 0 \tag{6.18}$$

whose solution is given by,

$$f_A = \left(e^{\beta \cdot p - \alpha} - \theta_A\right)^{-1} \tag{6.19}$$

After substituting Eq. (6.19) in Eq. (6.16), β_μ and α are determined to be $T = -(\beta.u)$ and $\mu = T\alpha$ where T and μ are the temperature and chemical potential of the gas corresponding to the local energy and number density of fluid. I.E, the maximum-entropy freeze-out of ordinary hydrodynamics, produces particles distributed according to Bose-Einstein/ Fermi-Dirac of Boltzmann distribution functions at a local temperature T and chemical potential μ determined from the local average energy and number densities at freeze-out.

Note that this is same as the Cooper-Frye freeze-out prescription described in Section. (5.1). Therefore, Cooper-Frye freeze-out coincides with the maximum entropy freeze-out when the equation of states are same between the hydrodynamic description and the Hadron Resonance Gas(HRG) description. If we freeze-out in a regime where the EoS between the two descriptions are not same, one needs to consider additional Lagrange parameters to match the pressure. In a viscous setting, the stress energy tensor has corrections due to the gradients. Therefore, one needs additional matching conditions for the gradients of these conserved densities. The maximum entropy principle with these extra matching conditions has already been utilized in freezing out viscous hydrodynamics in Ref. [216].

Cooper-Frye freeze-out cannot be employed when the two and higher point fluctuations of the hydrodynamic variables are out of equilibrium. In the Sections that follow, we'll introduce a freeze-out procedure, that generalizes the concept of maximum-entropy freeze-out to out-of-equilibrium higher point fluctuations of conserved densities. This becomes relevant when the relaxation rates of the higher point fluctuations become comparable to the expansion rate of the system. In-order to do this, we need to generalize the concept of thermodynamic entropy to entropy of out-of equilibrium fluctuations in a gas and then we maximize it subject to the matching conditions.

6.3 Entropy of fluctuations

The exponential of the entropy S_0 in a microcanonical ensemble given by Eq. (6.14) is proportional to the number of microstates of the system with given values of occupation numbers f_A of the hydrodynamic cells. In the thermodynamic (large volume) limit there is a large number of single-particle quantum states in each hydrodynamic cell and the number of possible ways to occupy these elementary quantum states is exponentially large, of order e^{S_0}. A macroscopic state is an ensemble of this exponentially large number of microscopic states with occupation numbers close to mean f_A. The values f_A are not the same in all microscopic states, but fluctuate. The magnitude of fluctuations is suppressed in the thermodynamic limit such that average over these states is fixed. If the fluctuations are in equilibrium and the mean distribution functions of each particle species is $\bar{f}_A$, then the probability distribution for f is given by (upto to a normalization factor):

$$P(f) \quad \propto \quad \exp\left[\int_C J_C f_C\right] \tag{6.20}$$

where

$$J_A = -\left(\frac{\partial S_0}{\partial f_A}\right)_{f_A=\bar{f}_A} \tag{6.21}$$

where S_0 is given in Eq. (6.14). Using this probability distribution one can calculate the expectation values $\bar{G}_{AB\ldots}$ of the fluctuation correlators in equilibrium which will depend on $\bar{f}_A$.

$$\bar{G}_{AB} = \left[\int Df_A \exp\left(S_0 + \int_C J_C f_C\right)\right]^{-1} \int \exp\left(S_0 + \int_C J_C f_C\right) \delta f_A \delta f_B \tag{6.22}$$

Note that $\exp(S_0)$ which is the number of microscopic states appears in the measure of the integration.

We can also consider states with (some of) the correlators $G_{AB\ldots}$ having specific values, not necessarily equal to $\bar{G}_{AB\ldots}$. These states must have lower entropy since more information is available about these states. To find their entropy we can consider the probability distribution perturbed by additional factor $\exp(K_{AB\ldots} f_A f_B \ldots)$, where $K_{AB\ldots}$ play the role similar to Lagrange multipliers.

$$P(f) = \exp\left(S_0[f] + \int_A J_A f_A + \frac{1}{2}\int_{AB} K_{AB} f_A f_B - W_2(J,K)\right) \tag{6.23}$$

where

$$W_2(J,K) = \int_f \exp\left(S_0[f] + \int_A J_A f_A + \frac{1}{2}\int_{AB} K_{AB} f_A f_B\right) \tag{6.24}$$

Integrating over fluctuations of f_A we can then obtain $\bar{f}_A$, $G_{AB\ldots}$, which will depend on J and $K_{AB\ldots}$s, we get the following relations:

$$\begin{aligned} C_A &= -J_A - K_{AB}\bar{f}_B \qquad (6.25) \\ G^{-1}_{AB} &= -C_{AB} - K_{AB} \qquad (6.26) \end{aligned}$$

where $C_{AB} \equiv \delta^2 S_0/(\delta f_A \delta f_B)$ and $C_A \equiv \delta S_0/\delta f_A$ are evaluated at the mean particle distribution function $\bar{f}_A$. From now on, we will use Cs to denote derivatives of thermodynamic entropy of S_0 with respect to f_As. The number of subscripts will denote the order of the derivative. Solving for K and substituting back into the probability distribution we find the joint probability distribution for f_A as well as the correlators $G_{AB\ldots}$.

$$P(f) = \exp\left(S_0[f] - \int_A (C_A + \left(G^{-1} + C\right)_{AB} \bar{f}_B) f_A - \frac{1}{2}\int_{AB} \left(G^{-1} + C\right)_{AB} f_A f_B - W_2 \right) \qquad (6.27)$$

The generalized entropy is then related to the probability distribution $P(f)$ as follows:

$$S[P] = -\int_f P(f) \log P(f) \qquad (6.28)$$

The expression for generalized entropy is similar to the von Neumann entropy used in quantum information. The calculation of the entropy of fluctuations along these lines for a two-point correlator can be found in Ref. [116], where it is also pointed out that the result mathematically resembles the 2-PI action in quantum field theory [223–227]. We we'll denote this entropy which is a function of $\bar{f}$ and G_2s by S_2. S_2 can be related to W_2 as follows:

$$S_2 = W_2(J,K) - J_A\bar{f}_A - \frac{1}{2}K_{AB}\bar{f}_A\bar{f}_B - \frac{1}{2}\mathrm{Tr}\left[K_{AC}G_{CB}\right] \tag{6.29}$$

In the saddle point approximation W_2 can be calculated as:

$$W_2(J,K) = S[\bar{f}] + J_A\bar{f}_A + \frac{1}{2}K_{AB}\bar{f}_A\bar{f}_B - \frac{1}{2}\log\det(-C-K) \tag{6.30}$$

The result is:

$$S_2 = S_1 + \frac{1}{2}\mathrm{Tr}\ \left[\log(-GC) + GC + 1\right]\ , \tag{6.31}$$

where $G \equiv G_2$. S_1 is the 1-PI effective action given by:

$$S_1 = S_0 - \frac{1}{2}\mathrm{Tr}\ \log(-C) \tag{6.32}$$

The difference $S_2 - S_1$ vanishes when G equals $-C^{-1} \equiv \bar{G}$ and can be viewed as the additional (negative) entropy of the state with additional constraints on correlators relative to the entropy of the state with correlations given simply by $\bar{G}$.

Our goal in this chapter to generalize maximum entropy freeze-out to Gaussian as well as non-Gaussian fluctuations of hydrodynamic densities. In particular, for practical applications to experiments, we need freeze-out prescriptions for atleast three and four point functions of hydrodynamic densities. In order to do this, one can proceed in a similar fashion as above i.e perturb the probability distribution function by additional factors of $\exp(K_{ABC}f_Af_Bf_C)$. etc.,

$$\begin{aligned} P(f) &= \exp\Bigg(S[f] + \int_A J_A f_A + \frac{1}{2}\int_{AB} K_{AB}f_Af_B + \frac{1}{6}\int_{ABC} K_{ABC}f_Af_Bf_C \\ &\quad + \frac{1}{24}\int_{ABCD} K_{ABCD}f_Af_Bf_Cf_D - W_4(J, K_2, K_3, K_D)\Bigg) \end{aligned} \tag{6.33}$$

where

$$\begin{aligned} W_4(J, K_2, K_3, K_D) &= \int_f \exp\Bigg(S[f] + \int_A J_A f_A + \frac{1}{2}\int_{AB} K_{AB}f_Af_B + \frac{1}{6}\int_{ABC} K_{ABC}f_Af_Bf_C \\ &\quad + \frac{1}{24}\int_{ABC} K_{ABCD}f_Af_Bf_Cf_D\Bigg) \end{aligned} \tag{6.34}$$

The n-particle irreducible entropy can then be calculated using Eq. (6.28). For an arbitrary states with all higher point fluctuations deviating from their equilibrium values, can be expressed mathematically as follows:

$$P(f) = \exp\left(-W_\infty[J, K^{(2)}, K^{(3)}, K^{(4)}, \ldots] + Jf + \frac{1}{2}K^{(2)}f^2 + \frac{1}{3!}K^{(3)}f^3 + \frac{1}{4!}K^{(4)}f^4 + \ldots\right) \tag{6.35}$$

where $J\Psi \equiv J_Af_A$, $K^{(2)}\Psi^2 \equiv K^{(2)}_{AB}f_Af_B$, $K^{(3)}\Psi^3 \equiv K^{(3)}_{ABC}f_Af_Bf_C$, $K^{(4)}\Psi^4 \equiv K^{(4)}_{ABCD}f_Af_Bf_Cf_D$ and so on. The indices represent both discrete and continuous sets of variables. The repeated indices $A, B, C\ldots$ imply summation over species and integration hydrodynamic phase space cells. The subscripts will be suppressed in some of the expressions that appear below for brevity. $W_\infty[J, K^{(2)}, K^{(3)}, K^{(4)}, \dots]$ is the normalization constant such that:

$$\int D\Psi P(\Psi) = 1 \tag{6.36}$$

i.e,

$$W_\infty[J, K^{(2)}, K^{(3)}, K^{(4)}, \dots] = \log\left[\int Df \exp\left(S_0[f] + Jf + \frac{1}{2}K^{(2)}f^2 + \frac{1}{3!}K^{(3)}f^3 + \frac{1}{4!}K^{(4)}f^4 + \dots\right)\right] \tag{6.37}$$

In order to evaluate $P(f)$, we need an expansion scheme in a small parameter so as to evaluate it in perturbation theory. There is a natural parameter that is hidden in the summations like $K^{(3)}_{ABC} f_A f_B f_C$. Note that the integration over hydrodynamic phase space cells involves summation over coarse grained spatial hydrodynamic cells. Since in the hydrodynamic limit, the length(l) of these cells are much larger than the microscopic length scales(a) in the theory, the averaging over these volumes already produces a small factor $\epsilon \equiv (a/l)^3$. This is the small parameter in which we are expanding. The expansion in this parameter is equivalent to an expansion in number of loops [214]. Below, we will discuss the calculation of S_4 upto $O(\epsilon^2)$ and in Section. (6.4) and Section. (6.5) maximize this entropy subject to constraints from matching conditions to hydrodynamics to obtain the Gs.

The n-point connected correlation functions of the deviations of f_As from its mean values $\bar{f}_A$ can be obtained using the W as follows:

$$\begin{aligned}
G_{AB} &= \left[2\frac{\partial W}{\partial K_{AB}} - \bar{f}_A\bar{f}_B\right]_{\overline{ABC}} && (6.38a)\\
G_{ABC} &= \left[6\frac{\partial W}{\partial K_{ABC}} - \bar{f}_A\bar{f}_B\bar{f}_C - G_{AB}\bar{f}_C\right]_{\overline{ABC}} && (6.38b)\\
G_{ABCD} &= \left[24\frac{\partial W}{\partial K_{ABCD}} - \bar{f}_A\bar{f}_B\bar{f}_C\bar{f}_D - 3G_{ABC}\bar{f}_D - 6G_{AB}\bar{f}_C\bar{f}_D - 3G_{AB}G_{CD}\right]_{\overline{ABCD}} && (6.38c)
\end{aligned}$$

where we have introduced the notation $\overline{}_{12\ldots n}$ (which will be repeatedly used in this chapter) to imply averaging over all permutations:

$$[\ldots]\,\overline{12\ldots n} = \frac{1}{n!}\,[\ldots]_{P_{1\ldots n}} \tag{6.39}$$

The entropy S_4 of a partial equilibrium state can be expressed as:

$$\begin{aligned}
S_4 &= -\int Df\, e^{S_0[f]+Jf+\frac{1}{2}K^{(2)}f^2+\frac{1}{3!}K^{(3)}f^3+\frac{1}{4!}K^{(4)}f^4-W_4[J,K^{(2)},K^{(3)},K^{(4)}]} \times \\
&\quad \left(Jf + \frac{1}{2}K^{(2)}f^2 + \frac{1}{3!}K^{(3)}f^3 + \frac{1}{4!}K^{(4)}f^4 - W_4[J,K^{(2)},K^{(3)},K^{(4)}]\right) && (6.40a)\\
&= W_4[J,K^{(2)},K^{(3)},K^{(4)}] - J\bar{f} - \frac{1}{2}\langle K^{(2)}f^2\rangle - \frac{1}{3!}\langle K^{(3)}f^3\rangle - \frac{1}{4!}\langle K^{(4)}f^4\rangle && (6.40b)
\end{aligned}$$

We can rewrite some of the expectation values in Eq. (6.40b) in terms of G_ns:

$$\langle K^{(2)} f^2 \rangle = K^{(2)} G_2 + K^{(2)} \bar{f}^2 \tag{6.41a}$$

$$\langle K^{(3)} f^3 \rangle = K^{(3)} G_3 + K^{(3)} \bar{f}^3 + 3K^{(3)} G_2 \bar{f} \tag{6.41b}$$

$$\langle K^{(4)} f^4 \rangle = K^{(4)} G_4 + K^{(4)} \bar{f}^4 + 4K^{(4)} G_3 \bar{f} + 6K^{(4)} G_2 \bar{f}^2 + 3K^{(4)} \left(G_2\right)^2 \tag{6.41c}$$

Substituting Eqs. (6.41) in Eq. (6.40b):

$$\begin{aligned} S_4 = {} & W_4[J, K^{(2)}, K^{(3)}, K^{(4)}] - J\bar{f} - \frac{1}{2}K^{(2)}\bar{f}^2 - \frac{1}{3!}K^{(3)}\bar{f}^3 - \frac{1}{4!}K^{(4)}\bar{f}^4 \\ & -\frac{1}{2}\left(K^{(2)} + K^{(3)}\bar{f} + \frac{1}{2}K^{(4)}\bar{f}^2\right) G_2 - \frac{1}{3!}\left(K^{(3)} + K^{(4)}\bar{f}\right) G_3 - \frac{1}{4!}K^{(4)}\left[G_4 + 3G_2^2\right] \end{aligned} \tag{6.42}$$

We can determine S_4 as a function of $\bar{f}$ and G_ns by inverting the relation between Ks and Gs obtained using Eq. (6.38). G_3 and G_4 can be expressed as sum of tree diagrams using the dressed vertices V_3 and V_4 as follows:

$$G_{ABC} = G_{AD} G_{BE} G_{CF} V_{DEF} \tag{6.43a}$$

$$G_{ABCD} = \left[G_{AE} G_{BF} G_{CH} G_{DI} V_{EFHI} + 3G_{AE} G_{BF} G_{CH} G_{DI} V_{EFJ} V_{JHI}\right]_{\overline{ABC}} \tag{6.43b}$$

The dressed vertices can be obtained as an expansion as shown in (Figure 41) in terms of classical vertices(V_{0n}) and classical propagator($\tilde{G}$) which we define in (Figure 40).

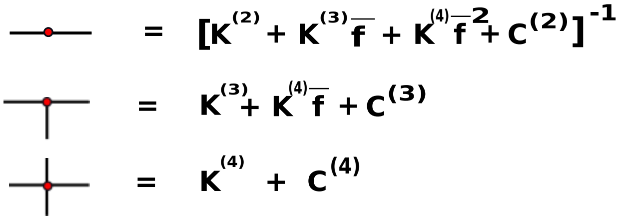

Figure 40: The symbols on the left hand side represent the classical propagator $\tilde{G}_2$, the classical vertices V_{03} and V_{04}. The RHS shows expressions for them in terms of the parameters, K that appear in Eq. (6.34) and n^{th} derivatives of S_0, denoted by $C^{(n)}$s.

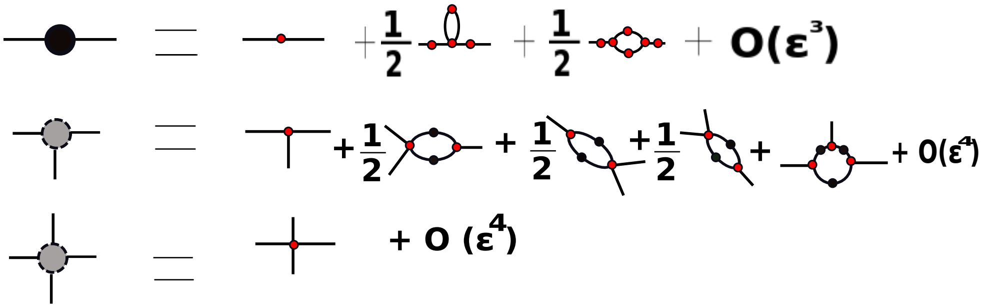

Figure 41: The black line with the solid black dot is the full propagator (G_2) which is obtained by summing an infinite set of 1PI diagrams involving the classical propagator defined in Figure 40. Similarly the dressed three point and four point vertices V_3 and V_4 (defined in Eq. (6.43))) are obtained by summing over an infinite set of 1PI diagrams involving the classical vertices. Notice that the propagators in these expansions have already been resummed and expressed in terms of the full propagator. Each of these expansions have been truncated at $O(\epsilon^4)$.

In terms of G_ns, S_4 is obtained and diagrammatically represented in Figure 42.

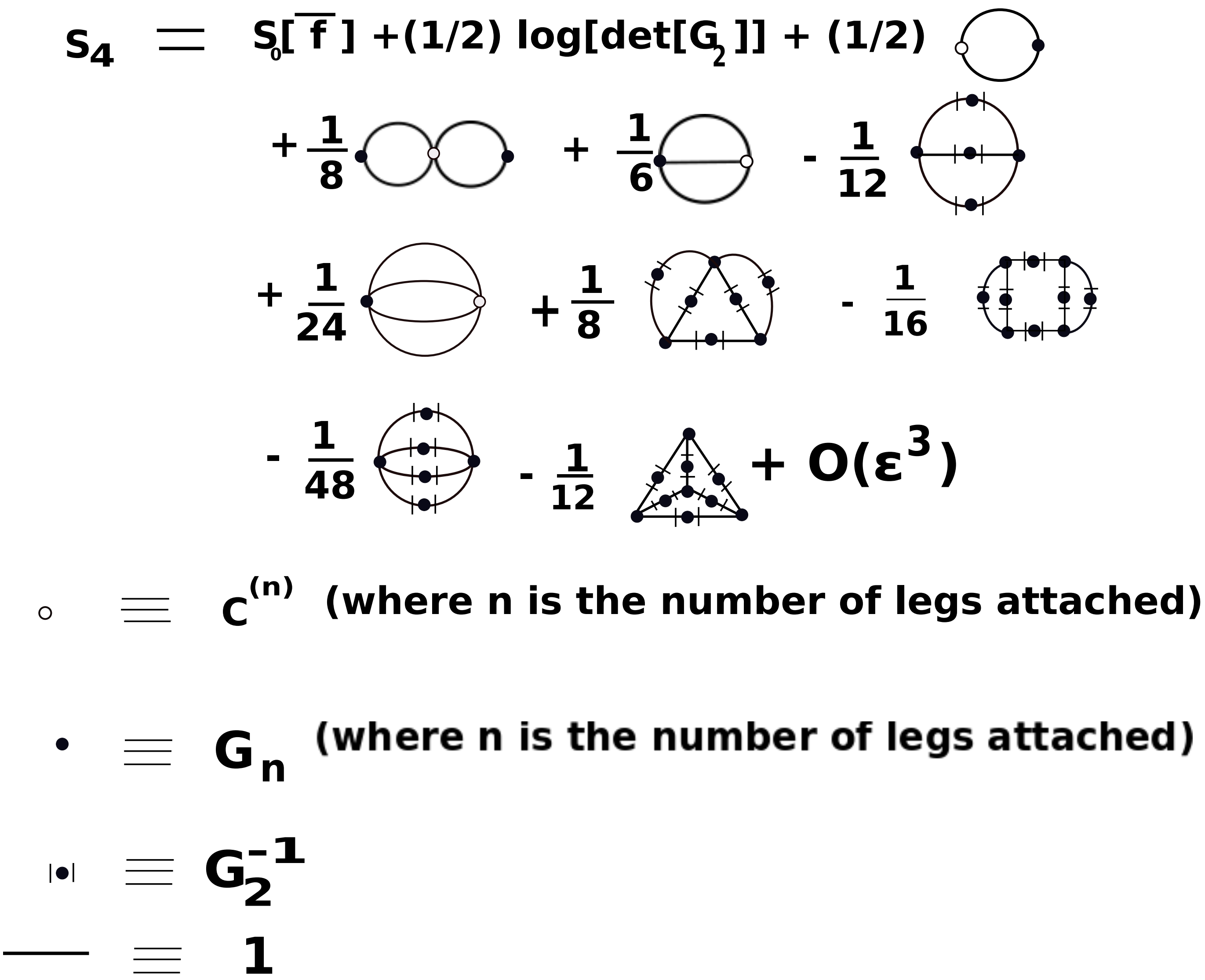

Figure 42: The figure shows S_4 obtained by evaluating Eq. (6.42).

Since we plan to maximize the entropy, it will be useful to get the expressions for derivatives of S_4 with respect to G_ns as shown below.

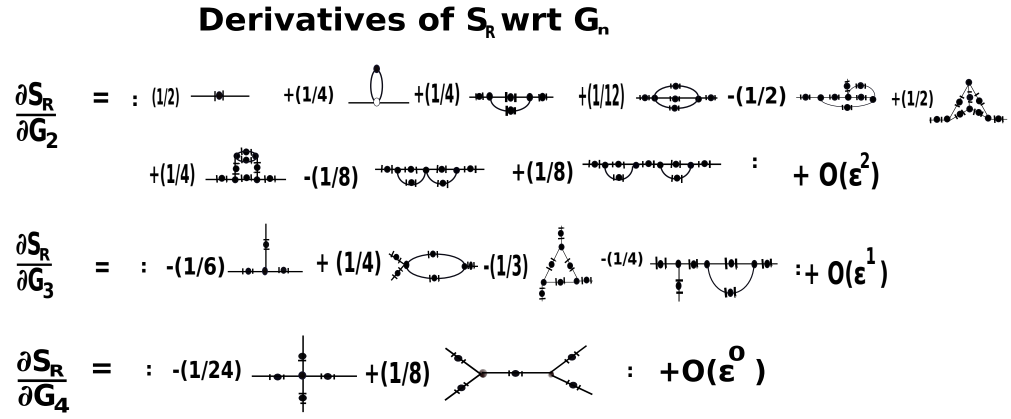

Figure 43: The figure shows the derivatives of S_4 with respect to $\bar{\Psi}, G_2, G_3, G_4$ obtained by taking derivatives of expression in (Figure 42). The notation $: X :\equiv X - X_{\mathrm{eq}}$ means difference of the diagram evaluated by with out-of equilibrium Gs from the diagram evaluated with correlation functions in equilibrium denoted by $\bar{G}$s.

6.3.1 Correlations in equilibrium

The two, three and four point correlation functions in equilibrium are obtained in terms of the derivatives of S_0 are obtained as:

$$\bar{G}_{AB} = -C^{-1}_{AB} \tag{6.44a}$$

$$\bar{G}_{ABC} = -C_{QRS}C^{-1}_{AQ}C^{-1}_{BR}C^{-1}_{CS} \tag{6.44b}$$

$$\bar{G}_{ABCD} = C^{-1}_{AQ}C^{-1}_{BR}C^{-1}_{CS}C^{-1}_{DT}\left[C_{QRST} - \left(C_{QRU}C_{STV} + C_{QSU}C_{RTV} + C_{QRT}C_{SUV}\right)C^{-1}_{UV}\right] \tag{6.44c}$$

Taking derivatives of S_0 defined in Eq. (6.14), we obtain:

$$C_{AB} = -\frac{1}{s\,f_A^2 + f_A}\,\delta_{AB}\,, \quad C_{ABC} = \frac{2f_A s + 1}{f_A^2(s\,f_A+1)^2}\,\delta_{ABC}\,, \quad C_{ABCD} = -\frac{6s\,f_A(s\,f_A+1)+2}{f_A^3(s\,f_A+1)^3}\,\delta_{ABCD} \tag{6.45}$$

i.e

$$\bar{G}_{AB} = f_A\,(s\,f_A+1)\delta_{AB}\,, \quad \bar{G}_{ABC} = f_A\,(s\,f_A+1)\,(2s\,f_A+1)\,\delta_{ABC}\,,$$
$$\bar{G}_{ABCD} = f_A\,(s\,f_A+1)\,(6s\,f_A(s\,f_A+1)+1)\,\delta_{ABCD} \tag{6.46}$$

Specifically for classical (Boltzmann) statistics, $(s=0)$

$$\bar{G}_{AB} = f_A\delta_{AB}\,, \quad \bar{G}_{ABC} = f_A\delta_{ABC}\,, \quad \bar{G}_{ABCD} = f_A\delta_{ABCD} \tag{6.47}$$

6.4 Maximum Entropy freeze-out of Gaussian fluctuations

In this Section, we describe the maximum entropy freeze-out procedure for two-point fluctuations. The generalized entropy which is maximized in equilibrium is the 2-PI entropy density (given by Eq. (6.31)) which is a functional of the particle distribution functions, f_As and also their two-point correlations, G_{AB}s. The maximization is subject to the matching conditions given by:

$$H^{ab}(x_a, x_b) = \int_{AB} G_{AB} P^a_A P^b_B \tag{6.48}$$

Define the Lagrange parameter 6×6 matrix Λ which depends on space time points x_A, x_B. The Lagrangian function for the 2-PI entropy with the above constraints is given by:

$$S_\Lambda \;=\; S + \frac{1}{2}\int_{\boldsymbol{x}_A}\int_{\boldsymbol{x}_B} \Lambda_{ab}(\boldsymbol{x}_A, \boldsymbol{x}_B)\left(H^{ab}(x_A, x_B) - \int_{\tilde{A}}\int_{\tilde{B}} G_{AB}\, P^a_A\, P^b_B\right) \tag{6.49}$$

Variation condition $\delta S_\Lambda / \delta G_{AB} = 0$ then gives

$$G^{-1}_{AB} = \bar{G}^{-1}_{AB} - \Lambda_{ab}(x_A, x_B)\, P^a_A\, P^b_B \tag{6.50}$$

Formally, Eq. (6.50) can be expanded in an infinite series as follows:

$$G_{AB} \;=\; \bar{G}_{AB} + \bar{G}_{AC}\Lambda_{cd}(x_C, x_D)P^c_C P^d_D \bar{G}_{DB} + \bar{G}_{AC}\Lambda_{cd}(x_C, x_D)P^c_C P^d_D \bar{G}_{DE}\Lambda_{ef}(x_E, x_F)P^e_E P^f_F \bar{G}_{FB} + \ldots \tag{6.51}$$

Substituting Eq. (6.51) in Eq. (6.48):

$$\begin{aligned}
H^{ab}(x_A, x_B) &= \int_{\tilde{A}} \int_{\tilde{B}} \bar{G}_{AB} P^a_A P^b_B \\
&\quad + \int_{\tilde{A}} \int_{\tilde{B}} \int_C \int_D \bar{G}_{AC} \Lambda_{cd}(x_C, x_D) P^c_C P^d_D \bar{G}_{DB} P^a_A P^b_B \\
&\quad + \int_{\tilde{A}} \int_{\tilde{B}} \int_C \int_D \int_E \int_F \bar{G}_{AC} \Lambda_{cd}(x_C, x_D) P^c_C P^d_D \bar{G}_{DE} \Lambda_{ef}(x_E, x_F) P^e_E P^f_F \bar{G}_{FB} P^a_A P^b_B + \dots \\
&= \bar{H}^{ab}(x_A, x_B) + \int_{x_C} \int_{x_D} \Lambda_{cd}(x_C, x_D) \bar{\phi}^{ac}(x_A, x_C) \bar{\phi}^{db}(x_D, x_B) \\
&\quad + \int_{x_C} \int_{x_D} \int_{x_E} \int_{x_F} \Lambda_{cd}(x_C, x_D) \Lambda_{ef}(x_E, x_F) \bar{\phi}^{ac}(x_A, x_C) \bar{\phi}^{de}(x_D, x_E) \bar{\phi}^{fb}(x_F, x_B) + \dots \\
&= \left[\bar{H}^{-1} - \Lambda\right]^{-1^{ab}} \qquad (6.52)
\end{aligned}$$

Rewriting Λ in terms of H,

$$\Lambda = \bar{H}^{-1} - H^{-1} \qquad (6.53)$$

Substituting Eq. (6.53) in Eq. (6.50), the two-point correlation function that maximizes the 2-PI entropy density on the kinetic side subject to the conservation laws is then given in terms of the hydrodynamic fluctuations as:

$$G^{-1}_{AB} = \bar{G}^{-1}_{AB} - \left[\bar{H}^{-1} - H^{-1}\right]_{ab} (x_A, x_B) P^a_A P^b_B \qquad (6.54)$$

Linearizing in $\Delta H = H - \bar{H}$, the G_{AB} which maximizes the S_Λ and satisfies Eq. (6.48) is:

$$G_{AB} = \bar{G}_{AB} + \Delta H_{ab} (\bar{H}^{-1} P \bar{G})^a_A (\bar{H}^{-1} P \bar{G})^b_B + \dots \qquad (6.55)$$

6.5 Maximum Entropy freeze-out of non-Gaussian fluctuations

In this Section we maximize the 4-PI entropy, S_4 given by Eq. (6.40a) and diagrammatically represented in Figure 42. Suppose the hydrodynamical simulation with fluctuations gives the following inputs, the two point (H_{ab}), three point (H_{abc})and four point (H_{abcd}) functions of conserved densities. H^{ab}, H_3^{abc} as the two point and three point fluctuation matrix of $\delta(\epsilon u^\mu), \delta n$. Then the matching conditions are :

$$
\begin{aligned}
H^{ab}(x_A, x_B) &= \int_{\tilde{A}} \int_{\tilde{B}} G_{AB} P_A^a P_B^b && (6.56a)\\
H^{abc}(x_A, x_B, x_C) &= \int_{\tilde{A}} \int_{\tilde{B}} \int_{\tilde{C}} G_{ABC} P_A^a P_B^b P_C^c && (6.56b)\\
H^{abcd}(x_A, x_B, x_C) &= \int_{\tilde{A}} \int_{\tilde{B}} \int_{\tilde{C}} G_{ABCD} P_A^a P_B^b P_C^c P_D^d && (6.56c)
\end{aligned}
$$

We define S_Λ as the quantity given below that we need to maximize with respect to G_ns that satisfy the matching conditions given in 6.56.

$$
\begin{aligned}
&S_\Lambda = S_4 + \frac{1}{2} \int_{\boldsymbol{x}_A} \int_{\boldsymbol{x}_B} \Lambda^{(2)}_{ab}(x_A, x_B) \left(H_2^{ab}(x_A, x_B) - \int_{\tilde{A}} \int_{\tilde{B}} G_{AB}\, P_A^a\, P_B^b \right) \\
&-\frac{1}{6} \int_{x_A} \int_{x_B} \int_{x_C} \Lambda^{(3)}_{abc}(x_A, x_B, x_C) \left(H_3^{abc}(x_A, x_B, x_C) - \int_{\tilde{A}} \int_{\tilde{B}} \int_{\tilde{C}} G_{ABC}\, P_A^a\, P_B^a P_C^c \right) \\
&-\frac{1}{24} \int_{x_A} \int_{x_B} \int_{x_C} \int_{x_D} \Lambda^{(4)}_{abcd}(x_A, x_B, x_C, x_D) \left(H_4^{abcd}(x_A, x_B, x_C, x_D) - \int_{\tilde{A}} \int_{\tilde{B}} \int_{\tilde{C}} \int_{\tilde{D}} G_{ABCD}\, P_A^a\, P_B^b P_C^c P_D^d \right)
\end{aligned}
\tag{6.57}
$$

The derivatives of S_4 with respect to G_2, G_3 and G_4 are given in (Figure 43). We will use the leading terms in ϵ in each of those equations to obtain the following equations:

$$\begin{aligned}
\frac{\partial S_4}{\partial G_{A_1A_2}} &= :\frac{1}{2}G^{-1}_{A_1A_2}:+\dots && \text{(6.58a)}\\
\frac{\partial S_4}{\partial G_{A_1A_2A_3}} &= :-\frac{1}{6}G^{-1}_{A_1B_1}G^{-1}_{A_2B_2}G^{-1}_{A_3B_3}G_{B_1B_2B_3}:+\dots && \text{(6.58b)}\\
\frac{\partial S_4}{\partial G_{A_1A_2A_3A_4}} &= :-\frac{1}{24}G^{-1}_{A_1B_1}G^{-1}_{A_2B_2}G^{-1}_{A_3B_3}G^{-1}_{A_4B_4}G_{B_1B_2B_3B_4}+\frac{1}{8}G_{A_1EA_2}G_{A_3FA_4}G^{-1}_{EF}:+\dots && \text{(6.58c)}
\end{aligned}$$

The notation $:X:\equiv X-X_{\mathrm{eq}}$ means difference of the diagram evaluated by with out-of equilibrium Gs from the diagram evaluated with correlation functions in equilibrium denoted by $\bar{G}$s. The variation conditions $\partial S_\Lambda/\partial G_{AB}=0$, $\partial S_\Lambda/\partial G_{ABC}=0$ and $\partial S_\Lambda/\partial G_{ABCD}=0$, give:

$$\begin{aligned}
G^{-1}_{AB} &= \bar{G}^{-1}_{AB}-\Lambda^{(2)}_{ab}(x_A,x_B)P^a_AP^b_B+\dots && \text{(6.59a)}\\
G_{ABC} &= C^{(3)}_{QRS}G_{AQ}G_{BR}G_{CS}+\Lambda^{(3)}_{qrs}(x_A,x_B,x_C)P^q_QP^r_RP^s_SG_{AQ}G_{BR}G_{CS}+\dots && \text{(6.59b)}\\
G_{ABCD} &= C^{(4)}_{QRST}G_{AQ}G_{BR}G_{CS}G_{DT}+G^{-1}_{JX}\left[G_{JAB}G_{XCD}+G_{JAD}G_{XBC}+G_{JAC}G_{XBD}\right]\\
&\quad+\Lambda^{(4)}_{abcd}(x_A,x_B,x_C,x_D)P^a_QP^b_RP^c_SP^d_TG_{AQ}G_{BR}G_{CS}G_{DT} && \text{(6.59c)}
\end{aligned}$$

We can substitute in the matching conditions Eqs. (6.56) to obtain $\Lambda^{(2)}, \Lambda^{(3)}$ and $\Lambda^{(4)}$. $\Lambda^{(2)}$ can be obtained as before and $\Lambda^{(3)}$ and $\Lambda^{(4)}$ are given by:

$$\Lambda^{(2)}_{ab}(x_1, x_2) = \bar{H}^{-1}_{ab}(x_1, x_2) - H^{-1}_{ab}(x_1, x_2) \tag{6.60a}$$

$$\Lambda^{(3)}_{abc}(x_1, x_2, x_3) = \left(H^{-1}\right)_{af}\left(H^{-1}\right)_{bd}\left(H^{-1}\right)_{ce}\left(H^{fde}_3(x_1, x_2, x_3) - D^{fde}_3(x_1, x_2, x_3)\right) \tag{6.60b}$$

$$\Lambda^{(4)}_{abcd}(x_1, x_2, x_3, x_4) = \left(H^{-1}\right)_{af}\left(H^{-1}\right)_{bg}\left(H^{-1}\right)_{ce}\left(H^{-1}\right)_{dh}\left[H^{fgeh}(x_1, x_2, x_3, x_4) - D^{fgeh}(x_1, x_2, x_3, x_4)\right] \tag{6.60c}$$

with D_3 and D_4 given by:

$$D^{fde}_3(x_1, x_2, x_3) = \int_{\tilde{A}}\int_{\tilde{B}}\int_{\tilde{C}} C^{(3)}_{QRS} G_{AQ} G_{BR} G_{CS} P^f_A P^d_B P^e_C \tag{6.61a}$$

$$\begin{aligned} D^{abcd}_4(x_1, x_2, x_3, x_4) = & \int_{\tilde{A}}\int_{\tilde{B}}\int_{\tilde{C}}\int_{\tilde{D}} P^a_A Pb_B P^c_C P^d_D \Big[G_{AQ} G_{BR} G_{CS} G_{DT} C^{(4)}_{QRST} \\ + & \int_X \int_Y G^{-1}_{XY} \left[G_{YAB} G_{XCD} + G_{YAC} G_{XBD} + G_{YAD} G_{XBC} \right] \Big] \end{aligned} \tag{6.61b}$$

We can express D_3 and D_4 in terms of the hydrodynamic correlations,

$$\widehat{\Delta} H^{fd} = H^{de} - \bar{H}^{de} \tag{6.62}$$

$$\widehat{\Delta} H^{fde} = \Delta H^{fde} - 3\left[\Delta H^{fg}(\bar{H}^{-1} H_3)^{gde}\right]_{\overline{fde}} \tag{6.63}$$

as follows. This is shown in Appendix. (D).

$$D_3^{fde} = \bar{H}^{fde} + 3\left[\Delta H_{fg}(\bar{H}^{-1}H_3)_{gde}\right]_{\overline{fde}} + \dots \tag{6.64a}$$

$$D_4^{abcd} = \Big[\bar{H}^{abcd} + 6\Delta\widehat{H}_3^{abe}(\bar{H}^{-1}\bar{H}_3)^{ecd} + 4\Delta\widehat{H}^{af}(\bar{H}^{-1}\bar{H}_4)^{fbcd} + 3\Delta\widehat{H}^{ef}(\bar{H}^{-1}\bar{H}_3)^{abe}(\bar{H}^{-1}\bar{H}_3)^{fcd}\Big]_{abcd} \tag{6.64b}$$

Substituting Λs back into Eq. (6.59), we get:

$$G^{-1}_{AB} = \bar{G}^{-1}_{AB} - \left[\bar{H}^{-1} - H^{-1}\right]_{ab} P^a_A P^b_B \tag{6.65a}$$

$$G_{ABC} = \int_Q\int_R\int_S G_{AQ}G_{BR}G_{CS}\left[C^{(3)}_{QRS} + \left(P_A H^{-1}\right)_f\left(P_B H^{-1}\right)_d\left(P_C H^{-1}\right)_e\left(H_3^{fde} - D_3^{fde}\right)\right] \tag{6.65b}$$

$$\begin{aligned} G_{ABCD} &= \int_Q\int_R\int_S\int_T G_{AQ}G_{BR}G_{CS}G_{DT}\Bigg(C^{(4)}_{QRST} + \left[3G_{JX}C^{(3)}_{JQR}C^{(3)}_{XST}\right]_{\overline{QRST}} \\ &+ \left(P_A H^{-1}\right)_f\left(P_B H^{-1}\right)_g\left(P_C H^{-1}\right)_e\left(P_D H^{-1}\right)_h\left(H_4^{fgeh} - D_4^{fgeh}\right)\Bigg) \end{aligned} \tag{6.65c}$$

In terms of the deviation from equilibrium correlations defined as below:

$$\Delta G_{AB} = G_{AB} - \bar{G}_{AB} \tag{6.66a}$$

$$\Delta G_{ABC} = G_{ABC} - \bar{G}_{ABC} \tag{6.66b}$$

$$\Delta G_{ABCD} = G_{ABCD} - \bar{G}_{ABCD} \tag{6.66c}$$

we can express G_{ABC}, G_{ABCD} as :

$$\begin{aligned} G_{ABC} &= \Big[\bar{G}_{ABC} + 3\Delta G_{AR}(\bar{G}^{-1}G_3)_{RBC} \\ &\quad + \hat{\Delta} H^{fde}(P_Q\bar{H}^{-1}\bar{G}_{AQ})_f(P_R\bar{H}^{-1}\bar{G}_{BR})_d(P_S\bar{H}^{-1}\bar{G}_{CS})_e\Big]_{\overline{ABC}} + \ldots \end{aligned} \tag{6.67}$$

$$\begin{aligned} G_{ABCD} &= \Big[\bar{G}_{ABCD} + 6\Delta\hat{G}_{ABF}(\bar{G}^{-1}\bar{G}_3)_{FCD} \\ &\quad + 4\Delta\hat{G}_{AF}(\bar{G}^{-1}\bar{G}_4)_{FBCD} + 3\Delta\hat{G}_{EF}(\bar{G}^{-1}\bar{G}_3)_{ABJE}(\bar{G}^{-1}\bar{G}_3)_{FJCD} \\ &\quad + \Delta\hat{H}^{fdeg}(Q\bar{G})_{fA}(Q\bar{G})_{dB}(Q\bar{G})_{eC}(Q\bar{G})_{gD}\Big]_{\overline{ABCD}} + \ldots \end{aligned} \tag{6.68}$$

Notice, that all but the last terms on the RHS of Eqs. (6.67) and (6.68) can be expressed entirely in terms of the lower order correlations. This decomposition gives important insight into

6.6 Irreducible Relative Cumulants

The $G_{AB\ldots}$ are the connected correlation functions between particles $A, B, \ldots$ with momenta $p_A, p_B, \ldots$ and spatial coordinate $x_A, x_B, \ldots$ on the freeze-out hypersurface. Even in a non-interacting ideal gas of hadrons, there are correlations , which we denote by $\bar{G}_{AB}$ which are non-zero. What we are interested in are the non-trivial correlations which arise due to the interactions between the particles or non-equilibrium effects. In order to distinguish these correlations, one needs to decompose the total n-point correlations $G_{AB\ldots}$ into a genuine n^{th} order correlation + terms which can be written in terms of lower order correlations that depend on $\bar{G}_{AB\ldots}$. This has been accomplished in the earlier sections and expressed in the form of Eqs. (6.55,6.67,6.68). From these equations, we can identify the term which cannot be written in terms of lower order kinetic correlations and define them as the *irreducible relative cumulants (IRCs)* of the kinetic distribution. The IRCs of the particle distribution functions are defined as follows:

$$\Delta\widehat{G}_{AB} \equiv G_{AB} - \bar{G}_{AB} \tag{6.69a}$$

$$\Delta\widehat{G}_{ABC} \equiv \Big[G_{ABC} - \bar{G}_{ABC} - 3\Delta\widehat{G}_{AE}(\bar{G}^{-1}\bar{G}_3)_{EBC}\Big]_{\overline{ABC}} \tag{6.69b}$$

$$\begin{aligned}\Delta\widehat{G}_{ABCD} \equiv \Big[&G_{ABCD} - \bar{G}_{ABCD} - 6\Delta\widehat{G}_{ABF}(\bar{G}^{-1}\bar{G}_3)_{FCD} \\ &- \Big[4\Delta\widehat{G}_{AF}(\bar{G}^{-1}\bar{G}_4)_{FBCD} + 3\Delta\widehat{G}_{EF}(\bar{G}^{-1}\bar{G}_3)_{ABJE}(\bar{G}^{-1}\bar{G}_3)_{FJCD}\Big]\Big]_{\overline{ABCD}}\end{aligned} \tag{6.69c}$$

We can now introduce similar correlation functions of the hydrodynamic fluctuations which we we will call hydrodynamic *irreducible relative cumulants (IRCs)*.

$$\Delta\widehat{H}^{ab} \equiv \Delta H^{ab} \tag{6.70a}$$

$$\Delta\widehat{H}_3^{abc} \equiv \Big[\Delta H_3^{abc} - 3\Delta\widehat{H}^{ae}(\bar{H}^{-1}\bar{H}_3)^{ebc}\Big]_{\overline{abc}} \tag{6.70b}$$

$$\Delta\widehat{H}_4^{abcd} \equiv \Big[\Delta H_4^{abcd} - 6\Delta\widehat{H}_3^{abe}(\bar{H}^{-1}\bar{H}_3)^{ecd} - \Big[4\Delta\widehat{H}^{af}(\bar{H}^{-1}\bar{H}_4)^{fbcd} + 3\Delta\widehat{H}^{ef}(\bar{H}^{-1}\bar{H}_3)^{abe}(\bar{H}^{-1}\bar{H}_3)^{fcd}\Big]\Big]_{\overline{abcd}} \tag{6.70c}$$

In terms of the kinetic and hydrodynamics IRCs, we can rewrite the linearized form of the freeze-out of the fluctuations as follows:

$$\Delta\widehat{G}_{AB} = \Delta\widehat{H}^{ab}(Q\bar{G})_{aA}(\bar{G}Q)_{bB} \tag{6.71}$$

$$\Delta\widehat{G}_{ABC} = \Delta\widehat{H}_3^{fde}(Q\bar{G})_{fA}(Q\bar{G})_{dB}(Q\bar{G})_{eC} \tag{6.72}$$

$$\Delta\widehat{G}_{ABCD} = \Delta\widehat{H}_4^{fdeg}(Q\bar{G})_{fA}(Q\bar{G})_{dB}(Q\bar{G})_{eC}(Q\bar{G})_{gD} \tag{6.73}$$

where $Q_a = \left(\bar{H}^{-1}\right)_{ac} P^c$. The linearized form of the freeze-out of a general higher point correlation function of fluctuations can be expressed compactly as follows :

$$\Delta\widehat{G}_{ABC\ldots} = \Delta\widehat{H}^{fde\ldots}(P_Q\bar{H}^{-1}\bar{G}_{AQ})_f(P_R\bar{H}^{-1}\bar{G}_{BR})_d(P_S\bar{H}^{-1}\bar{G}_{CS})_e\cdots + \ldots \tag{6.74}$$

Note that the factors $(\bar{G}^{-1}\bar{G}_n)_{ABC\ldots} \equiv \bar{G}^{-1}_{AX}\bar{G}_{XBC\ldots}$ in Eq. (6.74), in the case of classical(Boltzmann) statistics (Eq. (6.47)), are equal to $\delta_{ABC\ldots}$. Thus, in this case, the IRCs $\widehat{\Delta}G_n$

coincide with correlators $C_{ab\ldots}$ described in Ref. [111], whose phase space integrals give factorial cumulants. Such correlators and factorial cumulants play important role in the acceptance dependence of the fluctuation measures [104, 111]. For an arbitrary gas with arbitrary $\bar{G}$s, the integrals of $\Delta\widehat{G}_{ABC\ldots}$ over phase space, Eqs. (6.69) give the expression for the non-trivial out of equilibrium correlations that arise at that order.

We will now compare the results of the maximum entropy approach with other freezeout procedures used in the literature to implement freeze-out of fluctuations.

Ref. [130] considered fluctuations of f_A caused by fluctuations of hydrodynamic parameters such as temperature and chemical potential, J_a in our notations, i.e., $\delta f_A = (\partial f_A/\partial J_a)\delta J_a = (P\bar{G})^a_A \delta J_a$, where, as before, $\bar{G}_{AB} = f'_A \delta_{AB}$. Using hydrodynamic correlators $\langle \delta J_a \delta J_b \rangle = H^{-1}_{ab}$ one then finds:

$$G_{AB} = H^{-1}_{ab} (P\bar{G})^a_A (P\bar{G})^b_B \,, \tag{6.75}$$

as opposed to our Eq. (6.69a). We see that the problem with Eq. (6.75) is in the absence of the separate contribution of the ideal gas fluctuations, $\bar{G}_{AB} = f'_A \delta_{AB}$, which matches $\bar{H}$ in hydrodynamics, but does not describe *correlations* between two *different* particles [228, 229]. While the approach of Ref. [130] could satisfy the constraints (6.22), it does so, in part, via spurious two-particle correlations. This problem was addressed in Ref. [228, 229] for charge fluctuations, where the ideal gas (Poisson) contribution to H was subtracted before applying "freezeout (thermal) smearing" to the remainder, $H - \bar{H}$ in our notations. Thus, maximum entropy approach reproduces, in Eq. (6.74), the procedure in Ref. [228, 229] for two-point correlators. The subtractions of lower order terms in Eqs. (6.74) generalize this procedure to higher-order correlators.

6.7 Determining the coupling to critical fluctuations, g_As

Fluctuations near the QCD critical point *in equilibrium* have been described by considering a fluctuating critical mode σ coupled to the observed particles via their σ-dependent masses Refs. [9, 40, 56, 57, 105, 208]. This approach was further generalized in Ref. [2] to *non-equilibrium* critical fluctuations by mapping the correlators of σ to correlators of the specific entropy $m \equiv s/n$ – the critical field in Hydro+ [116]. This freeze-out procedure was discussed in detail in Chapter. (5). We can now compare this approach to the result of the maximum entropy method by considering only the matrix element $H^{\hat{s}\hat{s}}$ of hydrodynamic correlator H corresponding to the fluctuations of the specific entropy $\hat{s}$.

Furthermore, since this approach only considers the leading (most singular) critical contribution, for our comparison, we can neglect lower-order correlations, which contribute subleading behavior in terms of the dependence on the correlation length near the critical point [56]. In practice this means $\widehat{\Delta} G_n = \Delta G_n$ up to subleading (less critical) terms.

Near the critical point, the fluctuations of $\delta\hat{s}$ at constant pressure (p) are the slowest to evolve and also exhibit the most singular behavior. Fluctuation of $\delta(\epsilon u^\mu)$ and δn can be expressed in terms of the fluctuations of $\hat{s}$ and p as follows: Let,

$$\mathcal{E} = (\epsilon u^\mu, n) \quad \mathcal{M} = (u^\mu, p, \hat{s}) \tag{6.76}$$

Similar to H_n, which denotes the connected correlation functions of $\mathcal{E}$, let:

$$\tilde{H} = \langle \delta\mathcal{M}\delta\mathcal{M} \rangle\,, \quad \tilde{H}_3 = \langle \delta\mathcal{M}\delta\mathcal{M}\delta\mathcal{M} \rangle\,, \quad \tilde{H}_4 = \langle \delta\mathcal{M}\delta\mathcal{M}\delta\mathcal{M}\delta\mathcal{M} \rangle_c\,, \tag{6.77}$$

In general, the relationship between $\mathcal{E}$ and $\mathcal{M}$ are non-linear. However, near the critical point, the n-point fluctuations of $\mathcal{E}$ and $\mathcal{M}$ can be connected via linear transformations:

$$\Delta H^{ab} = X^a_c \Delta\tilde{H}^{cd} X^b_d + \dots \tag{6.78a}$$

$$\Delta H_3^{abc} = X^a_d X^b_e X^c_f \Delta\tilde{H}^{def} + \dots \tag{6.78b}$$

$$\Delta H_4^{abcd} = X^a_e X^b_f X^c_g X^d_h \Delta\tilde{H}^{efgh} + \dots \tag{6.78c}$$

where [124]:

$$X^a_c = \frac{\partial \mathcal{E}^a}{\partial \mathcal{M}^c} \equiv \begin{bmatrix} (\epsilon u^\mu)_{u^\nu} & (\epsilon u^\mu)_p & (\epsilon u^\mu)_{\hat{s}} \\ n_{u^\nu} & n_p & n_{\hat{s}} \end{bmatrix} = \begin{bmatrix} \epsilon \Delta^\mu_\nu & c_s^{-2} u^\mu & \epsilon_{\hat{s}} u^\mu \\ 0 & \frac{n}{wc_s^2} & \frac{n}{w}\left(\epsilon_{\hat{s}} - Tn\right) \end{bmatrix} \tag{6.79}$$

where subscript means derivative with respect to that variable when the others in the set $(u^\mu, p, \hat{s})$ are kept constant, $w = p + \epsilon$ is the enthalpy and c_s^2 is the square of the speed of sound. $\epsilon_{\hat{s}}$ is given by:

$$\epsilon_{\hat{s}} = Tn \left(1 - \frac{\dot{T}}{c_s^2} \right) \tag{6.80}$$

with

$$\dot{T} = \left(\frac{\partial \log T}{\partial \log n}\right)_{\hat{s}} \tag{6.81}$$

The $\ldots$ in Eq. (6.78) represent the terms that appear due to the non-linear terms in the transformation connecting the ϵ and n to $\hat{s}$ and p. Using the universal scaling behavior near the critical point, it can be argued that these terms vary as smaller powers in correlation length near the critical point. The elements of X^{-1} are defined as follows:

$$X_c^{-1^a} = \frac{\partial \mathcal{M}^a}{\partial \mathcal{E}^c} \equiv \begin{bmatrix} \delta(u^\mu)_{\epsilon u^\nu} & \delta(u^\mu)_n \\ p_{\epsilon u^\nu} & p_n \\ \hat{s}_{\epsilon u^\nu} & \hat{s}_n \end{bmatrix} = \begin{bmatrix} \epsilon^{-1}\Delta^\mu_\nu & 0 \\ p_\epsilon u_\nu & p_n \\ \hat{s}_\epsilon u^\nu & \hat{s}_n \end{bmatrix} \tag{6.82}$$

where subscript means derivative with respect to that variable when the others in the set $((\epsilon u)^\mu, n)$ are kept constant, Define $\bar{\tilde{H}}$ such that:

$$\left(\bar{\tilde{H}}^{-1}\right)_{ab} = (X)^c_a \left(\bar{H}^{-1}\right)_{cd} \left(X^T\right)^d_b \tag{6.83}$$

We'll show shortly that $\bar{\tilde{H}}$ is diagonal. We, now re-express Eq. (6.69a) as:

$$\begin{aligned} \Delta\widehat{G}_{AB} &= \bar{G}_{AC} P^c_C \left(\bar{H}^{-1}\right)_{ca} \Delta\widehat{H}^{ab} \left(\bar{H}^{-1}\right)_{bd} P^d_D \bar{G}_{DB} \\ &= \bar{G}_{AC} (P X^{-1})^c_C \left(X \bar{H}^{-1} X\right)_{ca} (X^{-1} \Delta\widehat{H} X^{-1})^{ab} \left(X \bar{H}^{-1} X\right)_{bd} (X^{-1} P)^d_D \bar{G}_{DB} \end{aligned} \tag{6.84}$$

Substituting Eqs. (6.83,), in Eq. (6.84), we get

$$
\begin{aligned}
\Delta\widehat{G}_{AB} &= \left(X^{-1}P\right)^{g}_{C}\left(\bar{\tilde{H}}^{-1}\right)_{gh}\Delta\widehat{\bar{\tilde{H}}}^{hj}\bar{G}_{AC}\left(\bar{\tilde{H}}^{-1}\right)_{ji}\left(PX^{-1}\right)^{i}_{D}\bar{G}_{DB} && \text{(6.85a)}\\
&= \Delta\widehat{\bar{\tilde{H}}}^{ab}(\tilde{Q}\bar{G})_{aA}(\tilde{Q}\bar{G})_{bB} && \text{(6.85b)}
\end{aligned}
$$

where

$$
\tilde{Q}_a = \left(X^{-1}\right)^{g}_{c}\left(\bar{\tilde{H}}^{-1}\right)_{ga}P^{c}_{C} \tag{6.86}
$$

We show below that $\bar{\tilde{H}}^{-1}$ is diagonal: From Eq. (6.83),

$$
\left(\bar{\tilde{H}}\right)_{ab} = \left(X^{-1}\right)^{c}_{a}\left(\bar{H}\right)_{cd}\left(X^{-1^{T}}\right)^{d}_{b} \tag{6.87a}
$$

$$
= \begin{bmatrix} \epsilon^{-1}\Delta^{\mu}_{\nu} & 0 \\ p_\epsilon u_\nu & p_n \\ \hat{s}_\epsilon u^\nu & \hat{s}_n \end{bmatrix}
\begin{bmatrix} \langle\delta(\epsilon u^\nu\delta(\epsilon u_\alpha))\rangle_{\text{eq}} & \langle\delta(\epsilon\delta(n))\rangle_{\text{eq}}u^\nu \\ \langle\delta(\epsilon\delta(n))\rangle_{\text{eq}}u_\alpha & \langle\delta n\delta n\rangle_{\text{eq}} \end{bmatrix}
\begin{bmatrix} \epsilon^{-1}\Delta^{\alpha}_{\beta} & p_\epsilon u_\alpha & \hat{s}_\epsilon u^\alpha \\ 0 & p_n & m_n \end{bmatrix} \tag{6.87b}
$$

$$
= \begin{bmatrix} \langle\delta u^\mu\delta u_\beta\rangle & 0 & 0 \\ 0 & p_\epsilon^2\langle\delta\epsilon\delta\epsilon\rangle + p_\epsilon p_n\langle\delta\epsilon\delta n\rangle + p_n^2\langle\delta n\delta n\rangle & (p\hat{s})_\epsilon\langle\delta\epsilon\delta\epsilon\rangle_{\text{eq}} + (p\hat{s})\langle\delta\epsilon\delta n\rangle + (p\hat{s})_n\langle\delta n\delta n\rangle \\ 0 & (p\hat{s})_\epsilon\langle\delta\epsilon\delta\epsilon\rangle + (p\hat{s})_{\epsilon n}\langle\delta\epsilon\delta n\rangle + (p\hat{s})_n\langle\delta n\delta n\rangle & m_\epsilon^2\langle\delta\epsilon\delta\epsilon\rangle + m_{\epsilon n}^2\langle\delta\epsilon\delta n\rangle + m_n^2\langle\delta n\delta n\rangle \end{bmatrix}_{\text{eq}} \tag{6.87c}
$$

Note that,

$$p_\epsilon \hat{s}_\epsilon \langle \delta\epsilon\delta\epsilon\rangle_{\rm eq} + (p_\epsilon \hat{s}_n + \hat{s}_\epsilon p_n)\langle \delta\epsilon\delta n\rangle_{\rm eq} + p_n \hat{s}_n \langle \delta n\delta n\rangle_{\rm eq} = \langle \delta p\delta\hat{s}\rangle_{\rm eq} = 0\,, \tag{6.88}$$

where we have used the thermodynamic relations

$$dp = \frac{w}{T}dT + Tnd\alpha\,, \quad d\hat{s} = \frac{1}{nT}d\epsilon - \frac{w}{n^2T}dn \tag{6.89}$$

and

$$\langle\delta\beta\delta\epsilon\rangle = \langle\delta n\delta\alpha\rangle \text{ and } \langle\delta\beta\delta n\rangle = \langle\delta\alpha\delta\epsilon\rangle = 0 \tag{6.90}$$

where $\beta = 1/T$ and $\alpha = \mu/T$. It follows from Eq. (6.88) that $\bar{\bar{H}}$ is diagonal. Eq. (6.88) simply means that in equilibrium fluctuations of pressure and entropy per baryon are not correlated. Near the critical point, the equilibrium n-point correlations of p are subleading relative to the most singular mode, corresponding to fluctuations of $\delta\hat{s}$,i.e while $\langle\delta\hat{s}\delta\hat{s}\rangle_{\rm eq} \sim C_p\xi^{2-\eta}$ where C_p is the specific heat capacity , $\langle\delta p\delta p\rangle \sim c_s^2 \sim \xi^{\alpha/\nu}$. We consider the case where the sub-leading singular corrections to the Hadron-Resonance Gas EoS due to the fluctuations of pressure are negligible. We also assume that in the regime we are interested in fluctuations of pressure are fast enough to relax to their equilibrium values such that $\langle\delta p\delta p\rangle = \langle\delta p\delta p\rangle_{\rm eq}$ which is equal to the pressure fluctuations in a HRG upto negligible corrections. Recall that the correlation functions of $\delta\hat{s}$ is the slowest non-hydrodynamic mode. Therefore, at times scales large enough for all correlations except $\langle\delta\hat{s}\delta\hat{s}\rangle$ to relax to equilibrium,

$$\Delta\widehat{G}_{AB} \;=\; \Delta\widehat{\tilde{H}}^{\hat{s}\hat{s}}(\tilde{Q}\bar{G})_{\hat{s}A}(\tilde{Q}\bar{G})_{\hat{s}B} \tag{6.91}$$

where $\Delta\widehat{\tilde{H}}^{\hat{s}\hat{s}} \equiv \Delta\widehat{\langle\delta\hat{s}\delta\hat{s}\rangle}$ and

$$\tilde{Q}_{\hat{s}A} = \left(X^{-1}\right)_{a}^{\hat{s}c}\left(\bar{\tilde{H}}^{-1}\right)_{c\hat{s}}P_{A}^{a} \tag{6.92}$$

$$\left(\bar{\tilde{H}}\right)_{ab} \;=\; \begin{bmatrix} \langle\delta u^{\mu}\delta u_{\beta}\rangle & 0 & 0 \\ 0 & p_{\epsilon}^{2}\langle\delta\epsilon\delta\epsilon\rangle + p_{\epsilon n}^{2}\langle\delta\epsilon\delta n\rangle + p_{n}^{2}\langle\delta n\delta n\rangle & 0 \\ 0 & 0 & \hat{s}_{\epsilon}^{2}\langle\delta\epsilon\delta\epsilon\rangle + \hat{s}_{\epsilon n}^{2}\langle\delta\epsilon\delta n\rangle + \hat{s}_{n}^{2}\langle\delta n\delta n\rangle \end{bmatrix}_{\mathrm{eq}} \tag{6.93}$$

From Eq. (6.93), one can read out $\left(\bar{\tilde{H}}\right)_{\hat{s}\hat{s}}$ as:

$$\begin{aligned} \left(\bar{\tilde{H}}\right)_{\hat{s}\hat{s}} &= \hat{s}_{\epsilon}^{2}\langle\delta\epsilon\delta\epsilon\rangle_{\mathrm{eq}} + 2\hat{s}_{\epsilon}\hat{s}_{n}\langle\delta\epsilon\delta n\rangle_{\mathrm{eq}} + \hat{s}_{n}^{2}\langle\delta n\delta n\rangle_{\mathrm{eq}} \\ &= \int_{\tilde{C}}\int_{\tilde{D}}\bar{G}_{CD}\frac{1}{nT}\frac{1}{nT}\left[(p_{C}\cdot u) - \frac{w}{n}q_{C}\right]\left[(p_{D}\cdot u) - \frac{w}{n}q_{D}\right] \end{aligned} \tag{6.94}$$

where we used $\hat{s}_\epsilon = (nT)^{-1}$, $\hat{s}_n = -w(n^2T)^{-1}$. Substituting Eq. (6.94) in Eq. (6.92):

$$\tilde{Q}_{\hat{s}A} = \left(X^{-1}\right)^{\hat{s}\hat{s}}_{a} \left(\bar{\tilde{H}}^{-1}\right)_{\hat{s}\hat{s}} P^a_A = \left(\bar{\tilde{H}}^{-1}\right)_{\hat{s}\hat{s}} \left[\hat{s}_\epsilon \left(p_D \cdot u\right) + \hat{s}_n q_D\right] = \left(\bar{\tilde{H}}\right)^{-1}_{\hat{s}\hat{s}} \frac{1}{nT} \left[(p_D \cdot u) - \frac{w}{n} q_D\right] \tag{6.95}$$

Substituting Eq. (6.92) in Eq. (6.91), we get the prescription for freeze-out of two-point fluctuations near the critical point as:

$$\Delta\widehat{G}_{AB} \quad = \quad \left(\bar{\tilde{H}}\right)^{-1}_{\hat{s}\hat{s}} \frac{1}{nT} \left[(p_C \cdot u) - \frac{w}{n} q_C\right] \left(\bar{\tilde{H}}\right)^{-1}_{\hat{s}\hat{s}} \frac{1}{nT} \left[(p_D \cdot u) - \frac{w}{n} q_D\right] \Delta\widehat{\bar{\tilde{H}}}^{\hat{s}\hat{s}} (\bar{G})_{AC} (\bar{G})_{DB} \tag{6.96}$$

The prescription for critical fluctuations discussed in detail in chapter (5) [2] was:

$$\Delta\widehat{G}_{AB} \quad = \quad g_A g_B Z^{-1} T^{-2} \frac{m_C}{E_C} \frac{m_D}{E_D} \Delta\widehat{\bar{\tilde{H}}}^{\hat{s}\hat{s}} \bar{G}_{AC} \bar{G}_{DB} \tag{6.97}$$

where Z is given by Eq.(5.11) and g_As were taken to be constants. [1] The absence of the energy dependence of g_A in Eq. (6.97) is a consequence of the simplifying assumption that the field σ couples to mass term. Maximum entropy method allows us to relax this assumption and determine the "coupling" g_A together with its energy dependence from the equation of state (EOS) of QCD. Comparing Eq. (6.96) and Eq. (6.97), we identify g_As as:

$$g_A = \sqrt{Z} \frac{E_A}{m_A} \left(\bar{H}^{-1}\right)_{\hat{s}\hat{s}} \frac{w_c}{n_c} \left(\frac{E_A}{w_c} - \frac{q_A}{n_c}\right) , \tag{6.98}$$

---

[1] Eq. (6.97) when integrated over pairs of particles of all momenta emitted from all points on the freeze-out hypersurface gives Eq. (5.14) in Chapter. (5).

where $(\bar{H}^{-1})_{\hat{s}\hat{s}}$ is the hadron gas contribution to the fluctuations of specific entropy $\hat{s}$, which can be also found from the *non-singular* contribution to the EOS [63] as $(\bar{H}^{-1})_{\hat{s}\hat{s}} = n^2/\bar{c}_p$.

Since the QCD EOS is not known (yet), we shall demonstrate how to estimate g_A using the parametric EOS introduced in Ref. [63]. First, following Ref. [2], we find Z by matching the leading singularity in the QCD EOS to that in the Ising model:

$$Z = \lim_{T,\mu\to T_c,\mu_c} \frac{c_p T}{n^2 (T\xi)^{2-\eta}} = \frac{M_0 T_c^4}{h_0 n_c^2 (T_c \xi_0)^{2-\eta}} \times \left(\cot\alpha_1 - \frac{s_c}{n_c}\right)^2 \left[\frac{\sin\alpha_1}{w\sin(\alpha_1-\alpha_2)}\right]^2 ,$$

where w, $\alpha_{1,2}$ and ξ_0 are parameters, defined in Refs. [63, 107], which control the orientation and strength of the critical point singularity located at $T = T_c$ and $\mu = \mu_c$, with enthalpy given by $w_c = n_c\mu_c + s_c T_c$. The same expression as in the square brackets determines the width of the critical region [1]. The values of M_0 and h_0 are fixed in Ref. [63].

Defining $\hat{g}_A$ so that $g_A \equiv \hat{g}_A \sin\alpha_1/[w\sin(\alpha_1-\alpha_2)]$, we can use parameters in Refs. [63, 107] ($\mu_c = 350\,\mathrm{MeV}$, $T_c = 143.2\,\mathrm{MeV}$, $\xi_0 = 1\,\mathrm{fm}$) to estimate the values of the couplings at zero momentum ($\boldsymbol{p}_A = \mathbf{0}$): $\hat{g}_{p,\mathbf{0}} \approx -3.1$, $\hat{g}_{\pi,\mathbf{0}} \approx 0.18$, $\hat{g}_{\bar{p},\mathbf{0}} \approx 5.5$. The factor $\sin\alpha_1/[w\sin(\alpha_1-\alpha_2)]$ is a measure of the size of the critical region where the fluctuations are enhanced. Larger this size, larger is the coupling between the σ field and the particles.

The approach in Refs. [2, 9, 40, 56, 57, 105, 208] leading to Eq. (6.97) leaves not only the magnitude, but also the sign of g_A undetermined. While the overall sign can be changed by redefining the critical field σ, the relative sign of g_A for different particles, or different momenta of the same particle, i.e., different A, is not arbitrary and can be found in the maximum entropy approach using Eq. (6.98).

Thus, we find that the critical mode (fluctuations of $\hat{s}$) coupling to (low momentum) protons is opposite in sign from the coupling to either pions or antiprotons. This is due to the fact that fluctuations of the number of protons contribute to the fluctuations of the ratio s/n with opposite sign from that of pions or antiprotons. More explicitly, pions contribute to the entropy density, s and protons contribute (mostly) to the denominator, baryon number density n of the ratio.

There could be experimental implications of the changing sign of $g_A \sim n_c E_A - w_c q_A$. These could be studied by considering cross-species correlators discussed in Ref. [105]. Another possible place to look for these implications are in the correlations between particles with different momenta. In both cases one would expect anticorrelation since $g_A g_B$ is negative.

6.8 Stochastic nature of freeze-out

In a heavy-ion collision experiment, hundreds of millions of events are collected and analyzed to determine the mean and cumulants of particle multiplicities. In each of these events, shortly after the collision, a strongly coupled QGP is formed which later freezes out into a gas of hadrons. This gas of hadrons at freeze-out may be characterized by a set of particle distribution functions $\{f_A(x_A, p_A)\}$s. There are infinitely many sets of these particle distribution functions that are consistent with the matching conditions at freeze-out (Eq. (6.5,6.11)). Let the probability of observing a set of particle distribution functions f, which solves the matching conditions be $\bar{p}(f)$. Let M be the total number of events and n_f be the number of events in which $\{f\}$ is realized. In reality, where M is finite the "observed" probability denoted by $p(f) = \frac{n_f}{M}$ need not be equal to $\bar{p}(f)$. p_f is characterized by the mean-multiplicity distribution $\bar{f}$, the cumulants of the distribution functions $G_2, G_3 \ldots$. The probability of having n_f events with distribution function f (or equivalently, observed probability being equal to $p(f)$) which we denote by capital P is given by [1]:

$$P(p) = \exp\left[M \int Df e^{S_0(f)} p(f) \log \frac{\bar{p}(f)}{p(f)}\right] \tag{6.99}$$

---

[1] See Appendix. (E) for an illustrative derivation of this result

where $e^{S_0(f)}$ is the number of states in a microcanonical ensemble of hadron gas with mean particle distribution function given by $\{f_A\}s$. Therefore, when $M \to \infty$, probability of obtaining the true probability distribution function,$\bar{p}$, which maximizes the integral

$$\int Df e^{S_0(f)} p(f) \log \frac{\bar{p}(f)}{p(f)} \tag{6.100}$$

subject to the condition that $\bar{p}$ is normalized is nearly 1. This is exciting except that our knowledge about $\bar{p}(f)$ is limited by the information we have about the system at freeze-out. Below, we will determine $\bar{p}(f)$ assuming the input from hydrodynamic simulation with fluctuations is sufficient to describe the "true" probability distribution at freeze-out. A hydrodynamic simulation with fluctuations gives us information about the averages of energy, momenta, charge densities and the higher point correlation functions of their fluctuations. Then $\bar{p}(f)$ with this information can be constructed as:

$$\bar{p}(f) = \exp\{-\beta_i \Psi_i - \lambda - \Lambda^{(n)} H_n(f)\} \tag{6.101}$$

where $\Lambda^{(n)} H_n(f)$ collectively refers to all the constraints on the higher point fluctuations of the conserved densities expressed as functions of f. The normalization constant λ ensures that $\bar{p}$ is normalized to 1. Rewriting the discrete N summation expressions to integral over continuous set of states, we get the general expression for P as follows:

$$P(p) = \exp\left[-M \int Df e^{S_0(f)} p(f) \left(\log p(f) + \beta_i \Psi_i + \lambda + \Lambda^{(n)} H_n(f)\right)\right] \tag{6.102}$$

When $M \to \infty$, the probability P tends to a delta function that picks the distribution which maximizes the integral:

$$-\int Df e^{S_0(f)} p(f) \left(\log p(f) + \beta_i \Psi_i(f) + \lambda + \Lambda^{(n)} H_n(f)\right) \tag{6.103}$$

which is essentially the $p(f)$ (or equivalently $\bar{f}, G_n$s) prescribed by the maximum-entropy freeze-out. Therefore, maximum entropy freeze-out gives us the most likely freeze-out scenario (in a heavy-ion collision with large number of events) that is consistent with all the information we have about the system at freeze-out.

6.9 Summary

Maximum entropy principle has been widely applied across diverse disciplines ranging from statistics, information theory, economics, data science, computation, pattern recognition to bioinformatics and biology. In fact, statistical mechanics itself can be derived from using maximum entropy principle [230, 231] . The thermodynamic state is, by definition, the state of maximum entropy, i.e., the most likely ensemble of microscopic states, given the known (i.e., measured) properties of the system, such as total energy. The application to freezeout could be viewed as answering the question of what is the most likely ensemble of free-streaming particles after freezeout given the information about the hydrodynamic conditions before the freezeout.

The central idea is that this information at freeze-out could include not only the values of conserved densities but also of the hydrodynamic fluctuations (i.e., correlators H_n) out of equilibrium. These can be obtained, for example, from a Hydro+ calculation [2, 116, 128, 129] similar to the one described in Section. (4), or by solving full hydrodynamic fluctuation equations [121,124,125]. Maximum entropy freezeout then determines the most likely ensemble of particles at freeze-out which matches all this available information (equation of state and the predictions of hydrodynamics with fluctuations).

Remarkably, the results are consistent with the picture, already considered in the literature, of hadron gas coupled to fluctuating fields inducing correlations thereby corroborating the existing picture. In addition, it provides nontrivial insight into the entropic origin of the correlations. Crucial for practical applications, the maximum entropy approach provides information about the couplings determining the magnitude of the correlations as well as the generalization to non-Gaussian fluctuations in or out of equilibrium.

The next step would be to implement this novel approach in heavy-ion collision simulations to explore the consequences and to compare the results with experimental data from the Beam Energy Scan at RHIC, which are currently being analyzed by the STAR collaboration. Studies in this direction are in progress.

CHAPTER 7

CONCLUSIONS

The study of QCD phase diagram is cardinal to broadening our understanding about the formation of nuclear matter, the early universe and the interior of neutron stars. The chiral symmetry restoring phase transition and confinement - deconfinement transitions are fundamental aspects of the theory of strong interactions. The nature of QCD phase transition in the physical realm will provide some clues to understanding these properties of QCD. This thesis was about using fluctuations as probes to map the phase diagram.

There are encouraging hints of the possible presence of a critical point in the phase diagram from Beam Energy Scan-I (BES-I). In order to make conclusive inferences from the data, we need a theoretical model/ framework to study fluctuations. Such a model should include a systematic treatment of fluctuations taking into account not only the aspects of the QCD EoS, but also its dynamics and the hybrid nature of the sources. We used quantum field theory to develop some components of such a model and demonstrate their applicability via simplified scenarios. The anticipated non-monotonic behavior of the cumulants of particle multiplicities with the collision energy is due to the enhancement of thermal fluctuations near the critical point (otherwise called critical fluctuations). The framework that we would have to use to make a systematic data-theory comparison must be capable of handling these non-critical sources as well. In addition, the magnitude of observed thermal fluctuations also depend upon various factors such as the strength of the singularity near the critical point determined by the *EoS*, the suppression due to *dynamics* due to competition between time scales and *freeze-out* parameters such as the closeness of the freeze-out line to the cross-over line. In this thesis we focus on the EoS, dynamics and freeze-out of fluctuations near the critical point.

In Chapter (3), we studied the Equation of State of QCD at high temperatures and number density near the conjectured critical point. Due to the universality of critical phenomenon, the physics near the QCD critical point can be mapped to that of ϕ^4 theory or Ising model in three dimensions. The mapping is in general dependent on the microscopics of QCD, and not based on symmetries and long distance dynamics and hence cannot be deduced based on universal arguments. Note, that due to the infamous sign problem the EoS at non-zero baryon chemical potential is unknown from first principles, and therefore, these mapping parameters cannot be determined from our current knowledge of QCD, although some aspects of these quantities could be inferred. As we show in Chapter. (3), these parameters can be directly related to higher order derivatives of pressure with respect to temperature and chemical potential, which can be connected to observables in heavy-ion collisions. We also discovered that in the limit of small quark masses, (which is a reasonable approximation for the case of real-world QCD), the mapping parameters show universal scaling features as a function of quark mass. These relations are particularly important as they allow us to place bounds on the values of non-universal mapping parameters, thereby allowing us to construct model EoS around the conjectured QCD critical point, which can then be used as input in hydrodynamical simulations of heavy-ion collisions. These also have phenomenological consequences.

In a heavy-ion collision, when the quark gluon plasma passes close to the critical point, it spends only a finite amount of time around regions where the equilibrium fluctuations are large. Due to critical slowing down, the fluctuations of the conserved quantities will not become as large as the maximum equilibrium values that may be expected using the EoS. In Chapter. (4), we studied the dynamics of the Gaussian fluctuations of the conserved quantities in semi-realistic analytical and numerical hydrodynamic backgrounds within the Hydro+ framework. In-order to describe the observables in heavy-ion collisions, i.e the particle distribution functions, we need a freeze-out procedure to convert these hydrodynamic fluctuations into correlations of particle multiplicities in momentum space. In Chapter. (5), we developed a freeze-out procedure that converts the hydrodynamic fluctuations near the critical point into cumulants of particle multiplicities. We demonstrated this procedure for the freeze-out of two-point fluctuations of hydrodynamic variables in semi-realistic scenarios. We observed that due to conservation and critical slowing down, the variances of particle multiplicities are suppressed relative to the equilibrium expectations and are also less sensitive to the exact location of freeze-out on the phase diagram. One of the lacunae of this framework is its regime of applicability which is restricted to the domain where fluctuations are dominated by the critical point. That brings us to the last part of this thesis.

We expect the critical fluctuations to dominate over non-critical sources close to the critical point. Loosely speaking, this is what we call the "critical region". In order to make quantitative estimates of fluctuations and thereby calculate cumulants of particle multiplicities as a function of center of mass energy, the non-critical sources of fluctuations also need to be included. In

Chapter. (6), we developed a generalization to the half a century old Cooper-Frye procedure to freeze-out all fluctuations (not just the critical fluctuations) of hydrodynamic densities into particle distribution functions using the principle of maximum entropy. Describing the entropy associated with particle multiplicity distributions, we were able to illustrate the stochastic nature of freeze-out. Applying the maximum entropy freeze-out to freeze-out of critical fluctuations, we were able to extract the g_As, the unknown couplings between the the critical σ field that couples to the hadrons in the effective field theory description near the critical point.

The crucial elements necessary for a fluctuation framework to estimate cumulants of particle multiplicities in HICs are now ready. In order to make direct comparisons with the experiment, it is necessary to perform simulations in more realistic settings than the example scenarios which we considered here. The next step would be an implementation of the hydrodynamic simulation with fluctuations of the slowest mode in a 3D realistic background (for eg., [232]) with realistic initial conditions and EoS, such as BEST EoS which agrees with lattice at zero baryochemical potential and includes a critical point [63] . The fluctuations can then be converted into cumulants of particle multiplicities with the maximum entropy freeze-out which was introduced in this thesis. In addition to the model parameters that appear in the modeling of the initial stage and the viscous coefficients, the fluctuation frame work with "BEST EoS"+ "Hydro+"+"Maximum-Entropy freeze-out" adds seven more parameters , six corresponding to the mapping parameters to 3D Ising model in the QCD EoS and the non-critical correlation length ξ_0 which sets the scale for the correlation length in QCD. A hadronic afterburner to account for resonance decays and elastic and inelastic scatterings could be coupled to this framework. Augmenting with Bayesian tools and comparing to experimental data, we hope to be equipped to understand the nature of phase transition from quark-gluon plasma to hadrons at non-zero baryon densities.

Our discussion about the dynamics of hydrodynamic fluctuations was restricted completely to the cross-over region. The dynamics becomes too non-trivial in the first-order regime where interesting phenomenon like meta stable phases, spinodal decomposition and nucleation could take place. While there have been some initial developments with regard to these phenomenon in the context of heavy-ion collisions, our understanding about how hydrodynamic fluctuations evolve and freeze-out when it encounters a first-order phase transition is rather limited. We defer these investigations to future work.

APPENDIX

LOCATION OF CRITICAL POINT FROM TAYLOR EXPANSIONS OF EOS AROUND ZERO CHEMICAL POTENTIAL

Numerical Monte Carlo methods cannot calculate the derivatives near the critical point due to the well-known sign problem. But these derivatives can be evaluated at zero baryon chemical potential. The radius of convergence or the distance to the closest singularity to the $\mu = 0$ axis can be inferred from the behavior of large n derivatives evaluated at $\mu = 0$. Suppose,

$$P(\mu, T) = \sum_{n=0}^{\infty} c_{2n}(t)\mu^{2n} \tag{A.1}$$

The odd Taylor coefficients are zero due to $\mu \to -\mu$ symmetry. The square of the radius of convergence as a function of temperature, $\mu_s^2(T)$, can be expressed as a limit of the ratios of the successive Taylor coefficients as:

$$|\mu_s^2(T)| = \lim_{n\to\infty} \frac{c_{2n}(T)}{c_{2n+2}(T)} \equiv \lim_{n\to\infty} R_{2n}(T) \tag{A.2}$$

If the closest singularity to $\mu = 0, T = T_c$ is the critical point located at (μ_c, T_c), i.e if $\mu_s^2(T_c) = \mu_c$, the behavior of R_{2n} for $n \gg 1$ can be predicted from the leading singular behavior of pressure. The leading singular behavior of the derivatives of pressure are same along any direction other than $h = 0$ are the same. This can be obtained by taking of the leading singular behavior in pressure expressed as follows:

$$P(\mu, T) \sim \left(1 - \frac{\mu}{\mu_c}\right)^{a_p(T_c)} + \left(1 + \frac{\mu}{\mu_c}\right)^{a_p(T_c)} \tag{A.3}$$

where $a_p(T_c) = (1 + \delta)/\delta$. For $n \to \infty$,

$$R^{2n}(T_c) \;=\; \frac{(2n+1)(2n+2)}{(a_p(T_c) - 2n)(a_p(T_c) - 2n - 1)} + \cdots = 1 + \frac{1 + 2\delta}{n\delta} + O(n^{-2}) \tag{A.4}$$

Since $\delta > -1/2$ in Ising model, for sufficiently large n, the radius of convergence estimators R_{2n} overestimate the value of chemical potential at the critical point.

Equivalently the radius of convergence estimators can also be defined as the coefficients of μ^{2n} in the Taylor series expansion of the second or higher order derivatives of pressure with respect to μ, which we denote by χ_k, where k is the order of the derivative. The radius of convergence estimators hence obtained can be denoted by $R_{2n}^{\chi_k}$:

$$R_{2n}^{\chi_k} = \frac{c_{2n}^{\chi_k}}{c_{2n+2}^{\chi_k}} \tag{A.5}$$

For the ratios the successive non-vanishing Taylor coefficients of χ^{2k} , we get:

$$\frac{R_{2n}^{2k}}{\mu_c^2} \;=\; 1 + \frac{a_p - 2k + 1}{n} + O(n^{-2}) \tag{A.6}$$

For $k = 1$, which corresponds to susceptibility we find that the radius of convergence estimators deviate much less from the actual value of μ_s than the estimates obtained using the Taylor coefficients of pressure. We also find that the radius of convergence estimators obtained using χ^{2k} where $k \geq 2$ underestimate the value of μ_c. This may be seen in the Random matrix model for $m_q = 5MeV$ in the following plot.

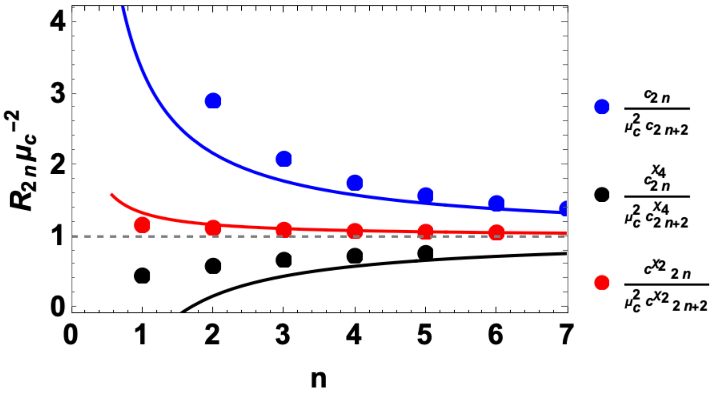

Figure 44: The estimates made using the Taylor coefficients of pressure(blue), susceptibility (red) and the fourth derivative of pressure(black) for RMM with m_q = 5MeV at $T = T_c$ is shown.

If the critical point is the closest singularity to the $\mu = 0$ line at $T = T_c$, the closest singularities for for sufficiently small positive and negative $\delta T = T - T_c \ll 1$, the closest singularities are the Lee-Yang singularities and the spinodal points respectively. In general these singularities occur at complex values of μ. The local of the spinodal singularities in the mean-field turns out to be at real values of μ.

The leading singular behavior of pressure and hence its derivatives if $\mu = 0$ line in a general case where the close singularity occurs at a complex value $\mu_s(T)$ can be captured by the following expression:

$$P(\mu, T) \quad = \quad N\left[\left(1-\frac{\mu}{\mu_s(T)}\right)^{a_p(T)} + \left(1+\frac{\mu}{\mu_s(T)}\right)^{a_p(T)}\right] + N^*\left[\left(1-\frac{\mu}{\mu_s^*(T)}\right)^{a_p(T)} + \left(1+\frac{\mu}{\mu_s^*(T)}\right)^{a_p(T)}\right] + .$$

(A.

where N is a constant and $a_p(T)$ is the scaling exponent which depends on the nature of singularity. The $\ldots$ represent the singular terms which are subleading near the singularity and the terms which are regular at the singularity.

A.0.0.1 Van der waals gas EoS

The EoS of a van der Waals gas was discussed in Section. (3.5). The gas being non-relativistic, there is no meaning for negative values of chemical potential.

$$P(\mu, T) = N\left(1-\frac{\mu}{\mu_s(T)}\right)^{a_p(T)} + N^*\left(1-\frac{\mu}{\mu_s^*(T)}\right)^{a_p(T)} + \ldots \tag{A.8}$$

In this case, there is no reason for odd derivatives of P with respect to μ at $\mu = 0$ to vanish. $R_n(T)$ is defined as:

$$R_n(T) = \frac{n+1}{n-a_p}\frac{\cos\left[(n-a_p)\,\theta + \theta_a\right]}{\cos\left[(n-a_p+1)\,\theta + \theta_a\right]} \tag{A.9}$$

where $\theta = \arg[\mu_s]$ and $\theta_a = \arg[N]$. For real singularities, $\theta = 0$.

We noticed earlier that $a_p(T_c) = (1+\delta)/\delta$, where the closest singularity is the critical point which lies on the real μ axis. For $T > T_c$ and $\delta = T - T_c << T_c$, it is reasonable to assume that the closest singularities are given by the Lee-Yang singularities. Below, we will determine a_p, θ and θ_a near the Lee-Yang singularities in the mean-field theory taking the universal ϕ^4 model near the critical point given by Eq. (3.43) for $T > T_c$. The Lee-Yang singularities are obtained as solutions to

$$\frac{\partial\Omega}{\partial\phi} = \frac{\partial^2\Omega}{\partial\phi^2} = 0 \tag{A.10}$$

The solution is [1]:

$$\left(\phi_{LY} = \sqrt{\frac{-r}{3u}}\,, h_{LY/sp} = \frac{2r}{3}\sqrt{\frac{-r}{3u}}\right) \text{and} \left(\phi^*_{LY/sp}, h^*_{LY/sp}\right)$$

Pressure in this model can be expanded near these singularities as:

$$\begin{aligned} P(\mu,T) &\sim \phi_{LY}^{-1/2}(h(\mu,T) - h_{LY/sp}(\mu_{LY/sp}(T),T))^{3/2} + \phi_{LY}^{*-1/2}(h(\mu,T) - h^*_{LY/sp}(\mu_{LY}(T),T))^{3/2} + \ldots \\ &\sim \phi_{LY}^{-1/2}(-\mu)_{LY}^{3/2}\left(1 - \frac{\mu}{\mu_{LY/sp}(T)}\right)^{3/2} + \phi_{LY}^{*-1/2}(-\mu)_{LY/sp}^{*3/2}\left(1 - \frac{\mu}{\mu^*_{LY}(T)}\right)^{3/2} \end{aligned} \tag{A.11}$$

---

[1] For $T < T_c$, the roots of these equations correspond to the spinodal singularities. They being real in mean-field is an artifact of mean-field theory.

APPENDIX (Continued)

Comparing with Eq. (A.8), we obtain $\theta = \arg\left[\mu_{LY/sp}\right]$, $\theta_a = \frac{3\pi}{2} - \frac{1}{2}\arg\left[\phi_{LY}\right] \approx \frac{3\pi}{2} - \frac{1}{4}\arg\left[r_{LY}\right]$, which is negligible when α_2 is small.

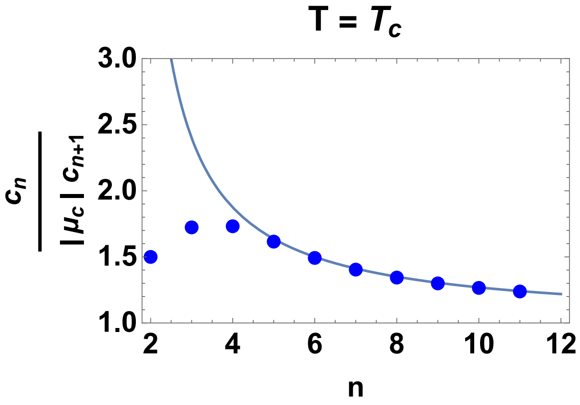

Figure 45: The estimates for radius of convergence scaled by their actual value plotted as a function of n in VDW gas for $a = 0.3, b = 0.3, \mu_c = 0.5, s_c = 0.1$. The black curve is the curve predicted by Eq. (A.9) with $a_p = 4/3, \theta = 0$.

APPENDIX (Continued)

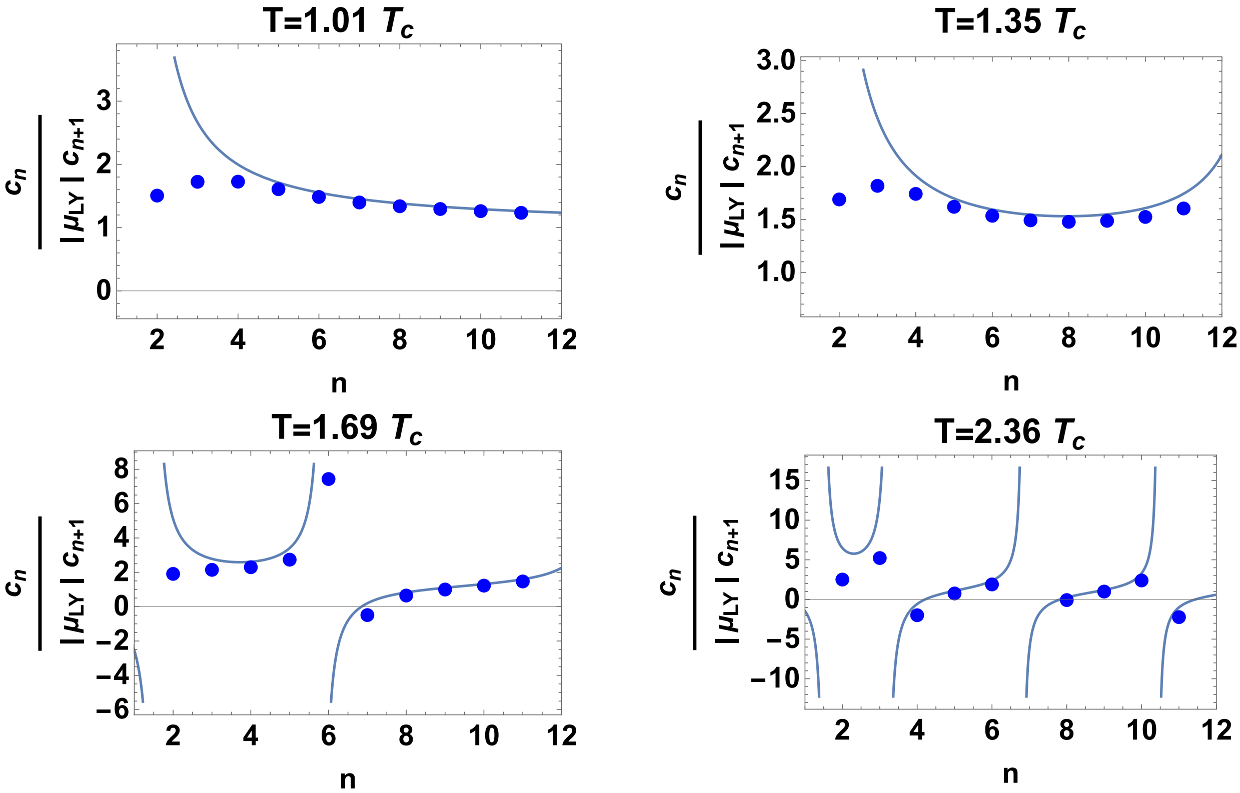

Figure 46: The estimates for radius of convergence scaled by the magnitude of the chemical potential at the Lee-Yang singularity in Van-der-waals gas (with $a = 0.3, b = 0.3, \mu_c = 0.5, s_c = 0.1$) plotted as a function of n at temperature corresponding to various temperatures $T > T_c$ compared to the universal prediction for large n obtained using Eq. (A.9) with $a_p = 3/2, \theta = \arg[\mu_{LY}]$ and $\theta_a \approx 3\pi/2$.

APPENDIX

SLOPE ANGLE α_1 FROM EOS AND DERIVATIVES AT $\mu = 0$

There are different ways to define the pseudo-critical temperature at lower baryon chemical potential values where we know the transition is a cross-over as a function of temperature T. The deviations between the pseudo-critical temperatures obtained using these different definitions goes to zero as one approaches the critical point. It is common to define the pseudo-critical temperature as the temperature at which the chiral susceptibility $\chi \equiv (\partial^2 P/\partial m_q^2)_{T,\mu}$ attains its maxima for a given μ in the cross-over region [18]. If the full form of $\chi(\mu, T)$ is known, one expects $\chi(\mu_c, T)$ to have the its maxima at $T = T_c$. α_1 is the slope of the first-order line or equivalently the pseudo-critical curve at the critical point, (μ_c, T_c) [63].

χ and its lower order derivatives with respect to μ along $\mu = 0$ axis can be calculated using lattice techniques. One can determine the maxima $T(\mu)$ of the function $\chi(\mu, T)$ expressed as a truncated Taylor expansion in μ (i.e polynomial in μ). Since the EoS near the critical point is not describable by a Taylor expansion, one might suspect the validity of the pseudo-critical curve obtained from the Taylor expansion for μ values close to $\mu = \mu_c$. In what follows, we'll compare the pseudo-critical curves obtained via evaluating the maxima of the chiral susceptibility in Random Matrix Model ([48], discussed in Section. (3.7) for $m_q = 5\,\mathrm{MeV}$ using the full expression for pressure in the model and that obtained from the truncated Taylor expansion for pressure at $\mu = 0$. In this model calculation, we find that that the pseudo-critical temperatures at the critical baryon chemical potential determined from the truncated Taylor expansion agrees with the known critical temperature within 12%.

Let the truncated Taylor expansion for χ upto $O(\mu^4)$ be:

$$\chi(\mu, T) = c_0(T) + c_2(T)\mu^2 + \frac{c_4(T)}{2}\mu^4 \tag{B.1}$$

and the truncated Taylor expansion for the pseudo-critical curve, denoted by $T_{pc}(\mu)$ be:

$$T_{pc}^2(\mu) = T_0^2 + \kappa_2\mu^2 + \frac{\kappa_4}{2}\mu^4 \tag{B.2}$$

Our objective is to obtain T_0, κ_2 and κ_4 by evaluating the maxima of Eq. (B.1) for a fixed μ. This can be done along lines of [233].

Taking derivative of χ given in Eq. (B.1) with respect to T^2:

$$\begin{aligned}
\frac{\partial\chi}{\partial T^2} &= c_0^{'}(T) + c_2^{'}(T)\mu^2 + \frac{c_4^{'}}{2}\mu^4 \\
&= \left(c_0^{'}(T_0) + c_2^{'}(T_0)\mu^2 + \frac{c_4^{'}(T_0)}{2}\mu^4 \right) + \left(c_0^{''}(T_0) + c_2^{''}(T_0)\mu^2 + \frac{c_4^{''}(T_0)}{2}\mu^4 \right)(T^2 - T_0^2) \\
&\quad + \left(c_0^{'''}(T_0) + c_2^{'''}(T_0)\mu^2 + \frac{c_4^{'''}(T_0)}{2}\mu^4 \right)\frac{(T^2 - T_0^2)^2}{2} + .. \\
&= c_0^{'}(T_0) + \left(c_2^{'}(T_0) + c_0^{''}(T_0)\kappa_2 \right)\mu^2 + \left(\frac{c_4^{'}(T_0)}{2} + c_2^{''}(T_0)\kappa_2 + \frac{c_0^{''}(T_0)}{2}\kappa_4 + \frac{c_0^{'''}(T_0)}{2}\kappa_2^2 \right)\mu^4 + O(\mu^6)
\end{aligned} \tag{B.3}$$

In the above Eqs., $'$ refers to differentiation by T^2. Equating $\partial\chi/\partial T^2$ to zero order by order in μ, one can obtain T_0 by solving $c_0^{'} = 0$ and

$$\kappa_2 = -\frac{c_2^{'}}{c_0^{''}} \tag{B.4}$$

$$\kappa_4 = -\frac{c_0^{'''}\kappa_2^2 + 2c_2^{''}\kappa_2 + c_4^{'}}{c_0^{''}} \tag{B.5}$$

We obtain, $T_0 \approx 174\,\mathrm{MeV}\,, \kappa_2 \approx -0.016\,, \kappa_4 \approx -8.0 * 10^{-9}\,\mathrm{MeV}^2$. Evaluating the slope angle α_1 from the pseudo critical curve defined by Eq. (B.2), we get $\alpha_1 \approx 10.5°$. (Compare it with $\alpha_1 \approx 13°$ obtained using the full EoS in Section. (3.7).

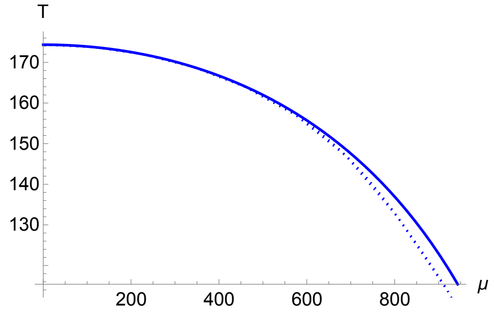

Figure 47: The dashed and solid lines correspond to the pseudo critical $T_{pc}(\mu)$ curve obtained from the full EoS and that which is truncated at $O(\mu^4)$ obtained by taking square root of Eq. (B.2) with $T_0 \approx 174\,\mathrm{MeV}\,, \kappa_2 \approx -0.016\,, \kappa_4 \approx -8.0 * 10^{-9}\,\mathrm{MeV}^2$ respectively. The pseudo-critical temperatures at the critical baryon chemical potential determined from the truncated Taylor expansion agrees with the known critical temperature within 12%.

APPENDIX

EQUATION OF STATE USED IN THE HYDRODYNAMICAL EVOLUTION

The equation of state that we have used in the analytical calculations of Section 4.3, done within a Bjorken scenario, as well as in the numerical Hydro+ simulations for a semi-realistic scenario done in Section 4.4, is taken from Ref. [128]. We describe this equation of state briefly in this Appendix. An aspect of the physics that the Hydro+ formalism is well-suited to describe is the way in which the out-of-equilibrium fluctuations of the slow modes modify the equation of state [116]. However, it has been observed in Refs. [128] and [129] that these backreaction effects are smaller than 1 % in most cases. For this reason, throughout the present work we neglect the feedback of Hydro+ modes on the equation of state. That is, in the notation of Refs. [116, 128, 129] we approximate the Hydro+ equation of state $p_+(\varepsilon)$ by the standard pressure $p(\varepsilon)$ given by

$$p = \frac{s}{\beta} - \varepsilon \tag{C.1}$$

where ε is the energy density, β is the inverse temperature, and where the entropy density s is given as a function of the local temperature by

$$s(T) = \int_0^T dT' \, \frac{c_V(T')}{T'} \tag{C.2}$$

with $c_V(T)$ being the specific heat capacity at fixed volume. In Ref. [128], the equation of state is specified close to and away from a critical temperature T_c by choosing

$$c_V(T) = \begin{cases} c_V^{\text{no C.P}}(T) & T \leq T_L \,\text{or}\, T \geq T_H \\ c_V^{\text{crit}}(T) + \sum_{n=0}^{5} c_n \left(\frac{T-T_c}{\Delta T}\right)^n & T_L < T < T_H \end{cases} \tag{C.3}$$

with $(T_L, T_H) = (T_c - \Delta T, T_c + \Delta T)$ and where ΔT, which parametrizes the width of the critical region, is the same parameter that arises in Eq. (4.9). Here as there, we take $\Delta T = T_c/5$. Following Ref. [128], we take $c_V^{\text{crit}}(T)$, the critical part of c_V that shows the leading singular behavior near the critical point, to have the form

$$c_V^{\text{crit}}(T) \equiv \frac{1}{2} \frac{1}{\xi_0^3} \frac{\xi(T)}{\xi_0}\,, \tag{C.4}$$

where the temperature dependence of the correlation length of critical fluctuations, $\xi(T)$, needs to be specified. Following Ref. [128], we do so as in Eq. (4.9). The prefactor 1/2 in Eq. (C.4) is a non-universal constant whose value depends on the mapping between the equation of state of the 3D Ising model and the equation of state of QCD, whose critical point is in the 3D Ising universality class. We have used a value that is reasonable for $\Delta T = T_c/5$; see the argument in Ref. [128]. Continuing to follow Ref. [128], away from the critical point we choose the form of the specific heat capacity $c_V^{\text{no C.P}}(T)$ as follows:

$$\frac{c_V^{\text{no C.P}}(T)}{T^3} \equiv \left[\frac{a_H + a_L}{2} + \frac{a_H - a_L}{2} \tanh \frac{T - T_{\text{crossover}}}{\Delta T_{\text{crossover}}}\right] \tag{C.5}$$

with

$$a_L = 0.1\, a_{\rm QGP}\,, \quad a_H = 0.8\, a_{\rm QGP}\,, \quad \text{and } a_{\rm QGP} \equiv \frac{4\pi^2(N_c^2-1)+21\pi^2 N_f}{15}\,, \tag{C.6}$$

where $N_c = 3$ and $N_f = 3$ are the number of flavors and colors respectively, and with

$$T_{\rm crossover} = T_c\,, \quad \Delta T_{\rm crossover} = 0.6\, T_c\,. \tag{C.7}$$

The specification of the equation of state is completed by choosing the six constant coefficients c_n that appear in Eq. (C.3) so as to enforce that $c_V(T)/T^3$ and its first two derivatives are continuous at $T = T_L$ and at $T = T_H$.

APPENDIX

DERIVATION OF D_3 AND D_4

In this Appendix we will derive Eq. (6.64a) and Eq. (6.64b).

D_3 was defined in Eq. (6.61a). Linearizing D^{fde} in $\Delta G_{ABC} = G_{ABC} - \bar{G}_{ABC}$ and $\Delta G_{AB} = G_{AB} - \bar{G}_{AB}$,

$$D_3^{fde}(x_1, x_2, x_3) = \bar{H}^{fde} + 3\left[\int_{\tilde{A},\tilde{B},\tilde{C}} \Delta G_{AQ} C^{(3)}_{QRS} \bar{G}_{BR} \bar{G}_{CS} P^f_A P^d_B P^e_C\right]_{\overline{fde}} + \dots \tag{D.1a}$$

$$= \bar{H}^{fde} + 3\left[\int_{\tilde{A},\tilde{B},\tilde{C}} \Delta G_{AQ} \bar{G}^{-1}_{QX} \bar{G}_{XY} C^{(3)}_{YRS} \bar{G}_{BR} \bar{G}_{CS} P^f_A P^d_B P^e_C\right]_{\overline{fde}} + \dots \tag{D.1b}$$

$$= \bar{H}^{fde} + 3\left[\int_{\tilde{A},\tilde{B},\tilde{C}} \Delta G_{AQ} \bar{G}^{-1}_{QX} \bar{G}_{XBC} P^f_A P^d_B P^e_C\right]_{\overline{fde}} + \dots \tag{D.1c}$$

Substituting ΔG_{AQ} given by Eq. (6.55):

$$D_3^{fde}(x_1, x_2, x_3) = \bar{H}^{fde} + 3\left[\int_{\tilde{A},\tilde{B},\tilde{C}} \Delta H_{ag} (\bar{H}^{-1} P \bar{G})^a_A (\bar{H}^{-1} P \bar{G})^g_Q \bar{G}^{-1}_{QX} \bar{G}_{XBC} P^f_A P^d_B P^e_C\right]_{\overline{fde}} + \dots \tag{D.1d}$$

$$= \bar{H}^{fde} + 3\left[\int_{\tilde{A},\tilde{B},\tilde{C}} \Delta H_{ag} (\bar{H}^{-1} P \bar{G})^a_A (\bar{H}^{-1}_{gq} P^g_X \bar{G}_{XBC} P^f_A P^d_B P^e_C\right]_{\overline{fde}} + \dots \tag{D.1e}$$

$$= \bar{H}^{fde} + 3\left[\int_{\tilde{A}} \Delta H_{ag} (\bar{H}^{-1} P \bar{G})^a_A (\bar{H}^{-1} H_3)_{gde} P^f_A\right]_{\overline{fde}} + \dots \tag{D.1f}$$

$$= \bar{H}^{fde} + 3\left[\Delta H^{ag} (\bar{H}^{-1} \bar{H})^{fa} (\bar{H}^{-1} H_3)^{gde}\right]_{\overline{fde}} + \dots \tag{D.1g}$$

$$= \bar{H}^{fde} + 3\left[\Delta H^{fg} (\bar{H}^{-1} H_3)^{gde}\right]_{\overline{fde}} + \dots \tag{D.1h}$$

Thus, we obtain Eq. (6.64a). D_4 was defined in Eq. (6.61b). Linearizing the first term in D^{abcd} in $\Delta G_{ABCD} = G_{ABCD} - \bar{G}_{ABCD}$, $\Delta G_{ABC} = G_{ABC} - \bar{G}_{ABC}$ and $\Delta G_{AB} = G_{AB} - \bar{G}_{AB}$,

$$\begin{aligned}
&\int_{\tilde{A}}\int_{\tilde{B}}\int_{\tilde{C}}\int_{\tilde{D}} P^a_A P b_B P^c_C P^d_D G_{AQ} G_{BR} G_{CS} G_{DT} C^{(4)}_{QRST} \\
= &\int_{\tilde{A}}\int_{\tilde{B}}\int_{\tilde{C}}\int_{\tilde{D}} P^a_A P b_B P^c_C P^d_D \bar{G}_{AQ} \bar{G}_{BR} \bar{G}_{CS} \bar{G}_{DT} C^{(4)}_{QRST} \\
&+4\int_{\tilde{A}}\int_{\tilde{B}}\int_{\tilde{C}}\int_{\tilde{D}} P^a_A P b_B P^c_C P^d_D \Delta G_{AQ} \bar{G}_{BR} \bar{G}_{CS} \bar{G}_{DT} C^{(4)}_{QRST}
\end{aligned} \tag{D.2}$$

Linearizing the second term in D^{abcd} in $\Delta G_{ABCD} = G_{ABCD} - \bar{G}_{ABCD}$, $\Delta G_{ABC} = G_{ABC} - \bar{G}_{ABC}$ and $\Delta G_{AB} = G_{AB} - \bar{G}_{AB}$,

$$\begin{aligned}
&\int_{\tilde{A}}\int_{\tilde{B}}\int_{\tilde{C}}\int_{\tilde{D}} P^a_A P b_B P^c_C P^d_D \int_X \int_Y 3 G^{-1}_{XY} \left[G_{YAB} G_{XCD}\right]_{\overline{ABCD}} \\
= &\int_{\tilde{A}}\int_{\tilde{B}}\int_{\tilde{C}}\int_{\tilde{D}} P^a_A P b_B P^c_C P^d_D \int_X \int_Y 3 \bar{G}^{-1}_{XY} \left[\bar{G}_{YAB} \bar{G}_{XCD}\right]_{\overline{ABCD}} \\
&+\int_{\tilde{A}}\int_{\tilde{B}}\int_{\tilde{C}}\int_{\tilde{D}} P^a_A P b_B P^c_C P^d_D \int_X \int_Y \left[6 \bar{G}^{-1}_{XY} \Delta G_{YAB} \bar{G}_{XCD} + 3\Delta (G^{-1})_{XY} \left[\bar{G}_{YAB} \bar{G}_{XCD}\right]_{\overline{ABCD}}\right]_{\overline{ABCD}}
\end{aligned} \tag{D.3}$$

Adding parts of Eq. (D.2) and Eq. (D.3) separately, we get

$$\int_{\tilde{A}}\int_{\tilde{B}}\int_{\tilde{C}}\int_{\tilde{D}} P^a_A P b_B P^c_C P^d_D \left[\bar{G}_{AQ} \bar{G}_{BR} \bar{G}_{CS} \bar{G}_{DT} C^{(4)}_{QRST} + 3\int_X \int_Y G^{-1}_{XY} G_{YAB} G_{XCD}\right]_{\overline{ABCD}} = \bar{H}^{abcd} \tag{D.4}$$

and

$$\int_{\tilde{A}}\int_{\tilde{B}}\int_{\tilde{C}}\int_{\tilde{D}} P_A^a P b_B P_C^c P_D^d \left[4\Delta G_{AQ}\bar{G}_{BR}\bar{G}_{CS}\bar{G}_{DT}C^{(4)}_{QRST} + \int_X\int_Y 6\bar{G}^{-1}_{XY}\Delta G_{YAB}\bar{G}_{XCD}\right]_{\overline{ABCD}}$$
$$= \left[6\Delta\widehat{H}_3^{abe}(\bar{H}^{-1}\bar{H}_3)^{ecd} + 4\Delta\widehat{H}^{af}(\bar{H}^{-1}\bar{H}_4)^{fbcd}\right]_{\overline{abcd}} \tag{D.5}$$

and

$$3\int_{\tilde{A}}\int_{\tilde{B}}\int_{\tilde{C}}\int_{\tilde{D}} P_A^a P b_B P_C^c P_D^d \int_X\int_Y G^{-1}_{XY}\left[G_{YAB}G_{XCD}\right]_{\overline{ABCD}} = 3\left[\Delta\widehat{H}^{ef}(\bar{H}^{-1}\bar{H}_3)^{abe}(\bar{H}^{-1}\bar{H}_3)^{fcd}\right]_{abcd} \tag{D.6}$$

Combining Eq. (D.4), Eq. (D.5) and Eq. (D.6), we get:

$$D^{abcd} = \left[\bar{H}^{abcd} + 6\Delta\widehat{H}_3^{abe}(\bar{H}^{-1}\bar{H}_3)^{ecd} + 4\Delta\widehat{H}^{af}(\bar{H}^{-1}\bar{H}_4)^{fbcd} + 3\Delta\widehat{H}^{ef}(\bar{H}^{-1}\bar{H}_3)^{abe}(\bar{H}^{-1}\bar{H}_3)^{fcd}\right]_{abcd} \tag{D.7}$$

Thus, we obtain Eq. (6.64b).

APPENDIX

REALIZATION OF MAXIMUM ENTROPIC FREEZE-OUT IN THE LIMIT OF LARGE NUMBER OF EVENTS

Let us assume that there are N possible states that can be realized at freeze-out. Let $\bar{p}_i$ be the probability that the state $\{i\}$ is realized at freeze-out in an event. Let n_i be the number of events in which $\{i\}$ is realized. The probability (P) that this happens is given by:

$$P(n_i;\bar{p}_i) = \frac{M!}{\prod_{i=1}^{N} n_i!}\prod_{i}^{N}\bar{p}_i^{n_i} \tag{E.1}$$

Let us denote :

$$p_i = \frac{n_i}{M} \tag{E.2}$$

In the limit of $n_i s, M \gg 1$, using Stirling's formula,

$$\frac{\log P(p_i;\bar{p}_i)}{M} = -\sum_{i}^{N} p_i \log\frac{p_i}{\bar{p}_i} \tag{E.3}$$

We notice that expression on the right hand side of Eq. (E.3) is the relative entropy of the probability distribution function p_i with respect to the "true" probability distribution function $\bar{p}_i$. Eq. (E.3) tells us that for large number of events, i.e $M \to \infty$, the

$$P(p_i;\bar{p}_i) \overset{M \to \infty}{=} \delta\left(p_i - \bar{p}_i\right) \tag{E.4}$$

probability of obtaining the true probability distribution function is nearly 1.

APPENDIX (Continued)

Reuse License for parts of Chapter. (3)

American Physical Society Reuse and Permissions License

02-May-2023

This license agreement between the American Physical Society ("APS") and Maneesha Sushama Pradeep ("You") consists of your license details and the terms and conditions provided by the American Physical Society and SciPris.

Licensed Content Information

License Number:	**RNP/23/MAY/065941**
License date:	02-May-2023
DOI:	10.1103/PhysRevD.100.056003
Title:	Universality of the critical point mapping between Ising model and QCD at small quark mass
Author:	Maneesha Sushama Pradeep and Mikhail Stephanov
Publication:	Physical Review D
Publisher:	American Physical Society
Cost:	USD $ 0.00

Request Details

Does your reuse require significant modifications: No

Specify intended distribution locations:	United States
Reuse Category:	Reuse in a thesis/dissertation
Requestor Type:	Author of requested content
Items for Reuse:	Whole Article
Format for Reuse:	Electronic

Information about New Publication:

University/Publisher:	University of Illinois at Chicago
Title of dissertation/thesis:	Mapping the phase diagram of Quantum Chromodynamics via fluctuations
Author(s):	Maneesha Sushama Pradeep
Expected completion date:	Aug. 2023

License Requestor Information

Name:	Maneesha Sushama Pradeep
Affiliation:	Individual
Email Id:	manishaspradeep@gmail.com
Country:	United States

American Physical Society
Reuse and Permissions License

TERMS AND CONDITIONS

The American Physical Society (APS) is pleased to grant the Requestor of this license a non-exclusive, non-transferable permission, limited to Electronic format, provided all criteria outlined below are followed.

1. You must also obtain permission from at least one of the lead authors for each separate work, if you haven't done so already. The author's name and affiliation can be found on the first page of the published Article.
2. For electronic format permissions, Requestor agrees to provide a hyperlink from the reprinted APS material using the source material's DOI on the web page where the work appears. The hyperlink should use the standard DOI resolution URL, http://dx.doi.org/{DOI}. The hyperlink may be embedded in the copyright credit line.
3. For print format permissions, Requestor agrees to print the required copyright credit line on the first page where the material appears: "Reprinted (abstract/excerpt/figure) with permission from [(FULL REFERENCE CITATION) as follows: Author's Names, APS Journal Title, Volume Number, Page Number and Year of Publication.] Copyright (YEAR) by the American Physical Society."
4. Permission granted in this license is for a one-time use and does not include permission for any future editions, updates, databases, formats or other matters. Permission must be sought for any additional use.
5. Use of the material does not and must not imply any endorsement by APS.
6. APS does not imply, purport or intend to grant permission to reuse materials to which it does not hold copyright. It is the requestor's sole responsibility to ensure the licensed material is original to APS and does not contain the copyright of another entity, and that the copyright notice of the figure, photograph, cover or table does not indicate it was reprinted by APS with permission from another source.
7. The permission granted herein is personal to the Requestor for the use specified and is not transferable or assignable without express written permission of APS. This license may not be amended except in writing by APS.
8. You may not alter, edit or modify the material in any manner.
9. You may translate the materials only when translation rights have been granted.
10. APS is not responsible for any errors or omissions due to translation.
11. You may not use the material for promotional, sales, advertising or marketing purposes.
12. The foregoing license shall not take effect unless and until APS or its agent, Aptara, receives payment in full in accordance with Aptara Billing and Payment Terms and Conditions, which are incorporated herein by reference.
13. Should the terms of this license be violated at any time, APS or Aptara may revoke the license with no refund to you and seek relief to the fullest extent of the laws of the USA. Official written notice will be made using the contact information provided with the permission request. Failure to receive such notice will not nullify revocation of the permission.
14. APS reserves all rights not specifically granted herein.
15. This document, including the Aptara Billing and Payment Terms and Conditions, shall be the entire agreement between the parties relating to the subject matter hereof.

VITA

Maneesha Sushama Pradeep Email : mprade2@uic.edu

Education

- **University of Illinois at Chicago** USA
  Ph.D. in Physics, GPA: 4.0/4.0 *Fall 2015-Summer 2023 (expected)*
- **National Institute of Science Education and Research** Bhubaneswar, India
  Integrated Master of Science, Physics, GPA: 8.3/10 *Aug. 2010 – July. 2015*

Awards and honors received

- UIC Dean Scholar Fellowship for the academic year 2022-23
- Vladimir N.Gribov Diploma awarded at the International School of Subnuclear Physics held at Ettore Majorana Foundation and Centre for Scientific Culture fron June 15-24, 2022
- Paul M. Raccah Award for Doctoral Studies in Physics in 2016 awarded for obtaining the highest score in the PhD qualifying examination at UIC
- Innovation in Science Pursuit for Inspired Research(INSPIRE) Scholarship Department of Science and Technology, Government of India (2010-2015)
- Indian Academy of Science(IAS) Fellowship Department of Science and Technology,Government of India (2012, 2013)

Publications and Preprints

- Maneesha Sushama Pradeep (Illinois U., Chicago), Mikhail Stephanov (Illinois U., Chicago), Maximum entropy freezeout of hydrodynamic fluctuations, arXiv: 2211.09142 [hep-ph]
- Maneesha Pradeep (Illinois U., Chicago), Krishna Rajagopal (MIT), Mikhail Stephanov (Illinois U., Chicago), Yi Yin (Lanzhou, Inst. Modern Phys.),Freezing out fluctuations in Hydro+ near the QCD critical point, arXiv: 2204.00639 [hep-ph], Published in: Phys.Rev.D 106 (2022) 3, 036017
- Maneesha Pradeep (Illinois U., Chicago), Krishna Rajagopal (MIT, Cambridge, CTP), Misha Stephanov (Illinois U., Chicago), Yi Yin (Lanzhou, Inst. Modern Phys.), Freezing out critical fluctuations, arXiv: 2109.13188 [hep-ph]
- Xin An (North Carolina U.), Marcus Bluhm (SUBATECH, Nantes), Lipei Du (Ohio State U.), Gerald V. Dunne (Connecticut U.), Hannah Elfner (Darmstadt, GSI and Frankfurt U. and Frankfurt U., FIAS) et al., arXiv: 2108.13867 [nucl-th], Published in: Nucl.Phys.A 1017 (2022), 122343
- Pradeep, Maneesha Sushama and Stephanov, Mikhail, Universality of the critical point mapping between Ising model and QCD at small quark mass, arXiv:1905.13247 [hep-ph], Published in : Phys.Rev.D 100 (2019) 5, 056003

CITED LITERATURE

1. M. S. Pradeep and M. Stephanov, Universality of the critical point mapping between Ising model and QCD at small quark mass, Phys. Rev. D **100**, 056003 (2019), 1905.13247.

2. M. Pradeep, K. Rajagopal, M. Stephanov, and Y. Yin, Freezing out fluctuations in Hydro+ near the QCD critical point, Phys. Rev. D **106**, 036017 (2022), 2204.00639.

3. M. Pradeep, K. Rajagopal, M. Stephanov, and Y. Yin, Freezing out critical fluctuations, PoS **CPOD2021**, 035 (2022), 2109.13188.

4. X. An *et al.*, The BEST framework for the search for the QCD critical point and the chiral magnetic effect, Nucl. Phys. A **1017**, 122343 (2022), 2108.13867.

5. M. S. Pradeep and M. Stephanov, Maximum Entropy Freeze-Out of Hydrodynamic Fluctuations, Phys. Rev. Lett. **130**, 162301 (2023), 2211.09142.

6. R. L. Workman *et al.*, Review of Particle Physics, PTEP **2022**, 083C01 (2022).

7. A. Aprahamian *et al.*, Reaching for the horizon: The 2015 long range plan for nuclear science (2015).

8. P. de Forcrand and M. D'Elia, Continuum limit and universality of the Columbia plot, PoS **LATTICE2016**, 081 (2017), 1702.00330.

9. M. A. Stephanov, K. Rajagopal, and E. V. Shuryak, Signatures of the tricritical point in QCD, Phys. Rev. Lett. **81**, 4816 (1998), hep-ph/9806219.

10. S. Borsanyi, Z. Fodor, C. Hoelbling, S. D. Katz, S. Krieg, and K. K. Szabo, Full result for the QCD equation of state with 2+1 flavors, Phys. Lett. B **730**, 99 (2014), 1309.5258.

11. N. Haque, A. Bandyopadhyay, J. O. Andersen, M. G. Mustafa, M. Strickland, and N. Su, Three-loop HTLpt thermodynamics at finite temperature and chemical potential, JHEP **05**, 027 (2014), 1402.6907.

12. A. Andronic, P. Braun-Munzinger, K. Redlich, and J. Stachel, Decoding the phase structure of QCD via particle production at high energy, Nature **561**, 321 (2018), 1710.09425.

13. C. Shen and S. Alzhrani, Collision-geometry-based 3D initial condition for relativistic heavy-ion collisions, Phys. Rev. C **102**, 014909 (2020), `2003.05852`.

14. M. Abdallah *et al.*, Cumulants and correlation functions of net-proton, proton, and antiproton multiplicity distributions in Au+Au collisions at energies available at the BNL Relativistic Heavy Ion Collider, Phys. Rev. C **104**, 024902 (2021), `2101.12413`.

15. M. Arslandok *et al.*, Hot QCD White Paper (2023), `2303.17254`.

16. W. Busza, K. Rajagopal, and W. van der Schee, Heavy Ion Collisions: The Big Picture, and the Big Questions, Ann. Rev. Nucl. Part. Sci. **68**, 339 (2018), `1802.04801`.

17. A. Bzdak, S. Esumi, V. Koch, J. Liao, M. Stephanov, and N. Xu, Mapping the Phases of Quantum Chromodynamics with Beam Energy Scan, Phys. Rept. **853**, 1 (2020), `1906.00936`.

18. A. Bazavov *et al.*, Chiral crossover in QCD at zero and non-zero chemical potentials, Phys. Lett. B **795**, 15 (2019), `1812.08235`.

19. H.-T. Ding, F. Karsch, and S. Mukherjee, Thermodynamics of strong-interaction matter from Lattice QCD, Int. J. Mod. Phys. **E24**, 1530007 (2015), `1504.05274`.

20. M. A. Stephanov, QCD phase diagram and the critical point, Prog. Theor. Phys. Suppl. **153**, 139 (2004), [Int. J. Mod. Phys.A20,4387(2005)], `hep-ph/0402115`.

21. R. D. Pisarski and F. Wilczek, Remarks on the Chiral Phase Transition in Chromodynamics, Phys. Rev. D **29**, 338 (1984).

22. M. Grahl and D. H. Rischke, Functional renormalization group study of the two-flavor linear sigma model in the presence of the axial anomaly, Phys. Rev. D **88**, 056014 (2013), `1307.2184`.

23. A. Pelissetto and E. Vicari, Relevance of the axial anomaly at the finite-temperature chiral transition in QCD, Phys. Rev. D **88**, 105018 (2013), `1309.5446`.

24. F. Basile, A. Pelissetto, and E. Vicari, Finite-temperature chiral transition in QCD with quarks in the fundamental and adjoint representation, PoS **LAT2005**, 199 (2006), `hep-lat/0509018`.

25. G. Fejos, Second-order chiral phase transition in three-flavor quantum chromodynamics?, Phys. Rev. D **105**, L071506 (2022), 2201.07909.

26. F. Wilczek, Application of the renormalization group to a second order QCD phase transition, Int. J. Mod. Phys. A **7**, 3911 (1992), [Erratum: Int.J.Mod.Phys.A 7, 6951 (1992)].

27. K. Rajagopal and F. Wilczek, Static and dynamic critical phenomena at a second order QCD phase transition, Nucl. Phys. B **399**, 395 (1993), hep-ph/9210253.

28. G. Aarts *et al.*, Phase Transitions in Particle Physics - Results and Perspectives from Lattice Quantum Chromo-Dynamics, in *Phase Transitions in Particle Physics: Results and Perspectives from Lattice Quantum Chromo-Dynamics* (2023), 2301.04382.

29. S. Sharma, Updates on the QCD phase diagram from lattice, AAPPS Bull. **31**, 13 (2021).

30. H. T. Ding *et al.*, Chiral Phase Transition Temperature in (2+1)-Flavor QCD, Phys. Rev. Lett. **123**, 062002 (2019), 1903.04801.

31. Y. Aoki, G. Endrodi, Z. Fodor, S. D. Katz, and K. K. Szabo, The Order of the quantum chromodynamics transition predicted by the standard model of particle physics, Nature **443**, 675 (2006), hep-lat/0611014.

32. A. Bazavov *et al.*, The chiral and deconfinement aspects of the QCD transition, Phys. Rev. D **85**, 054503 (2012), 1111.1710.

33. T. Bhattacharya *et al.*, QCD Phase Transition with Chiral Quarks and Physical Quark Masses, Phys. Rev. Lett. **113**, 082001 (2014), 1402.5175.

34. A. Bazavov, H. T. Ding, P. Hegde, F. Karsch, E. Laermann, S. Mukherjee, P. Petreczky, and C. Schmidt, Chiral phase structure of three flavor QCD at vanishing baryon number density, Phys. Rev. D **95**, 074505 (2017), 1701.03548.

35. G. Boyd, J. Engels, F. Karsch, E. Laermann, C. Legeland, M. Lutgemeier, and B. Petersson, Thermodynamics of SU(3) lattice gauge theory, Nucl. Phys. B **469**, 419 (1996), hep-lat/9602007.

36. A. M. Polyakov, Thermal Properties of Gauge Fields and Quark Liberation, Phys. Lett. B **72**, 477 (1978).

37. L. Susskind, Lattice Models of Quark Confinement at High Temperature, Phys. Rev. D **20**, 2610 (1979).

38. A. Bazavov *et al.*, Equation of state in (2+1)-flavor QCD, Phys. Rev. D **90**, 094503 (2014), 1407.6387.

39. A. Bazavov *et al.*, The QCD Equation of State to $\mathcal{O}(\mu_B^6)$ from Lattice QCD, Phys. Rev. D **95**, 054504 (2017), 1701.04325.

40. M. A. Stephanov, K. Rajagopal, and E. V. Shuryak, Event-by-event fluctuations in heavy ion collisions and the QCD critical point, Phys. Rev. D **60**, 114028 (1999), hep-ph/9903292.

41. A. Chodos, R. L. Jaffe, K. Johnson, C. B. Thorn, and V. F. Weisskopf, A New Extended Model of Hadrons, Phys. Rev. D **9**, 3471 (1974).

42. A. Chodos, R. L. Jaffe, K. Johnson, and C. B. Thorn, Baryon Structure in the Bag Theory, Phys. Rev. D **10**, 2599 (1974).

43. Y. Nambu and G. Jona-Lasinio, Dynamical Model of Elementary Particles Based on an Analogy with Superconductivity. 1., Phys. Rev. **122**, 345 (1961).

44. Y. Nambu and G. Jona-Lasinio, Dynamical model of elementary particles based on an analogy with superconductivity. II., Phys. Rev. **124**, 246 (1961).

45. S. P. Klevansky, The Nambu-Jona-Lasinio model of quantum chromodynamics, Rev. Mod. Phys. **64**, 649 (1992).

46. L. Stodolsky, Temperature fluctuations in multiparticle production, Phys. Rev. Lett. **75**, 1044 (1995).

47. M. A. Stephanov, Random matrix model of QCD at finite density and the nature of the quenched limit, Phys. Rev. Lett. **76**, 4472 (1996), hep-lat/9604003.

48. A. M. Halasz, A. D. Jackson, R. E. Shrock, M. A. Stephanov, and J. J. M. Verbaarschot, On the phase diagram of QCD, Phys. Rev. **D58**, 096007 (1998), hep-ph/9804290.

49. R. Rapp, T. Schäfer, E. V. Shuryak, and M. Velkovsky, Diquark Bose condensates in high density matter and instantons, Phys. Rev. Lett. **81**, 53 (1998), hep-ph/9711396.

50. M. G. Alford, K. Rajagopal, and F. Wilczek, QCD at finite baryon density: Nucleon droplets and color superconductivity, Phys. Lett. B **422**, 247 (1998), hep-ph/9711395.

51. J. Berges and K. Rajagopal, Color superconductivity and chiral symmetry restoration at nonzero baryon density and temperature, Nucl. Phys. **B538**, 215 (1999), hep-ph/9804233.

52. R. Critelli, J. Noronha, J. Noronha-Hostler, I. Portillo, C. Ratti, and R. Rougemont, Critical point in the phase diagram of primordial quark-gluon matter from black hole physics, Phys. Rev. D **96**, 096026 (2017), 1706.00455.

53. J. Grefa, J. Noronha, J. Noronha-Hostler, I. Portillo, C. Ratti, and R. Rougemont, Hot and dense quark-gluon plasma thermodynamics from holographic black holes, Phys. Rev. D **104**, 034002 (2021), 2102.12042.

54. T. Andrews, Xviii. <i>the bakerian lecture</i>.—on the continuity of the gaseous and liquid states of matter, Philosophical Transactions of the Royal Society of London **159**, 575 (1869), https://royalsocietypublishing.org/doi/pdf/10.1098/rstl.1869.0021.

55. M. v Smoluchowski, Molekular-kinetische theorie der opaleszenz von gasen im kritischen zustande, sowie einiger verwandter erscheinungen, Annalen der Physik. **330** (1908).

56. M. A. Stephanov, Non-Gaussian fluctuations near the QCD critical point, Phys. Rev. Lett. **102**, 032301 (2009), 0809.3450.

57. M. A. Stephanov, On the sign of kurtosis near the QCD critical point, Phys. Rev. Lett. **107**, 052301 (2011), 1104.1627.

58. R. Guida and J. Zinn-Justin, 3-D Ising model: The Scaling equation of state, Nucl. Phys. B **489**, 626 (1997), hep-th/9610223.

59. J. Zinn-Justin, *Quantum field theory and critical phenomena*, *International Series of Monographs on Physics*, volume 77 (Oxford University Press 2021).

60. S. Borsanyi, G. Endrodi, Z. Fodor, A. Jakovac, S. D. Katz, S. Krieg, C. Ratti, and K. K. Szabo, The QCD equation of state with dynamical quarks, JHEP **11**, 077 (2010), 1007.2580.

61. D. Bollweg, D. A. Clarke, J. Goswami, O. Kaczmarek, F. Karsch, S. Mukherjee, P. Petreczky, C. Schmidt, and S. Sharma, Equation of state and speed of sound of (2+1)-flavor

QCD in strangeness-neutral matter at non-vanishing net baryon-number density (2022), 2212.09043.

62. C. Nonaka and M. Asakawa, Hydrodynamical evolution near the QCD critical end point, Phys. Rev. **C71**, 044904 (2005), nucl-th/0410078.

63. P. Parotto, M. Bluhm, D. Mroczek, M. Nahrgang, J. Noronha-Hostler, K. Rajagopal, C. Ratti, T. Schfer, and M. Stephanov, Lattice-QCD-based equation of state with a critical point (2018), 1805.05249.

64. J. I. Kapusta and T. Welle, Extending a scaling equation of state to QCD, Phys. Rev. C **106**, 044901 (2022), 2205.12150.

65. D. Almaalol *et al.*, QCD Phase Structure and Interactions at High Baryon Density: Continuation of BES Physics Program with CBM at FAIR (2022), 2209.05009.

66. S. Leupold *et al.*, Bulk properties of strongly interacting matter, Lect. Notes Phys. **814**, 39 (2011).

67. V. Dexheimer, J. Noronha, J. Noronha-Hostler, C. Ratti, and N. Yunes, Future physics perspectives on the equation of state from heavy ion collisions to neutron stars, J. Phys. G **48**, 073001 (2021), 2010.08834.

68. R. Kumar *et al.*, Theoretical and Experimental Constraints for the Equation of State of Dense and Hot Matter (2023), 2303.17021.

69. A. Sorensen *et al.*, Dense Nuclear Matter Equation of State from Heavy-Ion Collisions (2023), 2301.13253.

70. P. Achenbach *et al.*, The Present and Future of QCD (2023), 2303.02579.

71. STAR, Studying the phase diagram of qcd matter at rhic, `https://drupal.star.bnl.gov/STAR/files/BES_WPII_ver6.9_Cover.pdf` (2014).

72. M. Floris, Hadron yields and the phase diagram of strongly interacting matter, Nucl. Phys. A **931**, 103 (2014), 1408.6403.

73. J. Cleymans, H. Oeschler, K. Redlich, and S. Wheaton, Comparison of chemical freeze-out criteria in heavy-ion collisions, Phys. Rev. C **73**, 034905 (2006), hep-ph/0511094.

74. J. C. Collins and M. J. Perry, Superdense Matter: Neutrons Or Asymptotically Free Quarks?, Phys. Rev. Lett. **34**, 1353 (1975).

75. T. Niida and Y. Miake, Signatures of QGP at RHIC and the LHC, AAPPS Bull. **31**, 12 (2021), `2104.11406`.

76. E. Shuryak, Strongly coupled quark-gluon plasma in heavy ion collisions, Rev. Mod. Phys. **89**, 035001 (2017), `1412.8393`.

77. U. Heinz and R. Snellings, Collective flow and viscosity in relativistic heavy-ion collisions, Ann. Rev. Nucl. Part. Sci. **63**, 123 (2013), `1301.2826`.

78. C. Gale, S. Jeon, and B. Schenke, Hydrodynamic Modeling of Heavy-Ion Collisions, Int. J. Mod. Phys. A **28**, 1340011 (2013), `1301.5893`.

79. L. Yan, A flow paradigm in heavy-ion collisions, Chin. Phys. C **42**, 042001 (2018), `1712.04580`.

80. P. Romatschke, New Developments in Relativistic Viscous Hydrodynamics, Int. J. Mod. Phys. E **19**, 1 (2010), `0902.3663`.

81. W. Florkowski, M. P. Heller, and M. Spalinski, New theories of relativistic hydrodynamics in the LHC era, Rept. Prog. Phys. **81**, 046001 (2018), `1707.02282`.

82. P. Romatschke and U. Romatschke, *Relativistic Fluid Dynamics In and Out of Equilibrium*, Cambridge Monographs on Mathematical Physics (Cambridge University Press 2019), `1712.05815`.

83. B. Schenke, C. Shen, and P. Tribedy, Running the gamut of high energy nuclear collisions, Phys. Rev. C **102**, 044905 (2020), `2005.14682`.

84. J.-Y. Ollitrault, Anisotropy as a signature of transverse collective flow, Phys. Rev. D **46**, 229 (1992).

85. B. Alver and G. Roland, Collision geometry fluctuations and triangular flow in heavy-ion collisions, Phys. Rev. C **81**, 054905 (2010), [Erratum: Phys.Rev.C 82, 039903 (2010)], `1003.0194`.

86. S. A. Voloshin, Collective phenomena in ultra-relativistic nuclear collisions: anisotropic flow and more, Prog. Part. Nucl. Phys. **67**, 541 (2012), `1111.7241`.

87. P. Kovtun, D. T. Son, and A. O. Starinets, Viscosity in strongly interacting quantum field theories from black hole physics, Phys. Rev. Lett. **94**, 111601 (2005), `hep-th/0405231`.

88. H. Petersen, D. Oliinychenko, M. Mayer, J. Staudenmaier, and S. Ryu, SMASH – A new hadronic transport approach, Nucl. Phys. A **982**, 399 (2019), `1808.06832`.

89. J. Novak, K. Novak, S. Pratt, J. Vredevoogd, C. Coleman-Smith, and R. Wolpert, Determining Fundamental Properties of Matter Created in Ultrarelativistic Heavy-Ion Collisions, Phys. Rev. C **89**, 034917 (2014), `1303.5769`.

90. S. Pratt, E. Sangaline, P. Sorensen, and H. Wang, Constraining the Eq. of State of Super-Hadronic Matter from Heavy-Ion Collisions, Phys. Rev. Lett. **114**, 202301 (2015), `1501.04042`.

91. W. Ke, J. S. Moreland, J. E. Bernhard, and S. A. Bass, Constraints on rapidity-dependent initial conditions from charged particle pseudorapidity densities and two-particle correlations, Phys. Rev. C **96**, 044912 (2017), `1610.08490`.

92. J. E. Bernhard, J. S. Moreland, S. A. Bass, J. Liu, and U. Heinz, Applying Bayesian parameter estimation to relativistic heavy-ion collisions: simultaneous characterization of the initial state and quark-gluon plasma medium, Phys. Rev. C **94**, 024907 (2016), `1605.03954`.

93. J. E. Bernhard, J. S. Moreland, and S. A. Bass, Bayesian estimation of the specific shear and bulk viscosity of quark–gluon plasma, Nature Phys. **15**, 1113 (2019).

94. D. Everett *et al.*, Multisystem Bayesian constraints on the transport coefficients of QCD matter, Phys. Rev. C **103**, 054904 (2021), `2011.01430`.

95. J. H. Putschke *et al.*, The JETSCAPE framework (2019), `1903.07706`.

96. Y. Nara *et al.*, *Dynamical Evolution of Heavy-Ion Collisions* (2022).

97. E. V. Shuryak, Event per event analysis of heavy ion collisions and thermodynamical fluctuations, Phys. Lett. B **423**, 9 (1998), `hep-ph/9704456`.

98. M. Gazdzicki and S. Mrowczynski, A Method to study 'equilibration' in nucleus-nucleus collisions, Z. Phys. C **54**, 127 (1992).

99. M. Gazdzicki, A. Leonidov, and G. Roland, On event by event fluctuations in nuclear collisions, Eur. Phys. J. C **6**, 365 (1999), hep-ph/9711422.

100. S. Jeon and V. Koch, Fluctuations of particle ratios and the abundance of hadronic resonances, Phys. Rev. Lett. **83**, 5435 (1999), nucl-th/9906074.

101. S. Jeon and V. Koch, Charged particle ratio fluctuation as a signal for QGP, Phys. Rev. Lett. **85**, 2076 (2000), hep-ph/0003168.

102. M. Asakawa, U. W. Heinz, and B. Muller, Fluctuation probes of quark deconfinement, Phys. Rev. Lett. **85**, 2072 (2000), hep-ph/0003169.

103. Y. Hatta and M. A. Stephanov, Proton number fluctuation as a signal of the QCD critical endpoint, Phys. Rev. Lett. **91**, 102003 (2003), [Erratum: Phys.Rev.Lett. 91, 129901 (2003)], hep-ph/0302002.

104. A. Bzdak and V. Koch, Rapidity dependence of proton cumulants and correlation functions, Phys. Rev. C **96**, 054905 (2017), 1707.02640.

105. C. Athanasiou, K. Rajagopal, and M. Stephanov, Using Higher Moments of Fluctuations and their Ratios in the Search for the QCD Critical Point, Phys. Rev. D **82**, 074008 (2010), 1006.4636.

106. L. Jiang, P. Li, and H. Song, Correlated fluctuations near the QCD critical point, Phys. Rev. C **94**, 024918 (2016), 1512.06164.

107. J. M. Karthein, D. Mroczek, A. R. Nava Acuna, J. Noronha-Hostler, P. Parotto, D. R. P. Price, and C. Ratti, Strangeness-neutral equation of state for QCD with a critical point, Eur. Phys. J. Plus **136**, 621 (2021), 2103.08146.

108. D. Mroczek, A. R. Nava Acuna, J. Noronha-Hostler, P. Parotto, C. Ratti, and M. A. Stephanov, Quartic cumulant of baryon number in the presence of a QCD critical point, Phys. Rev. C **103**, 034901 (2021), 2008.04022.

109. M. Luzum and H. Petersen, Initial State Fluctuations and Final State Correlations in Relativistic Heavy-Ion Collisions, J. Phys. G **41**, 063102 (2014), 1312.5503.

110. M. Asakawa, S. Ejiri, and M. Kitazawa, Third moments of conserved charges as probes of QCD phase structure, Phys. Rev. Lett. **103**, 262301 (2009), 0904.2089.

111. B. Ling and M. A. Stephanov, Acceptance dependence of fluctuation measures near the QCD critical point, Phys. Rev. C **93**, 034915 (2016), 1512.09125.

112. J. Brewer, S. Mukherjee, K. Rajagopal, and Y. Yin, Searching for the QCD critical point via the rapidity dependence of cumulants, Phys. Rev. C **98**, 061901 (2018), 1804.10215.

113. B. Berdnikov and K. Rajagopal, Slowing out-of-equilibrium near the QCD critical point, Phys. Rev. D **61**, 105017 (2000), hep-ph/9912274.

114. S. Mukherjee, R. Venugopalan, and Y. Yin, Real time evolution of non-Gaussian cumulants in the QCD critical regime, Phys. Rev. C **92**, 034912 (2015), 1506.00645.

115. S. Mukherjee, R. Venugopalan, and Y. Yin, Universal off-equilibrium scaling of critical cumulants in the QCD phase diagram, Phys. Rev. Lett. **117**, 222301 (2016), 1605.09341.

116. M. Stephanov and Y. Yin, Hydrodynamics with parametric slowing down and fluctuations near the critical point, Phys. Rev. D **98**, 036006 (2018), 1712.10305.

117. Y. Akamatsu, A. Mazeliauskas, and D. Teaney, A kinetic regime of hydrodynamic fluctuations and long time tails for a Bjorken expansion, Phys. Rev. C **95**, 014909 (2017), 1606.07742.

118. Y. Akamatsu, D. Teaney, F. Yan, and Y. Yin, Transits of the QCD Critical Point (2018), 1811.05081.

119. M. Bluhm and M. Nahrgang, Time-evolution of net-baryon density fluctuations across the QCD critical region, Springer Proc. Phys. **250**, 351 (2020), 1911.08911.

120. Y. Akamatsu, A. Mazeliauskas, and D. Teaney, Bulk viscosity from hydrodynamic fluctuations with relativistic hydrokinetic theory, Phys. Rev. C **97**, 024902 (2018), 1708.05657.

121. X. An, G. Basar, M. Stephanov, and H.-U. Yee, Relativistic Hydrodynamic Fluctuations, Phys. Rev. C **100**, 024910 (2019), 1902.09517.

122. M. Martinez and T. Schäfer, Stochastic hydrodynamics and long time tails of an expanding conformal charged fluid, Phys. Rev. C **99**, 054902 (2019), 1812.05279.

123. M. Martinez, T. Schäfer, and V. Skokov, Critical behavior of the bulk viscosity in QCD, Phys. Rev. **D100**, 074017 (2019), 1906.11306.

124. X. An, G. Başar, M. Stephanov, and H.-U. Yee, Fluctuation dynamics in a relativistic fluid with a critical point, Phys. Rev. C **102**, 034901 (2020), 1912.13456.

125. X. An, G. Başar, M. Stephanov, and H.-U. Yee, Evolution of Non-Gaussian Hydrodynamic Fluctuations, Phys. Rev. Lett. **127**, 072301 (2021), 2009.10742.

126. M. Bluhm *et al.*, Dynamics of critical fluctuations: Theory – phenomenology – heavy-ion collisions, Nucl. Phys. A **1003**, 122016 (2020), 2001.08831.

127. C. Shen and B. Schenke, Dynamical initial state model for relativistic heavy-ion collisions, Phys. Rev. **C97**, 024907 (2018), 1710.00881.

128. K. Rajagopal, G. Ridgway, R. Weller, and Y. Yin, Understanding the out-of-equilibrium dynamics near a critical point in the QCD phase diagram, Phys. Rev. D **102**, 094025 (2020), 1908.08539.

129. L. Du, U. Heinz, K. Rajagopal, and Y. Yin, Fluctuation dynamics near the QCD critical point (2020), 2004.02719.

130. J. I. Kapusta, B. Muller, and M. Stephanov, Relativistic Theory of Hydrodynamic Fluctuations with Applications to Heavy Ion Collisions, Phys. Rev. C **85**, 054906 (2012), 1112.6405.

131. K. Murase and T. Hirano, Relativistic fluctuating hydrodynamics with memory functions and colored noises (2013), 1304.3243.

132. C. Young, J. I. Kapusta, C. Gale, S. Jeon, and B. Schenke, Thermally Fluctuating Second-Order Viscous Hydrodynamics and Heavy-Ion Collisions, Phys. Rev. C **91**, 044901 (2015), 1407.1077.

133. K. Murase and T. Hirano, Hydrodynamic fluctuations and dissipation in an integrated dynamical model, Nucl. Phys. A **956**, 276 (2016), 1601.02260.

134. M. Singh, C. Shen, S. McDonald, S. Jeon, and C. Gale, Hydrodynamic Fluctuations in Relativistic Heavy-Ion Collisions, Nucl. Phys. A **982**, 319 (2019), 1807.05451.

135. M. Nahrgang, M. Bluhm, T. Schäfer, and S. Bass, Toward the description of fluid dynamical fluctuations in heavy-ion collisions, Acta Phys. Polon. Supp. **10**, 687 (2017), 1704.03553.

136. M. Nahrgang, M. Bluhm, T. Schaefer, and S. A. Bass, Diffusive dynamics of critical fluctuations near the QCD critical point, Phys. Rev. D **99**, 116015 (2019), `1804.05728`.

137. M. Nahrgang and M. Bluhm, Modeling the diffusive dynamics of critical fluctuations near the QCD critical point, Phys. Rev. D **102**, 094017 (2020), `2007.10371`.

138. A. Sakai, K. Murase, and T. Hirano, Rapidity decorrelation of anisotropic flow caused by hydrodynamic fluctuations, Phys. Rev. C **102**, 064903 (2020), `2003.13496`.

139. D. Schweitzer, S. Schlichting, and L. von Smekal, Critical dynamics of relativistic diffusion, Nucl. Phys. B **984**, 115944 (2022), `2110.01696`.

140. A. Florio, E. Grossi, A. Soloviev, and D. Teaney, Dynamics of the $O(4)$ critical point in QCD, Phys. Rev. D **105**, 054512 (2022), `2111.03640`.

141. N. Abbasi and M. Kaminski, Characteristic momentum of Hydro+ and a bound on the enhancement of the speed of sound near the QCD critical point, Phys. Rev. D **106**, 016004 (2022), `2112.14747`.

142. F. Cooper and G. Frye, Comment on the Single Particle Distribution in the Hydrodynamic and Statistical Thermodynamic Models of Multiparticle Production, Phys. Rev. D **10**, 186 (1974).

143. A. Kurkela, A. Mazeliauskas, J.-F. Paquet, S. Schlichting, and D. Teaney, Matching the Nonequilibrium Initial Stage of Heavy Ion Collisions to Hydrodynamics with QCD Kinetic Theory, Phys. Rev. Lett. **122**, 122302 (2019), `1805.01604`.

144. J. Berges, M. P. Heller, A. Mazeliauskas, and R. Venugopalan, QCD thermalization: Ab initio approaches and interdisciplinary connections, Rev. Mod. Phys. **93**, 035003 (2021), `2005.12299`.

145. H. Petersen, J. Steinheimer, G. Burau, M. Bleicher, and H. Stöcker, A Fully Integrated Transport Approach to Heavy Ion Reactions with an Intermediate Hydrodynamic Stage, Phys. Rev. C **78**, 044901 (2008), `0806.1695`.

146. J. Weil *et al.*, Particle production and equilibrium properties within a new hadron transport approach for heavy-ion collisions, Phys. Rev. C **94**, 054905 (2016), `1606.06642`.

147. J. Hammelmann and H. Elfner, Impact of hadronic interactions and conservation laws on cumulants of conserved charges in a dynamical model (2022), `2202.11417`.

148. B. Weiss, J.-F. Paquet, and S. A. Bass, Computational budget optimization for Bayesian parameter estimation in heavy ion collisions (2023), `2301.08385`.

149. S. Gavin, A. Gocksch, and R. D. Pisarski, QCD and the chiral critical point, Phys. Rev. **D49**, R3079 (1994), `hep-ph/9311350`.

150. L. P. Kadanoff, Scaling laws for Ising models near T(c), Physics Physique Fizika **2**, 263 (1966).

151. K. G. Wilson, Renormalization group and critical phenomena. 1. Renormalization group and the Kadanoff scaling picture, Phys. Rev. B **4**, 3174 (1971).

152. K. G. Wilson, Renormalization group and critical phenomena. 2. Phase space cell analysis of critical behavior, Phys. Rev. B **4**, 3184 (1971).

153. K. G. Wilson and J. B. Kogut, The Renormalization group and the epsilon expansion, Phys. Rept. **12**, 75 (1974).

154. K. G. Wilson, The Renormalization Group: Critical Phenomena and the Kondo Problem, Rev. Mod. Phys. **47**, 773 (1975).

155. K. G. Wilson, The renormalization group and critical phenomena, Rev. Mod. Phys. **55**, 583 (1983).

156. K. Rummukainen, M. Tsypin, K. Kajantie, M. Laine, and M. E. Shaposhnikov, The Universality class of the electroweak theory, Nucl. Phys. **B532**, 283 (1998), `hep-lat/9805013`.

157. T. D. Lee and C.-N. Yang, Statistical theory of equations of state and phase transitions. 2. Lattice gas and Ising model, Phys. Rev. **87**, 410 (1952), [,157(1952)].

158. M. E. Fisher, Yang-Lee edge singularity and ϕ^3 field theory, Phys. Rev. Lett. **40**, 1610 (1978).

159. P. Fonseca and A. Zamolodchikov, Ising field theory in a magnetic field: Analytic properties of the free energy (2001), `hep-th/0112167`.

160. X. An, D. Mesterhzy, and M. A. Stephanov, On spinodal points and Lee-Yang edge singularities, J. Stat. Mech. **1803**, 033207 (2018), `1707.06447`.

161. B. Widom, Equation of state in the neighborhood of the critical point, The Journal of Chemical Physics **43**, 3898 (1965).

162. J. J. Rehr and N. D. Mermin, Revised Scaling Equation of State at the Liquid-Vapor Critical Point, Phys. Rev. **A8**, 472 (1973).

163. F. Karsch, E. Laermann, and C. Schmidt, The Chiral critical point in three-flavor QCD, Phys. Lett. **B520**, 41 (2001), `hep-lat/0107020`.

164. Y. Hatta and T. Ikeda, Universality, the QCD critical / tricritical point and the quark number susceptibility, Phys. Rev. **D67**, 014028 (2003), `hep-ph/0210284`.

165. M. Bluhm and B. Kampfer, Quasi-particle perspective on critical end-point, PoS **CPOD2006**, 004 (2006), `hep-ph/0611083`.

166. D. J. Wallace and R. K. P. Zia, Parametric models and the Ising equation of state at order ε^3, J. Phys. C **7**, 3480 (1974).

167. I. D. Lawrie, Tricritical scaling and renormalisation of ϕ6operators in scalar systems near four dimensions, Journal of Physics A: Mathematical and General **12**, 919 (1979).

168. J. F. Nicoll, Critical phenomena of fluids: Asymmetric Landau-Ginzburg-Wilson model, Phys. Rev. **A24**, 2203 (1981).

169. D. J. Amit, *Field theory, the renormalization group, and critical phenomena* (Singapore, World Scientific 1984).

170. E. Brezin, D. J. Wallace, and K. G. Wilson, Feynman graph expansion for the equation of state near the critical point (Ising-like case), Phys. Rev. Lett. **29**, 591 (1972).

171. D. Poland, S. Rychkov, and A. Vichi, The Conformal Bootstrap: Theory, Numerical Techniques, and Applications, Rev. Mod. Phys. **91**, 015002 (2019), `1805.04405`.

172. R. Guida and J. Zinn-Justin, Critical exponents of the N vector model, J. Phys. **A31**, 8103 (1998), `cond-mat/9803240`.

173. J. C. Le Guillou and J. Zinn-Justin, Critical Exponents from Field Theory, Phys. Rev. **B21**, 3976 (1980).

174. A. Pelissetto and E. Vicari, Critical phenomena and renormalization group theory, Phys. Rept. **368**, 549 (2002), `cond-mat/0012164`.

175. J. Zinn-Justin, Quantum field theory and critical phenomena, Int. Ser. Monogr. Phys. **77**, 1 (1989).

176. K. E. Newman and E. K. Riedel, Critical exponents by the scaling-field method: The isotropic N-vector model in three dimensions, Phys. Rev. **B30**, 6615 (1984).

177. D. F. Litim and D. Zappala, Ising exponents from the functional renormalisation group, Phys. Rev. **D83**, 085009 (2011), `1009.1948`.

178. D. F. Litim and L. Vergara, Subleading critical exponents from the renormalization group, Phys. Lett. **B581**, 263 (2004), `hep-th/0310101`.

179. L. Adamczyk *et al.*, Energy Dependence of Moments of Net-proton Multiplicity Distributions at RHIC, Phys. Rev. Lett. **112**, 032302 (2014), `1309.5681`.

180. X. Luo, Energy Dependence of Moments of Net-Proton and Net-Charge Multiplicity Distributions at STAR, PoS **CPOD2014**, 019 (2015), `1503.02558`.

181. D. Mroczek, M. Hjorth-Jensen, J. Noronha-Hostler, P. Parotto, C. Ratti, and R. Vilalta, Mapping out the thermodynamic stability of a QCD equation of state with a critical point using active learning (2022), `2203.13876`.

182. X. An, G. Basar, M. Stephanov, and H.-U. Yee, Non-Gaussian fluctuation dynamics in relativistic fluid (2022), `2212.14029`.

183. D. T. Son and M. A. Stephanov, Dynamic universality class of the QCD critical point, Phys. Rev. **D70**, 056001 (2004), `hep-ph/0401052`.

184. P. C. Hohenberg and B. I. Halperin, Theory of Dynamic Critical Phenomena, Rev. Mod. Phys. **49**, 435 (1977).

185. K. Kawasaki, Kinetic equations and time correlation functions of critical fluctuations, Annals of Physics **61**, 1 (1970).

186. E. Nakano, V. Skokov, and B. Friman, Transport coefficients of O(N) scalar field theories close to the critical point, Phys. Rev. D **85**, 096007 (2012), `1109.6822`.

187. S. Wu, Z. Wu, and H. Song, Universal scaling of the σ field and net-protons from Langevin dynamics of model A, Phys. Rev. C **99**, 064902 (2019), 1811.09466.

188. L. Jiang and J. Chao, Non-equilibrium cumulants within model A from crossover to first-order phase transition side, Eur. Phys. J. A **59**, 30 (2023), 2112.04667.

189. T. Schaefer and V. Skokov, Dynamics of non-Gaussian fluctuations in model A, Phys. Rev. D **106**, 014006 (2022), 2204.02433.

190. S. Tang, S. Wu, and H. Song, Dynamical critical fluctuations near the QCD critical point with hydrodynamic expansion rate (2023), 2303.15017.

191. G. Pihan, M. Bluhm, M. Kitazawa, T. Sami, and M. Nahrgang, Critical net-baryon fluctuations in an expanding system, Phys. Rev. C **107**, 014908 (2023), 2205.12834.

192. C. Chattopadhyay, J. Ott, T. Schaefer, and V. Skokov, Dynamic scaling of order parameter fluctuations in model B (2023), 2304.07279.

193. J. D. Bjorken, Highly Relativistic Nucleus-Nucleus Collisions: The Central Rapidity Region, Phys. Rev. D **27**, 140.

194. R. Baier and P. Romatschke, Causal viscous hydrodynamics for central heavy-ion collisions, Eur. Phys. J. C **51**, 677 (2007), nucl-th/0610108.

195. R. Baier, P. Romatschke, and U. A. Wiedemann, Dissipative hydrodynamics and heavy ion collisions, Phys. Rev. C **73**, 064903 (2006), hep-ph/0602249.

196. P. Romatschke, Causal viscous hydrodynamics for central heavy-ion collisions. II. Meson spectra and HBT radii, Eur. Phys. J. C **52**, 203 (2007), nucl-th/0701032.

197. H. Grad, On the kinetic theory of rarefied gases, Communications on Pure and Applied Mathematics **2**, 331 (1949), https://onlinelibrary.wiley.com/doi/pdf/10.1002/cpa.3160020403.

198. J. Anderson and H. Witting, A relativistic relaxation-time model for the boltzmann equation, Physica **74**, 466 (1974).

199. S. Pratt and G. Torrieri, Coupling Relativistic Viscous Hydrodynamics to Boltzmann Descriptions, Phys. Rev. C **82**, 044901 (2010), 1003.0413.

200. M. McNelis, D. Everett, and U. Heinz, Particlization in fluid dynamical simulations of heavy-ion collisions: The iS3D module, Comput. Phys. Commun. **258**, 107604 (2021), 1912.08271.

201. M. McNelis and U. Heinz, Modified equilibrium distributions for Cooper–Frye particlization, Phys. Rev. C **103**, 064903 (2021), 2103.03401.

202. G. S. Denicol, C. Gale, S. Jeon, A. Monnai, B. Schenke, and C. Shen, Net baryon diffusion in fluid dynamic simulations of relativistic heavy-ion collisions, Phys. Rev. C **98**, 034916 (2018), 1804.10557.

203. A. Bzdak, V. Koch, and V. Skokov, Baryon number conservation and the cumulants of the net proton distribution, Phys. Rev. C **87**, 014901 (2013), 1203.4529.

204. D. Oliinychenko and V. Koch, Microcanonical Particlization with Local Conservation Laws, Phys. Rev. Lett. **123**, 182302 (2019), 1902.09775.

205. P. Braun-Munzinger, B. Friman, K. Redlich, A. Rustamov, and J. Stachel, Relativistic nuclear collisions: Establishing a non-critical baseline for fluctuation measurements, Nucl. Phys. A **1008**, 122141 (2021), 2007.02463.

206. S. Pratt and R. Steinhorst, Charge Conservation and Higher Moments of Charge Fluctuations, Phys. Rev. C **102**, 064906 (2020), 2008.08623.

207. V. Vovchenko, V. Koch, and C. Shen, Proton number cumulants and correlation functions in Au-Au collisions at sNN=7.7–200 GeV from hydrodynamics, Phys. Rev. C **105**, 014904 (2022), 2107.00163.

208. M. Bluhm, M. Nahrgang, S. A. Bass, and T. Schaefer, Impact of resonance decays on critical point signals in net-proton fluctuations, Eur. Phys. J. C **77**, 210 (2017), 1612.03889.

209. M. Szymański, M. Bluhm, K. Redlich, and C. Sasaki, Net-proton number fluctuations in the presence of the QCD critical point, J. Phys. G **47**, 045102 (2020), 1905.00667.

210. M. A. Stephanov, Evolution of fluctuations near QCD critical point, Phys. Rev. D **81**, 054012 (2010), 0911.1772.

211. V. Vovchenko, R. V. Poberezhnyuk, and V. Koch, Cumulants of multiple conserved charges and global conservation laws, JHEP **10**, 089 (2020), 2007.03850.

212. S. Floerchinger and U. A. Wiedemann, Kinetic freeze-out, particle spectra and harmonic flow coefficients from mode-by-mode hydrodynamics, Phys. Rev. **C89**, 034914 (2014), 1311.7613.

213. Y. Ohnishi, M. Kitazawa, and M. Asakawa, Thermal blurring of event-by-event fluctuations generated by rapidity conversion, Phys. Rev. C **94**, 044905 (2016), 1606.03827.

214. J. Berges, N-particle irreducible effective action techniques for gauge theories, Phys. Rev. D **70**, 105010 (2004), hep-ph/0401172.

215. S. Borsanyi, G. Endrodi, Z. Fodor, S. D. Katz, S. Krieg, C. Ratti, and K. K. Szabo, QCD equation of state at nonzero chemical potential: continuum results with physical quark masses at order mu^2, JHEP **08**, 053 (2012), 1204.6710.

216. D. Everett, C. Chattopadhyay, and U. Heinz, Maximum entropy kinetic matching conditions for heavy-ion collisions, Phys. Rev. C **103**, 064902 (2021), 2101.01130.

217. D. Teaney, The Effects of viscosity on spectra, elliptic flow, and HBT radii, Phys. Rev. C **68**, 034913 (2003), nucl-th/0301099.

218. K. Dusling, G. D. Moore, and D. Teaney, Radiative energy loss and v(2) spectra for viscous hydrodynamics, Phys. Rev. C **81**, 034907 (2010), 0909.0754.

219. W. Israel, Nonstationary irreversible thermodynamics: A Causal relativistic theory, Annals Phys. **100**, 310 (1976).

220. W. Israel and J. M. Stewart, Transient relativistic thermodynamics and kinetic theory, Annals Phys. **118**, 341 (1979).

221. A. Monnai and T. Hirano, Effects of Bulk Viscosity at Freezeout, Phys. Rev. C **80**, 054906 (2009), 0903.4436.

222. A. Jaiswal, R. Ryblewski, and M. Strickland, Transport coefficients for bulk viscous evolution in the relaxation time approximation, Phys. Rev. C **90**, 044908 (2014), 1407.7231.

223. J. M. Luttinger and J. C. Ward, Ground state energy of a many fermion system. 2., Phys. Rev. **118**, 1417 (1960).

224. G. Baym, Selfconsistent approximation in many body systems, Phys. Rev. **127**, 1391 (1962).

225. J. M. Cornwall, R. Jackiw, and E. Tomboulis, Effective Action for Composite Operators, Phys. Rev. D **10**, 2428 (1974).

226. R. E. Norton and J. M. Cornwall, On the Formalism of Relativistic Many Body Theory, Annals Phys. **91**, 106 (1975).

227. J. Berges and J. Serreau, Progress in nonequilibrium quantum field theory, in *5th Internationa Conference on Strong and Electroweak Matter* (2003), pp. 111–126, hep-ph/0302210.

228. B. Ling, T. Springer, and M. Stephanov, Hydrodynamics of charge fluctuations and balance functions, Phys. Rev. C **89**, 064901 (2014), 1310.6036.

229. A. De, C. Plumberg, and J. I. Kapusta, Calculating Fluctuations and Self-Correlations Numerically for Causal Charge Diffusion in Relativistic Heavy-Ion Collisions, Phys. Rev. C **102**, 024905 (2020), 2003.04878.

230. E. T. Jaynes, Information theory and statistical mechanics, Phys. Rev. **106**, 620 (1957).

231. E. T. Jaynes, Information theory and statistical mechanics. ii, Phys. Rev. **108**, 171 (1957).

232. L. Du and U. Heinz, (3+1)-dimensional dissipative relativistic fluid dynamics at non-zero net baryon density, Comput. Phys. Commun. **251**, 107090 (2020), 1906.11181.

233. P. Steinbrecher, The QCD crossover up to $O(\mu_B^6)$ from Lattice QCD, Ph.D. thesis, U. Bielefeld (main) (2018).